Computational Fluid Dynamics Investigation of Oscillatory Behaviour in Annular Combustors

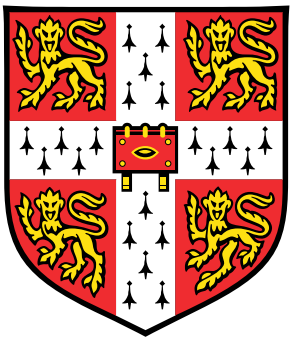

Audrey Sophie Lisa Valreau

Supervisor: Professor R. S. Cant

Department of Engineering

University of Cambridge

This dissertation is submitted for the degree of

Doctor of Philosophy

Downing College

October 2018

Declaration

This dissertation is the result of my own work and includes nothing which is the outcome of work done in collaboration except as declared in the Preface and specified in the text.

It is not substantially the same as any that I have submitted, or, is being concurrently submitted for a degree or diploma or other qualification at the University of Cambridge or any other University or similar institution except as declared in the Preface and specified in the text. I further state that no substantial part of my dissertation has already been submitted, or, is being concurrently submitted for any such degree, diploma or other qualification at the University of Cambridge or any other University or similar institution except as declared in the Preface and specified in the text.

This dissertation contains fewer than 65,000 words including appendices, bibliography, footnotes, tables and equations and has fewer than 150 figures.

Audrey Sophie Lisa Valreau
October 2018

Acknowledgements

I would first like to thank my supervisor, Professor Cant for his invaluable guidance and mentorship. It has been a privilege to work with him. His sense of humour and his drive have inspired me to push through difficult times and keep moving forward. He has been extremely encouraging all the way to the end of my degree. His dedication to the well-being of his students as well as ensuring high standards of research is remarkable, and an example to follow.

I also want to thank my advisor, Professor Juniper, who provided useful insight and comments on my work and supported me through numerous endeavours during my PhD. I also thank my collaborators from the Clean Sky DYNAMO project at Rolls-Royce Plc. and the Universities of Loughborough and Southampton, who provided me with valuable feedback on my research. I am also grateful for the experimental data from Drs. Worth and Dawson at NTNU. I want to thank Professor Ihme and his research group at the Stanford University Mechanical Engineering Department for welcoming me during the Lent term of my final year.

I would like to acknowledge the EU/EEC, Rolls-Royce Plc., Downing College, the Cambridge University Engineering Department (CUED), the Cambridge School of Technology, the Institution of Mechanical Engineers (IMechE), the Institution of Engineering and Technology (IET), the Society for Industrial and Applied Mathematics (SIAM) and the National Aeronautics and Space Administration (NASA) for providing financial support during my PhD and my visit to Stanford University.

To my friends in the Engineering Department, I would like to thank you for filling my PhD experience with great memories. I am immensely grateful for the support from Chin Yik both academically and personally. To Girish, Camille and Shrey, thank you for unforgettable adventures throughout my PhD. Thank you to Alex for being an incredible friend in my final year.

I am very grateful for Peter Benie, who has been an amazing shoulder to lean on. To Dr. Iain Dupère, I cannot thank you enough for all your support in the past eight years, which has kept me motivated throughout my time at University.

To my friends in Cambridge, I thank you for the amazing times we had and for those yet to come. My College family, Laurel, Michelle and Alison, I am so glad to have met you right at the start of this journey. Ayiba, Katharina, Jenny, thank you for making Wednesday evenings something to look forward to every week. To my band, Dave, Sam, Sam, Sami and Josh, thank you for making noise with me and making me re-discover the joy of playing live music. To John, Ross, Clare, Ed and Emma, thank you for all the movie nights, pub nights and game nights. Steph and Tina, thank you for supporting me and motivating me throughout

the years, I seriously could not have done this without you. To Emily and to Katherine, thank you for being wonderful human beings, I am extremely thankful to have you in my life.

Thank you to my amazing friends in Manchester, Lauren, Nick, Chris, Chyni, Charlotte, Adrian and Charlie, who have been incredible at keeping me grounded and focused. To my childhood friends Nil and Mary Ann, thank you for sticking by me, I am so grateful for you and for your love and support during all these years.

Finally, to my family in Paris. Merci pour tout ce que vous avez fait pour moi durant toutes ces années. Cindy, maman, papa, mamie, papi et Wanda, je n'ai pas assez de mots pour exprimer à quel point je vous aime tous. Cindy, je ne sais vraiment pas ce que j'aurais fait et où je serais sans toi. Je n'aurais jamais pu imaginer y arriver sans vous tous et votre support. Cette thèse a vu le jour grâce à vous, et vous est entièrement dédiée.

Abstract

The drive towards environmentally-friendly gas turbine engines imposes strict design constraints on combustion chambers to minimise harmful pollutant emission. Measures employed to counter this issue may result in oscillatory behaviour, which can cause substantial damage to the engine. Recent work has been undertaken on predicting this behaviour in annular combustors. The complexity of the annular design can give rise to an additional set of intricate oscillations due to the presence of interactions between neighbouring flames. The project is concerned with capturing trends in oscillatory behaviour in the laboratory-scale annular combustion chamber designed by Worth and Dawson.

Combustion-driven oscillations are studied by a variety of methods including experimental, analytical and Computational Fluid Dynamics (CFD) approaches. The cost associated with experimental studies and the limitations of most analytical models in representing complex flow phenomena both put CFD forward as a preferred tool for the present work. The aim was to create a modelling approach that maximises efficiency in both computational time and cost, to be fit for use in an industrial context. Three objectives are defined: to develop an efficient numerical methodology to bridge the gap between analytical and high-order CFD investigations; to identify ways in which to reduce computational demands in the CAD and meshing methods; and to compare the results obtained to available reference data.

A set of new inlet boundary conditions, a modular CAD geometry and a coarse meshing approach are developed to answer the computational efficiency constraint. The method also considers the use of lower-order turbulence models to reduce computational demands. Cyclic boundary conditions are applied to a single sector of the annular geometry to reduce the size of the domain.

The numerical methodology developed is compared to reference data in isothermal, reacting and forced-inlet reacting cases. Its adaptability to various operating conditions is explored by observing trends in flow behaviour with varying inlet velocity and temperature, fuel, equivalence ratio, and forcing amplitude. It is shown at each stage that the modelling approach is capable of representing expected trends. This is achieved at a fraction of the cost compared to full burner configuration studies or higher-order CFD simulations.

The thesis provides evidence that the computational methodology developed can be used to describe trends in forced oscillatory behaviour efficiently in the Worth and Dawson annular combustor rig, in the context of the reference cases studied. Additional work is necessary to determine the full scope of applicability of the new methodology.

Table of contents

List of figures

Nomenclature

Roman Symbols

A	Forcing amplitude
A_j	Pre-exponential factor
c	Progress variable
c^i	Concentration of species i
c_{coeff}	Off-centre Crank-Nicolson coefficient
C_{EBU}	Eddy Break Up model constant
C_{mix}	PaSR model constant
C_p	Specific heat
D_α	Species diffusivity
D_ϕ	Diffusivity of variable ϕ
d_i	Swirler inner diameter
d_o	Swirler outer diameter
D_t	Turbulent diffusivity
e	Internal energy
E_j	Activation energy
f	Forcing frequency
F_1, F_2	$k-\omega$ SST model blending functions

G	Filtering kernel
h	Enthalpy
h_f^0	Enthalpy of formation
$J_{\alpha,i}$	Species diffusion flux
k	Thermal conductivity
k	Turbulent kinetic energy
k_j	Reaction rate constant
L_T	Integral length scale
N	Unit normal to the surface area
p	Pressure
q	Heat release
R_0	Universal gas constant
$r_{\phi,i}$	Ratio of consecutive gradients
R_i	Chemical source term
R_w	Specific gas constant
S	Surface area
S_ϕ	Source term for variable ϕ
Sc_T	Turbulent Schmidt number
T	Temperature
t	Time
T^{nj}	Temperature in Arrhenius relation
u	Velocity
V	Cell volume
V_{enc}	Volume

W Effective reacting mixture weight

W_α Species molecular weight

x Streamwise coordinate

Y Mass fraction

y Axial location

Greek Symbols

β Sweby flux-limiter parameter

Δt Oscillation period

Δt Timestep

Δx Distance between cell surfaces

δx Distance between cell centres

Δ Filter width

δ_{ij} Kronecker delta

$\dot{\omega}$ Reaction rate

ε Turbulent kinetic energy dissipation

η Kolmogorov length scale

γ Crank-Nicolson coefficient

κ Reaction rate multiplier

λ Taylor length scale

μ Dynamic viscosity

μ_t Turbulent dynamic viscosity

ν_t Turbulent kinematic viscosity

ω Oscillation frequency

ω Specific dissipation rate

ϕ Equivalence ratio

ϕ Flow variable

ϕ Scalar

ρ Density

Σ Swirl number

$\sigma_k, \sigma_\varepsilon, C_{\varepsilon 1}, C_{\varepsilon 2}$ $k-\varepsilon$ model constants

$\sigma_k, \sigma_\omega, \beta, \beta^*, \gamma$ $k-\omega$ SST model constants

τ Numerical timestep

τ_c Chemical timescale

τ_{ij} Viscous stress tensor

τ_{ij}^s Subgrid scale stresses

τ_{mix} Turbulent timescale

Θ_e Vane angle

φ Flux-limiter operator

φ_{sw} Sweby flux-limiter

Superscripts

$'$ Subgrid quantity

$''$ Fluctuating value

$'$ Fluctuating quantity

Subscripts

0 Cell inlet

1 Cell exit

α Species

e, w East and west neighbouring cell faces

E, W, P Cell centre subscripts

f Fuel quantity

m Cell surface subscripts in three-dimensions

$n, n+1$ Consecutive timesteps

p Product quantity

r Reactant quantity

Other Symbols

$(C_s\Delta)^2$ Turbulent mixing length

$-$ Filtered value

$-$ Time-averaged value

$\overline{S_{ij}}$ Strain rate tensor

$\widehat{\ }$ Complex perturbation

$\widetilde{S}_{ij}$ Favre-filtered strain tensor

$\widetilde{\ }$ Favre-averaged value

$CD_{k\omega}$ Cross-diffusion term

F(ω) Flame function (transfer or describing)

Acronyms / Abbreviations

OH^* Chemically-excited OH

BC Boundary Condition(s)

BML Bray-Moss-Libby

CAD Computer-aided Design

CCW Counter-clockwise

CFD Computational Fluid Dynamics

CSD3 Cambridge Service for Data-driven Discovery

CW Clockwise

DNS Direct Numerical Simulation

EBU Eddy Break Up

EDC Eddy Dissipation Concept

ED Eddy Diffusivity

FDF Flame Describing Function

FSD Flame Surface Density

FTF Flame Transfer Function

FVM Finite Volume Method

LES Large Eddy Simulation

LRR Launder-Reece-Rodi

NOx Nitrogen Oxide

NS Navier-Stokes

PaSR Partially-stirred Reactor

PISO Pressure Implicit with Splitting of Operators

PVC Precessing Vertex Core

RANS Reynolds-averaged Navier-Stokes

RSM Reynolds Stress Model

SIBS Semi-Implicit Bulirsch Stoer

SSG Speziale-Sarkar-Gatski

SST Shear Stress Transport

TFSD Transported Flame Surface Density

UCAM University of Cambridge

URANS Unsteady Reynolds-averaged Navier-Stokes

Chapter 1

Introduction

1.1 Gas Turbine Engines

Gas turbines, or jet engines, are the most commonly used means of propulsion in modern aircraft. Air is directed through several stages of compression and expansion to produce thrust. Air and fuel are mixed in the combustion chamber to provide heat to the cycle. A gas turbine engine cutaway is presented in figure 1.1 where the location of the combustion chamber is indicated. The main components include the fan, compressor, combustion chamber, turbine, and exhaust nozzle. These engines are well understood and widely explained in engineering textbooks [1].

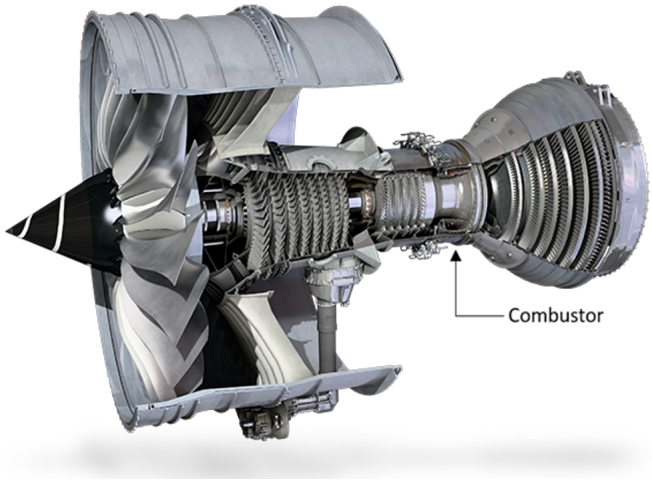

Fig. 1.1 Rolls-Royce Plc Trent 1000 engine [2], copyright Rolls-Royce, used with permission.

A major issue facing the design of gas turbines is that of harmful emissions such as NOx and soot, and engine noise [1]. Design constraints include environmental considerations

for which several solutions have been found. For instance, variable geometries can be used to adjust the armount of air entering the chamber depending on operating conditions [1]. The amount of air injected is increased at high pressure levels to reduce the fuel/air ratio and further reduce emissions of NOx and soot. In contrast, the amount of air injected is decreased at low pressures to maximise combustion efficiency. Due to the weight and cost of the complex feedback systems implemented in this solution however, variable-geometry combustors are more suited to industrial systems than aircraft combustors.

Constant operation in lean burn conditions is another solution that is typically employed in smaller systems such as aircraft engines [1], whereby the amount of air is higher than the stoichiometric amount of air required to burn the fuel. Whilst lean mixtures bring considerable improvements to the problem of emissions, they can lead to combustion instability, which under certain circumstances can damage the engine significantly. Combustion instability is thus a very topical field of interest for industrial research, in which mechanisms leading to instability and resulting flow behaviour are studied.

1.1.1 Combustion Chambers

The combustor, also called 'burner' or 'combustion chamber', is the part of a gas turbine engine where compressed air is mixed with fuel, reacted and directed to the turbine at a high temperature. The main components of a combustor are the air casing, diffuser, fuel injector, liner, swirler and three combustion zones including primary, secondary and dilution zones [1, 3]. Figure 1.2 shows a diagram of a typical combustor layout.

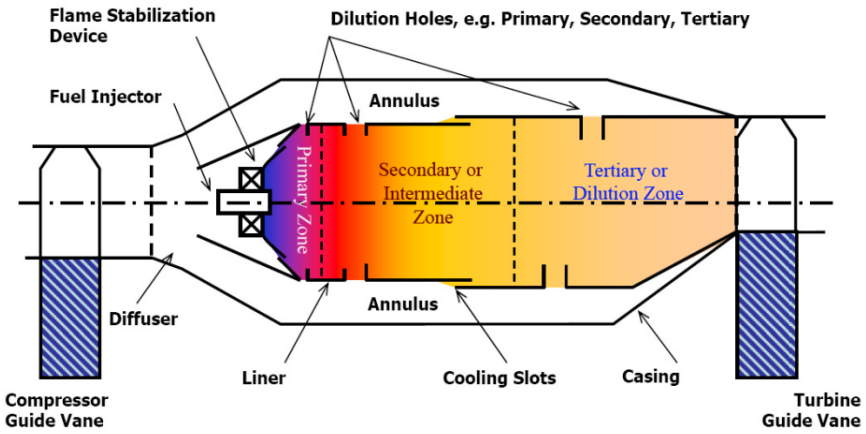

Fig. 1.2 Combustion chamber schematic diagram [4].

The diffuser minimises the pressure losses at the entrance of the burner by lowering the velocity of the incoming flow from the compressor. Swirlers are often used for flame

stabilisation. They generate flow reversal which creates a region of lower axial velocity where the flame can sit and remain alight, avoiding the risk of blow-off [1, 3]. An igniter is also usually located either at the entrance of the primary combustion zone or within it. The primary, secondary and dilution zones are used to guide the flow towards the turbine at an acceptable temperature.

1.1.2 Configurations

When designing a gas turbine engine for civil aircraft, the choice of combustor depends entirely on the overall shape of the engine [1]. Some of the most common burner configurations include tubular, tuboannular or annular combustors. Figure 1.3 illustrates the difference between the three types.

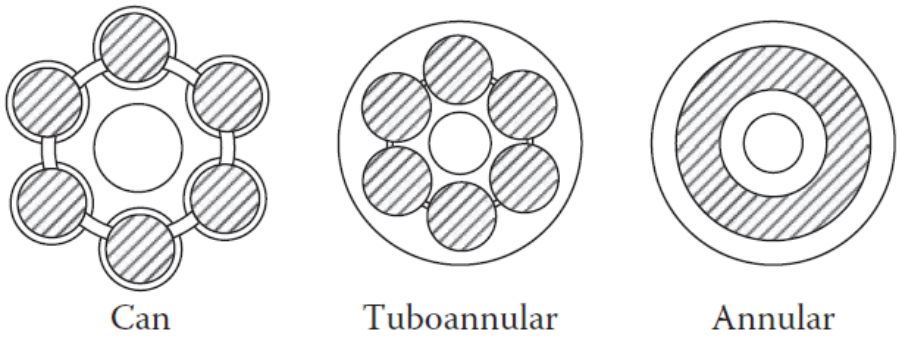

Fig. 1.3 Three basic burner configurations, top views [1].

The tubular, or 'can' combustor is made from several units all joined around a cylinder. Compressed air enters each of the chamber units, which contain an outer casing and liner [1]. Due to its considerable weight and size compared to the other two systems, this burner is not typically found in aircraft but is used in industrial plants [1].

The tuboannular, or 'can-annular' combustor provides a compromise between the structurally robust tubular type and more size-efficient annular burner. Once the mixture is ignited it is guided through the combustion chambers, or 'tubes', to the downstream annular liner [1]. The disadvantages for this type include the complexity of the diffuser design and the difficulty in obtaining a flow that is consistent across all the tubes [1].

The annular combustor consists of an annular cylindrical liner placed within an outer cylindrical casing [1]. The components along the combustor are very similar to that of a typical configuration described in section 1.1.1. The ignition process for this particular burner is referred to as the 'light-round' due to the placement of the fuel injectors around the circular

geometry. Once the combustion process has been started by the spark igniter, the flame will propagate from the originally ignited burner to its neighbours along the annulus until all the burners have been lit [5]. Potential disadvantages of this layout include issues with design and development, caused by the complexity of the flow output due to interacting flames around the annulus [6]. Maintenance of these combustors is also costly and difficult, as complete system disassembly is required to replace or repair an internal part [6]. Additionally, a high cost is associated with experimental testing due to high fluid temperature, flow rate and pressure requirements [1].

However, the compact nature of this design as well as the consistent flow at the outlet are part of the reason for which it is a preferred configuration in modern aircraft engines. Annular combustors generally require lower amounts of cooling air than can-annular burners as their surface area is typically smaller than other designs, thus this geometry is preferred when high-temperature gases are used [6]. Annular-type combustors can be found on current Rolls-Royce Trent engines [1]. As a result of the industrial interest in this configuration, the project considers annular combustor designs, for which a typical layout is presented in figure 1.4. The work presented is focused on a laboratory-scale annular burner designed by Worth and Dawson, referred to as the 'UCAM' annular rig in this thesis [7]. The burner is presented in figure 1.7.

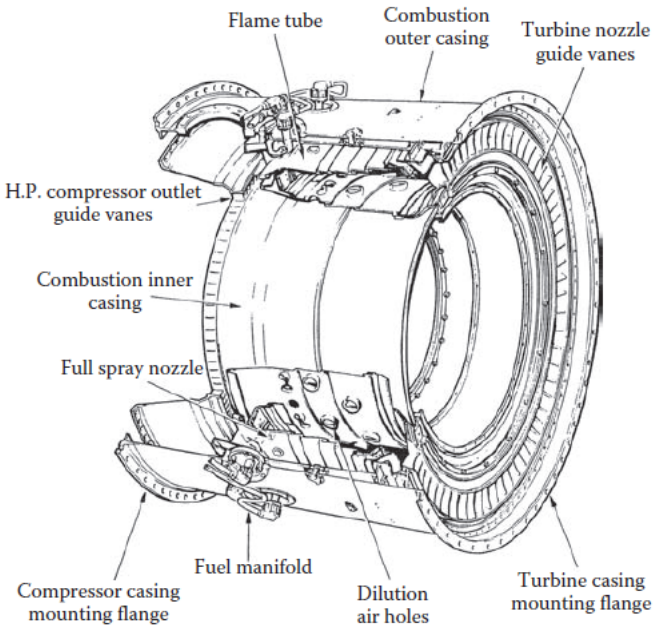

Fig. 1.4 Rolls-Royce RB211 annular combustor diagram [1].

1.2 Combustion Instability

The design requirements for a combustor include high combustion efficiency to ensure the complete combustion of the fuel, from which chemical energy is transformed into heat. Low pressure losses, reliable and maintained combustion, durability, and uniform temperature profiles at the exit are also important considerations [1, 3]. Another major requirement for modern combustion chambers is that of low pollutant emissions.

With a drive towards environmentally-friendly technologies, lean premixed combustion systems are now preferred in aircraft systems to fuel-rich approaches as they are found to produce lower NOx emissions due to the lower temperatures involved [1]. However, lean-burn systems are more prone combustion instability than fuel-rich systems. One of the major contributors to this phenomenon is thermoacoustic instability, which involves the coupling of the rate of combustion and acoustic waves [8]. Thermoacoustic instability can be quantified by the Rayleigh criterion, which is explained in further detail in chapter 2 [9, 10]. A diagram describing the feedback cycle of thermoacoustic instability is presented in figure 1.5.

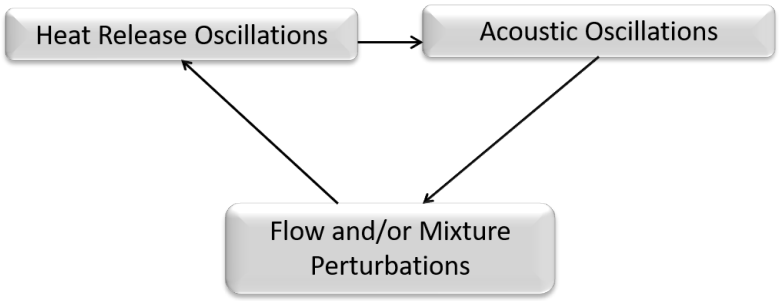

Fig. 1.5 Thermoacoustic instability feedback cycle.

The cycle depicts the interaction between acoustic waves in the chamber and unsteady combustion mechanisms. These include heat release and equivalence ratio fluctuations, and can be attributed to the lean nature of the mixtures, which are more likely to exhibit this behaviour than rich mixtures [11]. Acoustic waves can affect mixture and flow characteristics (e.g. pressure and equivalence ratio), feeding back into the existing fluctuations in heat release from unsteady combustion [8].

If sufficiently in phase with pressure oscillations, the heat release fluctuations add acoustic energy to the system and this coupling can lead to a limit cycle where a state of self-sustained, unstable oscillations is reached [12]. Resulting oscillations reduce the performance and durability of the combustor, as the vibrations generated can cause significant structural

damage [11]. Figure 1.6 below shows the damage caused by thermoacoustic instability in two NASA liquid rocket engines upon testing as shown by Poinsot [13].

Fig. 1.6 Physical damage caused by thermoacoustic instability in NASA liquid rocket engines, taken in 1957 (left) and 1963 (right) [13].

The combustor geometry can affect the acoustic modes generated by the mechanisms described above [14]. Annular combustors are subject to longitudinal, transverse, as well as azimuthal instabilities. Due to the small separation distance between burners, flame-flame interactions are an additional physical source of instability. Heat release oscillations can be significantly damped by introducing plates isolating the burners from each other, thus reducing the amount of interaction between neighbouring flames.

The study of thermoacoustics is particularly relevant and important in predicting the operability limits of a given design. Testing annular combustors experimentally can prove to be challenging and expensive [7], therefore more cost-efficient methods such as analytical modelling and computational fluid dynamics (CFD) are also commonly in use. Analytical models may require significant assumptions to be made concerning the flow, thus CFD is sometimes preferred when detailed flow characteristics need to be better represented.

CFD studies in an academic context tend towards higher-order, expensive tools for arguably better accuracy. However, industrial requirements in terms of time and cost often mean that restrictions must be applied to the modelling methods, with a preference towards efficiency rather than absolute accuracy. The work in this thesis was intended for use in industry, thus the project aimed to generate data efficiently and maintain minimal costs throughout.

1.3 UCAM Annular Combustor Design

The UCAM model burner is a plenum-burner-annular chamber configuration, which is a common design for annular combustors. The UCAM rig was found to exhibit similar characteristic oscillatory behaviour to annular burners in use in modern aircraft [15], thus data from this experimental setup can provide validation for analytical and CFD studies.

The UCAM model annular combustor is presented in figure 1.7. The rig contains a maximum of 18 burners that are equally-spaced around the annular chamber, and can be run for 12, 15 and 18-burner configurations for the same annular chamber diameters [7].

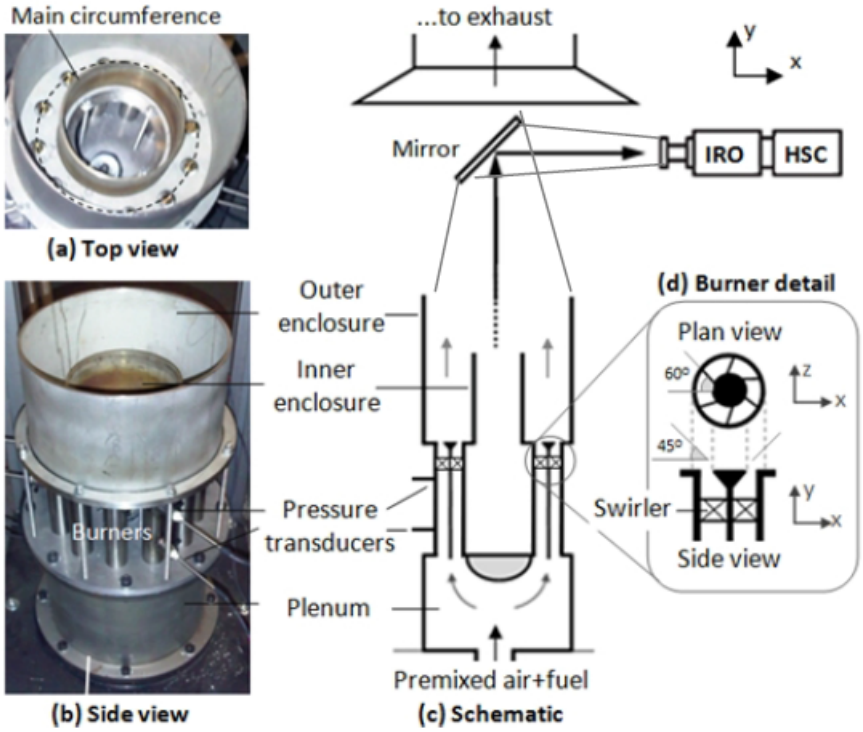

Fig. 1.7 Top, side views and diagrams of the UCAM annular rig [15].

All burners contain a bluff body with a conical end. The exit blockage ratio is set to 50%. Six-vane swirlers with an angle of 60° are fitted around the bluff bodies at a distance of 10mm to the exit of the burners [7]. The swirlers can be mounted either in the clockwise (CW) or the counter-clockwise (CCW) directions depending on the experimental requirements. Alternative swirl can also be achieved by varying the swirler direction in consecutive burners.

The primary fuel used for experiments is ethylene which is premixed with air prior to entering the chamber. Experiments have also been run using methane-air mixtures on this rig [7]. During a run the premixed flow enters the plenum chamber and is then divided by the

flow divider or 'bullet' into each of the burners upstream of the combustion chamber. The chamber is the annular region composed of the inner and outer enclosures labelled in figure 1.7, and is where the flame sits [15]. The inner and outer diameters of the annular chamber cylinders are 127mm and 212mm respectively [7].

1.4 Project Overview

1.4.1 Aims and Objectives

The project was aimed at creating an efficient methodology to represent the unsteady behaviour of the UCAM burner in response to acoustic waves using the open source CFD toolkit OpenFOAM. The work was performed from an industrial perspective, thus maximising simulation efficiency in both cost and time was a key requirement throughout. The ultimate goal of the study was to assess the use of lower-order CFD modelling as a tool to describe oscillatory behaviour in the UCAM burner. More specifically, the work was intended to:

1. Create a computational tool that is able to bridge the gap between more expensive CFD methods or experiments, and analytical modelling.

2. Create a modular, adaptable geometry that would allow for studies of any part of the combustor independently, as well as identifying ways in which to significantly decrease the time required for meshing and simulation setup.

3. Compare the tool both qualitatively and quantitatively to available and relevant data from previous CFD simulations and experiments.

1.4.2 Thesis Outline

Chapter 2 reviews combustion instability as a general phenomenon, as well as commonly used analysis methods. Chapter 3 details available CFD modelling methods and identifies the most relevant for the project. Chapter 4 describes the flame response to instability arising from the main components of an annular combustor design and explains the preliminary work undertaken on UCAM rig geometry and meshing.

The subsequent chapters outline the results obtained throughout the project. The analysis starts with method testing by comparing the data obtained to a reference case run by

Bainbridge on the UCAM rig in chapter 5 [16] and to other relevant CFD studies. Chapter 6 explores the capabilities of the tool with results for isothermal and stable and unstable reacting cases, each for a range of operating conditions. The results in chapter 6 are compared to theoretical, experimental and higher-order CFD data. Conclusions and potential directions for future work are presented in the final chapter.

Chapter 2

Literature Review

This chapter presents an overview of the physical phenomena causing oscillatory behaviour in combustion chambers. An introduction to relevant analysis methods is also provided.

Extensive literature exists with regards to fundamental physics of combustion-related oscillations, as well as their occurrence in simple systems such as bluff-body stabilised flames. More recent studies have also been published on complex combustor designs including annular combustors. However whilst recent focus has moved to complex geometries, instability mechanisms in complex systems are not yet well understood.

It is futhermore important to note that whilst the literature tends to detail the various instability processes independently for clarity purposes, they are occurring simultaneously and can interact with each other [16].

2.1 Physical Phenomena

2.1.1 Combustion Noise

The processes associated with combustion generate noise that can affect the overall performance of the engine and its lifetime [1]. Combustion noise can be divided into two separate categories that depend on the way in which the noise is generated and propagated: direct and indirect noise.

Direct noise is produced by the pressure fluctuations within the chamber [1]. As observed by Lighthill [17], pressure fluctuations caused by turbulence in flows generate noise. In reacting flows, turbulence can also affect the heat release rate in the combustion region. The resulting unsteadiness in flow expansion creates further pressure fluctuations, and thus additional noise is generated.

Direct combustion noise can be categorised as either presenting characteristics specific to 'roar' or to combustion-induced oscillations. Combustion roar, as described by Strahle [18], is found for a wide range of frequencies. In contrast, oscillations occur at frequencies that are system-dependent, and during which a feedback cycle converts energy released from chemical reactions into acoustic energy.

Indirect noise is produced by the convection of hot products away from the chamber, which create pressure fluctuations when entering the turbine and nozzle. In this case, unsteady vortical, entropy and mixture composition structures interact with the mean flow and pressure gradients aft of the chamber. Extensive analytical work has been undertaken on the subject, most notably by Marble and Candel [19] who derived an approach to characterise indirect noise in high Mach number systems. Recent studies by Ihme et al. [20] and Morgans et al. [21] have combined analytical methods and CFD to analyse the effects of indirect noise on flow behaviour. Entropy noise has been investigated experimentally by the Hochgreb group in Cambridge [22].

The work in this thesis is concerned with direct noise, in which the combustion process is prominant in generating instablity and oscillatory behaviour in combustion chambers.

2.1.2 Combustion-driven Instabilities

Poinsot and Veynante [13] described the instabilities arising from combustion as pertaining to distinctive categories according to the magnitude of their driving mechanisms. Williams [23] identified three separate categories: intrinsic, chamber and system instabilities.

Intrinsic instabilities occur locally and include small-scale interactions between the chemical and kinetic properties of the fluid, thermodiffusive instability, and hydrodynamic instability. Chamber instabilities involve the entire flame and occur when it is contained within a closed environment. Examples include thermoacoustic and shock instabilities. Finally, system instabilities involve the interaction between chamber acoustics and acoustic waves arising from other components of the engine.

Amplifiers and Oscillators

Instability refers to instances where perturbations are not sufficiently damped and can thus grow in time. As these perturbations gain energy in a particular system, the flow can be defined as either convectively or absolutely unstable [24].

Convective instabilities tend to grow in amplitude in a single direction towards the outlet of the system. For this reason, they are referred to as 'amplifiers'. These types of instabilities

will eventually exit the system, and self-excitation would only occur if there is an external disturbance continuously perturbing the flow [25].

In contrast, absolute instabilities tend to grow both in time and space thus creating a loop which allows oscillations to be fed back upstream. These instabilities are referred to as 'oscillators' or 'resonators'. As information naturally propagates in the upstream direction, the disturbance is self-sustaining [25].

In combustion chambers, the confinement of the flame can result in acoustic waves being reflected off the system boundaries back into the combustion zone. It can thus be expected that combustion chambers are prone to global flow instabilities. The presence of recirculation zones and swirl can further facilitate self-sustained oscillations in heat release and pressure by propagating perturbations upstream.

As mentioned in section 2.1.1, a particular excitation frequency is required for self-sustained oscillations to emerge as a result of the interaction between acoustic and combustion processes, which depend on the chamber design. In this specific set of conditions, a limit cycle can be reached. This is illustrated in figure 2.1, where the plot shows the evolution in time of pressure waves after an initial disturbance. The perturbation grows exponentially in amplitude before saturating in a limit cycle. A switch from a linear to a non-linear regime is found as the amplitude increases. The initial growth rate of the oscillation can be approximated by linear methods as the amplitude remains small. At larger amplitudes, non-linear behaviour in the growth rate is observed.

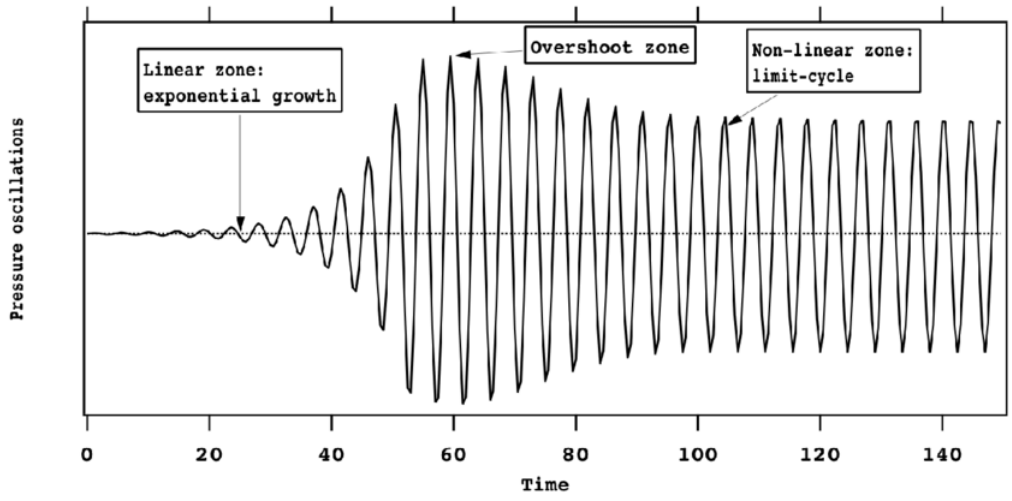

Fig. 2.1 Pressure oscillation plot against time during the formation of a limit cycle [13].

The following subsections describe the major factors in generating absolute instability. The review is divided between sources that are first inherent to the flow in combustion chambers, then to the coupling of combustion processes with acoustics. The effects of burner geometry and operating conditions on oscillatory behaviour are also introduced.

Flow Instability

Hydrodynamic Instability

The study of hydrodynamic stability is concerned with determining the state of a fluid flow, which can either be stable or unstable. Drazin [26] explains the difference between the two as stemming from their change in state after a disturbance is applied. If the disturbance does not affect the flow or only has a negligible effect on its future steady-state, it can be deemed stable. If the disturbance affects the flow in time, then the flow is defined as unstable.

Helmholtz [27] first observed instability in flows where velocity shearing occurs. It was found that vortices would form when perturbations were applied at the boundary between fluids of varying densities. Kelvin later provided a mathematical model describing this phenomenon [28], starting from linearised equations of motion. The Kelvin-Helmholtz instability forms the basis of hydrodynamic stability theory, from which a number of numerical models such as spatial and temporal methods have been developed to determine the state of a system [26].

As shown in figure 2.1, if a disturbance reaches a limit cycle, non-linear mechanisms would dictate flow behaviour in the combustion chamber. Combustion systems are also subject to hysteresis, which is defined by the dependence of their current state to the history of their previous states. In addition, bifurcations can occur in real systems when a change in control parameter affects the behaviour of the flame, transitioning from stability to instability. Bifurcations and hysteresis have been observed numerically and experimentally by Knoop et al. [29] and Lieuwen et al. [30]. Huang and Yang [31] identified flow parameters such as equivalence ratio and temperature as potential sources of instability. This is discussed further in the subsection concerned with the effects of operating conditions and burner design.

These inherent flow characteristics in combustion chambers add complexity to the non-linear behaviour of a flame and limit the applicability of linear stability theory. Whilst linear stability theory can consider the onset of instability, the method cannot predict limit cycle parameters [16]. Recently, extensive numerical and experimental work has been undertaken on determining the stability limits of combustion systems presenting non-linear flow behaviour. Work on linear stability analysis has been performed to improve its correlation with experimental and CFD data.

An example is the analytical study performed by Juniper [32], where linear stability theory was applied to three swirling reacting flow cases: a swirling wake, a swirling fuel injector, and a lean premixed gas tubine. The analysis separated phenomena pertaining to convective and absolute instability. The first case study showed that linear stability theory was capable of predicting the growth rate, frequency and the most unstable region of the flow. The study on the swirling fuel injector flow showed that the method could highlight the areas in the flow where hydrodynamic oscillations were produced. Juniper also found that the presence of a central jet weakened the oscillations, as absolute instabilities in the core then became convective. Finally, the third study showed that separate areas in the flow of a gas turbine engine are unstable and generate oscillations of varying frequency and amplitude. The study also illustrates the presence of precessing vertex cores, which are explained in further detail in the next section.

More in-depth reviews of the wider literature pertaining to the recent developments in stability analysis are beyond the scope of this thesis, where the focus is on physical effects of the instabilities in aircraft combustion chambers.

Swirl Instability

The presence of swirl in a reacting flow is often used to stabilise the flame by means of large recirculation zones[1]. Adding swirl to a combustor design is an effective way of ensuring maintained combustion through flow reversal, which creates interactions between reactants and products. In addition, swirl produces high levels of turbulence around the recirculation zones, which in turn increases the levels of mixing. The presence of swirl also shortens the flame thus improving the compactness of the combustor design. These benefits make swirl a preferred option when choosing a method for flame stabilisation.

However, due to the rotational components it induces in the flow, swirl can itself lead to flow instability. Gupta et al. [33] have found that vortex breakdown can occur in strong swirling flows. New absolute instabilities due to the rotational components of the velocity also emerge. Figure 2.2 shows an experimental swirling water jet pattern on the left, and a diagram representing the flow instabilities along the flame on the right. As shown in the diagram, characteristic ‘S-shape’ spirals form gradually as the flow approaches the outlet of the system, and vortex breakdown is seen to cause the jet to roll up [34].

Another effect arising from swirl is that of precessing vortex cores (PVC). This phenomenon is explained by Poinsot in the diagram presented in figure 2.3 [13]. Vortices at the

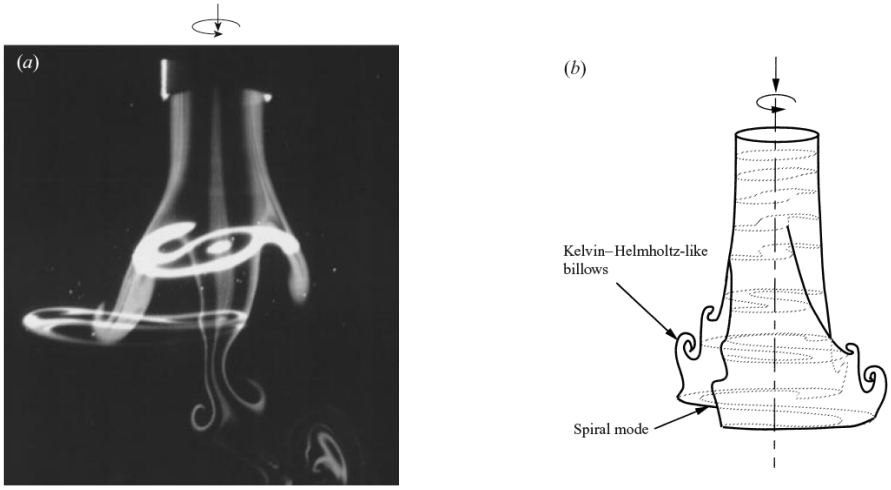

Fig. 2.2 Experimental view (left) and diagram (right) of swirling flow instability patterns [34].

centre of the flow structure are shown to precess around the central axis of the swirl. The PVC stems from a stagnation point towards the burner exit and grows until strong turbulence at the reaction zone breaks it down.

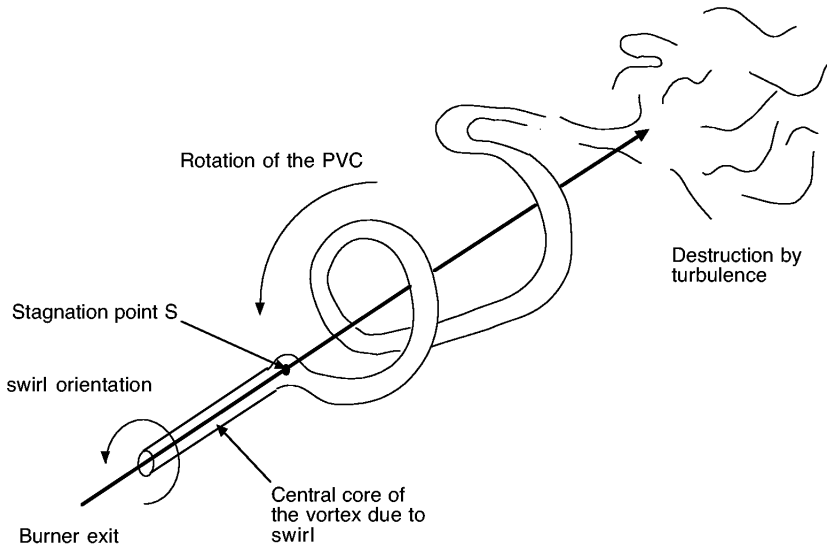

Fig. 2.3 Precessing vertex cores induced by swirl [13].

Gupta et al. [33] demonstrated the presence of PVC resulting from the vortex breakdown in swirling flames. Isothermal and reacting flow experiments were run on rigs designed for this purpose. Correlations between swirl, Reynolds number and other flow characteristics with the PVC frequency were found from isothermal studies. The reacting flow experiments

showed that the swirl parameters such as direction and angle, as well as flame confinement affect the oscillation patterns. Experimental studies by Oberleithner et al. [35] also relate to the vortex breakdown in swirling flows. Results showed that the presence of absolute instability lead to helical flow structures rotating in the opposite direction to the mean flow, or a PVC. Analytical studies by Manoharan et al. [36] have demonstrated that a PVC was present for a constant density flow, and that adding a density gradient in the profile suppressed this phenomenon.

A number of other studies concerning the effects of swirl parameters on the oscillatory response of a flame exist in the literature [7, 37]. The most relevant with regards to annular combustor designs are presented in chapter 4.

Thermoacoustic Instability

Characteristic turbulent flow features in combustion chambers give rise to absolute instabilities that are detrimental to the engine. Another major source of instability is the coupling between acoustic waves produced by the pressure fluctuations due to the confinement of the flame, and heat release fluctuations due to unsteady combustion processes.

Rijke Tube

The interaction between heat release and pressure fluctuations was first demonstrated in experiments by Rijke [38]. The Rikje tube experiment consisted of a vertical open-ended pipe with a heat source. For this rig, a heated metal gauze was placed in the lower half of the tube. The mean flow is convected in the axial direction due to the heat source. Additional heat is provided by the gauze, which creates pressure fluctuations in the form of acoustic waves, and lead to velocity fluctuations. Heat release fluctuations follow the velocity variations with a time delay that is system-specific.

A mathematical relation for this phenomenon was first provided by Rayleigh [9, 10], from which oscillatory behaviour can be expressed analytically [12, 39].

Rayleigh Criterion

Rayleigh [10] derived an expression to represent the physical effect of the phase between pressure and heat release for a confined flame. This is shown in equation 2.1, where V_{enc} is

the volume of the enclosure, t is the time, Δt is the oscillation period, and p' and q' are the fluctuating pressure and heat release respectively.

$$\int_{V_{enc}} \int_0^{\Delta t} p'q' dt dV > 0 \tag{2.1}$$

If the integral is positive during a period of oscillation, the instability grows as acoustic energy increases. Conversely, if the integral is negative, the oscillation is damped. If the integral is exactly zero, there is no exchange of energy between the acoustics and the heat release.

The Rayleigh criterion is used to quantify the thermoacoustic growth rate, or qualify the nature of the oscillations in a given system. However, the method presents some shortfalls that can hinder its applicability to real combustion chambers. One of the major setbacks of the approach is the lack of dissipation terms [12]. Whilst oscillations may grow or decay over time, the Rayleigh criterion describes either constant growth or constant decay. Nicoud and Poinsot [40] derived an expression that introduced dissipation to the criterion to account for non-linear behaviour. The new formulation improved the quantitative results obtained for thermoacoustic instability. Bainbridge [16] argued that even with these changes in place, the application of the criterion to industrial problems is debatable.

Thermoacoustic Coupling

A number of fundamental mechanisms generate thermoacoustic instability. The thermoacoustic feedback mechanism described in figure 1.5 of chapter 1 is driven by the coupling of heat release and pressure fluctuations. If sufficiently in phase, the fluctuations can lead to self-sustained oscillations. The analysis can be divided into two separate phenomena: pressure fluctuations induced by unsteady heat release, and heat release fluctuations further induced by unsteady pressure.

Pressure fluctuations can arise from unsteady heat release in the event of interaction between the flame and the system boundaries. When reaching a wall, the shape of the flame can be distorted, which may lead to local extinction and quenching. The sudden change in aspect of a steady flame surface can produce heat release fluctuations, which can further produce pressure fluctuations and vortical instability [41].

Flow instability mechanisms such as Kelvin-Helmholtz and swirl instabilities produce heat release fluctuations. The vortices present due to shear in turbulent reacting flows produce regions of high mixing, which induces high local heat release [41]. The vortex rollup created by flow instabilities may carry unburnt reactant and product mixtures downstream of the

main combustion region, which will ignite in time and add to the unsteadiness of the heat release [37].

Pressure fluctuations can affect the mixture composition as the steadiness in supplies of air and fuel is dictated by the pressure drop across the inlets. An increase in pressure in the air supply leads to a decrease in air injection, and thus causes an increase in heat release [30]. In the same way, a decrease in pressure would decrease the heat release. Due to the upstream propagation of acoustic waves by mechanisms described in previous sections, it can be expected for pressure fluctuations to be fed back into the injection system. This leads to variations in air supply (and thus equivalence ratio ϕ) and results in heat release fluctuations [12].

Crocco and Cheng [42] detailed the emergence of self-sustained oscillations from equivalence ratio instabilities. They divided the interaction between pressure fluctuations and supply of reactants in three incremental steps, each corresponding to a specific time delay. In the initial stage, the chamber pressure fluctuations are 180° out of phase with pressure fluctuations in the injectors. The first step involves a time delay between the oscillation in pressure and the resulting oscillation in inlet mass flow rate of reactants. The second time delay occurs between the variations in mass flow rate and their effects on the equivalence ratio in the combustion region. Finally, a third time delay occurs between equivalence ratio fluctuations and resulting oscillations in heat release. The sum of these time delays can result in the initial pressure disturbances to be in phase with the heat release oscillations, which causes self-sustained oscillatory behaviour.

Another source of heat release oscillations stems from the unsteady atomisation in liquid fuels, which cause fluctuations in the flame shape and local density of the fuel [1]. Liquid fuels are not considered for this project and are thus not investigated in further detail in this section.

Operating Conditions and Burner Design

Operating conditions such as inlet equivalence ratio, inlet temperature and fuel type affect the susceptibility of a combustor to combustion instability [1]. The burner geometry and the interaction between its components is also an important factor in promoting oscillatory behaviour.

Inlet Equivalence Ratio

The tendency towards operation in lean, premixed conditions leads to higher risk of instability. In aero-engine lean burners, the air is supplied by a single injector and dilution is provided only by a minimal amount of cooling air [16]. This helps reduce the overall temperature in the combustion chamber and prevent the formation of harmful emissions. However, the lack of holes in the liner to inject air and the lack of wall cooling, both being systems that can provide physical damping of oscillations, decreases the absorption of acoustic energy through the system [1]. The effects of equivalence ratio on the flame response are greater in very lean mixtures, where small changes in ϕ lead to large fluctuations in heat release [1, 43].

The effects of equivalence ratio on acoustics have been previously analysed via experiments by Zhao et al. [44]. The experimental setup consisted of a scale swirl combustor, injected with a premixed methane-air mixture. The equivalence ratio was varied from lean to rich, 0.8 to 1.2. For ϕ values of 1 to 1.2, the maximum sound pressure level increased and then decreased again, peaking at $\phi = 1.1$. The maximum value of the root-mean-square of the pressure was also found to be at $\phi = 1.1$, with flow oscillations being more pronounced at this value. This was explained by the peak in mean temperature and heat release in these conditions.

The lean mixtures from 0.8 to 0.9 did not exhibit evident limit cycle oscillations, contrary to richer mixtures from equivalence ratios of 0.9 to 1.2. When analysing pressure spectrum data, two modes were prominent, the fundamental mode and its harmonic, with two corresponding peaks in sound pressure level. For equivalence ratios of 0.8 to 0.9, the sound pressure level was almost equivalent at the frequencies corresponding to the two peaks. For richer mixtures at a given fuel volume flow rate, mode switching is observed, with the dominant mode varying from harmonic to fundamental.

From this, it is evident that the value of ϕ affects the acoustic excitation and thus the modes in the chamber. Another study on equivalence ratio was performed by Worth and Dawson on the UCAM annular rig [45], in which similar observations were made concerning mode switching. Experiments were run for equivalence ratios ranging from lean (0.875) to stoichiometric for an ethylene-air mixture. In previous work by Worth and Dawson [7], it was found that the annular combustor exhibited a bimodal behaviour with varying equivalence ratio, in which spinning or standing modes were dominant. This paper [45] instead detailed a gradual shift between spinning modes at lower equivalence ratios to standing modes at higher equivalence ratios. From $\phi = 0.9$ to 0.925, it was reported that the dominant mode of oscillation was alternating between spinning and standing. This variation in dominant mode decreased when moving towards stoichiometry, with a fully dominant standing mode at $\phi = 1$.

Worth and Dawson further described the possible mechanisms behind the mode switching that was shown by the experimental data [45]. Time-dependent behaviour of the spin ratio and node orientation were analysed. It was observed that both parameters were intrinsically linked to convective mechanisms. It was also found that the oscillations of these quantities with respect to each other occurred in a specific order, depending on the equivalence ratio chosen. Despite the presence of damping, high turbulence experimental setups led to constantly changing modes.

The two studies [44, 45] illustrated the importance of capturing equivalence ratio effects on the flow in an analysis of oscillatory behaviour.

Fuel Type and Inlet Temperature

The properties specific to a particular fuel can affect the acoustic flame response. Lefebvre [1] states that the oscillation parameters are dependent on the the fuel composition. With a variation in reaction time, there is a change in phase difference between oscillations from combustion processes and from chamber acoustics. Keller [43] confirmed that the frequency and amplitude of the oscillations was modified by fuel composition.

A number of numerical and experimental studies have analysed the effects of fuel on combustion instability. The most relevant for this work include experimental observations by Worth and Dawson on the UCAM rig [7]. A numerical investigation by Zettervall et al. [46] also modelled the effects of methane-air and ethylene-air mixtures on self-excited modes in the UCAM annular combustor. The studies are further explained in chapter 6 along with corresponding numerical simulations performed for this thesis.

Lefebvre describes a series of experiments carried out to determine the stability map of a combustor according to inlet temperatures [1]. It was concluded that due to the lower reaction time compared to corresponding acoustic time, operating at higher inlet temperatures would result in a more stable system. It was also argued that this result is not to be generalised. In small scale combustors, high frequencies are found to lead an increase in inlet temperature to produce higher instability. This is particularly relevant to the UCAM annular rig, for which in order to generate self-sustained oscillations via CFD, Bainbridge [16] set the inlet temperature to be 100K higher than the experimental inlet temperature of 300K.

Burner Geometry

It was mentioned that the confinement of a flame promotes instability. The chamber shape and size also affect the nature of the resulting instability. An annular configuration allows

for a variety of interacting acoustic modes to emerge, such as longitudinal, transversal and azimuthal (or circumferential) modes. Bainbridge [16] also specified that the frequency of azimuthal waves is lower than that of longitudinal waves. This is due to the typical shape of the annular enclosure cylinders being larger in diameter than height.

The components of the combustion chamber can also add to the existing instabilities. Typical annular combustors contain a plenum chamber, injectors, bluff bodies and swirlers to stabilise the flame, and an annular enclosure where the flame would sit. Each of the cylindrical bodies can independently produce a variety of instabilities that can interact. Annular combustors also contain a number of flames around an annulus, and it was widely found that flame-flame interactions produce additional heat release fluctuations, thus contributing to thermoacoustic instability.

The wide range of analytical, experimental and numerical studies concerned with the effects of annular combustor components on thermoacoustic stability is explored in chapter 4.

2.1.3 Control Systems

From the previous sections, it is clear that combustion chambers are prone to a very complex network of interactions between sources of oscillatory behaviour that can have devastating consequences on the system. It is thus necessary to investigate ways in which to limit the effects of combustion instability.

A variety of techniques is available to control instability in combustion chambers, and can be divided into two categories: active and passive control [1]. Passive control systems usually involve modifying physical components of the combustor. Geometry changes relevant to this category of control include flame stabiliser design to alter the frequency of vortex shedding, chamber dimensioning to alter natural acoustic modes, and injector design to decrease pressure fluctuations at the inlet [12]. Damping systems can also be included in the form of baffles, acoustic liners, and Helmhotz resonators [1, 12] to convert acoustic energy into kinetic energy. Whilst passive methods have proved to be effective in afterburners, they do not perform as well in combustion chambers where low frequencies are encountered. Due to the nature of the methods, the cost associated with passive control systems can also be an issue. Testing of each modification brought to the original component is required to optimise the design.

Active control prevents acoustic energy gain by continuously altering parameters such as reactant flow and pressure to maintain a phase difference between pressure and heat release fluctuations [12]. A feedback loop between sensors and inlet parameters is created. This type of active control is referred to as a ‘closed-loop’ system [1]. ‘Open-loop’ systems, on

the other hand, do not depend on the combustor's response to inlet conditions. They instead apply a continuous disturbance to the flow (e.g. an oscillation at a defined amplitude and frequency), with a view to peturb the relation between pressure and heat release fluctuations. Physically, this involves either implementing devices such as valves to produce an oscillatory flow, or mechanical vibrations. Problems associated with open-loop systems include the requirement for careful calibration [1].

2.2 Analytical Analysis Methods

This section is dedicated to the review of analytical methods used in stability investigations of practical systems.

2.2.1 Analytical Modelling

The main issue regarding modelling is the accurate representation of the link between heat release and pressure. Stow and Dowling [8, 47] developed a model that treats acoustic waves as a linear disturbance in a duct, with a heat source in the form of an acoustically compact flame. As part of their work, they applied the model to sections of annular combustion chambers. The models used were successful in predicting the mode shapes of the oscillations and relevant frequencies, in good agreement with experiments. It was, however, recognised by Stow and Dowling [8] that modelling a single sector (one of the burners around the annulus) using one-dimensional methods failed to describe all oscillations expected from experimental data, as the lack of information concerning neighbouring burners affected the modes observed. The models were then extended to full annular configurations by incorporating wave propagation in the azimuthal direction [47].

It was concluded by Dowling and Stow [47] that, in addition to the speed and low cost of these studies, linear analytical methods provide a good representation of the stability limits of a combustor, with comparable results to experiments in the linear regime depicted in figure 2.2. Extensions to limit-cycle amplitude prediction can also be formulated, however the flame model in this case would be dependent on the amplitude of oscillation. In this regime, non-linear flame transfer functions (described in the following section), or network models may be applied, as was done by Fanaca [48].

Despite the benefits of linear approximations listed by Dowling and Stow [47], applying linear analysis to complex mechanisms presents a number of shortfalls that make other methods more suited to this type of study, depending on the information that is to be extracted. Bainbridge [16] highlighted the importance of capturing the effects of recirculation

on the flame response. The sensitivity of combustion instabilities to these highly non-linear processes require their accurate representation in any model. Treating recirculation patterns as linearised flow behaviour may induce error.

Laera [49] argued that linear analysis may fail to characterise oscillatory behaviour in real, complex geometries. In the case of annular combustor, the numerical and experimental literature widely states that the flame-flame interactions are key features in producing thermoacoustic instability. As mentioned by Staffelbach and Wolf [50, 51], linear modelling for annular combustors cannot be universally applied as it is typically assumed that the local propagation of acoustic waves occurs purely in the longitudinal direction [50, 51]. In reality, this is not the case as interaction between flames may give rise to acoustic modes in the transverse direction. All burners are also assumed to be independent from each other and their flame transfer functions are considered equal, meaning that all flames would behave and oscillate in the same way. In real systems, swirl and other flow parameters may induce asymmetry to the flow, and flames may differ in shape from one burner to the next.

Ghirardo et al. [52] developed an analytical tool to investigate the effects of transverse excitation on azimuthal modes in axisymmetric annular combustors. An artificial parameter was derived to describe the effect of transverse forcing on heat release fluctuations quantitavely. A gradual shift from predominantly spinning to standing modes was observed with an increase in transverse parameter. It was concluded that transverse modes can significantly affect flame behaviour and should be accounted for. Ghirardo later derived a non-linear model for thermoacoustic instability in axisymmetric annular combustors [53]. The tool allowed for the analysis of a number of burners without assuming a uniform flame response across the annulus. The data gathered from the new model was in good agreement with experimental data.

2.2.2 Flame Transfer Functions

Flame transfer functions (FTFs) are used to quantify the flame response to oscillations in the frequency domain and can be used to compare the behaviour of combustion systems of varying designs or operating conditions. The typical formulation of an FTF is given by:

$$F(\omega) = \frac{\widehat{q}(\omega)/\overline{q}}{\widehat{u}(\omega)/\overline{u}} \tag{2.2}$$

Here, q refers to the heat release rate, u to the velocity and ω to the oscillation frequency. The bar represents mean quantities, and the hat, the oscillation amplitude of the parameter at a frequency ω. $F(\omega)$ is a complex number, from which the gain and phase of oscillations can be calculated. The parameter on the denominator shown in this equation is velocity. This can

be changed to any potential source of instability such as equivalence ratio or pressure [12]. An FTF formulated as such is only applicable to linear systems as the gain is independent of oscillation amplitude [16]. The comments made by Stow and Dowling [47] concerning linear modelling are relevant here. The assumption of linearity in the flame response may not be suited to unstable complex systems, but this approximation still provides valuable information from which behaviour in the limit-cycle regime can be extrapolated.

Analytical models have been developed to incorporate the time delays associated to combustion instability. Bloxsidge et al. [54] derived expressions both in the time and frequency domain to account for the time delays, according to the design and operating conditions considered. In general, the approach predicted the gain and phase of oscillations in good agreement with experimental results, but had limited success in doing so for complex systems. This was also found in studies by Armitage et al. [55, 56], who performed similar calculations on flows with swirl. Adding this new flow parameter affected the accuracy of the results when compared to experimental data.

Extensions to FTFs to account for the amplitude dependence of the flame response are found in flame describing functions (FDFs) [12]. This essentially incorporates some non-linearity effects into the linear relations. The typical formulation of an FDF is given by:

$$F(\omega) = \frac{\widehat{q}(\omega,\widehat{u})/\overline{q}}{\widehat{u}(\omega)/\overline{u}} \tag{2.3}$$

Some of the limitations of the FTF method in complex systems can be overcome by using the FDF approach. In studies by Laera [57] and Ghirardo [53], non-linear analytical investigations have been undertaken on annular combustor geometries using the FDF relations with time delay parameters. In both studies, the results obtained for the linear and non-linear operating conditions were comparable to expected behaviour from theory and experimental data.

2.3 Summary

The chapter reviewed the major processes associated to combustion instability. The analysis was divided between mechanisms emerging from turbulent flow and thermoacoustic interactions. The influence of operating conditions and burner geometry was also discussed. These mechanisms interact in a complex network of instability and lead to highly non-linear behaviour such as limit-cycles. Methods developed to control instability in combustion chambers were then detailed.

Following this, analytical analysis methods for combustion instability were explored. This part of the review was split into the analysis of fundamental behaviour pertaining to instability, and its quantitative representation. Linear modelling presented advantages in its simplicity and speed. However the approximation failed to capture limit-cycle behaviour, in which non-linear analytical models have been more successful in prediciting the mode shapes and oscillation parameters.

Whilst analytical models are beneficial in that they allow for a rapid assessment of the acoustic response of a combustor, they present limitations in the analysis of interacting flow processes in complex geometries. Historically, key flow parameters such as swirl and convection have not been well captured by purely analytical studies [49]. FDFs may be included in the analysis to preserve some of the flow features and thus improve on the accuracy of analytical studies [53, 57].

However, as it is of interest for industry to obtain a full and accurate representation of the instability mechanisms in a combustor design, alternative methods such as experiments or CFD may be considered to represent complex flow phenomena directly. The shortfalls of experimental investigations have been presented in chapter 1, with higher costs and less flexibility in the design to be tested. CFD provides a cost-effective solution that allows for complex flows to be directly represented.

FTFs and FDFs can further be evaluated from CFD results. The effect of geometry on the FDFs in annular combustors has been analysed by Xia et al. [58]. Studies used as reference for the numerical work in this thesis also used CFD to evaluate transfer functions. They include Armitage et al. [41] for an acoustically forced reacting flow, Bainbridge [16] for a self-excited annular combustor and Lee et al. [59] for a forced annular combustor. The last two used the UCAM annular rig as a reference geometry.

There is a wealth of CFD methods available for the study of complex reacting flows. The computational demands in terms of time and cost depends heavily on the approach chosen in geometry, flow and combustion modelling. The industrial view taken in this thesis calls for efficiency in the modelling methods used. A review of CFD techniques is necessary to assess their suitability in the context of this work. The next chapter provides on overview of CFD modelling approaches.

Chapter 3

Numerical Modelling Methods

This chapter introduces the fundamental concepts of numerical fluid modelling. A wide range of methods can apply to the modelling of thermoacoustics depending on the physical setup that is to be represented and the aims of the investigation. The turbulence and combustion models detailed here are those employed in the present and previous CFD studies on the UCAM annular rig and in other reference studies used to validate the simulation results in chapters 5 and 6.

3.1 Computational Fluid Dynamics

3.1.1 Fundamental Concepts

Computational Fluid Dynamics (CFD) is an effective way of modelling flow behaviour. Governing equations of fluid flow are solved by discretising the geometry that is implemented. A compressible, unsteady viscous flow is described by means of the Navier-Stokes (NS) equations that account for conservation of continuity, momentum and energy. The conservation of species is an additional consideration for reacting flows. The concepts presented in section 3.1 are developed further in major textbooks [60] and are also explained in detail by Bainbridge [16] and Lee [12].

Continuity

The continuity equation is given by:

$$\frac{\partial \rho}{\partial t} + \frac{\partial}{\partial x_i}(\rho u_i) = 0 \tag{3.1}$$

where ρ is density, u is velocity and t is time.

Momentum

The momentum equation is given by:

$$\frac{\partial}{\partial t}(\rho u_j) + \frac{\partial}{\partial x_i}(\rho u_i u_j) = -\frac{\partial p}{\partial x_j} + \frac{\partial \tau_{ij}}{\partial x_i} \tag{3.2}$$

Here, p is the static pressure and τ_{ij} is the viscous stress tensor. This term is further related to the velocity gradient in a Newtonian fluid:

$$\tau_{ij} = \mu \left[\left(\frac{\partial u_i}{\partial x_j} + \frac{\partial u_j}{\partial x_i} \right) - \frac{2}{3}\delta_{ij} \frac{\partial u_k}{\partial x_k} \right] \tag{3.3}$$

where μ is the dynamic viscosity, and δ_{ij} is referred to as Kronecker delta, which is equated to 1 in cases where $i = j$ and zero in all others.

Energy

The energy equation is given by:

$$\frac{\partial}{\partial t}(\rho e) + \frac{\partial}{\partial x_i}(\rho u_i e) = -\frac{\partial}{\partial x_i}(p u_i) + \frac{\partial}{\partial x_j}(u_i \tau_{ij}) + \frac{\partial}{\partial x_i}\left(k\frac{\partial T}{\partial x_i} - \sum_{\alpha=1}^{N} h_\alpha J_{\alpha,i} \right) \tag{3.4}$$

where k is the thermal conductivity, T is temperature, subscript α refers to the species, h_α to the species enthalpy, and $J_{\alpha,i}$, to the species diffusion flux.

In the last term on the right hand side of equation 3.4, $\left(k\frac{\partial T}{\partial x_i}\right)$ corresponds to the Fourier law for heat conduction. The term $\left(\sum_{\alpha=1}^{N} h_\alpha J_{\alpha,i}\right)$ is the heat transport by mass diffusion of the species. The diffusion flux can be expressed using Fick's law as:

$$J_{\alpha,i} = -\rho D_\alpha \frac{\partial Y_\alpha}{\partial x_i} \tag{3.5}$$

where D_α is the species diffusivity and Y_α is the species mass fraction.

The internal energy e is related to the absolute temperature as follows:

$$e = \int_{T_0}^{T} C_p dT + \sum_{\alpha=1}^{N} h^0_{f,\alpha} Y_\alpha - \frac{p}{\rho} + \frac{1}{2} u_i u_i \tag{3.6}$$

where C_p is the specific heat taken at constant pressure and $h^0_{f,\alpha}$ is the enthalpy of formation of the species.

Species

The species mass fraction can be used to represent the evolution of the species during a reaction. Species mass fraction conservation is defined by the following:

$$\frac{\partial}{\partial t}(\rho Y_\alpha) + \frac{\partial}{\partial x_i}(\rho u_i Y_\alpha) = -\frac{\partial}{\partial x_i}\left(J_{\alpha,i}\right) + \dot{\omega}_\alpha \tag{3.7}$$

The variable $\dot{\omega}_\alpha$ refers to the reaction rate. A description of methods available to model the reaction rate is provided in section 3.3. The species diffusion flux $J_{\alpha,i}$ is given by equation 3.5.

Equation of State

The equation of state describes the relation between pressure and the conserved quantities and is required to provide closure to the system of equations. The ideal gas equation is used to relate the pressure to the density and temperature as follows:

$$p = \rho R_w T \tag{3.8}$$

Here, R_w is the specific gas constant, defined by the ratio of universal gas constant R_0 to the effective molecular weight of the reacting mixture W, given by:

$$\frac{R_0}{W} = R_0 \sum_{\alpha=1}^{N} \frac{Y_\alpha}{W_\alpha} \tag{3.9}$$

where W_α is the molecular weight of species α.

3.1.2 Numerical Discretisation

Finite Volume Method

The most common approach used to solve the Navier-Stokes equations is the finite volume method (FVM). In this approach, the geometry of interest is divided in distinct control volumes where information concerning flow variables is stored at the centre. The collection of control volumes, or cells, forms the mesh representing the computational domain. Figure 3.1 shows a one-dimensional control volume.

In figure 3.1, e and w represent the east and west edges (or surfaces for multi-dimensional control volumes) of the cell respectively. E and W represent the centre of the neighbouring cells, and P is the centre of the cell considered. Δx is the distance between cell edges or surfaces, and δx_e and δx_w are the distances between P and E, and P and W respectively. The

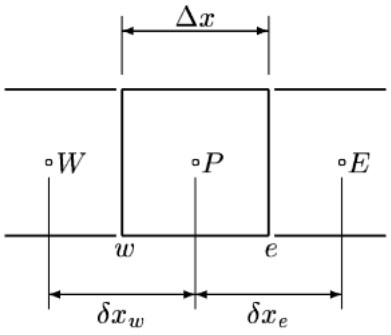

Fig. 3.1 Example of a one-dimensional cell [61].

flow is assumed here to move from west to east.

The differential formulation of the Navier-Stokes equations are integrated over each computational cell [12]. The Gauss divergence theorem converts the spatial derivatives of a quantity ϕ into integrals over the cell surfaces and is given by:

$$\int_V (\nabla.\phi) dV = \int_S N.\phi \mathrm{d}S \tag{3.10}$$

where V is the volume, S is the cell surface and N is the unit normal to the surface [12]. This equation can be extended to three-dimensional control volumes and forms the basis for the spatial discretisation of the NS equations described in the next section.

Discretisation Schemes

Spatial Discretisation

A generalised form of the conservation equations can be formulated as follows [62]:

$$\frac{\partial \rho \phi}{\partial t} = S_\phi + \frac{\partial}{\partial x_i}\left[\Gamma_\phi \frac{\partial \phi}{\partial x_i} - \rho u_i \phi\right] \tag{3.11}$$

where ϕ is the transported variable, Γ_ϕ is the diffusivity specific to ϕ, and S_ϕ is the source term containing all other relevant terms for the transport of ϕ. The steady transport equation can be formulated from equation 3.11 by neglecting the transient term as follows:

$$\frac{\partial}{\partial x_i}\left(\rho u_i \phi - \Gamma_\phi \frac{\partial \phi}{\partial x_i}\right) = S_\phi \tag{3.12}$$

Using the Gauss theorem described in equation 3.10, equation 3.12 can be written in its integral form for three-dimensional control volumes as follows:

$$\sum_m \int_{S_m} \frac{\partial}{\partial x_i}\left(\rho u_i \phi - \Gamma_\phi \frac{\partial \phi}{\partial x_i}\right) \mathrm{d}S_m = \int_V S_\phi \mathrm{d}V \tag{3.13}$$

where subscript m represents the cell surfaces in three-dimensions. In equation 3.13, the term on the right hand side is the volume integral of the source term, which can be evaluated by approximating [62]:

$$\int_V S_\phi \mathrm{d}V \approx S_\phi V \tag{3.14}$$

The terms in the surface integral on the left hand side of equation 3.13 are the convective and diffusive fluxes through the cell respectively. For both of these terms, ϕ can be evaluated using linear interpolation and the central differencing scheme respectively as shown in equations 3.15 and 3.16. These equations are given for a one-dimensional control volume for clarity but can be expanded to three-dimensional cells if required.

$$\int_w^e \frac{\partial}{\partial x_i}(\rho u_i \phi)\mathrm{d}x \approx (\rho u)_e \frac{\phi_E + \phi_P}{2} - (\rho u)_w \frac{\phi_P + \phi_W}{2} \tag{3.15}$$

$$\int_w^e \frac{\partial}{\partial x_i}\left(\Gamma_\phi \frac{\partial \phi}{\partial x_i}\right)\mathrm{d}x = \left(\Gamma_\phi \frac{\partial \phi}{\partial x_i}\right)_e - \left(\Gamma_\phi \frac{\partial \phi}{\partial x_i}\right)_w \approx \Gamma_{\phi,e} \frac{\phi_E - \phi_P}{\delta x_e} - \Gamma_{\phi,w} \frac{\phi_P - \phi_W}{\delta x_w} \tag{3.16}$$

As in figure 3.1, the subscript P represents the cell centre considered and E and W represent the east and west cell centres respectively. The subscripts e and w represent the east and west surfaces of the cell. The linear interpolation scheme for the convection flux equation is often referred to as central differencing, due to its similarities with the classical scheme used in the diffusion flux approximation [61].

The schemes result in a second-order accurate approximation of the variable ϕ. The central differencing scheme presents advantages in its computational efficiency, good accuracy in combustion problems and easy implementation [62]. However, the use of this scheme may generate unphysical oscillatory behaviour in a transient numerical solution, and becomes unstable for Peclet numbers greater than 2 [61, 63]. First-order schemes such as first-order upwind may be preferred for their higher numerical stability but are less accurate than second-order schemes.

Methods used to counter the disadvantages of both first and second-order approaches include flux limiters, which implement first-order schemes in regions of high gradients and

maintain second-order accuracy otherwise. For example, a flux-limiting operator can be applied to a discretised flux F, centred at cell i as follows:

$$F_{i+\frac{1}{2}} = F_i + \varphi(r_{\phi,i})\frac{(F_{i+1} - F_i)}{2} \tag{3.17}$$

where φ is the flux-limiting operator, subscript $i+\frac{1}{2}$ corresponds to the downstream edge or surface of the cell, and $r_{\phi,i}$ is the ratio of consecutive gradients of a variable ϕ, given by:

$$r_{\phi,i} = \frac{\phi_i - \phi_{i-1}}{\phi_{i+1} - \phi_i} \tag{3.18}$$

If the limiter is set to zero, the fluxes are represented by a first-order scheme. In contrast, a value of one would implement a higher-order scheme. Various flux limiters exist that differ in their formulation of the switch between first-order and higher-order schemes [61]. These include the Sweby flux limiter [64], for which the formulation is provided below:

$$\varphi_{sw}(r_{\phi,i}) = \max[0, \min(\beta r_{\phi,i}, 1), \min(r_{\phi,i}, \beta)] \tag{3.19}$$

where φ_{sw} is the Sweby flux-limiter function, and β is a value between 1 and 2, with $\lim_{r_{\phi,i}\to\infty} \varphi_{sw}(r_{\phi,i}) = \beta$.

In this work, spatial discretisation was achieved by means of the second-order accurate central differencing scheme for smooth regions. The Sweby flux-limiter was used to ensure boundedness in high-gradient areas as was made available in the standard OpenFOAM solution schemes.

Temporal Discretisation

The generalised transport equation presented in equation 3.11 can be expressed in its integral form to account for transient effects as:

$$\frac{1}{\Delta t}\int_t^{t+\Delta t}\int_w^e \frac{\partial}{\partial t}(\rho\phi)\mathrm{d}x\mathrm{d}t + \frac{1}{\Delta t}\int_t^{t+\Delta t}\int_w^e (\rho u_i \phi)\mathrm{d}x\mathrm{d}t = \frac{1}{\Delta t}\int_t^{t+\Delta t}\int_w^e \frac{\partial}{\partial x_i}\left(\Gamma_\phi \frac{\partial \phi}{\partial x_i}\right)\mathrm{d}x\mathrm{d}t + \frac{1}{\Delta t}\int_t^{t+\Delta t}\int_w^e S_\phi \mathrm{d}x\mathrm{d}t \tag{3.20}$$

where Δt is the timestep size. Spatial integrals are approximated using the method described in the previous section, and the transient term $\frac{\partial}{\partial t}(\rho\phi)$ is integrated in space using

the same approximation as for the source term S_ϕ in equation 3.14. The resulting transient term is integrated over time as follows:

$$\frac{1}{\Delta t}\int_{t}^{t+\Delta t}\frac{\partial}{\partial t}(\rho\phi)\Delta x \mathrm{d}t = \frac{\Delta x}{\Delta t}\left((\rho\phi_P)^{n+1} - (\rho\phi_P)^{n}\right) \tag{3.21}$$

The temporal discretisation of convective and diffusive fluxes can be achieved via numerical schemes of varying accuracy. Second-order accurate schemes include the Crank-Nicolson scheme, which in a similar fashion to the central differencing procedure yields the following convective and diffusive terms respectively [61, 65]:

$$\begin{aligned}\frac{1}{\Delta t}\int_{t}^{t+\Delta t}\Big((\rho u_i\phi)_w - (\rho u_i\phi)_e\Big)\mathrm{d}t \approx \\ \frac{1}{2}\left(\rho u_e^{n+1}\frac{\phi_P^{n+1}+\phi_E^{n+1}}{2} + \rho u_e^{n}\frac{\phi_P^{n}+\phi_E^{n}}{2}\right) \\ -\frac{1}{2}\left(\rho u_w^{n+1}\frac{\phi_P^{n+1}+\phi_W^{n+1}}{2} + \rho u_w^{n}\frac{\phi_P^{n}+\phi_W^{n}}{2}\right)\end{aligned} \tag{3.22}$$

$$\begin{aligned}\frac{1}{\Delta t}\int_{t}^{t+\Delta t}\left(\left(\Gamma_e\frac{\phi_E-\phi_P}{\delta x_e}\right) - \left(\Gamma_w\frac{\phi_P-\phi_W}{\delta x_w}\right)\right)\mathrm{d}t \approx \\ \left(\Gamma_e\frac{\phi_E^{n+1}-\phi_P^{n+1}}{2\delta x_e}\right) - \left(\Gamma_w\frac{\phi_P^{n+1}-\phi_W^{n+1}}{2\delta x_w}\right) + \\ \left(\Gamma_e\frac{\phi_E^{n}-\phi_P^{n}}{2\delta x_e}\right) - \left(\Gamma_w\frac{\phi_P^{n}-\phi_W^{n}}{2\delta x_w}\right)\end{aligned} \tag{3.23}$$

The Crank-Nicolson scheme can be subject to similar issues as the central differencing scheme, with unphysical oscillations arising in the solution over time [61, 63]. Flux-limiters can also be applied here to reduce this effect. A limiter function is built into the OpenFOAM Crank-Nicolson formulation, which switches the temporal scheme to the first-order accurate Euler-implicit method when required to ensure boundedness [66].

Similarly to the spatial discretisation flux-limitation process presented in equation 3.17, the temporal discretisation flux-limitation approach can be described by the following [67]:

$$y^{n+1} - y^n \approx \left(\gamma F^{n+1} + (\gamma - 1) F^n \right) \Delta t \tag{3.24}$$

where the term $y^{n+1} - y^n$ is a function of the timestep Δt and flux F. The term on the left hand side of equation 3.24 gives rise to various scheme formulations depending on the value of γ. Here, γ is the Crank-Nicolson coefficient, equal to $\frac{1}{2}$ for the classical, fully-centred formulation of the scheme [66], to zero for the forward explicit first-order Euler scheme and to one for the implicit first-order backward Euler scheme.

A weighting coefficient c_{coeff} is prescribed in OpenFOAM, taking a value between zero and one. This is used to 'off-centre' the numerical scheme, favouring the Euler-implicit scheme when the value tends to zero and Crank-Nicolson scheme when the value tends one [66]. The weighting coefficient is related to the Crank-Nicolson coefficient as follows:

$$\gamma = 1/(1 + c_{coeff}) \tag{3.25}$$

In this work, the flux-limited Crank-Nicolson scheme described above was implemented. A value of 0.9 for c_{coeff} was found to be suited to most complex flow cases historically [66] and was thus applied. The scheme was prescribed alongside the standard Pressure Implicit with Splitting of Operators (PISO) numerical procedure [68] for time-marching. The PISO scheme is described extensively in the literature [12, 16, 68], and its combination with the Crank-Nicolson scheme has been validated in a range of combustion CFD studies [12, 69, 70].

3.2 Turbulence Modelling

3.2.1 CFD Methods

There are many options to model turbulent reacting flow problems by solving the Navier-Stokes equations. CFD approaches can be divided into three categories: Reynolds-Averaged Navier-Stokes (RANS), Large-Eddy Simulation (LES) and Direct Numerical Simulation (DNS). To illustrate the core difference between them, energy cascade plots are shown in figures 3.2 and 3.3.

The plot of turbulent kinetic energy against wavenumber in figure 3.2 represents the energy cascading down from larger eddies (integral length scale L_T), to smaller eddies (Taylor (λ) and Kolmogorov (η) length scales). Figure 3.3 illustrates the three different

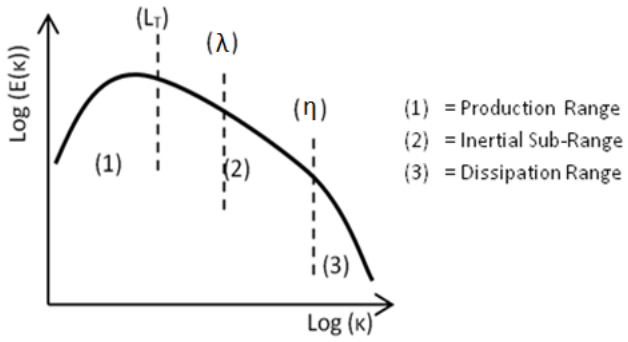

Fig. 3.2 Energy cascade diagram, adapted from Staffelbach [14].

modelling approaches. In the dashed regions, the Navier-Stokes equations are solved directly. Conversely, a turbulence model is applied in the regions under the red-dotted line.

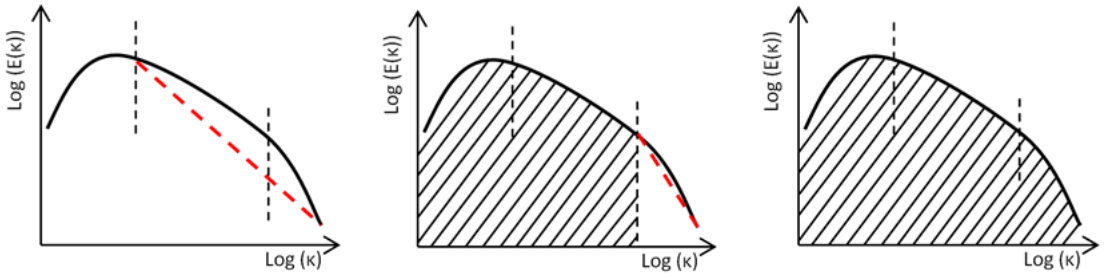

Fig. 3.3 Energy cascade for RANS (left), LES (centre) and DNS (right).

As shown on the right-most plot in figure 3.3, Direct Numerical Simulation (DNS) solves the NS equations for all turbulent length and time scales directly and no models are necessary. Complex, small scale turbulent mechanisms occur in combustion flows and are captured in detail by this method. DNS is the most expensive of the three methods, as it requires high mesh resolution and small time steps to resolve the full range of turbulent scales. In addition, both the number of mesh points and time step requirements rise significantly with Reynolds number, which implies that the cost increases rapidly with domain size. In general, DNS is used in fundamental studies as its computational cost limits its applicability to complex geometries.

RANS and LES approaches introduce models to represent some or all of the turbulent scales such that they do not need to be resolved directly. These methods are thus less computationally expensive and are preferred for simulations involving real systems in industry.

3.2.2 Steady and Unsteady RANS

The left-most plot in figure 3.3 shows that RANS methods model all scales of turbulence and are thus the least computationally demanding out of the three CFD categories. The following sections detail the implementation of RANS to solve the Navier-Stokes equations.

Averaging Methods

Turbulence induces fluctuations in the flow that are modelled in RANS through a variety of averaging methods. Steady RANS and unsteady RANS (URANS) approaches can be chosen depending on the nature of the problem [60].

The flow variables are first decomposed into their averaged and fluctuating values, and are then applied to the NS equations. For steady flows, a time-averaging method can be applied and this would result in the Reynolds-averaged Navier-Stokes (RANS) system of equations. For unsteady flows, ensemble averaging is used through which URANS equations are obtained. Unsteady flows are of interest for this thesis.

Combustion processes can lead to local changes in density. The chosen ensemble averaging method must account for this effect. In these types of problem, density-weighted approaches such as Favre-averaging are employed. The variables are decomposed into mean and fluctuating quantities:

$$\varphi = \widetilde{\varphi} + \varphi'' \tag{3.26}$$

where φ is the flow variable considered, the tilde represents Favre-averaged value, and double prime, the fluctuating value. The Favre-averaged term can be expressed as:

$$\widetilde{\varphi} = \frac{\overline{\rho\varphi}}{\overline{\rho}} \tag{3.27}$$

The relation between Favre and Reynolds-averaged values is presented below:

$$\widetilde{\varphi} = \overline{\varphi} + \frac{\overline{\rho'\varphi'}}{\overline{\rho}} \tag{3.28}$$

where the bar represents Reynolds-averaging. Implementing Favre-averaging into the NS equations results in the following system of URANS equations for continuity, momentum, energy and scalar (mass fraction or other relevant parameter):

$$\frac{\partial\overline{\rho}}{\partial t} + \frac{\partial(\overline{\rho}\widetilde{u_i})}{\partial x_i} = 0 \tag{3.29}$$

$$\frac{\partial(\overline{\rho}\widetilde{u}_j)}{\partial t}+\frac{\partial(\overline{\rho}\widetilde{u}_i\widetilde{u}_j)}{\partial x_i}=-\frac{\partial\overline{p}}{\partial x_j}+\frac{\partial\overline{\tau}_{ij}}{\partial x_i}-\frac{\partial}{\partial x_i}(\overline{\rho}\widetilde{u_i''u_j''}) \tag{3.30}$$

$$\frac{\partial(\overline{\rho}\widetilde{e})}{\partial t}+\frac{\partial(\overline{\rho}\widetilde{u}_i\widetilde{e})}{\partial x_i}=-\overline{\frac{\partial}{\partial x_i}(pu_i)}-\frac{\partial\overline{q}_i}{\partial x_i}+\overline{\frac{\partial}{\partial x_j}(u_i\tau_{ij})}-\frac{\partial}{\partial x_i}(\overline{\rho}\widetilde{u_i''e''}) \tag{3.31}$$

$$\frac{\partial(\overline{\rho}\widetilde{\phi})}{\partial t}+\frac{\partial(\overline{\rho}\widetilde{u}_i\widetilde{\phi})}{\partial x_i}=-\overline{\frac{\partial}{\partial x_i}(\rho D_\phi\frac{\partial\phi}{\partial x_i})}-\frac{\partial}{\partial x_i}(\overline{\rho}\widetilde{u_i''\phi''})+\overline{\dot{\omega}} \tag{3.32}$$

The URANS equations are not closed, and unclosed variables are evaluated via modelling. The unclosed term $\overline{\frac{\partial}{\partial x_i}(\rho D_\phi\frac{\partial\phi}{\partial x_i})}$ refers to the mean molecular diffusion and is considered negligible for large Reynolds numbers. Other unclosed terms include the Favre-averaged Reynolds stresses ($\overline{\rho}\widetilde{u_i''u_j''}$), Reynolds flux of internal energy ($\overline{\rho}\widetilde{u_i''e''}$), reactive scalar flux ($\overline{\rho}\widetilde{u_i''\phi''}$) and mean turbulent reaction rate $\overline{\dot{\omega}}$. Closure of the Reynolds stresses and fluxes is provided by means of turbulence models, and combustion models are used to close the mean reaction rate.

Turbulence Closure Problem

The most commonly used turbulence closure methods are eddy-diffusivity models [60]. The Reynolds stresses are represented using the Boussinesq hypothesis, which introduces turbulent viscosity. The equations for turbulent transport of momentum and scalar are presented below:

$$\overline{\rho}\widetilde{u_i''u_j''}=-\mu_t\overline{S_{ij}}+\frac{2}{3}\overline{\rho}\widetilde{k}\delta_{ij} \tag{3.33}$$

$$\overline{\rho}\widetilde{u_i''\phi''}=-\overline{\rho}D_t\frac{\partial\widetilde{\phi}}{\partial x_i} \tag{3.34}$$

where μ_t is the turbulent dynamic viscosity, k is the turbulent kinetic energy, $\overline{S_{ij}}$ is the strain rate tensor and D_t is the turbulent diffusivity specific to the scalar ϕ.

A number of methods can be applied to evaluate the diffusivity and viscosity terms. Zero-equation (Mixing Length Hypothesis) and one-equation (Spalart-Allmaras) models are very cost-effective. However, they present some limitations in representing complex turbulence features which limits their applicability. Two-equation models such as $k-\varepsilon$ and $k-\omega$ are very often applied to overcome this issue. More computationally intensive methods that do not rely on the Boussinesq relation can also be employed, including Reynolds Stress

Models (RSM).

$k-\varepsilon$ Models

The standard $k-\varepsilon$ model was derived by Launder et al. [71]. An expression for the conservation of turbulent kinetic energy k is first derived from the RANS equations:

$$\frac{\partial \overline{\rho}\widetilde{k}}{\partial t}+\frac{\partial \overline{\rho}\widetilde{u}_j\widetilde{k}}{\partial x_j}=\left[-\frac{1}{2}\overline{\rho}\frac{\partial \widetilde{u_j''u_i''u_i''}}{\partial x_j}-\frac{\partial \widetilde{u_i''p''}}{\partial x_j}+\mu\frac{\partial^2\widetilde{k}}{\partial x_j^2}\right]-\overline{\rho}\widetilde{u_i''u_j''}\frac{\partial \widetilde{u}_i}{\partial x_j}-\mu\widetilde{\left(\frac{\partial u_i''}{\partial x_j}\right)^2} \tag{3.35}$$

The terms on the right are representative of transport, production and dissipation of turbulent kinetic energy respectively [71]. All three terms require closure, which is achieved via modelling [16]. Transport is assumed to occur in the direction of the mean gradient. The production term is evaluated using equation 3.31. The dissipation term is evaluated using an empirical formulation for the turbulent kinetic energy dissipation ε. The resulting closed system of equations for k and ε is shown below for high Reynolds number flows:

$$\frac{\partial \overline{\rho}\widetilde{k}}{\partial t}+\frac{\partial \widetilde{u}_j\overline{\rho}\widetilde{k}}{\partial x_j}=\frac{\partial}{\partial x_j}\left(\frac{\mu_t}{\sigma_k}\frac{\partial \widetilde{k}}{\partial x_j}\right)+\mu_t\left(\frac{\partial \overline{u_i}}{\partial x_j}\right)^2-\overline{\rho}\widetilde{\varepsilon} \tag{3.36}$$

$$\frac{\partial \overline{\rho}\widetilde{\varepsilon}}{\partial t}+\frac{\partial \widetilde{u}_j\overline{\rho}\widetilde{\varepsilon}}{\partial x_j}=\frac{\partial}{\partial x_j}\left(\frac{\mu_t}{\sigma_\varepsilon}\frac{\partial \widetilde{k}}{\partial x_j}\right)+C_{\varepsilon 1}\frac{\widetilde{\varepsilon}}{\widetilde{k}}\mu_t\left(\frac{\partial \widetilde{u}_i}{\partial x_j}\right)^2-C_{\varepsilon 2}\frac{\overline{\rho}\widetilde{\varepsilon}^2}{\widetilde{k}} \tag{3.37}$$

where σ_k, σ_ε, $C_{\varepsilon 1}$ and $C_{\varepsilon 2}$ are constants that typically take values of 1, 1.3, 1.44 and 1.92 respectively [66].

The turbulent diffusivities are given by:

$$\mu_t=C_\mu\overline{\rho}\frac{\widetilde{k}^2}{\widetilde{\varepsilon}} \tag{3.38}$$

$$\overline{\rho}D_t=\frac{\mu_t}{Sc_T} \tag{3.39}$$

where C_μ is a constant of typical value 0.09 and Sc_T is the turbulent Schmidt number defined by the ratio of momentum to scalar transport due to turbulent motion. This variable is generally specified as 0.7 [16].

The standard $k-\varepsilon$ model has been used in a wide variety of CFD studies and its shortfalls are well documented and understood. The model is known to produce error in complex flows if not properly calibrated. Pope [72], Weber [73] and Durbin [74] state that the model is prone

to overpredicting turbulence intensity in the presence of flow features such as recirculation, stagnation points and streamline curvature.

The most prominent source of error in the $k-\varepsilon$ formulation is the modelling of boundary layers, thus $k-\varepsilon$ is generally applied to problems where detail in the mean flow is of greater importance than in the near-wall regions. Wall functions are used to counter this effect, the most common of which was developed by Launder and Spalding [75].

Alternative versions of the $k-\varepsilon$ model have been developed to account for complex boundary layer flows. These include the $k-\varepsilon$ re-normalisation group (RNG) [76] and realisable $k-\varepsilon$ [77]. Both new models have proven to be more accurate than the standard formulation for a range of applications [78].

$k-\omega$ Models

The standard $k-\omega$ model was derived by Wilcox [79]. Diffusivity here is modelled by the variable ω, which is the specific dissipation rate. A major benefit of using $k-\omega$ is its better accuracy in the turbulent boundary layer compared to the $k-\varepsilon$ models, which allows for greater detail to be captured in the near-wall regions. A drawback of the use of $k-\omega$ lies in the sensitivity of the model to the prescribed value of ω at the inlet [80].

A separate model derived from the standard $k-\omega$ formulation was detailed by Menter [81]. The $k-\omega$ Shear Stress Transport (SST) model uses a blend of $k-\omega$ transport equations in the near-wall regions, and $k-\varepsilon$ in the free stream and at the inlet and outlet. This approach has been preferred in a number of complex flow cases [82, 83].

The equations used in the SST formulation are similar to the those detailed for the standard $k-\varepsilon$ model. The standard $k-\varepsilon$ equations are first transformed into $k-\omega$ formulations [81]. The resulting ω-equation differs from the original $k-\omega$ formulation with an additional cross-diffusion term as well as different model constants.

Mixing of the two models is achieved by means of a blending function F_1. The original $k-\omega$ model equations are multiplied by the function F_1, and the transformed $k-\varepsilon$ model equations are multiplied by $(1-F_1)$. Both sets of equations are added together respectively to form the final $k-\omega$ SST formulation. The function F_1 is defined as one in the near wall region, and zero away from the boundaries of the domain. Blending occurs in between these regions, with the blending function F_1 changing gradually between zero and one.

The SST equations for k and ω are given by:

$$\frac{\partial \overline{\rho}\widetilde{k}}{\partial t}+\frac{\partial \widetilde{u}_j\overline{\rho}\widetilde{k}}{\partial x_j}=\tau_{ij}\frac{\partial \widetilde{u}_i}{\partial x_j}-\beta^*\overline{\rho}\widetilde{\omega}\widetilde{k}+\frac{\partial}{\partial x_j}\left[(\mu+\sigma_k\mu_t)\frac{\partial \widetilde{k}}{\partial x_j}\right] \tag{3.40}$$

$$\frac{\partial \overline{\rho}\widetilde{\omega}}{\partial t}+\frac{\partial \widetilde{u}_j\overline{\rho}\widetilde{\omega}}{\partial x_j}=\frac{\gamma}{\nu_t}\tau_{ij}\frac{\partial \widetilde{u}_i}{\partial x_j}-\beta\overline{\rho}\widetilde{\omega}^2+\frac{\partial}{\partial x_j}\left[(\mu+\sigma_\omega\mu_t)\frac{\partial \widetilde{\omega}}{\partial x_j}\right]+2\overline{\rho}(1-F_1)\sigma_{\omega 2}\frac{1}{\widetilde{\omega}}\frac{\partial \widetilde{k}}{\partial x_j}\frac{\partial \widetilde{\omega}}{\partial x_j} \tag{3.41}$$

The last term on the right hand side of equation 3.36 stems from the cross-diffusion term in the transformed $k-\varepsilon$ model. Menter [81] annotated all constants such as σ_ω and σ_k from the original $k-\omega$ model with subscript 1, and all corresponding constants from the transformed $k-\varepsilon$ model with subscript 2. For any constant ϕ, the relation between values with subscripts 1 and 2 is given by:

$$\phi=F_1\phi_1+(1-F_1)\phi_2 \tag{3.42}$$

The values of σ_k, σ_ω, β, β^* and γ are known for both subscripts 1 and 2 [81]. The set of constants with a subscript of 1 are applied exclusively to the near-wall region, and those with a subscript of 2 are applied to the free shear-layers [81]. The blending function F_1 is defined as:

$$F_1=\tanh\left(\min\left(\max\left(\frac{\sqrt{\widetilde{k}}}{0.09\widetilde{\omega}x_j};\frac{500\nu}{x_j^2\widetilde{\omega}}\right);\frac{4\overline{\rho}\sigma_{\omega 2}\widetilde{k}}{CD_{k\omega}x_j^2}\right)\right)^4\right) \tag{3.43}$$

where $CD_{k\omega}$ is the cross-diffusion term in the transformed $k-\varepsilon$ model.

The eddy kinematic viscosity ν_t is defined using another blending function, F_2:

$$\nu_t=\frac{a_1\widetilde{k}}{\max(a_1\widetilde{\omega};\Omega F_2)} \tag{3.44}$$

where a_1 is a known constant, Ω is given by $\frac{\partial \widetilde{u}_i}{\partial x_j}$ and:

$$F_2=\tanh\left(\left(\max\left(2\frac{\sqrt{\widetilde{k}}}{0.09\widetilde{\omega}x_j};\frac{500\nu}{x_j^2\widetilde{\omega}}\right);\right)^2\right) \tag{3.45}$$

The blending function F_2 applies an eddy-viscosity ν_t equal to $\left(\frac{a_1\widetilde{k}}{\Omega}\right)$ in areas of adverse pressure gradients, and applies the general formulation $\left(\nu_t=\frac{\widetilde{k}}{\widetilde{\omega}}\right)$ in the remainder of the boundary layer.

Second Moment Closure

The problems associated with eddy-diffusivity can be solved by higher-order RANS turbulence models [84]. Models where Reynolds stresses are treated directly are an intermediate step between low-order RANS and LES/DNS. The Reynolds Stress Model (RSM) [85]

considers an equation for each of the six independent Reynolds stresses. It also generally includes an additional equation to solve for ε. The most notable variants of the model include the Launder-Reece-Rodi (LRR) [85] and the Speziale-Sarkar-Gatski (SSG) [86] formulations.

RSM models are applicable to a wider range of cases than eddy-diffusivity models [16]. The higher number of equations to solve at each timestep however leads to higher computational demands than for eddy-diffusivity models. Furthermore, the use of the ε transport equation can introduce error stemming from similar sources to the $k-\varepsilon$ model [87].

Application to Swirling Flows

Some of the intrinsic characteristics of the URANS turbulence models may lead to inaccuracies when dealing with complex flow features such as swirl, which are relevant to studies on the UCAM annular rig. The question of using either eddy-diffusivity or second moment closure models does not have a universally-applicable answer and is very much case-specific. In the interest of computational efficiency, the capabilities of eddy-diffusivity models are investigated in the present work. This choice is discussed further in section 3.4.

Swirl and flame-flame interactions are assumed in this thesis to dominate the response of the flame to acoustic waves, as explained further in section 3.4.2 and in chapter 4. The representation of near-wall phenomena is thus of particular interest in this work to capture these features accurately. The ability to capture pressure variations in detail is also key to obtain a good representation of oscillatory flame behaviour.

In work by Nazri [82] and Abdel-Gayed [83] concerned with reacting flows in swirling gas turbine combustors, the use of the $k-\omega$ SST model was preferred for its more accurate representation of the flow in the near-wall region and its higher efficiency in time to convergence. It can be anticipated from these studies that the $k-\omega$ SST model would be a good option to fit the requirements set for the simulations in this thesis. A brief study was performed to explore the effects of turbulence models on the flow in the UCAM annular rig and to finalise the choice of turbulence modelling method. This is detailed in chapter 5.

3.2.3 LES

As illustrated in the centre plot of figure 3.3, the LES method solves for the larger turbulent scales directly and uses a model for the smaller scales. As this process reduces the range of scales to be resolved, the method is less computationally demanding than DNS. However,

resolving the larger scales increases the computational costs when compared to RANS and URANS methods.

Filtering

The LES procedure starts with a filtering step to separate the large and small flow features, with a view to identify locations where a turbulence model must be applied. The filtering function is presented below [88].

$$\overline{\varphi}(x,t) = \int_V G(x-x';\Delta(x))\varphi(x',t)dx' \tag{3.46}$$

The bar over the variable φ indicates that it has been filtered. Δ is the width of the filter, to which the mesh size is often assumed to be proportional. V is the volume of the domain and G is the filtering kernel. From this operation, the chosen variable φ can be divided between, or 'decomposed' into a filtered quantity indicated by an overbar, and a subgrid quantity indicated by a prime symbol. A turbulence model is applied to the subgrid quantities [89].

$$\varphi(x,t) = \overline{\varphi}(x,t) + \varphi'(x,t) \tag{3.47}$$

Applying this decomposition method to the Navier-Stokes equations is done in a similar fashion to what was described for URANS. Density-weighting is applied to the variable φ:

$$\widetilde{\varphi}(x,t) = \frac{\overline{\rho\varphi}}{\overline{\rho}} \tag{3.48}$$

The filtering process here would also be density-weighted as follows:

$$\overline{\rho\varphi(x,t)} = \int_V \rho G(x-x';\Delta(x))\varphi(x',t)dx' \tag{3.49}$$

Favre-filtering is then applied instead of Favre-averaging, which leads to the following Navier-Stokes equations for continuity, momentum, energy and scalar:

$$\frac{\partial\overline{\rho}}{\partial t} + \frac{\partial(\overline{\rho}\widetilde{u}_i)}{\partial x_i} = 0 \tag{3.50}$$

$$\frac{\partial(\overline{\rho}\widetilde{u}_j)}{\partial t} + \frac{\partial(\overline{\rho}\widetilde{u}_i\widetilde{u}_j)}{\partial x_i} = -\frac{\partial\overline{p}}{\partial x_j} + \frac{\partial\overline{\tau}_{ij}}{\partial x_i} - \frac{\partial\tau^s_{ij}}{\partial x_i} \tag{3.51}$$

$$\frac{\partial(\overline{\rho}\widetilde{e})}{\partial t}+\frac{\partial(\overline{\rho}\widetilde{u}_i\widetilde{e})}{\partial x_i}=-\overline{\frac{\partial}{\partial x_i}(pu_i)}-\frac{\partial\overline{q}_i}{\partial x_i}+\overline{\frac{\partial}{\partial x_j}(u_i\tau_{ij})}-\frac{\partial}{\partial x_i}[\overline{\rho}(\widetilde{u_ie}-\widetilde{u}_i\widetilde{e}] \tag{3.52}$$

$$\frac{\partial(\overline{\rho}\widetilde{\phi})}{\partial t}+\frac{\partial(\overline{\rho}\widetilde{u}_i\widetilde{\phi})}{\partial x_i}=-\overline{\frac{\partial}{\partial x_i}(\rho D\frac{\partial\phi}{\partial x_i})}+\overline{\dot{\omega}}-\frac{\partial}{\partial x_i}[\overline{\rho}(\widetilde{u_i\phi}-\widetilde{u}_i\widetilde{\phi}] \tag{3.53}$$

As for URANS, closure is required to solve the system of equations. The internal energy scalar flux $(\widetilde{u_ie}-\widetilde{u}_i\widetilde{e})$ and the reactive scalar flux $(\widetilde{u_i\phi}-\widetilde{u}_i\widetilde{\phi})$ can be resolved using a standard gradient assumption [89].

The subgrid scale stresses (τ^s_{ij}) are represented using turbulence models presented in the next subsection and mean reaction rate $(\overline{\dot{\omega}})$ by means of combustion models, which are presented in section 3.3.

Subgrid Scale Modelling

One of the most common subgrid scale models was formulated by Smagorinsky [90], and developed futher by Lilly [91]. The subgrid stress tensor is expressed as:

$$\tau^s_{ij}=\overline{\rho}(\widetilde{u_iu_j}-\widetilde{u}_i\widetilde{u}_j) \tag{3.54}$$

The tensor can be split into an isotropic and anisotropic term. The isotropic part can be included in the filtered pressure term. The anisotropic part is expressed by the compressible Smagorinsky formulation as:

$$\tau^s_{ij}-\frac{1}{3}\delta_{ij}\tau^s_{kk}=-2\mu_t\left(\widetilde{S}_{ij}-\frac{\delta_{ij}}{3}\widetilde{S}_{kk}\right) \tag{3.55}$$

The Favre-filtered variables $\widetilde{S}_{ij}$ and $\widetilde{S}_{kk}$ are the strain tensor and trace of strain tensor respectively. μ_t is the subgrid eddy viscosity and is given by:

$$\mu_t=\overline{\rho}(C_s\Delta)^2|\widetilde{S}_{ij}| \tag{3.56}$$

Here, $(C_s\Delta)^2$ is the turbulent mixing length, and C_s is a pre-defined constant. As before, Δ is the width of the filter, which is given by the cubic root of the cell volume. Finally, the Favre-filtered strain tensor terms are given by:

$$\widetilde{S}_{ij}=\frac{1}{2}\left(\frac{\partial\widetilde{u}_j}{\partial xi}+\frac{\partial\widetilde{u}_i}{\partial xj}\right) \tag{3.57}$$

$$|\widetilde{S}_{ij}| = \sqrt{2\widetilde{S}_{ij}\widetilde{S}_{ij}} \tag{3.58}$$

3.3 Combustion Modelling

The progress variable for a given reaction can be expressed in terms of the mass fraction of the species involved [92]:

$$c = \frac{Y_f - Y_{fr}}{Y_{fp} - Y_{fr}} \tag{3.59}$$

Here, for example, Y_f is the mass fraction of fuel. The subscript r represents reactant quantities, and p, product quantities. The progress variable is chosen as a scalar input to the corresponding Favre-averaged equation for URANS and Favre-filtered equations for LES. The transport equation for progress variable as expressed in the URANS formulation is given by:

$$\frac{\partial \overline{\rho}\tilde{c}}{\partial t} + \frac{\partial (\overline{\rho}\tilde{u}_i\tilde{c})}{\partial x_i} = \frac{\partial}{\partial x_i}(\overline{\rho}\widetilde{u_i''c''}) + \overline{\dot{\omega}} \tag{3.60}$$

The turbulent scalar flux term $\widetilde{u_i''c''}$ can be represented by a gradient transport approximation [89].

The closure of the mean reaction rate term $\overline{\dot{\omega}}$ in Favre-averaged or filtered scalar equations is performed by means of combustion models. A wide variety of combustion models pertaining to both premixed and non-premixed applications are available. Their use is also case-dependent, and a combustion modelling study is often performed to assess the effect of models on the final solution. The range of combustion models presented in the following sections is limited to those used in the reference studies in section 3.4, which demonstrate their compatibility with investigations that have similar aims to the ones in this thesis.

3.3.1 Premixed Combustion Models

Reacting flows can be qualified as premixed or non-premixed [92]. Modelling methods have also been developed to account for cases where non-premixed and premixed reactions occur simultaneously in different areas of the domain. Non-premixed flows refer to cases where reactants (fuel and oxidiser) are introduced independently into the combustion chamber. In contrast, premixed combustion refers to cases where reactants are mixed in the flow prior to entering the burner. Only premixed combustion models are considered for this thesis, as

the experiments carried out on the UCAM annular rig have been and still are performed for premixed reactions.

Eddy Break Up Model

The Eddy Break Up Model (EBU) model developed by Spalding [93] is the least complex form of premixed combustion models. This model has been extended to non-premixed combustion in the Eddy Dissipation Concept (EDC) formulation [94]. EBU assumes fast chemistry, whereby the reaction is solely controlled by mixing induced by turbulence. This is quantified by high values of the Damköhler number, which is defined by the ratio of physical to chemical timescale. The EBU formulation for reaction rate is presented below:

$$\overline{\dot{\omega}}_f = -C_{EBU}\rho\frac{\varepsilon}{k}\overline{Y}_f(1-\overline{Y}_f) \tag{3.61}$$

The variables k and ε are turbulence parameters described in section 3.2 that can be changed according to the turbulence model implemented.

Whilst the EBU model is applicable to a variety of flows, the constant C_{EBU} is very much case-specific and needs to be appropriately tuned. The reaction rate is inversely proportional to the turbulent time scale, which indicates that any error stemming from the turbulence model is amplified here. In particular, this would imply that shortfalls in the wall treatment will affect the modelled near-wall reaction rate directly. The EBU reaction rate formulation also neglects chemistry, which limits its applicability.

The shortfalls of the EBU model can be overcome in several ways. A solution would be to extend EBU to account for finite rate chemistry, as is done in the partially stirred reactor model (PaSR). The fundamental concept and reaction rate modelling for PaSR are detailed in the next section. This combustion model performed well in the reference cases by Bainbridge [16] and Zettervall et al. [46] presented in section 3.4.

Partially Stirred Reactor Model

Incorporating finite rate chemistry in the EBU model can be achieved by adding a time delay to account for chemical reaction timescales. The Partially Stirred Reactor model is an EBU/EDC-type model that accounts for finite rate chemistry [95].

Computational cells are divided into two sections, the first reacting and second non-reacting. Homogeneous mixing and completed reactions are considered in the reacting section. The reaction rate formulation for PaSR is provided below:

$$\overline{\dot{\omega}}_f = \kappa R_i(c_1^i) = \frac{c_1^i - c_0^i}{\tau} \tag{3.62}$$

The c quantities represent concentration of species i, subscript 0 indicates the cell inlet and 1 indicates the cell exit. τ is the numerical timestep, and R_i is the chemical source term. The latter is dependent on the density, molecular weight and molar concentration of species in the computational cell, stoichiometric coefficients, and the reaction rate constant. The reaction rate constant k_j is defined by the Arrhenius relation, where reaction pre-exponential factor, temperature exponential constant and activation energy are prescribed respectively as A_j, n_j and E_j:

$$k_j = A_j T^{n_j} e^{-E_j/RT} \tag{3.63}$$

Species concentration is determined by linear interpolation between values at cell inlets (subscript 0) and exits (subscript 1):

$$c_1 = \kappa c_{un} + (1-\kappa)c_0 \tag{3.64}$$

where c_{un} is the unknown concentration. The κ coefficient is the reaction rate multiplier, which is defined by:

$$\kappa = \frac{\tau_c}{\tau_c + \tau_{mix}} \tag{3.65}$$

where τ_c is the chemical timescale, which can be evaluated by solving the system of ordinary differential equations defining the reaction. This is achieved in this work using the Semi-Implicit Bulirsch Stoer (SIBS) approach [96], as was done by Bainbridge [16] and Lee et al. [59] and was implemented in the standard OpenFOAM solvers.

The variable τ_{mix} is the turbulent timescale, which depends on the turbulence model prescribed. For the $k-\varepsilon$ model, τ_{mix} would be expressed as:

$$\tau_{mix} = C_{mix}\frac{k}{\varepsilon} \tag{3.66}$$

where C_{mix} is a constant typically taking the value of 0.1.

Flame Surface Density Models

Flamelet-based formulations of reaction rate such as Flame Surface Density (FSD) and FSD-derived models can also be implemented [97]. These include Bray-Moss-Libby (BML) and Transported Flame Surface Density (TFSD) models, which were used in the URANS reference studies by Armitage et al. [41] and LES reference studies by Lee et al. [59] respectively. Both models are detailed extensively in the literature [12, 92].

Whilst BML and TFSD performed well in both of these reference cases, PaSR was preferred as a combustion model for the URANS simulations presented in chapters 5 and 6. Several tests were carried out prior to finalising the choice of combustion model using both flamelet-based and PaSR models. It was found that the PaSR model was the most compatible for the numerical setup used in OpenFOAM v2.4.0 throughout the project, allowing for better numerical stability. Improving the formulation of other combustion models for the chosen solver was considered beyond the scope of this work.

3.4 Reference CFD Investigations on Oscillatory Behaviour

This section details the studies used as validation for the work in this thesis. The aims, experimental configuration and numerical setup are presented for each investigation. Meshing methods are presented in chapter 4. Results that are used for validation are presented alongside relevant data obtained during this project in chapters 5 and 6.

3.4.1 Self-Excited Oscillations

The two self-excited oscillation CFD studies presented in this section were performed on the UCAM annular rig, which is shown in chapter 1. The first was performed by Bainbridge [16] and is referred to as the 'Bainbridge case' in this thesis for convenience. The investigation was aimed at reproducing the self-excited modes found in experiments by Worth and Dawson [7] via CFD. The CFD toolkit OpenFOAM was used with the reactingFoam solver. The PaSR combustion model was implemented and a range of turbulence modelling methods were tested to find an appropriate match with experimental data.

The fuel used was ethylene to match the experimental setup. Simulations were run on a single sector (one burner cut from the annulus) to initialise the solution, and then on the full 18-burner configuration. The plenum chamber and swirlers were cut out of the model to reduce computational expenses, and the height of the annular enclosure cylinders were adjusted so they would match the inner enclosure height of 130mm. Swirl was still represented using a custom swirl inlet velocity boundary condition, with a swirl angle that matched the physical part. The effects of geometrical simplifications on the oscillatory behaviour in annular chambers are detailed in chapter 4.

Steady single burner reacting flow simulations were run using the experimental setup values. The inlet mass flow rate was set to 3.1g/s, the temperature to ambient (300K) and the equivalence ratio to 0.8. The Reynolds number evaluated from the diameter around the

flame holder and axial velocity was $1.37\text{x}10^4$. The results from this configuration are used for validation in the first part of chapter 6.

Full burner geometry simulations were then performed. Adjusting the cylinder heights resulted in failure to generate self-sustained oscillations [16], which was also found to happen in physical testing [7]. The original experimental operating conditions were thus changed to promote self-excitation in this geometry [16]. Parameters mentioned in chapter 2 were altered: the inlet temperature was raised from 300K to 400K, the inlet mass flow rate was increased to 5g/s, and the inlet equivalence ratio was increased from 0.8 to 0.86. The equivalence ratio remained in the range of values that reportedly led to oscillations [7]. This led to an increase in Reynolds number to $1.92\text{x}10^4$. Instantaneous data from initial timesteps in the linear oscillatory regime was used as reference in chapter 5. The fluctuations at this stage were considered negligible, thus the results could be used as validation for steady flow cases.

An extensive study on the capabilities of turbulence models to capture self-excited oscillations was performed on the full burner configuration [16]. Eddy-diffusivity models tested included $k-\varepsilon$, $k-\omega$ SST and realisable $k-\varepsilon$. RSM with LRR formulation and LES with Smagorinsky subgrid scale modelling were also investigated. LES and RSM results agreed with experimental behaviour, with standing and circumferential modes well captured by the models. Realisable $k-\varepsilon$ showed significant improvement over other eddy-diffusitvity models in representing oscillatory behaviour. The standard $k-\varepsilon$ and $k-\omega$ SST formulations indeed failed to capture self-excited modes as error stemming from their limitations in representing streamline curvature produced high levels of turbulent kinetic energy, and oscillations were damped as a result. It can thus be said that without a constant input of oscillatory motion, the two-equation models were deemed insufficient to represent flow behaviour accurately.

Another study was performed by Zettervall et al. [46] on the UCAM rig, this time to appreciate the effects of fuel on self-excited behaviour. The plenum chamber was cut from the geometry but the swirlers were included in the mesh. LES simulations were run with the PaSR combustion model. The two fuels were methane and ethylene, which were found to produce different flame responses in experiments [7]. Methane flames generated purely longitudinal acoustic modes, whereas ethylene flames allowed for circumferential modes to appear.

The LES confirmed this behaviour and was able to capture the effects of flame speed in detail [46]. The lower flame speeds associated with methane led to more extensive interaction between neighbouring flames. The use of methane resulted in two counter-rotating azimuthal modes, thus weakening the global mode in this direction and favouring longitudinal modes.

Conversely, the use of ethylene resulted in two co-rotating azimuthal modes thus promoting oscillations in the azimuthal direction.

The mechanisms behind this variation in oscillatory behaviour lies in the phase difference between pressure and heat release fluctuations. This was detailed in chapter 2 and is further detailed in work by Ghirardo et al. [52]. A difference in timing between heat release and pressure oscillations can lead to varying modal dynamics between the two fuels.

A brief investigation concerned with fuel effects on a steady flame was performed for this thesis and is presented in chapter 6. Comparative data was provided by steady flame results from Zettervall et al. [46] and expected theoretical flame temperature values.

3.4.2 Forced Oscillations

Oscillatory behaviour has been monitored via acoustic forcing on a variety of combustor designs [41]. By controlling the oscillating variable, parametric studies can be set up to investigate the effects of flow parameters on the flame response [98]. A common approach to forcing consists in prescribing oscillatory behaviour to one of the inlet variables [12]. For instance, the inlet velocity was forced in studies by Kim et al. [98], Armitage et al. [41] and Lee et al. [59] to observe how resulting velocity fluctuations affect the flame. Polifke et al. noted that inlet velocity was usually the preferred parameter to force in the case of premixed flows [99].

A forced flame can provide information on the onset of instability and behaviour in a limit cycle regime [12, 41]. CFD methods are an effective way of studying forced oscillations as they allow for more flexibility in input parameters than experimental approaches [41]. Flame describing functions can be extracted from forced CFD cases to quantify the response of the flame to oscillations. The FDFs can further be used as means to compare different designs or operating conditions quantitatively [12, 41, 59, 100].

Forced oscillation CFD studies are thus of great interest for the flexibility they allow in choosing the design, operating conditions and specifically perturbed parameter, as well as for the conclusions that can be drawn from them regarding flame behaviour.

The first forced oscillation reference case used for comparison in this thesis was performed by Armitage et al. [41] and is referred to as the ‘Armitage case’ for convenience. The aim was to reproduce experimental observations concerning the effects of forcing amplitude on the flame response via CFD. URANS was preferred to LES as a modelling method due to its lower computational demands. RSM was employed with the LRR formulation. The BML combustion model was used to close the reaction rate term in the scalar equation. The

geometry was based on the experimental rig run by Balachandran [100]. A diagram of the rig is shown in figure 3.4.

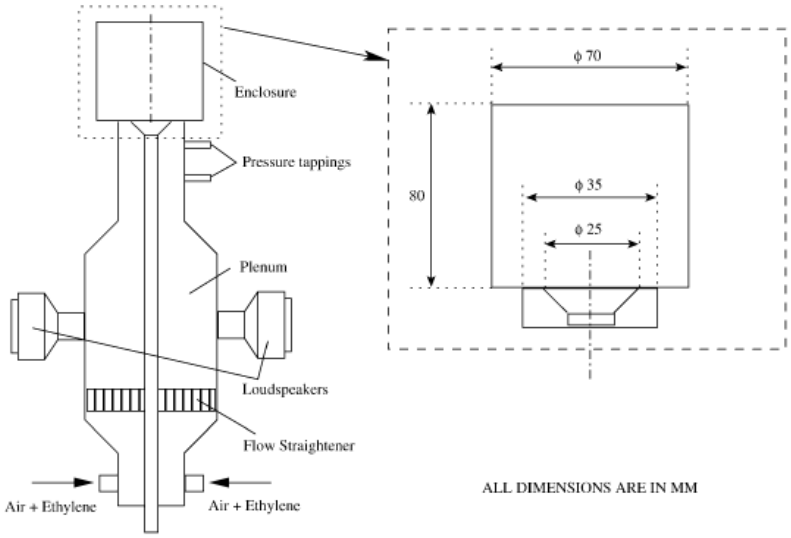

Fig. 3.4 Balachandran experimental rig [100].

Premixed ethylene and air enter a duct containing a bluff body and the flame sits in the enclosure at the top of the rig. Loudspeakers on either side provide acoustic forcing at a chosen frequency f and amplitude A. Both forcing parameters were varied to analyse the corresponding effects on the flame response. The geometry implemented in the CFD only accounted for the flame enclosure to reduce the size of the computational domain. A fixed lean equivalence ratio of 0.55 and non-swirling velocity of 9.9m/s were prescribed at the inlet to match the experimental setup. Results from the CFD were extensively compared to experimental data and good agreement was found. Investigations on the effects of swirl, swirl angle and inlet equivalence ratio were performed by Balachandran experimentally [37] but were not included in this CFD by Armitage et al. [41].

Whilst the Balachandran rig differs from the full annular combustor considered in this thesis, results can be used as comparison for simulations that were carried out on a similar geometry from the UCAM rig consisting of an enclosed single burner. Chapter 5 presents results for forced oscillation of this UCAM rig configuration. It can be expected that effects of high forcing amplitude on the flame observed in the Armitage case be also found in this particular UCAM rig case.

In chapter 6, the forcing amplitude was varied for a single burner of the UCAM rig. The impact of varying this parameter on the flame is well acknowledged and understood in the Armitage case [41]. Results from Armitage et al. can thus help identify characteristic

behaviour in the UCAM rig for this simulation as well.

The second forced oscillation reference case was conducted by Lee [59] on the UCAM annular rig and is referred to as the 'Lee case' in this thesis. This was a first attempt regarding the CFD modelling of the UCAM rig in the context of forced oscillation. LES was used in OpenFOAM with the Smagorinsky subgrid scale model for stresses and transported flame surface density model for reaction rate. The plenum chamber was cut from the model, but as in the study by Zettervall et al. [46], the swirlers were kept in the geometry and mesh [59]. The annular enclosure cylinder heights were matched, as was previously done in the Bainbridge case [16]. The fuel used was ethylene and the inlet velocity was calibrated to match available experimental data.

Several configurations and operating conditions were investigated including single, twin and full annular burner geometries and equivalence ratios of 0.65 and 0.8. The forcing amplitude was also varied for a single burner model. This study [59] is used extensively in this thesis as case setups in chapter 6 were based on those used by Lee et al. to allow for direct comparisons to be performed.

3.5 Summary and Modelling Methodology

This chapter reviewed fundamental concepts and equations pertaining to computational fluid dynamics of swirling reacting flows. Common modelling methods for turbulence and combustion were detailed. The most relevant previous CFD studies concerning oscillations in combustion chambers were explored. The modelling strategy for the work in this thesis is presented below. The methods chosen had to answer the core aim of computational efficiency set for the project.

Section 3.2.1. concluded that RANS and LES methods were more suited to industrial studies due to the high computational costs associated with DNS. Both URANS and LES modelling approaches have been used previously for the analysis of combustion instability [16, 41, 46, 59]. The validity of URANS methods for these types of investigations in annular combustors has been questioned in the literature [101]. However, Bainbridge clearly demonstrated that URANS was capable of capturing key features of self-excited flame behaviour and fare well against more expensive LES in the UCAM rig [16]. URANS methods thus were considered in this thesis to keep computational requirements to a minimum.

The choice of lower-order eddy-diffusivity modelling as opposed to second moment RSM modelling was detailed in the case of swirling flows in section 3.2.2. Section 3.4.1 explained findings by Bainbridge on the UCAM rig [16], which concluded that the eddy-diffusivity models did not exhibit self-excited behaviour due to the presence of damping that hinders the natural development of high amplitude acoustic waves. RSM yielded results that were more conclusive when compared to LES and experimental data on oscillatory behaviour in this case.

The geometry tested by Bainbridge was somewhat simplified to reduce the computational cost, and some of the major features (detailed in chapter 4) that generated self-excited modes in the UCAM rig experimentally were not represented in the mesh. With this in mind, the studies on the use of eddy-diffusivity models in this context were not complete. As a first step towards testing and implementing eddy-diffusivity models on the real UCAM rig geometry, this thesis intended to assess their use in forced oscillation studies, where better control of the oscillatory parameters can be achieved. Data from the LES performed by Lee [59] on the UCAM rig is used for comparison in chapter 6. A brief turbulence model study conducted in chapter 5 details the choice of eddy-diffusivity model for the rest of the simulations carried out.

In keeping with previous work on the UCAM rig, a blended Crank-Nicolson scheme was implemented for time-marching, with first-order Euler-implicit scheme to ensure stability during transients and second-order Crank-Nicolson otherwise. Spatial discretisation was achieved in a similar fashion to what was described in section 3.1.2 for studies by Lee [12], with second-order central differencing scheme for smooth regions and first-order in regions of high gradients. The PISO numerical scheme was implemented, as was done by Bainbridge [16] and Lee [59].

The combustion model chosen for reaction rate closure was PaSR due to its proven applicability to studies in the UCAM rig in both LES [46] and URANS [16]. The reactingFoam solver within OpenFOAM is a solver for combustion with chemical reactions that readily incorporates the PaSR model and was previously employed by Bainbridge [16]. ReactingFoam was thus a good option to choose for this project. One-step chemistry for ethylene-air and methane-air reactions was implemented throughout. Corresponding Arrhenius coefficients were prescribed from OpenFOAM libraries.

Table 3.1 summarises the test cases used for comparison in chapters 5 and 6 of the thesis and table 3.2 summarises the geometries and aims of the reference cases.

Table 3.1 Summary of modelling methodologies in the reference cases.

Case	Rig	Acoustic Forcing	Turbulence	Combustion
Bainbridge [16]	UCAM	Self-Excited	RSM	PaSR
Zettervall [46]	UCAM	Self-Excited	LES	PaSR
Armitage [41]	Balachandran	Forced Oscillation	RSM	BML
Lee [59]	UCAM	Forced Oscillation	LES	FSD

Table 3.2 Summary of aims and objectives of the reference cases.

Case	Aim
Bainbridge [16]	Model self-excitation in the UCAM rig
Zettervall [46]	Methane / Ethylene flame comparison
Armitage [41]	Effects of forcing frequency and amplitude
Lee [59]	Model forced oscillation in the UCAM rig

At each step, modelling methods were chosen with a view to limit the computational demands. In addition to finding ways to reduce the computational costs in the CFD methodology, the aim of the project was also to identify potential solutions to the cost issue in the physical representation of the UCAM rig. For this, both small and large-scale simulations were run to account for various parts of the annular geometry. Smaller-scale simulations were run locally on a machine consisting of two nodes, each containing an Intel Xeon E5-2609, 2.40GHz 4-core processor and 32GB of RAM. Larger-scale simulations were run on the Cambridge Service for Data-Driven Discovery (CSD3) high-performance cluster Peta4 [102] which consists of 768 nodes, each containing two Intel Xeon Skylake 6142, 2.6GHz 16-core processors and 192GB of RAM.

The next chapter reviews the effects of physical components specific to annular combustor designs on the flame response, and details the resulting geometrical and meshing approaches for this thesis.

Chapter 4

CAD and Meshing Methodologies

The objective of the work presented in this chapter was to create a CAD model of the UCAM rig based on design specifications by Worth and Dawson [7]. The aim was to create a model that was easily adaptable to the cases that were going to be run. This was done with a view to facilitate the setup for each simulation and thus in turn to reduce the overall time required per case study. For this purpose, the full UCAM rig CAD model was produced in a modular fashion that allows any section of the burner to be extracted for investigation. This chapter details the approach taken to generating the modular combustor geometries and meshes.

4.1 CAD Modelling Approach

A functional CAD model was produced for the modular geometry purpose stated above using the SolidWorks CAD software package. Geometry repairs were applied and new parts were created to provide physical inlet, outlet, and other surfaces to be included in the mesh at a later stage.

4.1.1 Original Geometry

Figure 4.1 shows a picture and schematics of the rig along with CAD renderings of the combustor in SolidWorks for comparison. Particular attention was paid to the swirler and bluff body parts within each of the injectors as it can be expected from studies on swirl and bluff-body stabilised flows that their dimensions would have a significant impact on the flow behaviour [12, 37]. It was anticipated at this stage that the swirler part would be difficult to mesh due to the curvature of the vanes. A CAD representation of the swirler is shown in figure 4.4.

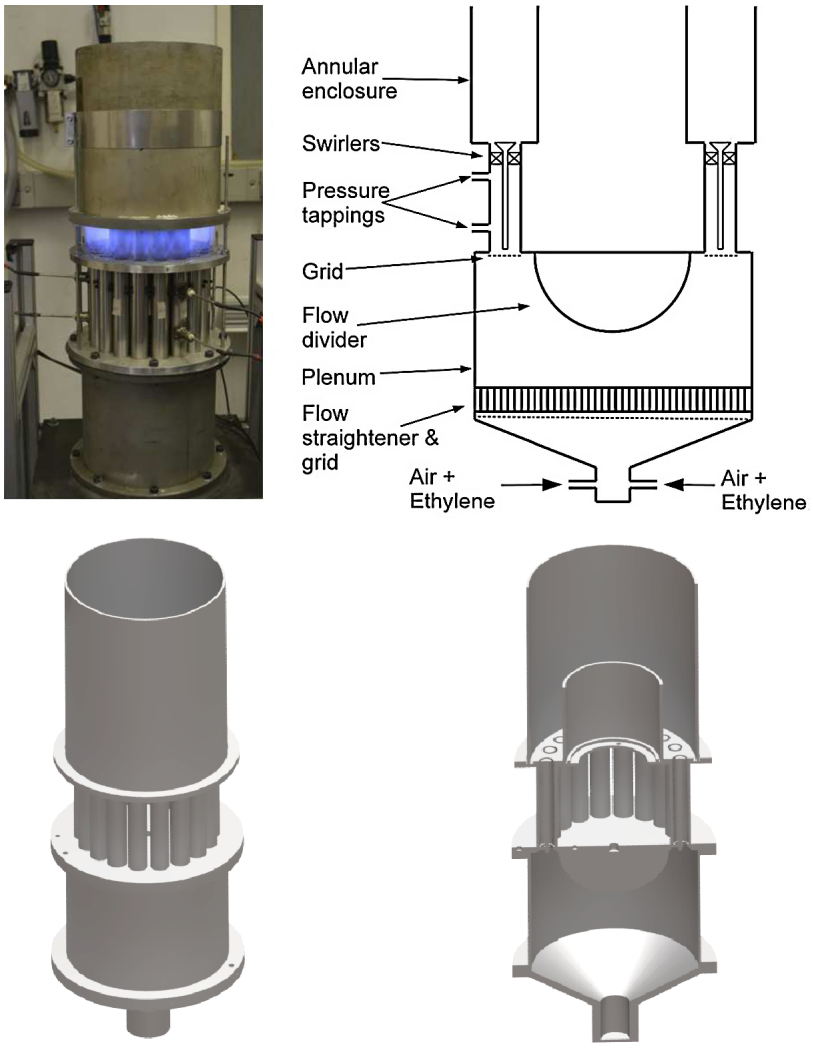

Fig. 4.1 UCAM Annular Rig Design [7] (top) and CAD rendering of each view (bottom).

4.1.2 Geometry Repair

After generating the full burner in the CAD format, the geometry was repaired and adjusted to be fit for meshing. Figure 4.2 shows the final CAD representation which was used for the preliminary meshing work detailed in section 4.3.2.

Inconsistencies in the surfaces (i.e. holes and other uneven features) were deleted to ease the meshing process. As an example, the holes on the circular plate sections at the top and bottom of the plenum chamber were filled. It was verified prior to performing any change to the original CAD that the deleted features were present for practical purposes such as mounting the burner on the support rig, and would thus not affect the fluid flow inside it. The middle picture of figure 4.2 shows that the inner and outer chamber cylinder heights

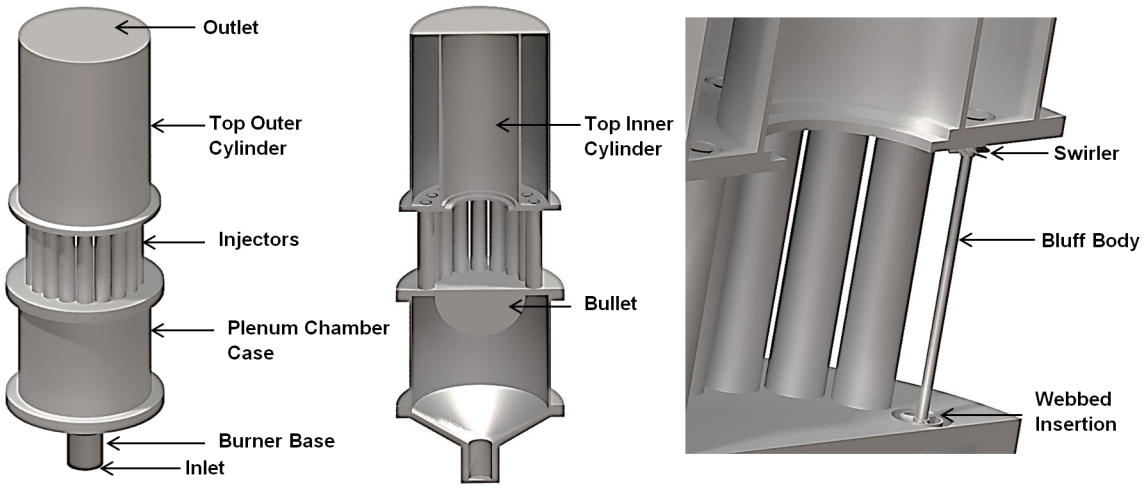

Fig. 4.2 Full modified burner CAD side view (left), cut view (middle) and inner view of an injector (right).

were matched, as was done in the Bainbridge and Lee cases [16, 59]. The impact of cylinder height on the flame response is discussed in section 4.2.1.

Before making any additional modifications to the geometry, the effects of the main components of the burner on the flame response had to be understood. A part-by-part analysis isolating the impact of these components is conducted in section 4.2. The resulting configurations extracted from the CAD are also presented.

4.2 Effects of Physical Components on the Flame Response

The main components investigated in this section include the combustion chamber cylinders, plenum chamber and swirlers. The effects of modifying the number of burners around the annulus were also of interest for the project and are detailed here. The implications of these part-specific observations for the modular CAD model of the UCAM rig are explained at each stage.

4.2.1 Combustion Chamber Cylinders

Literature Review

Worth and Dawson varied the combustor chamber cylinder lengths on the UCAM rig as part of a parametric analysis [7]. The study was aimed at finding an optimal experimental setup that would give rise to self-excited circumferential modes. Three cylinder lengths

were investigated: 70, 130 and 300mm. Each length was chosen to either damp or generate specific acoustic modes. The shorter length was used to damp the purely longitudinal modes, and the longer length, to excite purely circumferential modes. The length of 130mm was used to obtain an equivalent flame response in longitudinal and circumferential directions.

Results from this study showed that any combination of cylinder height would give rise to self-excited modes in the longitudinal direction. Using an equal length of 70mm for both the inner and outer cylinders damped all the instability modes. The most prominent case of self-excited circumferential modes was found for an inner cylinder length of 130mm and outer length of 300mm. This is the geometry shown in figure 4.1, where the cut plane on the right shows that the inner and outer concentric cylinders at the top differ in height according to this experimental setup.

UCAM Rig CAD Modelling

For all of the simulations presented in this thesis, the combustion chamber outer cylinder height was adjusted to match that of the inner cylinder. The shortest length of 70mm was not considered for this project but can be rapidly modelled if required in the future, as facilitated by the modular CAD. Only the 130mm length was considered in this thesis to provide comparable data to the Bainbridge [16] and Lee [59] cases. The final CAD model for the full annular rig is shown in figure 4.5 and other geometries used in this thesis are presented in section 4.2.5.

4.2.2 Plenum Chamber

Literature Review

An experimental study was performed by Bauerheim and Poinsot [103] to observe the effects of the plenum chamber on the azimuthal modes that propagate in annular combustors. In theory, due to the difference in radii and mean sound speeds between the plenum and combustion chamber, azimuthal modes could be found in only one of these parts at a time. Experiments have however shown that azimuthal modes can be present in both sectors simultaneously.

The paper proceeds to identify three separate occurences of azimuthal modes in a plenum, burner and annular sector configuration: fully decoupled, weakly coupled, and strongly coupled. In the first two cases, the acoustic modes can be treated independently as either fully ‘plenum’ or fully ‘chamber’ modes. In the last case, when the frequency in one of the annular sectors corresponds to the resonant frequency of the other, the entire combustor is considered

to be in a resonant state and the 'plenum' and 'chamber' modes cannot be distinguished.

Work by Benoit [104] used a linearised acoustic code to solve for plenum chamber modes. The annular combustor geometry considered was close to the one developed by Worth and Dawson [7]. The plenum chamber here was connected to 12 burners that each contained a swirler, which were then themselves connected to the combustion chamber [104]. The effects of flame shape, flame position and swirl on plenum chamber modes were investigated. As the flame developed in the combustion chamber, the flame shape and flame position affected modes in the chamber only. The swirler, however, had an impact on the plenum longitudinal modes. This was attributed to the decrease in area in the geometry introduced by the physical part, and led to a shift in frequency in the corresponding modes. An additional shift was then observed in the combustion chamber as a result, thus demonstrating that modes in the plenum chamber may affect the modes in the combustion chamber.

UCAM Rig CAD Modelling

An assumption was made for the work in this thesis that the response of the flame to acoustic excitation in the UCAM rig would be dominated by the effects of flow features such as swirl and burner-burner interactions. To analyse these effects in detail and to reduce the size of the computational domains considered, it was therefore decided to omit the plenum chamber and cut the CAD models downstream of this part. This also allowed for direct comparisons with geometries considered by Bainbridge [16] and Lee [59]. Plenum chamber effects were treated as a subject for potential future investigations, where a comparison between a simple burner-chamber and plenum-burner-chamber geometry could be performed via CFD. The modular geometry created allows for the plenum chamber to be added at a later stage if required.

4.2.3 Swirlers

Literature Review

Placing a swirler in or around the fuel injector is an effective way of creating recirculation zones to anchor the flame [1]. The high rotation would provide higher and faster levels of mixing than other means such as bluff bodies. The swirler design can have a significant impact on flow behaviour and must be considered carefully. The size of the resulting recirculation zones and the reverse mass flow rates are two of the parameters affected by the vane geometry.

The vanes on the UCAM annular rig swirlers are curved at an angle of 60° as shown in figure 4.4. The swirl number representing the level of rotation that is supplied to the flow is given by the equation [7]:

$$\Sigma = 2/3 \tan(\Theta_e)[(1-(d_i/d_o)^3)/(1-(d_i/d_o)^2)] \tag{4.1}$$

Here, Θ_e is the vane angle, and d_i and d_o represent the inner and outer diameters of the swirler respectively. Design specifications by Worth and Dawson [7] give a swirl number of $\Sigma = 1.22$ for the UCAM rig.

Balachandran [37] conducted an experiment on the single burner rig presented in chapter 3 to observe the effects of swirl angle on a forced oscillating flame. The rig was subjected to premixed combustion with ethylene as fuel, equivalence ratio of 0.52 and bulk flow velocity of 9.9m/s in the combustion chamber. Two swirler geometries were investigated: the first with a vane angle of 45° producing low swirl, the other with an angle of 60° producing high swirl. For an increase in swirl, the flame height decreased and flame thickness increased. Under forced conditions, the smaller vane angle produced a flame that responded in a similar fashion to one without swirl for varying forcing frequencies and amplitudes [37]. Conversely, the higher angle design led to a different response, which confirms findings by Worth and Dawson [7].

An experiment on the effects of swirl direction was carried out by Worth and Dawson on the UCAM rig [7]. Counter-clockwise (CCW) swirl was first implemented with similar swirlers placed in each burner. The CCW swirlers introduced a bulk flow swirl at the chamber walls. A comparison between this setup and an alternating swirl configuration was performed for a full 18-burner model. In the second experiment, the bluff bodies were fitted with alternating CCW and clockwise (CW) swirlers consecutively around the annulus. This was done to reduce the potential effects of the bulk flow swirl on the flame structure. Figure 4.3 shows the OH* chemiluminescence results for varying swirl directions taken from a top view of the rig. High levels of OH* chemiluminescence are indicated by red colouring, and low levels by blue colouring. The highest values correspond to reaction zones, thus providing a good overview of flame front locations [16]. For CCW swirl, the flame-merging areas represented by red regions tend to the CCW direction at the outer chamber cylinder and CW at the inner cylinder. Adding alternating swirl leads to more symmetric flame-merging zones around the annulus as can be noted by the more regular shapes of the high OH* regions around the annulus in the snapshot on the right-hand side [7].

The significant impact of swirl on the flame shape and its response to acoustic waves has been highlighted by these experimental studies. The effects of swirl have also been investigated via CFD modelling. A micro-gas turbine combustion chamber was studied

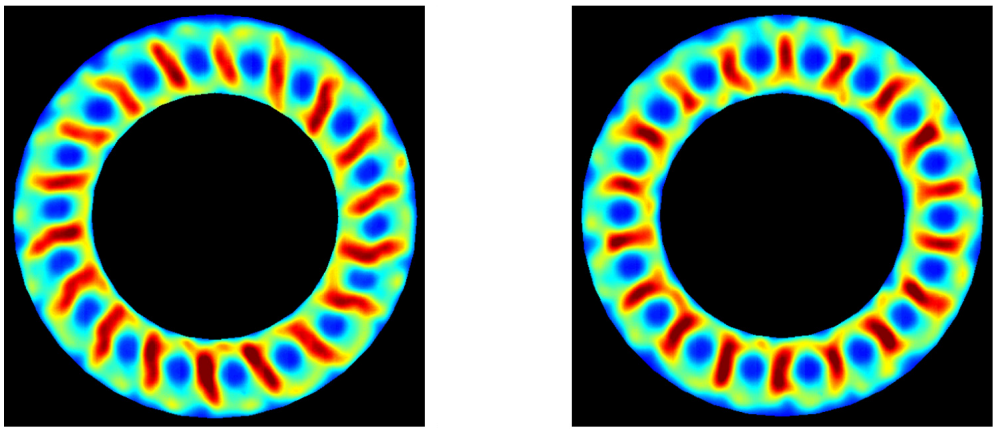

Fig. 4.3 Experimental results showing top views of the annular combustor exit for varying swirl directions: CCW (left) and alternating swirl (right) [7].

numerically by Basson [105]. Two separate models were created for comparison, one without swirl and one with swirl. The inlet flow in the first case would be purely axial, whereas tangential components would be introduced by swirl in the second case. The presence of swirl affected the recirculation pattern within the combustor following explanations by Lefebvre [1]. The authors stressed the importance of representing the swirler accurately in any geometry containing this feature.

Due to the complexity of the swirler geometry in the UCAM annular rig, it would be beneficial to implement an efficient solution to generating swirl at the inlet of the domain that could reduce the potentially time-consuming meshing step, in line with the industrial objectives of this project. This has been achieved in investigations by Fureby on the Triple Annular Research Swirler (TARS) [70], by Staffelbach on a rig built by DLR and Siemens [14], and by Bainbridge on the UCAM rig [16]. In all three studies, a swirl inlet velocity boundary condition was formulated to represent the effects of the swirler part. Results from the Fureby investigation [70] were validated against experimental observations from Balachandran [37] on the aspect of the flame with varying swirl number. The results were further compared to experimental velocity profiles from the TARS rig and good agreement was found. Results from the Bainbridge case [16] and from Staffelbach [14] were also validated against relevant experimental data with good agreement. A swirl boundary condition would thus be an effective way of simplifying the geometry and accelerating the simulation setup for this thesis.

UCAM Rig CAD Modelling

The first simulations carried out in this project were focused on swirl effects and the ability to represent them in cost-effective manner. Figure 4.4 shows a CAD rendering of the swirler design from the UCAM rig.

Fig. 4.4 Swirler CAD rendering.

As mentioned in section 4.1.1, it was anticipated that the swirler would be a challenging geometry to mesh. Using the physical part would also limit the flexibility of a single mesh to account for varying swirl parameters, and additional computational costs would ensue to produce a new mesh for every swirler geometry that is required for the investigation.

The first step in the project was aimed at calibrating a swirl velocity inlet boundary condition based on work by Fureby [70], Staffelbach [14] and Bainbridge [16]. With this, effects of counter-rotating swirl could also potentially be captured by adjusting the swirl direction in the tangential velocity input of the boundary condition for each individual burner. The swirl velocity boundary condition is detailed in chapter 5. CAD geometries used to calibrate the swirl boundary condition are presented in figure 4.7.

4.2.4 Modular Full UCAM Annular Rig Model

Taking into account the assumptions on combustion chamber cylinders, plenum chamber and swirlers, a modified version of the full annular rig CAD was generated and is presented in figure 4.5. The picture on the left is taken from the CAD software package, and the transparent view on the right is taken from the flow visualisation software as it provides a better view of the components inside the chamber.

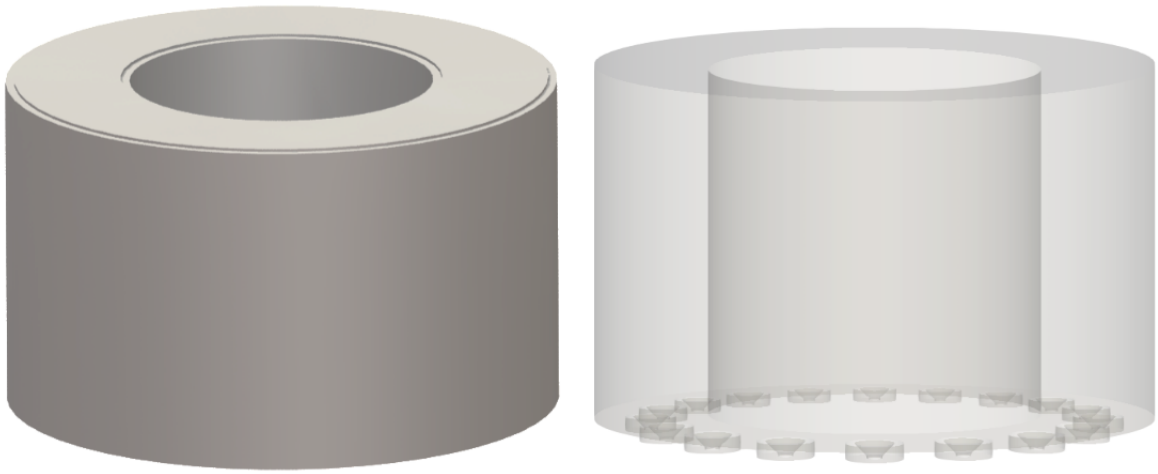

Fig. 4.5 Modular UCAM rig CAD model side view (left) and transparent view of the computational domain (right).

The geometry was cut 5mm below the entrance to the combustion chamber which meant that whilst swirlers were omitted, the conical shape at the tip of the bluff bodies was still represented in the CAD. The UCAM rig accounted for all 18 burners of the experimental design. However, the test rig could be run with varying numbers of equidistantly placed burners around the annulus (12, 15 and 18). The effects of varying the number of burners on the flame response is discussed in the next section.

4.2.5 Flame Separation Distance and Flame-Flame Interactions

Literature Review

Flame separation distance can have a direct impact on the burner as early as the ignition stage, or 'lightround'. An experiment aimed at observing the lightround process in the UCAM annular rig was carried out for 12 and 18-burner cases by Machover et al. [106]. This corresponded to a uniform separation distance of 44mm and 29.5mm between burners around the annulus respectively, measured between the centres of bluff bodies. The analysis concluded that the flame propagation in the azimuthal direction during the light-round process was affected by local quenching and convection mechanisms induced by flame-flame interactions. A lower separation distance increased those effects due to stronger interactions between neighbouring flames.

The importance flame-flame interactions on the flame structure was also studied in the parametric analysis by Worth and Dawson [7] and in experiments carried out by Makuni [15]. Three flame separation distances were tested corresponding to 12, 15 and 18-burner designs.

The three distances were referred to as S = 2.33D, 1.87D and 1.56D respectively, where D is the inner diameter of the inlet cylinder and S is the arc-distance between the centres of neighbouring bluff bodies. All three configurations only accounted for CCW swirl in this case. Figure 4.6 shows the effects of separation distance on the OH* chemiluminescence results in steady reacting flows. The snapshots were taken and coloured in the same way as in figure 4.3.

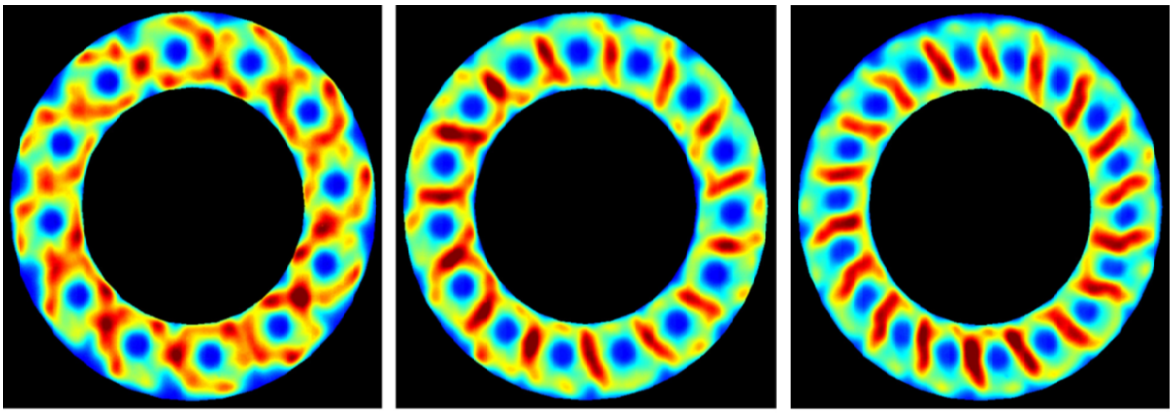

Fig. 4.6 OH* chemiluminescence experimental results showing top views of the annular combustor for varying flame spacings [7].

The high OH* regions reduced in size progressively with a decrease in flame separation distance between pictures 4.6(a) to 4.6(c). This indicates that flame-merging is more prominant for smaller separation distances, which can be expected as the flames would have a smaller amount of space to develop individually. Resulting dominant acoustic modes switched from a CW spinning mode to a standing mode from figure 4.6(a) to 4.6(b), then to a CCW spinning mode in 4.6(c). In all plots of figure 4.6, high OH* regions differ in shape and size around the annulus. This non-uniformity in stable conditions is analysed in greater detail in chapter 6.

Burner-burner interaction effects on the flame response in annular combustors have also been investigated using CFD. Simulating acoustic oscillations for an entire annular combustor can be very computationally demanding [16, 50, 51]. Previous CFD studies have been performed on sections of annular combustors instead to reduce computational costs [14, 50, 51, 59, 101]. These typically carried out single sector simulations corresponding to a single burner of the annulus, which were compared to full burner simulations for validation.

Staffelbach et. al [50] performed simulations to model self-excited modes in a helicopter annular combustor. The combustor was composed of 15 burners equally spaced around an annulus, each containing counter-rotating swirlers. An initial simulation was performed on a single burner with cyclic boundary conditions to represent the neighbouring burners in the domain, before rotating the mesh around the centre of the annulus and running a full burner configuration. This approach was also used for URANS simulations in this thesis and cyclic boundary conditions are investigated further in chapters 5 and 6. The Staffelbach study [50] concluded that each burner exhibited similar oscillation amplitudes and delays. It was inferred from this that in the event of self-sustained oscillation caused by azimuthal modes in this geometry, the burners were only affected by flow rate variations in the axial direction. As such, a single sector was capable of capturing the effects of a full burner model accurately. The burners could be considered independent from each other and all resulted in equivalent transfer functions, which led the authors to encourage the use of linear analytical models.

The universality of the last statement was refuted in a study by Wolf et al. [51], where it was said that transfer functions cannot be equal for all burners in all annular combustor designs. This was attributed to large-scale flame-merging which may cause the emergence of transverse modes and further instability, as discussed in greater detail in chapter 2. Wolf et al. [51] also questioned the use of single burner geometries to represent the full annulus as this may not be sufficient to capture all acoustic modes.

Fureby and Fedina [101] made similar observations in their CFD study of a 12-burner annular combustor. A single burner was extracted for comparison to oscillatory behaviour in the full annulus. As in the Staffelbach investigation [50], the single sector was meshed with cyclic boundary conditions then replicated around the annulus to form the full burner model [101]. The data showed that the single burner configuration could potentially be used to model flow behaviour in isothermal cases, but would not provide enough useful detail downstream to be considered sufficient for thermoacoustic analysis. The merging of central recirculation zones between burners was not well represented by the single burner. In the full annulus, the flame-flame interactions led to high local variations in equivalence ratio which affected the flame shape and behaviour in each burner in a different way.

Observations by Fureby and Fedina [101] were confirmed by Fedina [70], Chapuis et al. [69] and in other work by Staffelbach [14]. The latter differed from previous CFD studies in that instead of only modelling single and full burner configurations, a larger portion of the annulus was also represented. Single and triple burner geometries were extracted out of a 24-burner annular combustor. Increasing the number of burners improved the accuracy of the results when compared to a full burner model. The burner interactions found in the triple

burner captured effects on flame stabilisation and anchoring that could not be represented by a single burner.

UCAM Rig CAD Modelling

The modular CAD allowed for any part of the annular burner to be extracted for analysis. Figures 4.2 and 4.5 show that all burners in the UCAM rig are joined by a solid plate placed on top of the flow divider, which was subsequently cut to obtain the single sector geometry in figure 4.7. Increasing the burner separation distance would result in increasing the solid plate area between consecutive injectors. In the modular CAD model, this could be achieved efficiently by extending the solid plate area on either side of the single burner model in figure 4.7, and replicating this new geometry around the annulus. An example of the extension is shown in figure 4.7 by the dotted area δ. In all studies in this thesis, however, the separation distance was kept at its minimum value to account for all 18 burners.

Staffelbach [14] and Fureby and Fedina [101] found that a single burner model could capture essential information concerning isothermal flow, including swirling velocity profiles. In the rendered pictures of figure 4.7, the inlet, injector, solid annulus and inner chamber cylinder were made transparent in the CAD to show all the chamber components within the domain. The picture on the right shows a version of the single burner geometry containing the swirler part, which was used to validate the swirl boundary condition implemented when running the modular geometries such as the one on the left.

The studies described above concluded that in most cases, a single burner configuration would not be sufficient to capture the flame-merging effects, which in turn affect oscillatory behaviour [14, 69, 70, 101]. Staffelbach [14] however found that adding two burners improved results significantly when compared to full burner geometries. Based on this result, a twin-burner geometry was extracted for comparison between single, twin and full UCAM rig configurations. A twin-burner configuration was also investigated by Lee [59] via LES on the UCAM rig. The twin-burner CAD model is shown in figure 4.8.

4.2.6 Summary

This section reviewed previous studies concerning the effects of annular combustor components on the acoustic response of the flame. Appropriate adjustments were made to the UCAM annular rig geometry. It was decided to adjust the height of the combustion cylinders and omit the plenum chamber to reduce the size of the computational domain. It was also decided to extract single, twin and full burner configurations to analyse flame-flame interaction effects in more detail. It was finally concluded that adding swirl using a boundary condition

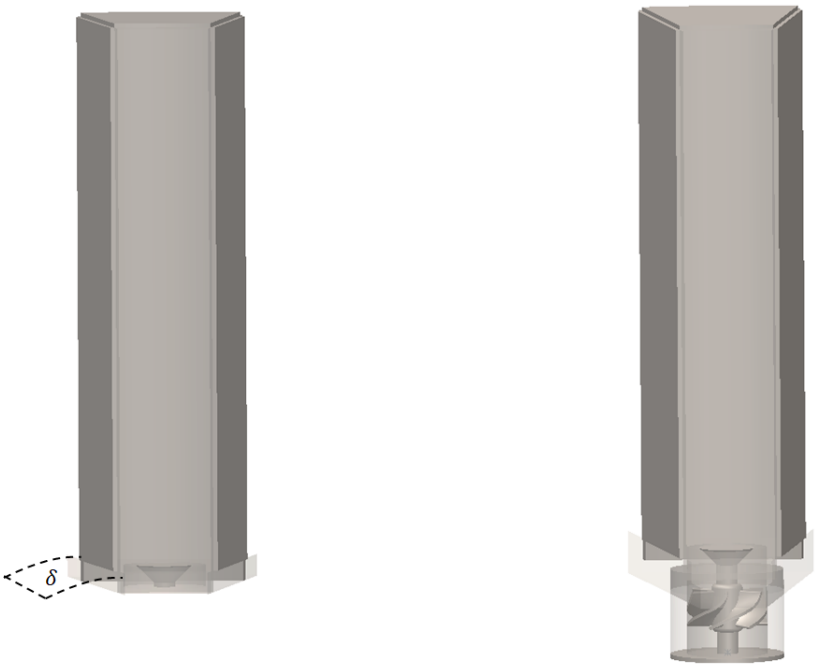

Fig. 4.7 Single burner CAD renderings, modular geometry (left) and geometry with swirler (right).

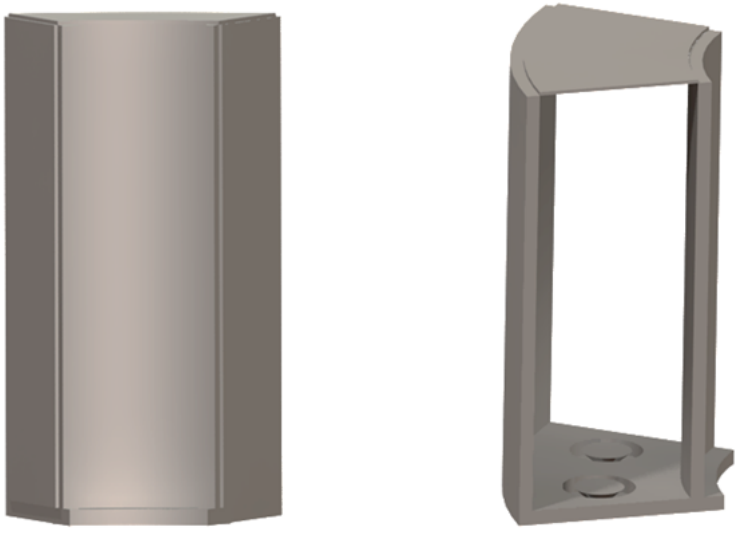

Fig. 4.8 Twin burner CAD renderings, front view (left), side - inner view (right).

would be an effective way of reducing computational costs. With the final set of geometries defined for the URANS simulations on the UCAM annular rig, meshing methods were then investigated and are presented in the next section.

4.3 Meshing Methodology

Generating an appropriate mesh can decrease the time to convergence and increase the quality of results obtained [107, 108], hence the importance of this step in the simulation setup. Meshing methods were investigated to find the most suitable approaches to producing grids for the different geometries considered in this project. This was done with a view to identify solutions that would best answer the time and cost-efficiency constraint.

This section includes a brief introduction to meshing methodologies currently available and the approaches chosen for the work presented in the thesis.

4.3.1 Overview

Structured and Unstructured Meshes

Mesh types commonly in use for 3-dimensional CFD studies include structured, unstructured and hybrid [107–109]. The first is formed of purely hexahedral cells, either composed of a single block of cells or multiple blocks with varying refinements. The blocking allows for cell connections to be consistent with each other in orientation, following a regular pattern [108]. This type of mesh is suited to less complex geometries, as all lines in the grid have to extend from one end of the computational domain to the other [107]. This is often not possible if the geometry considered contains several parts of different dimensions and shapes, as is the case for the UCAM annular rig.

Unstructured grids are defined by their irregular cell patterns and are commonly used for CFD studies involving real geometries as they allow more flexibility in their implementation [108]. Typical cells types including tetrahedral and hexahedral are typically chosen for 3-dimensional simulations [109]. Unstructured meshes are often regarded as more computationally demanding than structured meshes, as they require memory allocation for both calculated data and irregular connections between cells during a simulation [108].

Hybrid meshes mix both structured and unstructured grids at appropriate locations in the geometry [107]. One of the most common combination of elements for this is the hexacore mesh, with tetrahedral cells at the walls (on the surfaces of the geometry), and hexahedral cells in the core (interior fluid). A major benefits of using this above purely tetrahedral meshes despite the potential increase in setup time, is a lower overall cell count and time to convergence as the grid in the interior fluid would be consistent and regular where possible [108].

Quality Measures

The measure of cell quality is an important factor in choosing the appropriate mesh type for a given problem. Three main measures are typically used: skewness, smoothness and aspect ratio [107–109].

Skewness represents the deviation of the shape a cell from the one that is originally intended, due to the geometry around it. Figure 4.9 below shows an example for a tetrahedral cell:

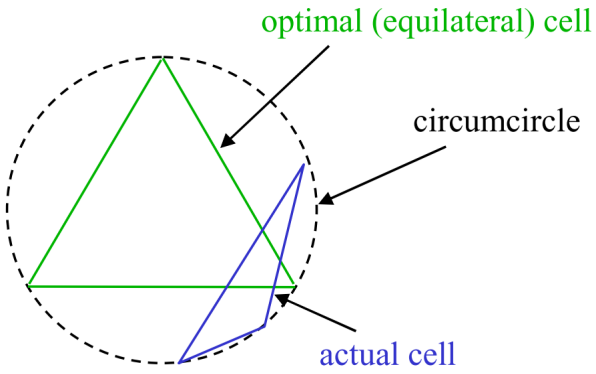

Fig. 4.9 Example of optimal (green) and skewed (blue) tetrahedral cell [107].

Here, the skewness level is defined by the ratio between the difference in size of the two cells and the size of the equilateral cell. For hexahedral cells, the skewness level is not measured based on the size but rather based on the difference between the corner angle of a cell and the intended 90° angle in the optimal shape [107]. OpenFOAM defines skewness as the shortest distance between a line connecting two neighbouring cell centres, and the centre point of the connecting face between these two cells [110]. The skewness parameter ranges from 0 to 1 with 0 corresponding to the optimal shape of a cell. An acceptable quality mesh would result in skewness levels that do not surpass 0.85 [108].

Smoothness represents the transition between one cell size to the next for grids with varying refinements [108]. Figure 4.10 below shows examples of ideal and high cell size changes for a tetrahedral cell.

It is accepted that the difference in size (or spacing for grid lines in hexahedral meshes) between two neighbouring cells should not exceed 20% to yield reliable results [107]. Various smoothing algorithms can be applied after the generation of the mesh to increase the overall cell quality.

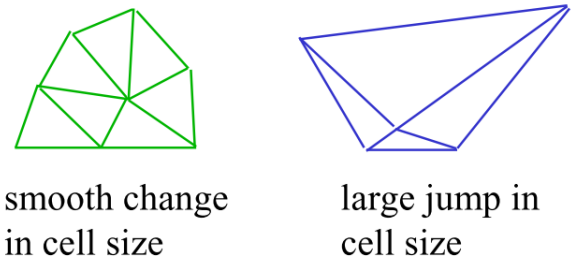

Fig. 4.10 Example of smooth (green) and large (blue) change in size for a tetrahedral cell [107].

Finally, the aspect ratio represents the ratio between the longest and the shortest edges of a cell [108]. Figure 4.11 below shows examples of ideal and high aspect ratios for a hexahedral and tetrahedral cell.

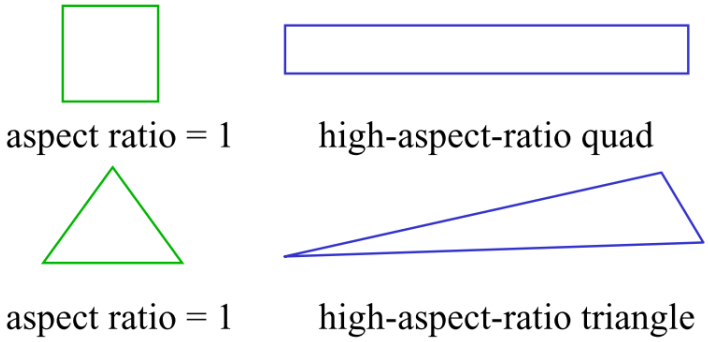

Fig. 4.11 Example of ideal (green) and high (blue) aspect ratio for a hexahedral (top) and tetrahedral (bottom) cell [107].

A high aspect ratio would lead to a lower mesh quality, which could in turn affect the reliability of the solution [107].

In-depth research into the differences between capabilities of hexahedral (hexa) and tetrahedral (tetra) cells is considered beyond the scope of this work. However, general trends in meshing studies state that hexa meshes provide better accuracy than tetra meshes for lower cell counts in a given case [108]. However, tetra meshes are easier to implement, and are a better fit for geometries containing complex features. This trade-off led to the choices in mesh types for this project.

Meshing Algorithms

Several meshing algorithms for automatic unstructured grid generation are available within common meshing softwares. These include the octree, Delaunay and advancing front methods amongst others [111].

The octree method is considered the simplest and most time-efficient of the three. An initial box surrounding the domain is defined, which is divided into 4 sectors. Each sector is further divided into 4 of their own, until corners of the resulting squares match the edges of the domain. The empty cells are then deleted. This method can lead to high skewness levels and irregularities in the mesh, which are both undesirable [111].

The advancing front method is initialised via a mesh accounting for the boundaries of the computational domain [111]. Initial nodes are placed on these boundaries. From one of the edges formed by two nodes, the algorithm chooses a point within the domain to form a first triangular computational cell that is ideally shaped (equilateral). A new edge is then selected on the domain boundary, adjacent to the initial edge. A new point is chosen inside the computational domain to form an ideal cell shape with this edge. The algorithm searches nearby regions for a defined node from the initial mesh, and if one is found, the new point is moved to this location. This forms the second computational cell. The process is repeated until the domain is entirely meshed. This method is slower than the octree approach. However, it offers better flexibility in defining the mesh at the boundaries by allowing for the initial edge parameters to be specified.

Finally, the Delaunay method is considered the most robust of the three [111]. The method is initialised by defining a large triangular domain from a surrounding box on the geometry. Points are gradually added to the mesh which is then updated. The Delaunay method allows for a variety of techniques to be used to generated the grid based on the ways in which the original domain is defined, on the algorithm chosen to place the points, and on the ways in which the cells are formed from the set of mesh points. These are not discussed here but can have a significant impact on the time taken to produce an acceptable mesh. The overall advantages of using this more complex method is the control on many key aspects of the algorithm, which makes it more adaptable to different geometries [108]. The method is also less expensive than the advancing front, as there is no intermediate step in locating nearby nodes before defining the final form of a computational cell.

Refinement

In general, a refined mesh would allow for finer details of the flow to be captured. Mesh resolution is an issue specific to all CFD simulations that needs to be addressed on a case-

by-case basis as it is geometry and flow-dependent. However, some general approaches to applying necessary refinements can be identified.

Mesh refinement refers to the introduction of additional cells in the domain, either uniformly or in specific areas of the geometry. Ideally, the cell aspect ratio neighbours 1 where the flow is likely to be more complex and finer detail needs to be captured [107], for increased solution accuracy. Larger cells or aspect ratios can be acceptable in other areas where the flow is either uniform or does not feature complicated structures.

The final local mesh refinement levels can be selected in three steps [107, 108]. The first would be to apply refinements where complex flow behaviour is expected from the geometry. The second would be to further refine the mesh in the areas of interest based on initial results from the previous mesh. The third would be to perform a mesh refinement study on the whole domain to assess the accuracy of the results obtained from the initial meshes. For the work on the UCAM annular rig in this project, a refinement study was performed and is presented in chapter 5.

A study was performed by Tiribuzi et al. on the capabilities of a coarse mesh to provide an initial appreciation of flow behaviour and basic acoustic phenomena in an annular combustor [112]. The rig contained 24 burners with swirlers around an annulus, and used methane as the fuel. The entire length of the domain was represented, from plenum to outlet with a hexahedral mesh counting a total of 74,000 cells. The coarseness of the mesh meant that some of the smaller detail of the geometry would not be accounted for and were thus introduced via modelling. The study concluded that despite the low number of cells, the URANS simulations performed were able to represent the main characteristic aspects of flow behaviour subject to thermoacoustic instability and proved to agree well with the key features found in experimental data.

4.3.2 Preliminary Meshing

Mesh types, quality measures, algorithms and refinement methods are detailed extensively in the literature, as shown above, and in user-guides specific to meshing software such as ANSYS ICEM. The meshing methods considered were ones that would best answer the time and cost-efficiency constraint put on the simulations by the industrial nature of the work. This section and the next present the initial mesh produced for the UCAM annular rig and the subsequent meshes used in chapters 5 and 6 respectively.

An initial mesh for the complete UCAM annular rig in figure 4.2 was produced to trial different parameters and export options to OpenFOAM, as well as finding the specific areas that required additional refinements to obtain a stable solution. The study by Tiribuzi [112] detailed earlier successfully captured general trends in oscillatory behaviour with a minimal

number of cells. Whilst LES studies such as ones by Lee [59] and Fureby [70] required a number of cells in the order of millions, Tiribuzi [112] represented key features of flow behaviour with only around 74,000 cells. Such coarseness is not suitable for this thesis as flame interactions and swirl effects are of interest, which both require appropriate refinement. However, the study showed that very fine grids would not be required for initial meshes aimed at testing compatibility and stability within the OpenFOAM environment.

All grids in this work were produced using the ANSYS ICEM meshing software package. The geometries mentioned in the previous section were all extracted from the CAD software and imported into the ICEM workspace. Once a final mesh was generated in ICEM, it was exported and converted to an OpenFOAM-compatible format and viewed in the analysis and visualisation software Paraview. Figure 4.12 shows the mesh generated for the full annular burner geometry including all the parts of the original design presented in figure 4.2.

A Delaunay, tetra/hexacore meshing technique was chosen. A structured grid would not suit the complex model, as blocks could not capture the areas such as swirlers and top of bluff bodies effectively. The hexahedral core reduced computational costs significantly by decreasing the total cell count around five times compared to a purely tetrahedral grid. Investigating hybrid meshing methods is considered beyond the scope of this work as the added complexity of these meshing approaches would increase the time required in this step of the simulation setup.

The mesh presented in figure 4.12 had a total cell count of 13 million and was sufficient to obtain an initial view of the computational domain. The quality of the grid was tested in OpenFOAM and results were satisfactory with no error arising from the transfer from ICEM to OpenFOAM. The more astute reader will notice that the swirlers represented in this particular mesh are placed in the opposite direction to the experimental setup, however this was not deemed a major issue in the context of this initial study as the simulation results were not used further on in the project. Indeed, this mesh was not aimed at obtaining data for analysis but was rather used to test initialisation settings and simulation setup options in OpenFOAM. The meshes used to obtain relevant data for this thesis are presented in the next sections.

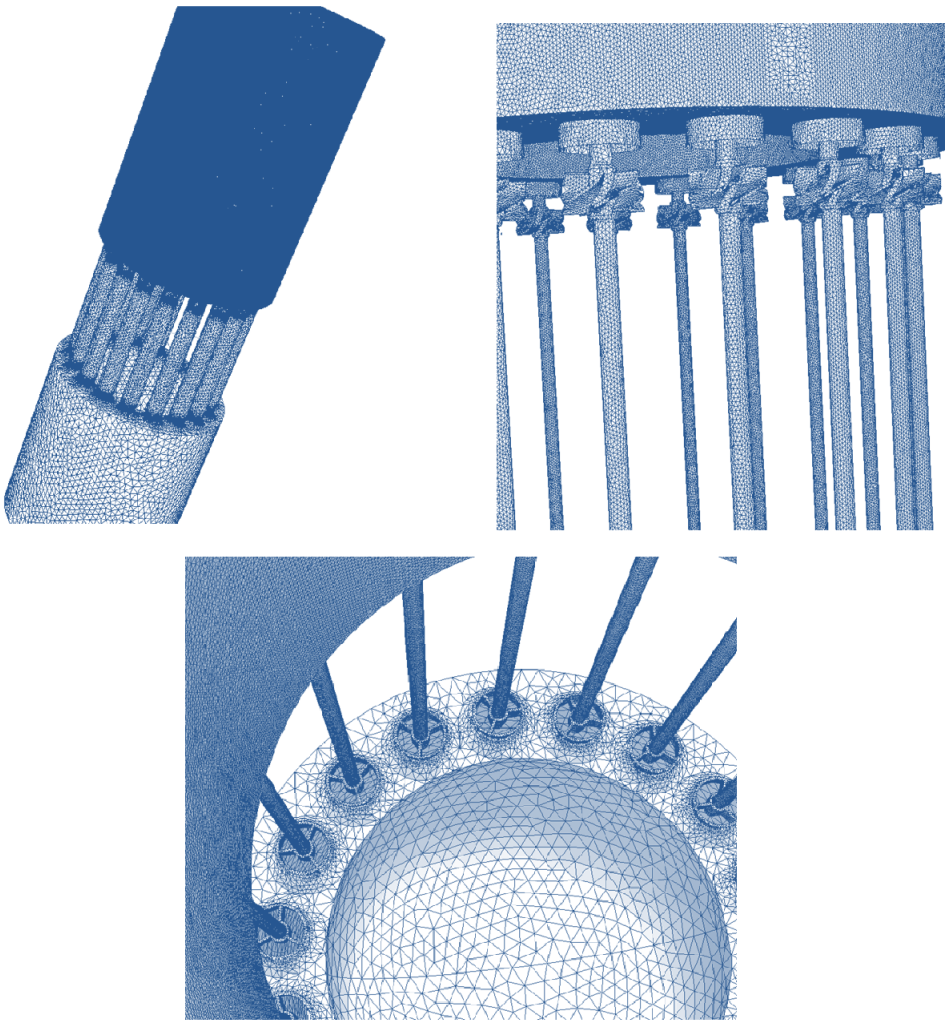

Fig. 4.12 Initial full burner mesh, side (top left), swirler / bluff body (top right) and internal (bottom) views.

4.3.3 Meshes Generated for Analysis

With Swirler

The meshes with the swirler part were produced following the same methodology as for the full UCAM rig in figure 4.12. Figure 4.13 shows the meshes produced by Lee [59] for single, twin and full burner configurations. After a mesh refinement study, the final single burner domain on the left had a total of 6.5 million cells. When rotating this around the annulus for a full 18-burner configuration, the mesh counted 120 million cells. The high number of cells required by the LES underlined the importance of testing alternative methods such as URANS to keep computational demands as low as possible to test new industrial designs.

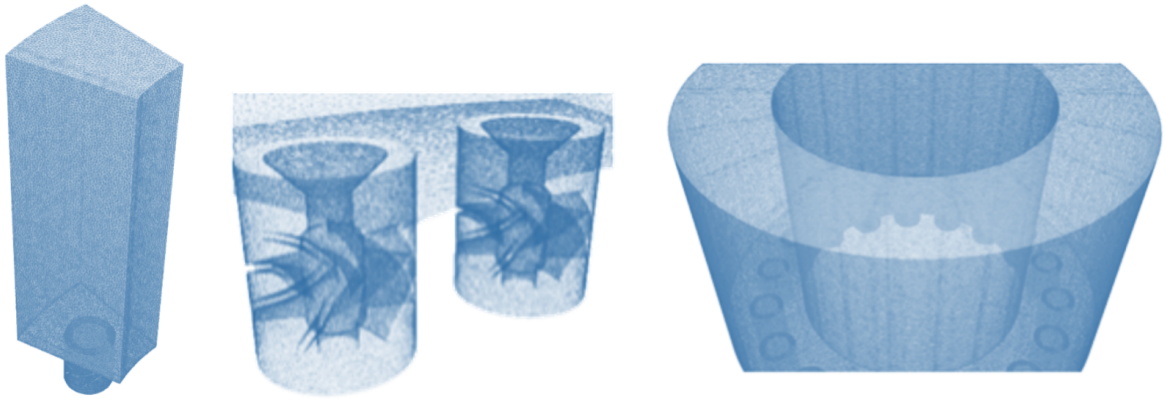

Fig. 4.13 LES meshes for single (left), twin (middle), and full (right) burner configurations [59].

Figure 4.14 shows a schematic view of a cut plane of the computational domain with the swirler part, as used in the URANS simulations in chapter 5 to calibrate the swirl boundary condition. In this diagram, a, b and c represent the local refinements applied to the mesh respectively. Zone a represents the inlet area, where a tetra-dominant mesh was applied and extruded through to the combustion chamber inlet. Further refinements of the tetra grid were applied in zone b which covers the volume around the swirler. It was anticipated that the flow in region b would need to be represented in greater detail to obtain an accurate swirling velocity profile. Finally, zone c extends from the combustion chamber entrance to the outlet. A hexa-core was defined in this region to decrease the total cell count. A gradual decrease in refinement was also specified from the inlet of zone c to the outlet of the domain to decrease the cell count. This was implemented as previous studies showed that more complex flow features occured in the upstream region of zone c.

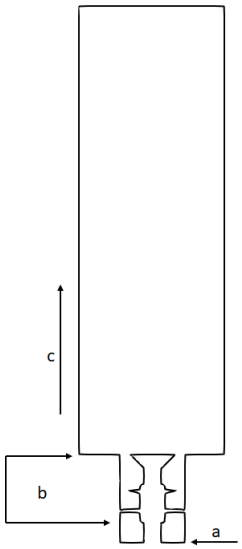

Fig. 4.14 Schematic view of local mesh refinements for URANS mesh with swirler.

Figure 4.15 shows the mesh produced for the domain in figure 4.14. The total cell count was 5 million, which is lower than its equivalent in the Lee case [59] but still high enough that replicating it around the annulus would not be cost-efficient. A separate mesh was produced using the same methodology on the same single burner cut without the swirler to assess the impact of including the physical part on the cell count. The minimum number of cells required to generate a suitable mesh for the new configuration was reduced by a factor of five, which emphasised the benefits of formulating a boundary condition to replicate the effects of the swirler part.

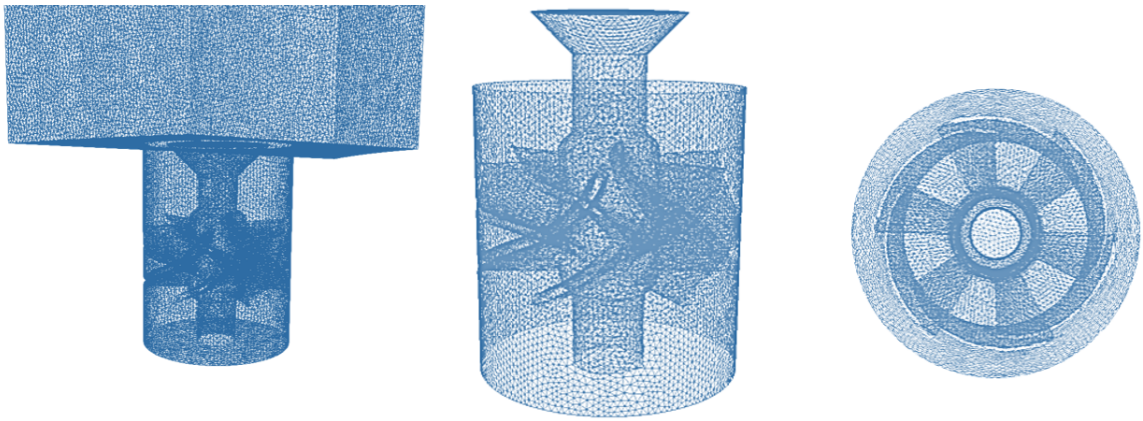

Fig. 4.15 Single burner mesh with swirler side view (left), injector view (centre) and top-down view (right).

Without Swirler

The methods used to produce meshes without the swirler were based on the grid generated by Bainbridge [16] shown in figure 4.16. Without the complex swirler part, more computationally efficient meshing methodologies such as unstructured blocking can be employed. The benefits of using these meshing approaches are well acknowledged and understood [111]. O-grids were created at each of the circular inlets of the burners around the annulus, and extruded through to the outlet. The total cell count for the Bainbridge mesh was 2 million cells, which is significantly lower than that of meshes with the swirler.

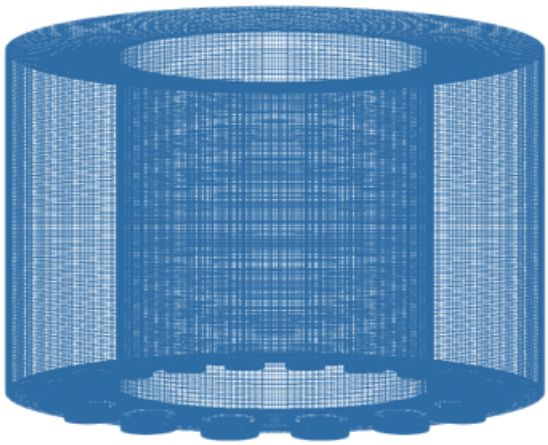

Fig. 4.16 Side view of Bainbridge case mesh [16].

Figure 4.17 shows a schematic view of a cut plane of the computational domain without the swirler part. This type of domain was used in simulations for which a swirl boundary condition was implemented, as presented in chapters 5 and 6. As in figure 4.14, regions a, b and c represent the various mesh refinements applied to the domain respectively. Zone a is the inlet area where an o-grid block was defined and extruded through to the outlet of the chamber. Due to the inlet geometry, the extrusion resulted in a cylindrical volume of more refined cells at the centre of the domain. This is represented by the arrows in region b inside the combustion chamber, and is reflected in the right-most cut plane of the mesh shown in figure 4.18 where regions of higher refinement can be noted to extend from the inlet to the outlet in the axial direction. Zone c represents the gradual decrease in mesh refinement from the entrance of the combustion chamber to the outlet, as was done in the mesh with the swirler part.

Meshes produced for URANS simulations in this thesis are presented in figures 4.18 and 4.19. The single burner mesh in figure 4.18 had a total cell count of 200,000 cells, which when rotated around the centre point of the annulus resulted in a total cell count of 3.6 million

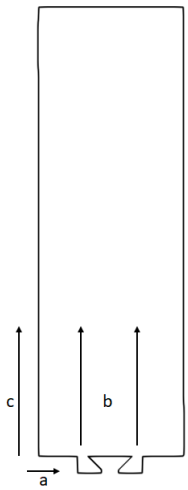

Fig. 4.17 Schematic view of local mesh refinements for URANS mesh without swirler.

for the full UCAM annular rig. A mesh refinement study was performed for which results are shown in chapter 5.

The higher number of cells compared to the Bainbridge case was due to additional refinements applied in the single burner mesh. This was done with a view to assess the feasibility of representing oscillatory behaviour with a single burner configuration by using cyclic boundary conditions. The process is detailed further in chapters 5 and 6.

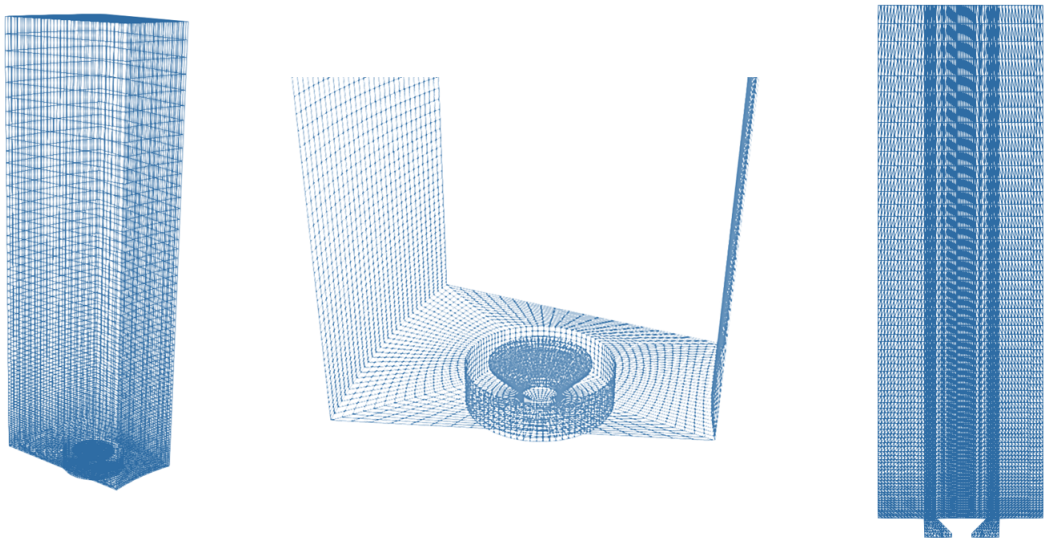

Fig. 4.18 Side (left), inner (middle), and tangential-normal cut plane view of the mesh without a swirler.

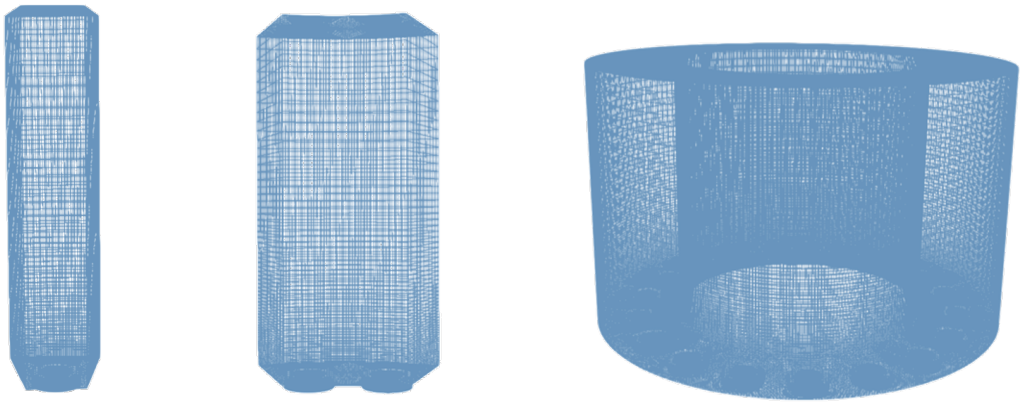

Fig. 4.19 URANS meshes for single (left), twin (middle), and full (right) burner configurations.

4.3.4 Summary

The meshing strategies used for the geometries investigated in the project were presented. The complexity of the swirler geometry limited the cost-efficient techniques that could be employed. Meshing a geometry without the swirler decreased the minimum number of cells significantly and emphasised the advantages of using a swirl inlet velocity boundary condition instead of a mesh containing the physical part.

The characteristics of the different meshes used for analysis on the UCAM rig are summarised in table 4.1 below.

Table 4.1 Summary of UCAM rig mesh characteristics.

Case	Mesh Type	Single burner	Full burner
Lee [59]	Tetra / hexa-core	6.5 million cells	120 million cells
Zetterval [46]	Hexa-dominant	∼4 million cells	∼72 million cells
Bainbridge [16]	Hex mesh	∼110,000 cells	∼2 million cells
Present Work with swirler	Tetra / hexa-core	5 million cells	Not applicable
Present work without swirler	Hex mesh	200,000 cells	3.6 million cells

Numerical modelling methods, geometries and meshes have been introduced in chapters 2, 3 and 4. Model validation is carried out in the next chapter based on the references CFD studies by Bainbridge [16] and Armitage et al. [41].

Chapter 5

Model Validation

5.1 Overview

5.1.1 Simulation Setup

This chapter presents the results obtained for the URANS simulations of the UCAM rig using eddy-diffusivity turbulence modelling. Simulations for this part of the analysis were carried out on a single burner geometry. The flame was first considered enclosed by walls with no-slip boundary conditions at the sides in section 5.2, thus completely confining it within a single burner geometry. Results for this were validated against experimental data by Billant et al. [34], the Bainbridge case [16] and the Armitage case [41]. The flame was then considered as part of the whole annular geometry by implementing cyclic boundary conditions at the sides. This is developed in section 5.3 where results were compared to the Bainbridge case [16].

All simulations were performed using OpenFOAM v2.4.0. As mentioned in chapter 3, the fully compressible reactingFoam solver was used with the PaSR combustion model. Reactions were turned off for isothermal cases and turned on for reacting cases. Ethylene was used as a fuel throughout and was premixed with air at an equivalence ratio of 0.8 to mirror the experimental setup by Worth and Dawson [7]. The inlet temperature was set to the Bainbridge case inlet temperature of 400K [16], and defined as constant. The pressure was set to atmospheric at the outlet with a non-reflecting boundary condition. The inlet velocity and turbulence parameters are detailed in section 5.2.

5.1.2 Presentation of Results

The meshes extracted for analysis were presented in section 4.3.2 of the previous chapter. The computational domain as viewed in the visualisation software Paraview is shown in figure 5.1.

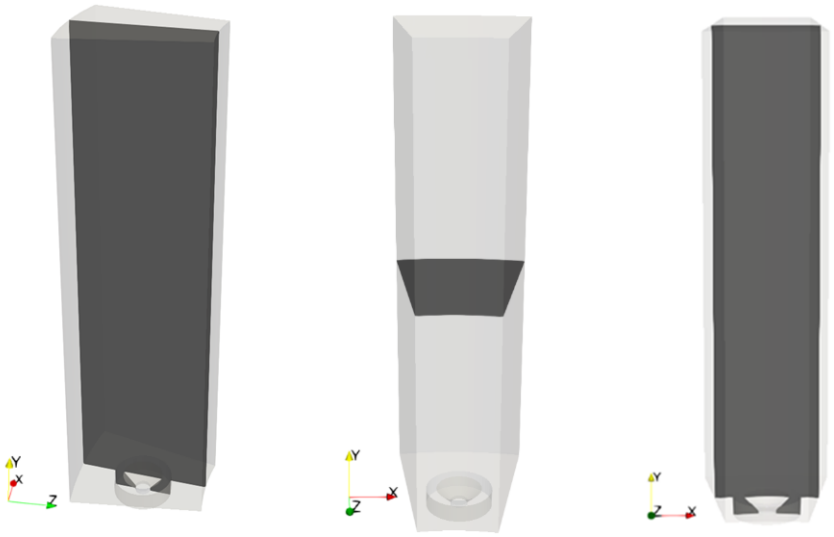

Fig. 5.1 Tangential-normal (left) and axial-normal (centre) planar cuts, and radial-normal (right) cylindrical cut of the single burner geometry.

The x-axis represents the tangential direction, y-axis, the axial direction and z-axis, the radial direction. The origin is placed at the centre of the inlet plane of the computational domain. The entrance to the combustion chamber is located 5mm downstream of the inlet plane at $y = 0.005$m.

In figure 5.1, the outline of the computational domain is represented by the shaded grey colour. The black planes inside the domain show the various types of cuts that could be extracted from the 3-dimensional geometry for analysis, all taken along the central axes. The first on the left is a tangential-normal plane, and is the most commonly used in this and the next chapter as it lends well for comparison with the reference cases. The middle axial-normal cut is also used at various heights to visualise the flame front. Radial-normal cylindrical cuts are presented on the right.

5.1.3 Cases Summary

The reference cases used in this part of the work are listed in section 5.1.1 and detailed in chapters 2 and 3. Table 5.1 below summarises the studies performed for this part of the project. All the cases in table 5.1 are detailed in the following sections of this chapter.

Table 5.1 Summary of cases presented in chapter 5.

Study	Type	Aim
Swirl BC	Isothermal	Calibrate inlet BC
Turbulence Model	Isothermal	Finalise model choice
Mesh Refinement	Isothermal	Finalise mesh refinement
Ignition	Reacting	Test ignition algorithm
Forcing BC	Forced reacting	Test inlet forcing BC
Cyclic BC	Isothermal / reacting / forced reacting	Compare wall / cyclic BC

5.2 Closed Single Burner Configuration

The swirl inlet velocity boundary condition mentioned in chapter 4 is detailed here. Ignition methods are also investigated in this section. In the final part, a combined oscillating and swirling inlet velocity boundary condition is formulated. The cases run with the swirl inlet velocity boundary condition throughout the project are referred to as the 'eddy-diffusivity' or 'ED' cases for convenience.

5.2.1 Isothermal Flow

The isothermal cases were run using the simulations setup described in section 5.1. An additional constraint was put on the global temperature in OpenFOAM to not exceed 400K to enforce isothermal conditions. Without this condition, the temperature was seen to rise by around 0.1 to 0.2K, and return to the intended 400K when reaching steady state. The condition was used as means to test the compatibility between the OpenFOAM constraint options algorithm and the new boundary conditions created for the project.

The swirl inlet velocity boundary condition formulation, turbulence model study and mesh refinement study were performed in isothermal cases to keep the computational demands at a minimum.

Swirl Boundary Condition

The new swirl inlet velocity boundary condition in this thesis was based on the OpenFOAM swirling mass flow rate inlet velocity boundary condition used by Bainbridge [16]. The version of OpenFOAM used in this project, however, did not include a boundary condition capable of accounting for the tangential component of velocity induced by swirl and thus a new boundary condition had to be created.

In the experimental setup, the flow is directed axially through the inlet of the combustor. A tangential velocity component is introduced by the swirlers upstream of the combustion

chamber. The new boundary condition was formulated based on axial, radial and tangential velocity components and a swirl vector, where the direction and angle of swirl could be specified. An axis and centre of rotation were also included in the code to account for the origin and propagation of the swirling flow.

The boundary condition code was formulated as follows:

- Extract an axial unit vector according to the axis of rotation and multiply it by the axial velocity to obtain the total axial velocity vector.
- Define the origin of the axis of rotation unit vector to be at the centre of rotation.
- Create a new unit vector along the radial direction and multiply it by the radial velocity to obtain the total radial velocity vector.
- Obtain the tangential direction unit vector from a cross product between the radial and axial unit vectors and multiply it by the tangential velocity to obtain the total tangential velocity vector.
- Perform a vector addition between the three components to obtain a total velocity magnitude vector.

Isothermal flow simulations were run to test the new boundary condition using the $k-\omega$ SST turbulence model as an initial approach. As the Bainbridge case [16] was run for a reacting flow, it was not possible to compare the test cases in their entirety. However, the velocity profiles at the inlet plane were not affected by reactions as they were prescribed values. As both geometries were cut at the same axial distance of 5mm below the entrance to the combustion chamber, the inlet planes were directly comparable.

Experimental velocity profiles were taken at the entrance to the combustion chamber [7] thus it was important to also compare the velocity field at this point. As the flame sat in the annular enclosure, it can be assumed that the velocity profile would not be affected by combustion processes until reaching the chamber. As such, data from the Bainbridge case [16] could be used to compare isothermal velocity profiles from the inlet to the top of the bluff body at the entrance to the combustion chamber.

The inlet velocity magnitude in the Bainbridge case was 43m/s [16], as explained in chapter 3. This resulted in an axial velocity of 21m/s and a tangential velocity of 37m/s for a swirl angle of 60°. A jet velocity of 58m/s was obtained at the entrance to the combustion chamber. It has to be noted that the Bainbridge geometry [16] was placed at a 90° angle from the geometries in this thesis, with the x-axis as the axial direction and y-axis as the tangential

direction. A single burner was isolated from the full UCAM rig geometry run by Bainbridge for comparison.

Figure 5.2 shows axial-normal plots of the velocity field for magnitude (top), and axial (middle) and tangential (bottom) components. The circular hole in the middle corresponds to the location of the bluff-body. The first column on the left shows results from the geometry with the swirler, which was run to visualise the differences between flow behaviour induced by the physical part and the boundary condition. The axial-normal plots for this configuration were taken 5mm below the top of the bluff body, corresponding to the inlets of the Bainbridge (second column) [16] and eddy-diffusivity (third column) cases. Plots for the last two were taken at their respective inlet planes.

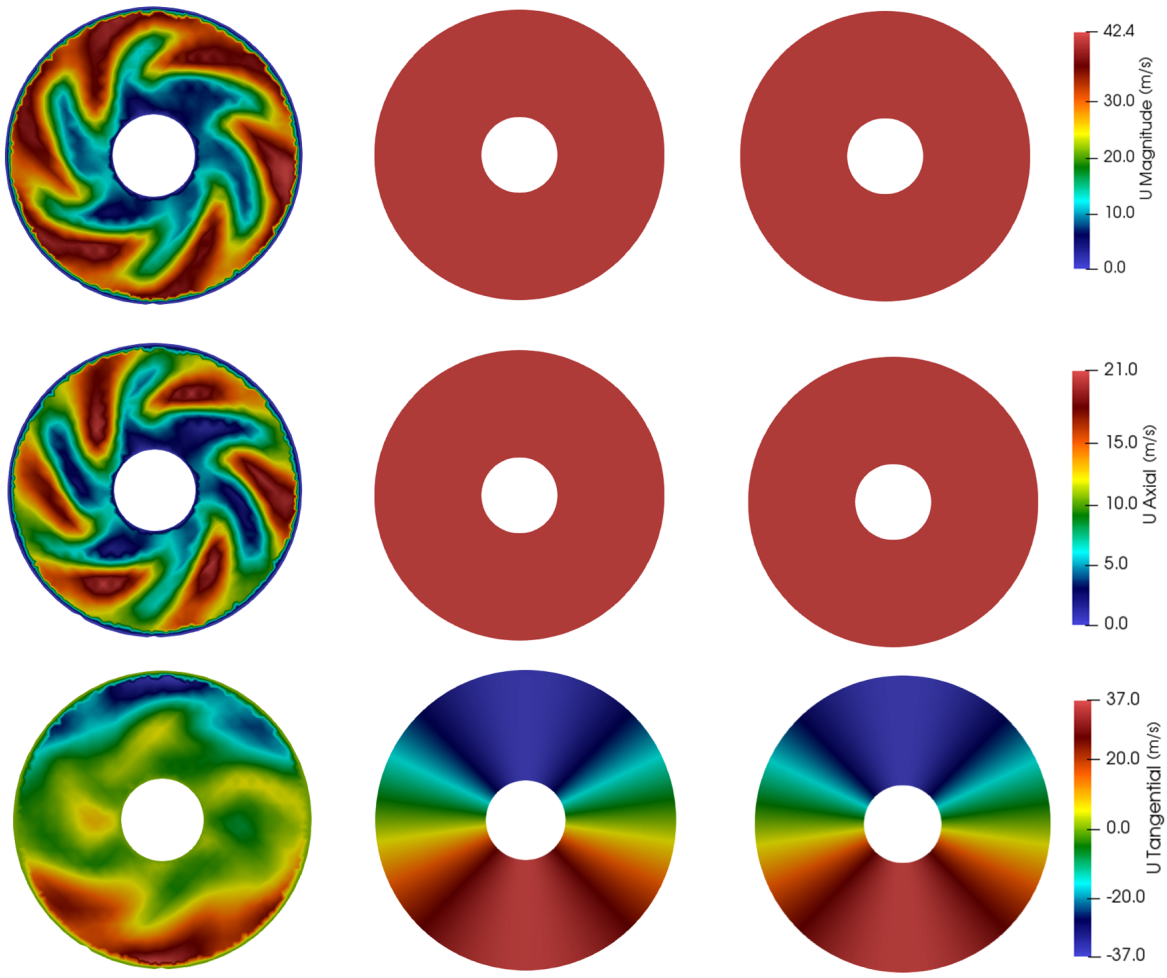

Fig. 5.2 Velocity field comparison between case with the swirler (left), Bainbridge case [16] (centre) and eddy-diffusivity case (right). Velocity magnitude shown on the top row, axial component on the middle row and tangential component on the bottom row.

The velocity magnitude and axial velocity plots on the top and middle row show similar behaviour in the Bainbridge and ED cases with constant values across the plane. For the eddy-diffusivity case in the third column, both velocities are consistent across the inlet. In the Bainbridge case, a variation of around 1% was observed for axial and magnitude values. This can be attributed to the differences in boundary condition formulation or in mesh refinement compared to the ED case. The variations from the inner to the outer part of the inlet plane are, however, considered small enough to be negligible.

The tangential velocity field in the bottom row is quite consistent between the Bainbridge and eddy-diffusivity cases. Both boundary conditions illustrate the positive and negative values induced by swirl indicated by red and blue regions respectively. The plots are also very similar qualitatively with a gradual shift from positive to negative values in the circumferential direction. Additional work on this part of the study can include more in-depth analysis of the data in terms of cylindrical or azimuthal coordinates, to obtain a direct comparison of the swirl component between the three cases.

More noticeable differences arise in the comparison between the Bainbridge / ED cases and the simulation including the physical part represented by the column on the left. The no-slip condition applied to the solid boundaries of the domain result in zero-velocity at the walls, thus creating zero-velocity regions at the inner and outer boundaries of the cut plane and around the swirler and bluff-body upstream. A distinctive S-shape spiral with six 'branches' can be observed stemming from the inner wall in the velocity magnitude and axial component fields. The zero-velocity and number of branches in this region suggests that this behaviour is an effect of the swirler part upstream, and that the spiral is formed by wakes generated by the six vanes. Asymmetry can be seen with varitions in shape from one 'branch' to the next, which can be attributed to the coarseness of the mesh.

The tangential velocity field on the bottom row is similar for all three cases qualitatively with positive values in red and negative in blue. The variation in peak tangential velocity values between all three cases was in the region of 1%, which is again negligible. The most prominant difference between the three plots is the larger region of zero-velocity towards the centre of the plane in the swirler case. This can be attributed to mesh coarseness at the core of the geometry with the swirler, compared to the geometries without the swirler part. A zero-velocity 'ring' is also found at the outer wall of the swirler case, which as for other velocity components, is attributed to the no-slip boundary condition applied.

The discrepancies observed at the inlet needed to be investigated further downstream to ensure that the wakes of the vanes would not have a significant impact on the flow in

the combustion chamber. Quantitative velocity profiles were taken across tangential-normal planes at the inlet and at the top of the bluff-body and are presented in figure 5.3. The blue lines represent the case with the swirler, the black lines, the Bainbridge case and the red lines, the ED case. The plots on the left represent the inlet velocity profiles and the plots on the right show the profiles taken at the entrance to the combustion chamber.

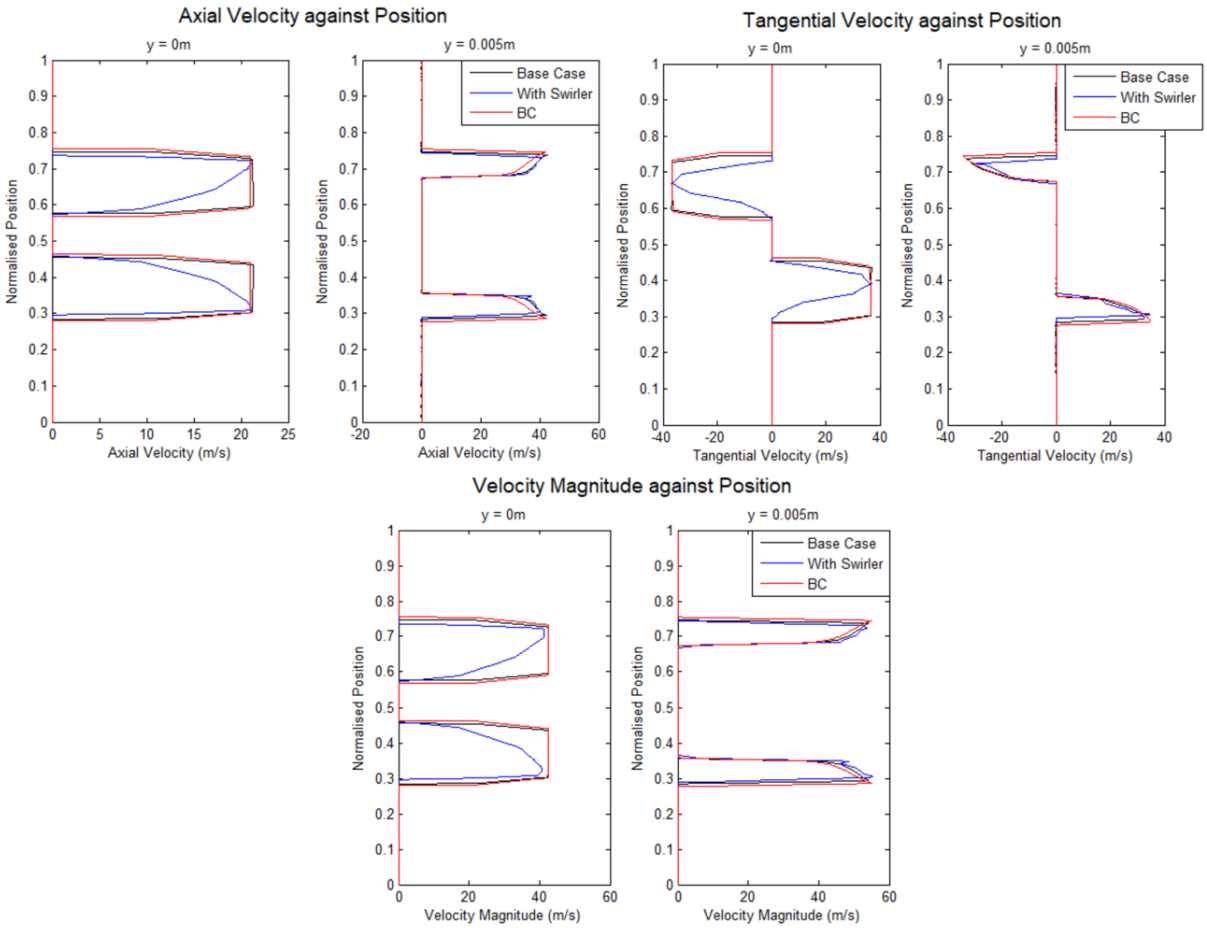

Fig. 5.3 Velocity profile comparison for axial component (top left), tangential component (top right) and velocity magnitude (bottom).

The effect of the no-slip boundary condition on the velocity at the inlet plane is noticeable on the plots on the left for each component. Whilst the boundary condition cases show an abrupt decrease and increase in velocity around the bluff-body, velocity changes occur more gradually for the case with the swirler. This behaviour is corrected downstream where walls are defined for all three configurations. The plots on the right show better agreement between the boundary condition cases and the case with the swirler.

The plots at y = 0.005m show good agreement between the three cases. The plot on the top right shows that the positive and negative values of tangential velocity imposed by swirl are shown by all configurations. At y = 0.005m, the axial velocity is slightly under-predicted and the tangential velocity is slightly over-predicted by the ED case. These effects seem to counter each other in the total velocity magnitude where all three cases are in better agreement. The small discrepancies in the component velocity profiles are outweighed by the computational benefits of using a swirl boundary condition and eddy-diffusivity model for the purpose of this project.

The new velocity boundary condition was capable of representing the characteristics of swirling flow behaviour in the UCAM rig that were described in the Bainbridge case. Good agreement was found between the ED and RSM Bainbridge case [16] both qualitatively and quantitatively.

A more in-depth analysis on the differences between configurations containing the swirler part and those run with a swirl boundary condition is required to assess the potential effects of the vane wakes on forced reacting data. This was not performed at this stage where the aim was to calibrate the boundary condition. This is instead investigated in chapter 6 where comparisons with LES data from the Lee case [59] are performed.

Turbulence Model Study

Chapter 3 explained the importance of choosing an appropriate eddy-diffusivity model for a given simulation. The characteristics of the $k-\varepsilon$ and $k-\omega$ models affect their applicability to certain types of problems. It was therefore decided to conduct a brief turbulence model study to assess the suitability of the options available to the work in this thesis. The eddy-diffusivity models available within OpenFOAM 2.4.0 include standard $k-\varepsilon$, realisable $k-\varepsilon$, $k-\varepsilon$ RNG and $k-\omega$ SST. The single burner mesh presented in chapter 4 was used for this part of the project.

The time to convergence was higher for realisable $k-\varepsilon$ and $k-\varepsilon$ RNG turbulence models with an average increase of 10% in computational time compared to standard $k-\varepsilon$ and $k-\omega$ SST. In addition, both realisable $k-\varepsilon$ and $k-\varepsilon$ RNG converged to an unsteady solution with noticeable flow oscillations in the axial direction over time that were not detected in standard $k-\varepsilon$ and $k-\omega$ SST simulations. This results was also found in converged unforced reacting RSM data by Bainbridge [16], and attributed to numerical error. As such, only the standard $k-\varepsilon$ and $k-\omega$ SST results were chosen for comparison in this analysis.

The standard $k-\varepsilon$ and $k-\omega$ SST turbulence models are compared in figure 5.4, which shows tangential-normal planar cuts of the converged isothermal computational domain. In

both cases, slight oscillations of the high velocity jets in the radial direction were found. These oscillations were found to be of negligible amplitude when at steady state. They can be caused by numerical error in the standard boundary conditions implemented at the sides of the domain. A more in-depth investigation is required to correct the boundary conditions, which was considered as potential future work on the project. For the purpose of this work, it was found that these small radial oscillations did not impact the trends that were to be replicated by the new modelling methodology.

The plot on the left shows the $k-\omega$ SST domain, and the plot on the right, standard $k-\varepsilon$ data. Both plots show similarities in flow behaviour around the bluff body region. The flow is seen to enter the combustion chamber at high velocities represented by red regions, and expands towards the outer walls of the domain. Recirculation zones can be noticed on the outside of the high velocity jets with non-zero velocities represented by lighter-blue regions. Inner recirculation zones are also present in the centre of the burner downstream of the bluff body.

The shape of the two jets is asymmetric for both turbulence model plots. This can be attributed to swirl and to the shape of the single burner configuration. The tangential-normal cut extends from the outer cylinder of the annular chamber to the inner cylinder. The larger radius of the outer cylinder would allow more volume for the flow to evolve in compared to the inner cylinder. This introduces a radial velocity component to the flow, and furthers the asymmetry observed in the tangential-normal cuts of the single burner. This behaviour is reflected in all tangential-normal cuts presented in this chapter and the next.

Key differences can be seen in the shape of the inner and outer recirculation zones, as well as the expansion of the jets at the walls. The inner region of the $k-\omega$ SST plot shows nearly distinct recirculation patterns for each jet with a zone of low velocity in between them. In contrast, the inner region of the $k-\varepsilon$ plot shows that the recirculation zones are almost entirely merged into one. The differences are illustrated by the velocity plots in figure 5.5 below.

The velocity magnitude here was normalised against the bulk flow velocity. The data was taken across the combustion chamber in the tangential-normal plane at axial positions y = 0.025m, y = 0.03m and y = 0.035m from left to right, which correspond to the axial position of the recirculation regions in both cases. The plots show variations in velocity profile between the $k-\omega$ SST and $k-\varepsilon$ cases, which are more pronounced towards the outer walls and at the centre of the domain. As described in figure 5.4, these locations correspond to the inner and outer recirculation regions.

The discrepancies in outer recirculation region and flow expansion at the walls is attributed to the differences in wall treatment between the two turbulence models, and affects the

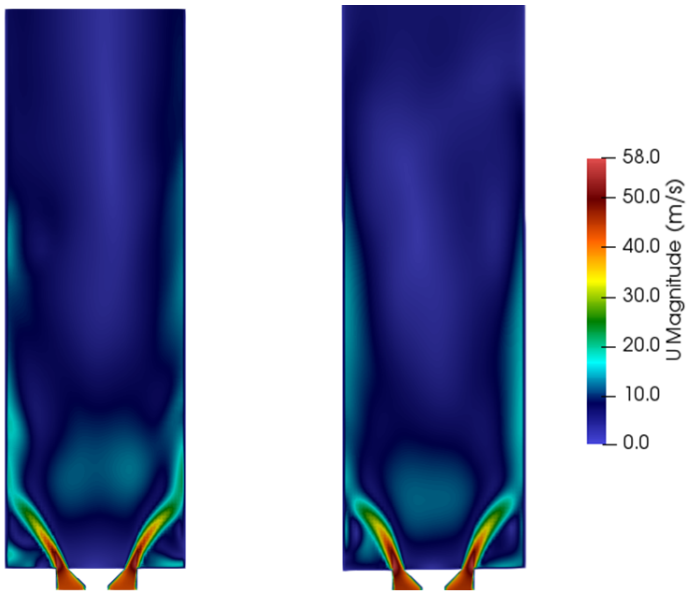

Fig. 5.4 Tangential-normal planar cuts of the velocity magnitude field for k-ω SST (left) and k-ε (right).

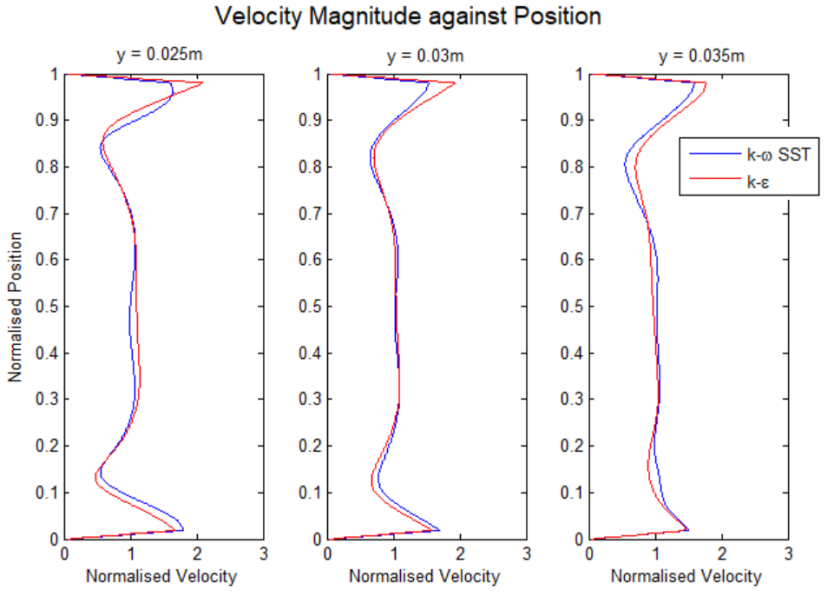

Fig. 5.5 Comparative plot of velocity magnitude for k-ω SST and k-ε along the recirculation regions.

quantitative velocity magnitude results. The plots in figure 5.6 show the velocity magnitude profiles obtained at the inlet and at the top of the bluff body. The quantitative data from the $k-\omega$ SST model was compared in figure 5.3 to RSM simulations by Bainbridge [16] and simulations with the swirler part.

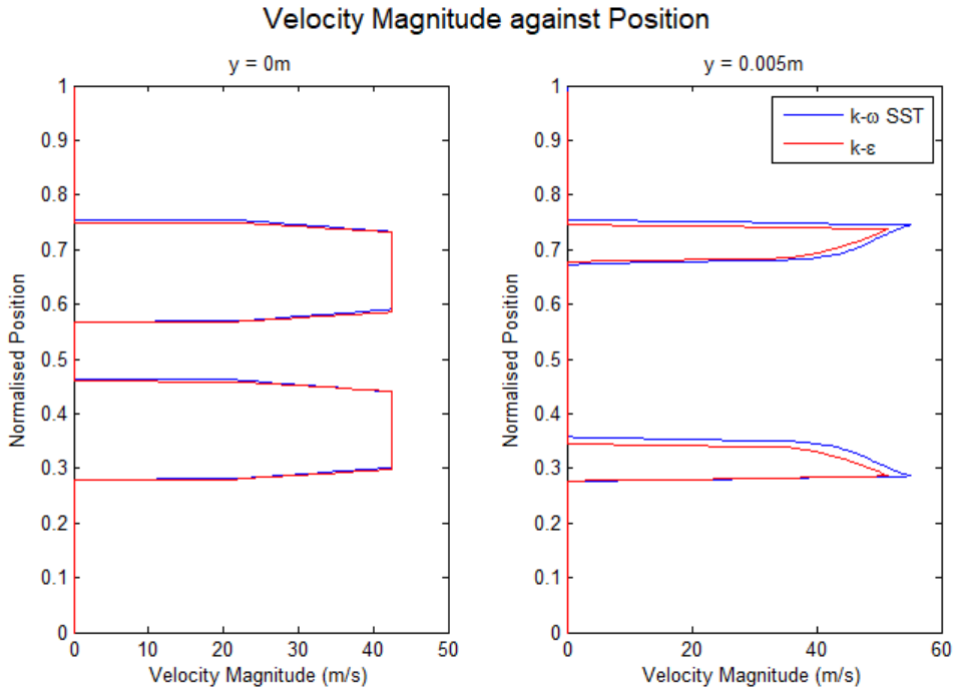

Fig. 5.6 Comparative plot of velocity magnitude for k-ω SST and k-ε at the inlet and combustion chamber entrance.

Chapter 4 showed that the accurate representation of swirling velocity profiles are essential to obtaining good agreement in the flame shape and flame response with reference data. Downstream profiles indicate that the standard $k-\varepsilon$ under-predicts the velocity by 5% compared to $k-\omega$ SST at the entrance to the combustion chamber. It can be expected that the discrepancies in velocity in the isothermal case would be present in a reacting case. The difference in velocity magnitude between reference values and those obtained using the standard $k-\varepsilon$ model is sufficiently large to justify the use of $k-\omega$ SST in future simulations.

Mesh Refinement Study

A mesh refinement study was carried out on isothermal simulations using the $k-\omega$ SST turbulence model. The original mesh was refined twice in all directions, leading to three separate cases with a total number of 230,000 cells, 500,000 cells and 1,000,000 cells respectively. The three meshes are presented in figure 5.7, where the planar tangential-normal cut views show the different refinement levels of the core. Isothermal flow profiles are presented in figure 5.8.

The time to convergence from the least to the most refined cases increased by a factor of 5, which indicated a significant increase in computational cost. Despite the additional

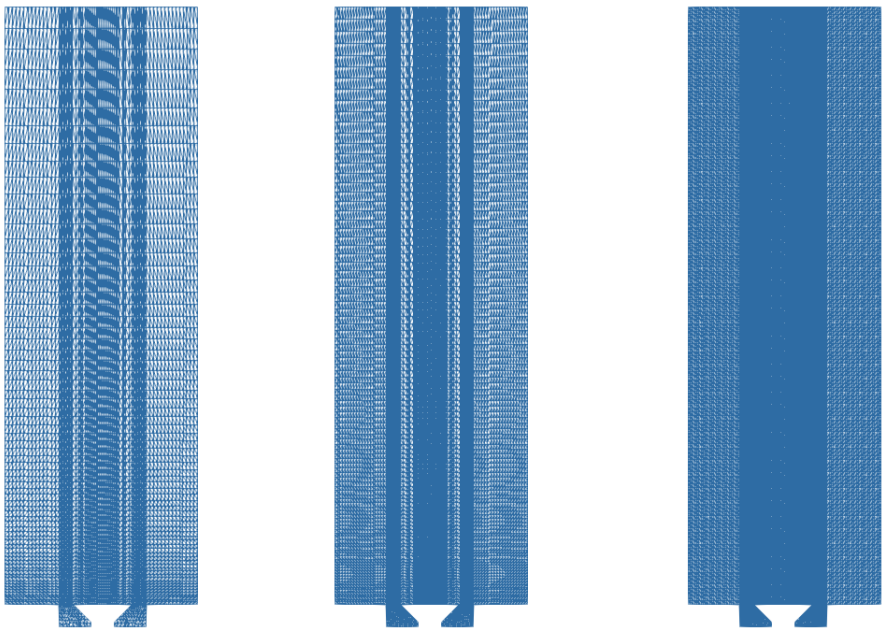

Fig. 5.7 Meshes for convergence study, from coarsest (left) to finest (right).

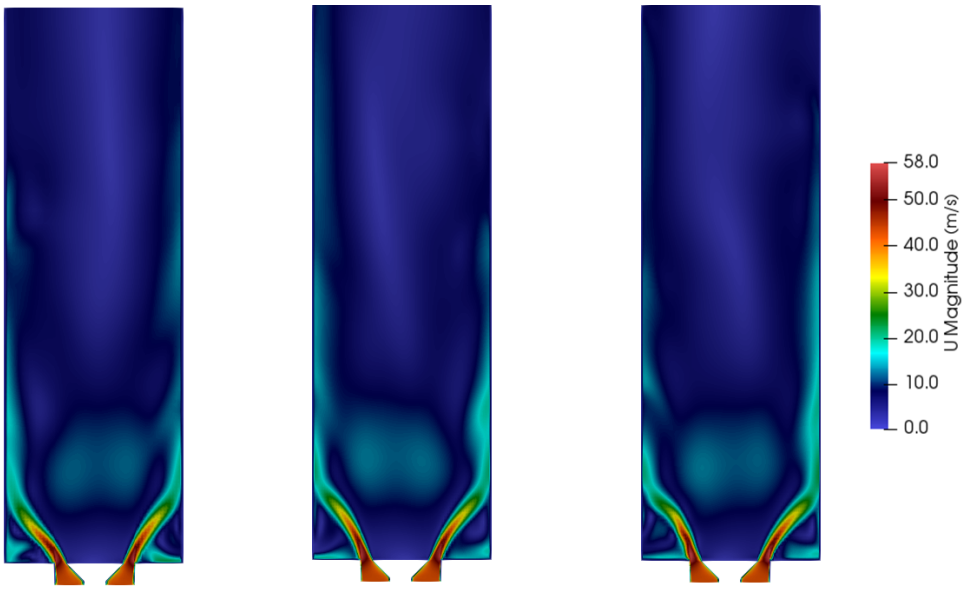

Fig. 5.8 Tangential-normal planar cuts of velocity magnitude for least (left) to most (right) refined test cases.

refinements, all three plots are similar qualitatively. The main difference lies in the recirculation zone patterns and expansion along the walls, as highlighted by the velocity magnitude

profiles plotted along the chamber and shown in figure 5.9. The velocity here was normalised by bulk flow velocity.

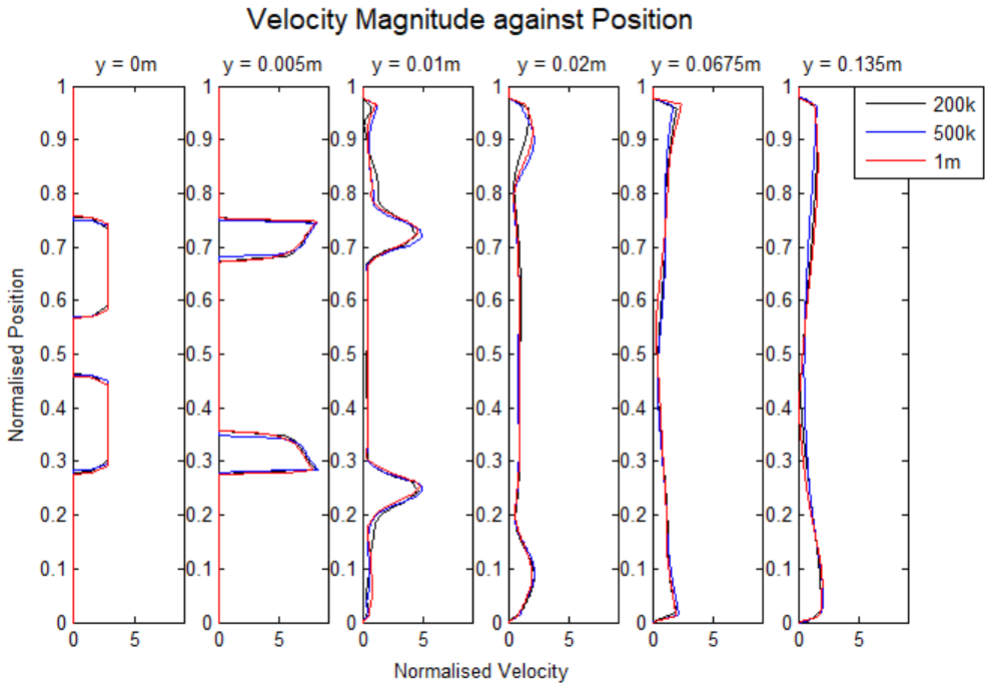

Fig. 5.9 Velocity magnitude comparative plot for the three mesh refinement profiles.

Measurements were taken at various axial positions in the domain. The black lines represent the coarser mesh, blue lines, the intermediate mesh and red lines, the finer mesh. The three results agree well up to y = 0.02m. From then, noticeable discrepancies start to appear in the profiles at the left-most velocity peak and in the centre of the domain.

Complex flow processes are likely to occur in the region from the entrance to the combustion chamber up to the front of the jets, as it is where the swirling flow would develop. This corresponds to axial positions up to y = 0.02m according to the plots in figure 5.8 and 5.9. The velocity profiles are comparable qualitatively and quantitatively in this region. The trends in complex swirling flow behaviour are thus represented by the lower-resolution mesh and the added computational expense of running finer meshes can therefore be deemed unnecessary.

5.2.2 Unforced Reacting Flow

The isothermal flow solution for the chosen mesh and turbulence model was ignited to obtain a steady reacting flow profile. The simulation setup for reacting flows in this chapter was

presented in section 5.1.1. An investigation was carried out on ignition methods before validating the swirling flame profiles against available data from the literature.

Ignition Methods

The reactingFoam solver in OpenFOAM does not provide a numerical tool to the ignite an isothermal flow field. Bainbridge [16] initialised the flow with hot products from the combustion process and introduced cold reactants in the chamber by prescribing mass fraction values of each component at the inlet. This approach was tested for the project, but the significant time taken to convergence on a single burner geometry led to investigating other potential ignition methods.

Lee [12] described an approach that is similar to ones implemented within other OpenFOAM solvers. It consisted in defining a region of high progress variable, and letting the zone spread naturally as it is 'caught' by the recirculation patterns in the flow. As reactingFoam did not export the progress variable directly, it was decided to formulate an ignition algorithm based on another parameter that was defined, such as enthalpy.

The ignition algorithm implemented is presented below:

- Read in the ignition sites, durations and strength factor. Ignition sites were high-enthalpy 'spheres' defined by centre coordinates in the domain and a diameter. The duration of ignition was defined as values in seconds corresponding to the time during which the algorithm would be in operation for a specific ignition spot. The ignition strength was defined as the factor by which enthalpy would rise at each iteration of the algorithm in each spot. A high strength factor decreased the time taken to spread the ignition zone, but could lead to numerical error as unphysical enthalpy levels could be reached.
- Note the local temperature of the cells within the ignition regions. The temperature was taken as a parameter to determine whether the enthalpy had to be raised to ensure complete combustion in this zone. If the cell temperature was below 2000K, the local enthalpy would be multiplied by the strength factor specified for the zone. The threshold value of 2000K was chosen based on the expected adiabatic flame temperature of around 2200K for an ethylene reaction with air at equivalence ratio of 0.8 [23, 113].
- Repeat this algorithm until all required cells have been ignited and a steady reacting solution is obtained.

The process of ignition in the single burner configuration is presented in figure 5.10. The three plots correspond to three separate steps in the spread of the ignition spot. The plot on

the left shows the ignition region prescribed in the algorithm, with the red region of high temperature representing the high-enthalpy zone. The centre plot shows the spread of the high temperature zone in the inner shear layer of the flame. The third plot shows the ignition of outer shear layers, and represents the steady solution for the ethylene flame in the enclosed single burner configuration.

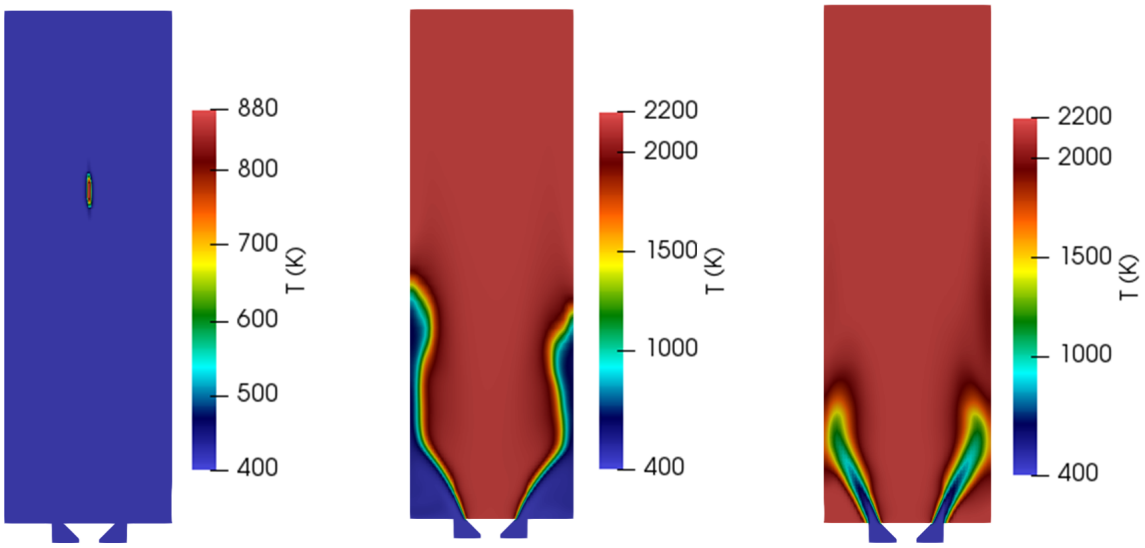

Fig. 5.10 Tangential-normal planar cuts of temperature during ignition phase.

The asymmetry in the low-temperature jets in the right-most plot of figure 5.10 reflects the asymmetry in velocity profiles found in the isothermal cases explained in section 5.2.1. As can be seen at the walls, the jet on the right hand side tends to curl inwards whilst the jet on the left expands further in the chamber. The following temperature profile in figure 5.11 was taken across the burner at the entrance of the combustion chamber, and shows that the expected temperature of around 2200K is achieved.

Swirling Profiles

No experimental or numerical data from the UCAM rig is currently available to compare the particular temperature profile in figure 5.10, which was used to illustrate the ignition procedure. This is due to the fact that the inlet conditions were calibrated on the specific case run by Bainbridge [16] in which higher inlet temperature and inlet velocity values were defined compared to experiments and other CFD studies.

The accuracy of the combination of swirl boundary condition, turbulence model and mesh refinement was thus assessed by observing trends in swirling reacting flow behaviour that

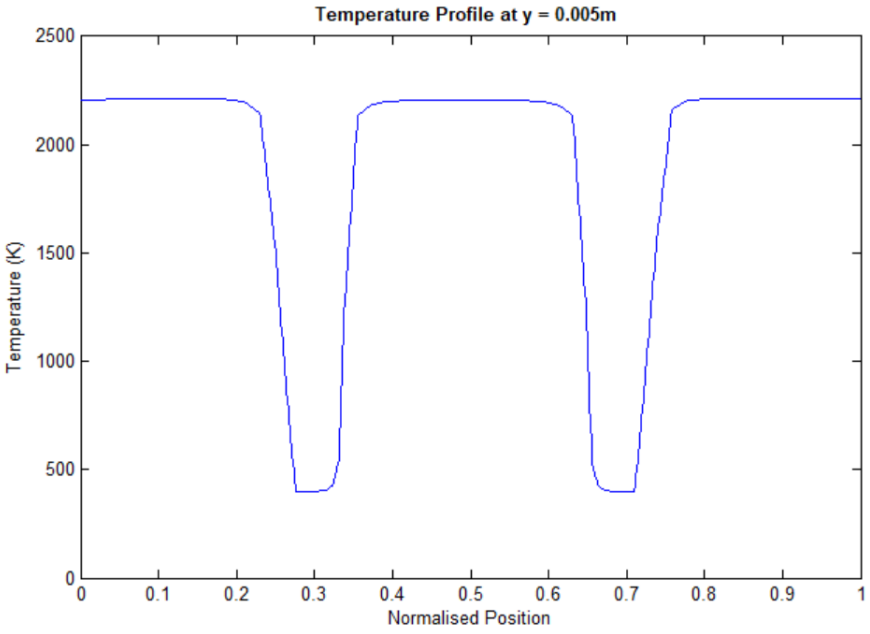

Fig. 5.11 Temperature profile at y = 0.005m.

were represented. For this, the steady solution was compared to the experimental swirling jet profiles obtained by Billant et al. [34] introduced in chapter 2. Figure 5.12 compares the experimental profile on the left, and an axial-normal cut of the single burner UCAM rig solution on the right.

The experimental view on the left was obtained by producing laser sheets at an angle from the horizontal plane [34]. The UCAM rig view on the right was taken at the outlet of the combustion chamber and coloured by velocity magnitude. Corresponding streamlines were traced to highlight the flow behaviour.

The two sets of results share similar qualitative characteristics. A helical pattern centred around the longitudinal axis of the burner is created and rotates in the azimuthal direction. The two branches of the helix in the experimental snapshot [34] are visible in the ED data, as is the recirculation zone at the centre of the S-shape.

The ED velocity field in figure 5.12 shows the differences in flow expansion at the inner and outer chamber cylinder walls noted in the previous sections of this chapter. The branch of the S-shape at the inner cylinder wall is noticeably smaller than that at the outer cylinder wall due to limitations in space. The helix is therefore asymmetric, which is reflected in the jet propagation in all axial-normal and tangential-normal plots extracted from the geometry.

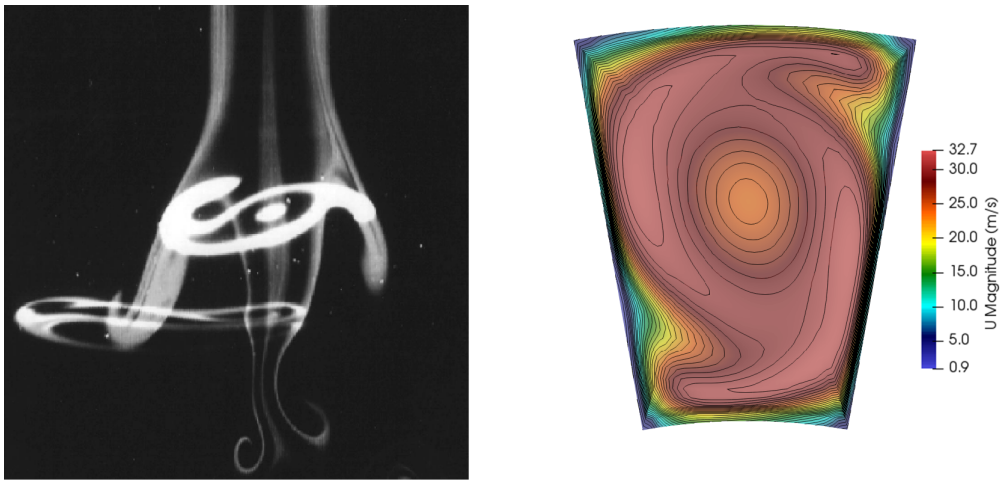

Fig. 5.12 Experimental swirling jet profile [34] (left) and axial-normal planar cut of UCAM single burner (right).

This part of the study demonstrated that the ignition method employed led to sensible adiabatic flame temperatures and faster time to convergence than the ignition approach taken in the Bainbridge case [16]. It was also shown that the inlet velocity boundary condition formulated was capable of representing expected features in a swirling reacting flow, such as the characteristic helical pattern.

5.2.3 Forced Reacting Flow

This section details the procedure and results obtained for the forced reacting simulations of the single burner configuration. The inlet velocity was chosen as a forced parameter to gather data that was directly comparable to the reference cases. An acoustic forcing boundary condition was written to account for swirl at the inlet. Results from the Armitage case [41] were studied and trends were compared to results from the single burner UCAM rig configuration.

Armitage Case

No acoustic forcing cases on an enclosed single burner geometry of the UCAM annular rig are detailed in the literature. Validation of the flame behaviour in response to acoustic excitation was performed with reference to the trends observed in the RSM case by Armitage et al. [41] for this part of the project. Due to the similarities in configurations, it can be expected that some of the characteristic features of forced enclosed single flames in the Armitage case would be represented in the UCAM rig.

The Balachandran et al. [100] bluff-body stabilised enclosed flame was forced by Armitage et al. [41] at varying amplitudes and frequencies. For a frequency of 40 Hz, the amplitudes chosen were 0.15 and 0.65. For a frequency of 160Hz, the amplitudes chosen were 0.10, 0.25 and 0.50. The effects of forcing amplitude on the UCAM rig are investigated in chapter 6. For this part of the analysis, it was decided to focus on the effects of high amplitude and frequency forcing as it was anticipated that this condition would lead to strong flame deformations in response to the inlet oscillating signal.

Characteristic behaviour from the forced flames modelled by Armitage et al. [41] at a frequency of 160Hz and amplitude of 0.50 is shown in figure 5.13. Snapshots of velocity vectors (left) and heat release (right) for six timesteps during a full period of oscillation are presented. Frames 1 to 6 were taken from the lowest velocity peak to the next lowest velocity peak in the sinusoidal wave inlet signal. These results were used as reference for the qualitative trends in flame distortion observed in the UCAM annular rig.

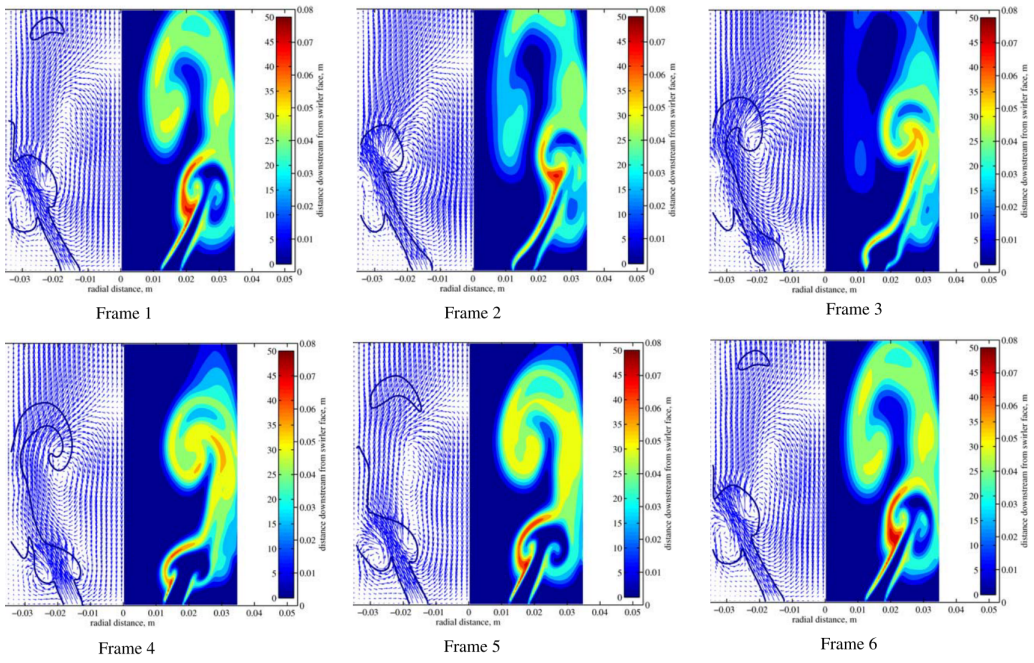

Fig. 5.13 Velocity vector (left) and heat release (right) response of the flame during one period of oscillation in the Armitage case [41].

Armitage et al. [41] found that flame deformation increased significantly with forcing amplitude. An increase in forcing frequency also altered the response of the flame more noticeably with varying amplitude. The distortion of the flame at high amplitude and high frequency forcing is shown in figure 5.13. An in-depth analysis of the flame shape during this oscillation cycle is provided by Armitage et al. [41]. For the purpose of comparing this data

to results from the UCAM rig simulation, the most notable flame characteristics obtained are listed below.

- The first consists of mushroom-like formations at the flame front, as visible in frames 1, 2, 5 and 6. This is found near the region of interaction between the jets and the walls, were vortices cause the inner and outer flames to roll up.
- The second can be observed in frames 1, 5 and 6 and consists in the detached flame region propagating towards the outlet of the combustion chamber. This is indicated in the vector fields on the left by the small region of high velocity downstream of the anchored flame.
- The third consists in the repeatability of the cycle. The flame shape varies greatly from frames 1 to 5 in response to the inlet signal. In frame 6, the velocity has returned to its original value of frame 1. The physical aspect of the flame is remarkably similar between frames 6 and 1, indicating that the cycle is starting once more.

These three characteristic flame behaviours can be explained by the vortex formation processes induced by velocity variations during the oscillating cycle [41]. The vortices at the inner and outer flames cause the flame front to roll up at the point of interaction with the walls and form the mushroom shapes in frame 1. The outer vortices expand at the walls in frames 2 and 3 as the inlet velocity increases, bringing the flame front with them. Simultaneously, the inner vortices move in the downstream direction causing the inwards rollup of the flame in frame 3.

At this point, secondary vortices are also forming towards the centre and near the walls at the entrance of the domain. In frame 3, the secondary vortices cause a second region of inner and outer flame rollup respectively. Frames 4 to 6 illustrate the interaction between the primary and secondary vortex mechanisms. In frame 4, the outer vortex downstream collapses at the wall and secondary vortices provoke a 'roll down' of the flame upstream, which starts to regain its mushroom-like aspect.

The downstream inner vortices have moved further towards the outlet. The stretching of the flame front due to this movement leads to the collapse of the inner flames in frames 5 and 6, which further causes the detachment of a flame region. The cycle repeats itself when the primary and secondary vortex formations merge between frames 6 and (new) frame 1.

Armitage et al. extracted a transfer function from simulation data for each input signal [41]. The gain and phase of the transfer functions were used to quantify the differences in heat release response compared to the inlet signals. Trends observed in transfer function at

high frequency and varying amplitudes are detailed in chapter 6 in comparison with data from the UCAM rig.

This part of the analysis only considered one amplitude and frequency setting for the UCAM rig, thus providing one transfer function result for the UCAM single burner configuration. As the configuration and forcing parameters differed from the Armitage case [41], the values of the transfer functions could not be compared directly. Instead, the trends in time-series and frequency domain representations of the inlet signal and heat release were analysed. These were plotted explicitly for the Armitage cases using a forcing frequency of 40 Hz [41].

Figure 5.14 shows the time-series plots of normalised inlet velocity (top) and heat release response (bottom) for six stable oscillating cycles at an amplitude of 0.65, which was the highest tested for this frequency. Results were recorded after the initial transient phase.

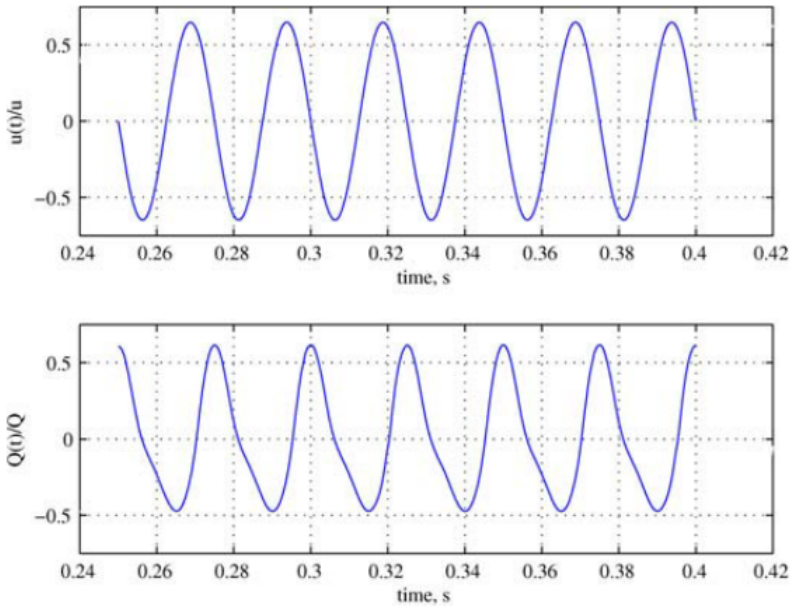

Fig. 5.14 Time series of normalised inlet signal (top) and heat release (bottom) for the Armitage case [41], $f = 0.40$ and $A = 0.65$.

The repeatability of the cycle is shown quantitatively in the regular patterns of inlet velocity and heat release obtained. The sinusoidal signal represented by the plot at the top is regularly oscillating between -0.65 and 0.65, corresponding to the forcing amplitude. However, a loss of sinusoidal shape can be seen in the time-series pattern of the normalised heat release response [41]. The plot at the bottom shows varying gradients between increase

and decrease in heat release, as well as varying peak amplitudes. A phase shift can also be observed by the time delays between the peaks in velocity signal and heat release.

The distortion of the heat release response mirrors the distortion of the flame at high amplitude forcing [41]. The plots in figure 5.15 illustrate this occurence in the frequency domain.

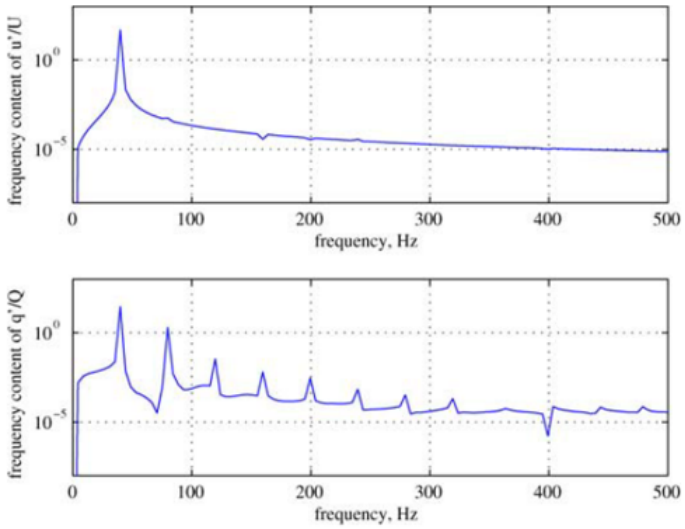

Fig. 5.15 Frequency domain representations of normalised inlet signal (top) and heat release (bottom) for the Armitage case [41], f = 40Hz and A = 0.65.

In both plots, the peak at the forcing frequency of 40Hz is clearly visible [41]. Additional harmonic peaks can be seen in the heat release plot at frequencies corresponding to multiples of the original forcing frequency. This behaviour in the heat release response was characterised as non-linear [41]. Armitage et al. also concluded that a higher number of harmonic peaks and higher harmonic amplitudes were proof of further non-linearity in the system.

Acoustic Forcing Boundary Condition

An acoustic forcing boundary condition was formulated for the UCAM rig simulations based on the existing OpenFOAM oscillating inlet value condition. Forcing was provided by means of a sinusoidal signal imposed on velocity components, taking the form:

$$u' = u(1 + A\sin(2\pi f t)) \tag{5.1}$$

where u is the chosen inlet velocity component, A is the amplitude of oscillation, f is the frequency of oscillation, and t is time. The frequency and amplitude values were

defined within the code and were easily changed by recompiling the boundary condition in OpenFOAM.

The combination of this forcing signal and swirl velocity boundary condition allowed for any of the velocity components to be forced independently or simultaneously with varying amplitudes and frequencies. An assumption was made in that the components responded to acoustic forcing uniformly by applying the signal to the total velocity magnitude. In reality, the velocity components may respond in different ways to acoustic forcing applied upstream of the swirler. Investigating specific effects of forcing on velocity components was, however, considered beyond the scope of this work.

The interpretation of the signal by the solver was tested on the inlet of the computational domain. The velocity magnitude was averaged over the inlet surface and plotted against time in figure 5.16. The black circles on the plot represent the times at which a tangential-normal cut of the temperature field was extracted for analysis in figure 5.17. The inlet velocity magnitude was set to 43m/s to match the Bainbridge case [16]. The oscillation amplitude was set to 0.65 and frequency to 160Hz to compile the boundary condition to match data from Lee on the UCAM rig exactly [59], thus preparing future investigations in chapter 6. From these oscillation parameters, the velocity is expected to vary from 15.05m/s to 70.95m/s in a total time of 62.5ms per cycle. The plot in figure 5.16 shows that these values are respected by the boundary condition over time, and thus the oscillation parameters input in the boundary condition are exported to the inlet velocity field correctly.

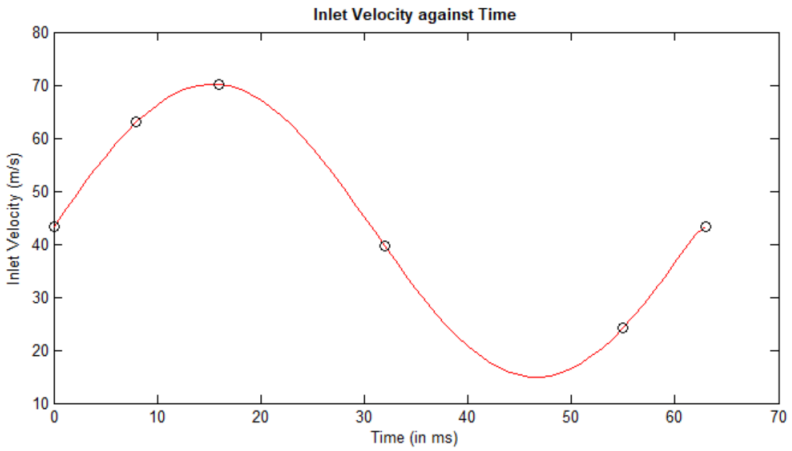

Fig. 5.16 Inlet velocity magnitude plot against time for one oscillation cycle.

Forced UCAM Single Burner Configuration

The reference case by Armitage et al. [41] illustrated expected behaviour qualitatively and quantitatively for high amplitude forcing. As a result, it was expected that the flame shape in the enclosed UCAM single burner would be noticeably distorted for the forcing parameters implemented. It was also expected for the time and frequency domain representations of the data to reflect this distortion. The following analysis assessed the capabilities of the boundary conditions created, mesh generated, and combustion and turbulence models used to represent the key features of flame behaviour described above.

Figure 5.17 shows tangential-normal planar cuts coloured by temperature (top) and heat release rate (bottom) during one period of oscillation. Individual plots are referred to as frame 1 to frame 6 in order from left to right. The coarseness of the mesh can be seen to affect the visibility of the heat release rate data towards the centre of the mesh. However, both the temperature and heat release rate plots show comparable flame structures throughout. Additionally, similar behaviour to what was described in the Armitage case [41] is represented.

Compared to the steady reacting case presented in figure 5.10, the flame front is rolled up towards the walls in frame 1. This is explained by the presence of vortices at the inner and outer shear layers of the flame. The mushroom shapes observed in the Armitage case [41] are less pronounced here as the burner configuration differs. However, these shapes become more evident in frame 2 where the vortices are expanding the flame along the wall. The flame front is also curving inwards due to the downstream movement of the inner recirculation, as was found in frame 3 of the Armitage case [41]. In frame 3 of the UCAM rig case, simultaneous detachments of flame region at the left and right-hand-side jets can be noticed. These can be seen to propagate downstream and have exited the system in frame 4. The formation process of these detachment regions was explained in the Armitage case [41].

At the inlet of the combustion chamber, secondary vortices are formed as the velocity increases again in frame 5. The mushroom shapes at the flame front start to form at this point. The flame in frame 6 is remarkably similar to the flame in frame 1 in both temperature and heat release rate plots, with the exception that the jet on the left extends further towards the wall than the jet on the right. This can be attributed to the natural asymmetry of the flow induced by the burner geometry. Figure 5.16 shows that the velocity had returned to its original value in frame 6 after completing one period of oscillation. The otherwise identical flame shapes obtained in frames 6 and 1 are indicators of the repeatability of the cycle.

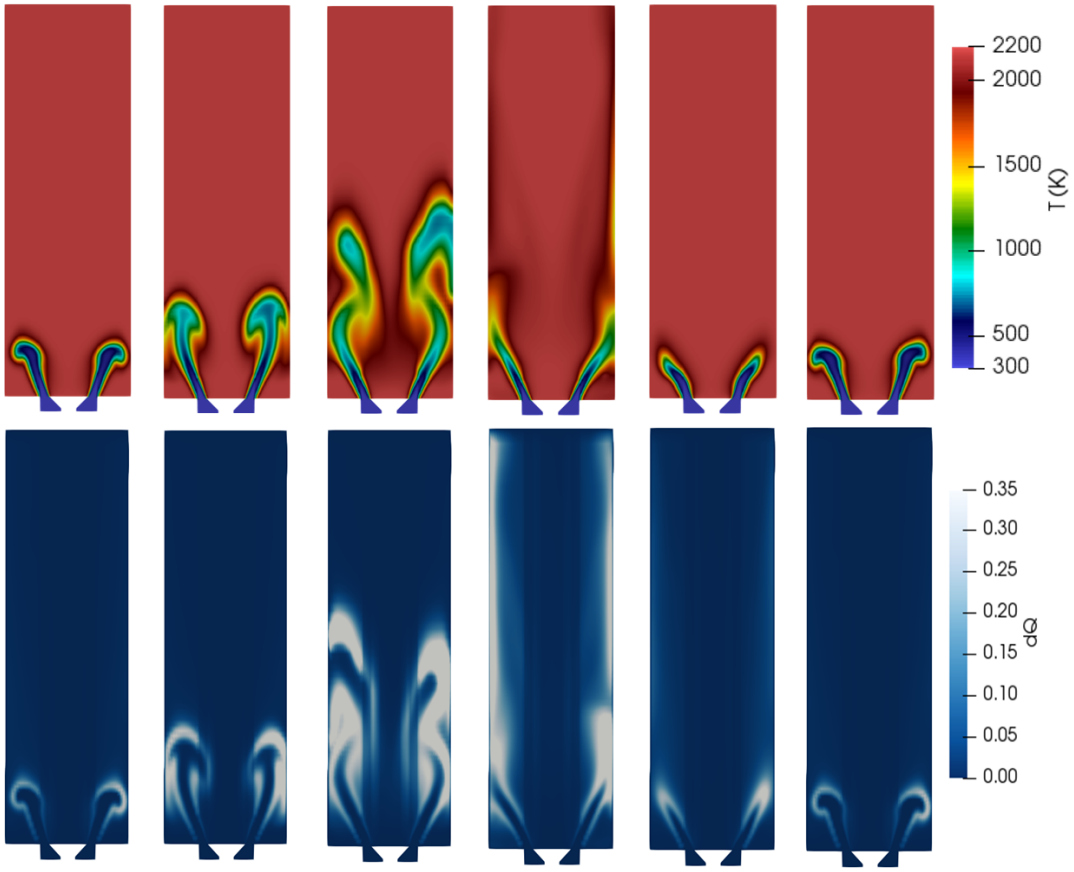

Fig. 5.17 Tangential-normal plots of temperature field (top) and heat release rate (bottom) during one oscillating cycle.

Figure 5.18 shows the corresponding vorticity profiles for the six timesteps indicated in figure 5.16, normalised against bulk vorticity. The frames are numbered 1 to 6 from left to right. The regions of high vorticity are represented by the white colouring. The profiles highlight the formation of vortical structures described above and by Armitage et al. [41], which cause the heat release oscillations illustrated by figure 5.17. Frame 1 shows primary high-vorticity regions at the inner and outer flame regions, which as per explanations by Armitage [41] lead to the mushroom-like aspect of the flame front in frame 1 of figure 5.17. Frames 2 and 3 of figure 5.18 shows that the high-vorticity regions at the outer flame have expanded along the wall. Higher vorticity regions are also found at the inner flame and are seen to move downstream along with the outer vortices. This causes the downstream movement of the flame front in frames 2 and 3 of figure 5.17.

In frames 3 and 4 of figure 5.18, the formation of new, secondary high-vorticity regions towards the entrance of the combustion chamber can be noticed by the lighter colouring at

the inner and outer flames at this axial location. This leads to a secondary flame rollup in frames 3 and 4 of figure 5.17. Frame 4 of figure 5.18 shows that the vortical structures at the outer flame have collapsed at the wall, and that the high-vorticity region at the inner flame has propagated downstream in the chamber. This causes the outer flame to roll down in frame 4 of figure 5.17.

In frame 5 of figure 5.18, the high-vorticity region at the inner flame collapsed due to the stretching of the flame front as the vortical structures move towards the outlet. At this stage, the primary and secondary high-vorticity regions are merging and cause the flame to start to regain its mushroom-like aspect in frame 5 of figure 5.17. Finally, the primary and secondary vortical structures have merged entirely in frame 6 of figure 5.18, where the cycle starts again. This causes the similarities between frames 6 and 1 of figure 5.17, and further demonstrates the repeatability of the cycle.

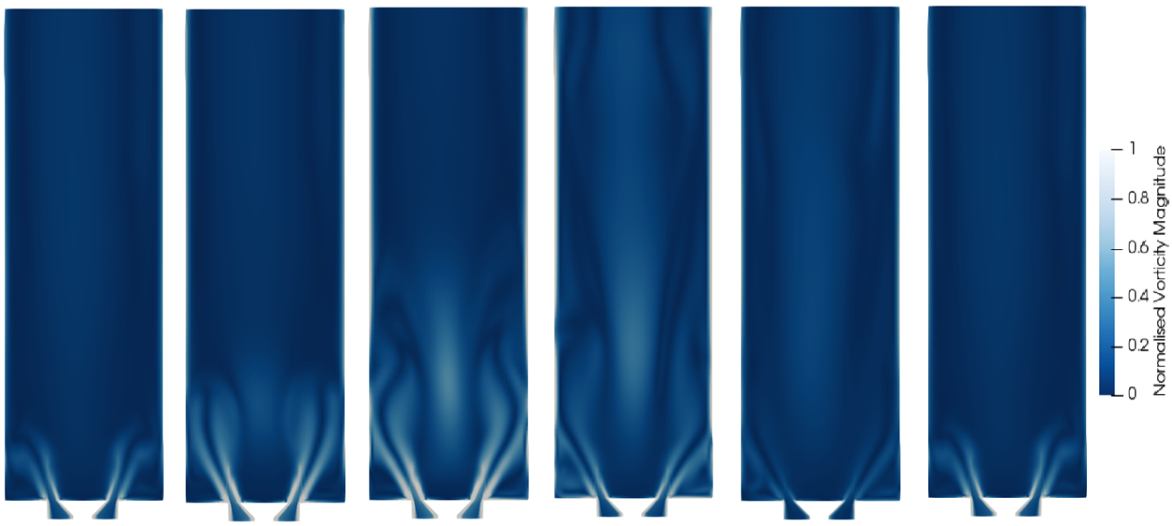

Fig. 5.18 Tangential-normal plots of vorticity during one oscillating cycle.

The qualitative behaviour obtained in the UCAM rig simulations thus presents the three major characteristics observed in the high-amplitude forcing Armitage case [41]. These included the roll-up of the flame, the flame detachment regions and the repeatability of the cycle.

The distortion of the flame shape during the cycle is made evident by the qualitative plots in figure 5.17 and 5.18, and was analysed further quantitatively in figures 5.19 and 5.20. Figure 5.19 shows time series of the normalised inlet velocity (top) and normalised heat release response (bottom). The data was plotted over three oscillating cycles after initial transients, with a time of 62.5ms per cycle. The normalised inlet velocity plot mirrors the data in figure 5.16 with a regular sinusoidal pattern oscillating between -0.65 and 0.65

corresponding to the forcing amplitude. The heat release response, however, presents some distortion in the sinusoidal pattern obtained. Steep gradients can be seen in the increasing phase of the heat release cycle. A phase shift can also be observed between the inlet signal and heat release response. These results reflect the data obtained in the Armitage case [41], and are indicative of non-linearity between inlet signal and response.

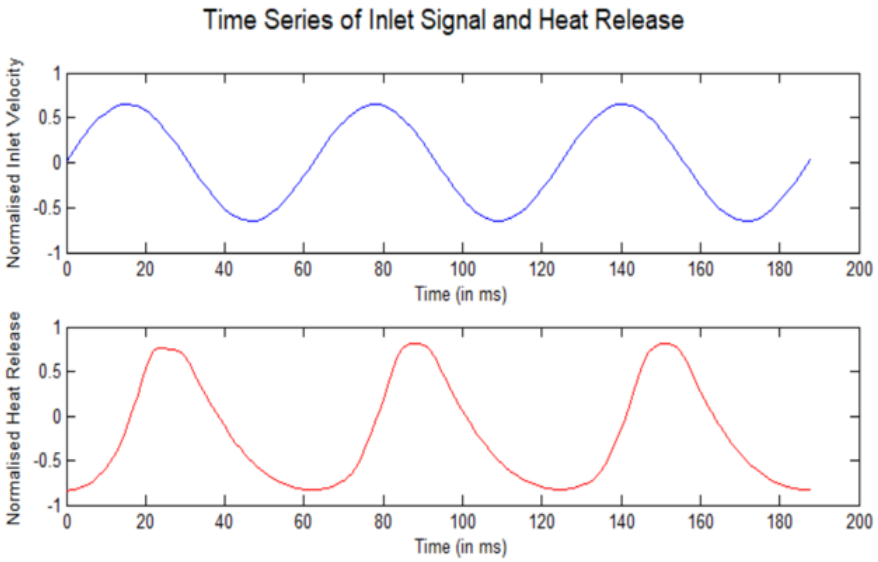

Fig. 5.19 Time series of normalised inlet signal (top) and heat release (bottom) for the enclosed single burner UCAM configuration, f = 160Hz and A = 0.65.

Further proof of non-linear behaviour was found in the frequency domain plots presented in figure 5.20. The inlet velocity (top) and heat release response (bottom) spectra were obtained to highlight the distortion observed in the time series patterns of heat release. Noticeable peaks of amplitude can be found at the forcing frequency of 160Hz for both plots. However, whilst the inlet velocity plot shows a single peak at 160Hz, harmonic peaks at multiples of the forcing frequency are found for the heat release response. The amplitude of the harmonics decreases past the forcing frequency, as was found in the Armitage case [41].

It may be concluded that the combination of swirl boundary condition, turbulence model, combustion model, mesh refinement and acoustic forcing boundary condition resulted in comparable behaviour to the reference data for the enclosed UCAM single burner configuration at each stage of the investigation. The coarse mesh resolution and eddy-diffusivity model used were capable of representing non-linearity effects induced by high amplitude forcing in this context.

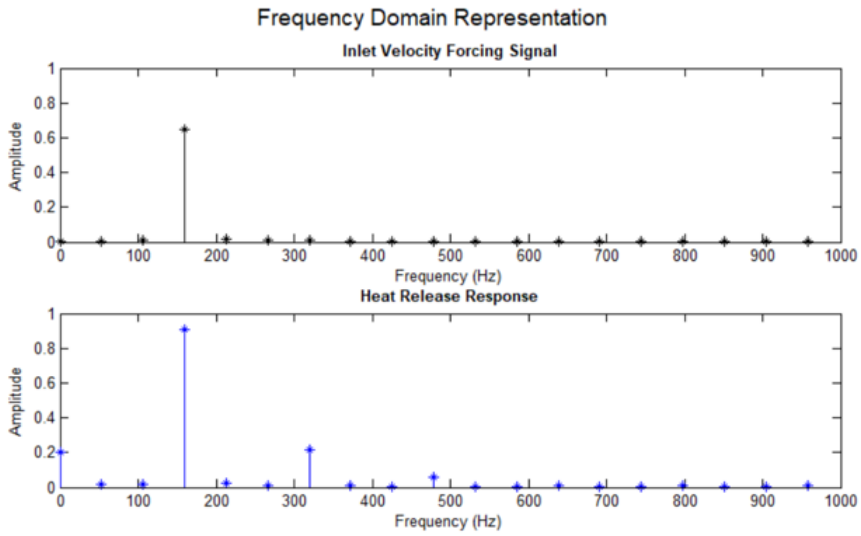

Fig. 5.20 Frequency domain representations of normalised inlet signal (top) and heat release (bottom) for the enclosed single burner UCAM configuration, f = 160Hz and A = 0.65.

The UCAM rig contains a total of 18 burners around the annulus that can interact and alter the flame as explained in chapter 4. The next section studies methods in which to represent the full annular rig efficiently.

5.3 Cyclic Single Burner Configuration

The previous analyses have been performed on a single burner configuration for which the side boundaries joining the inner and outer cylinders of the combustion chamber were defined as walls. 'Periodicity' or cyclic boundary conditions are methods often employed to represent repeating geometry around a central axis without including the repeated parts in the mesh. Introducing cyclic boundary conditions to the UCAM rig could be a solution to representing flame-flame interactions on a single burner model, which would drastically reduce the size of the computational domain compared to a full 18-burner annulus. The single burner mesh shown in figure 4.18 allows for the side boundaries of the domain to be prescribed as either walls or cyclic fluid faces in OpenFOAM.

The interaction between flames and their subsequent effects introduced by cyclic boundary conditions are referred to as 'notional' in this thesis, in contrast with 'physical' flame-flame interactions occuring due to the presence of additional burners in the mesh. A comparative study between cyclic boundary conditions and multi-burner configurations in the UCAM rig

is detailed in chapter 6. The aim for this part of the project was to set up the cyclic boundary conditions and note key differences with results obtained in section 5.2.

5.3.1 Periodicity in the UCAM Rig

Rotational cyclic boundary conditions can be used to replicate the single burner geometry around the annulus. For this, a centre point, axis and angle of rotation must be defined. During this process, the side walls are re-assigned as repeating fluid interfaces.

Complete alignment between the nodes on each cyclic face was required for the boundary condition to operate successfully. A major benefit of applying a block-type mesh to the geometry was the easier node alignment of the side boundaries within the OpenFOAM environment. The sides faces were first defined as 'periodic' in ANSYS ICEM and exported as fluid patches during the mesh conversion stage in OpenFOAM. OpenFOAM 2.4.0 then required additional specifications to align the node numbers on each boundary correctly.

The cyclic condition parameters were defined as illustrated in figure 5.21, which shows a view of the internal mesh cut at the top of the bluff body for two neighbouring burners. The angle of rotation θ was defined as 20°, corresponding to the 18 burners placed around 360°. The centre of rotation was defined as the centre of the burner, corresponding to the centre point location of the inner and outer cylinders of the combustion chamber. The rotation was defined around the axial-direction axis.

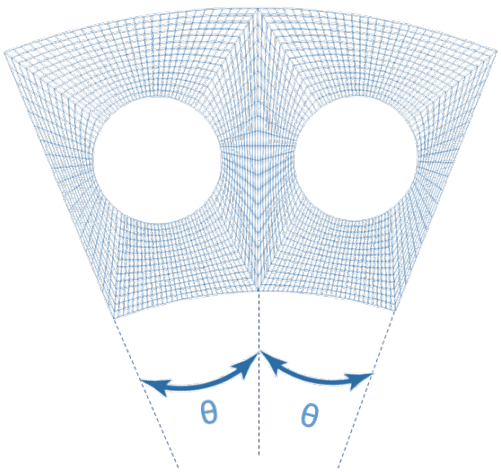

Fig. 5.21 Periodic face coupling in the mesh.

The mesh used in this section was identical to the coarse mesh used in section 5.2 and is thus not shown here.

5.3.2 Isothermal Flow

An isothermal simulation was run with cyclic boundary conditions to check for node alignment in OpenFOAM. The simulation setup was similar to the final isothermal flow studies of section 5.2, with the exception that the initial conditions for the sides of the geometry were re-defined as cyclical. Figure 5.22 shows the two cyclic faces on the left and centre, and an isometric view of the faces in the model on the right. The plots were coloured by velocity magnitude to provide a benchmark parameter for comparison. The velocity field matched exactly between both faces, which indicated that the nodes on either side were aligned correctly.

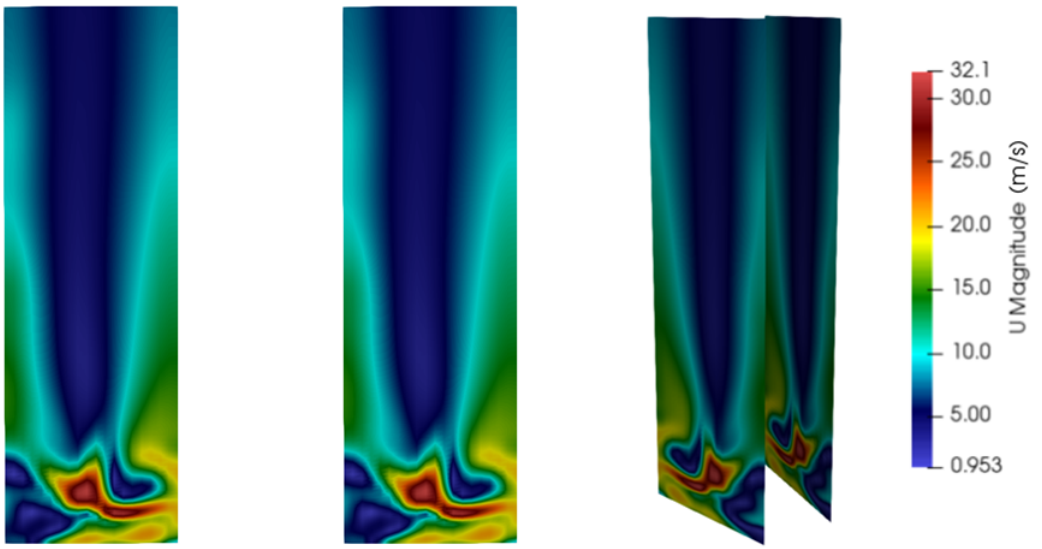

Fig. 5.22 Cyclic faces (left and centre) and isometric view of cyclic faces (right) coloured by velocity magnitude.

This is further demonstrated by the plots in figure 5.23 showing velocity magnitude profiles normalised by bulk velocity, and taken across the faces at various axial positions along the combustion chamber. The profiles for the two cyclic boundary faces (boundary 1 and boundary 2 on the plot) are represented by the blue and red lines respectively. All lines are identical at all axial locations shown, thus only a single colour stands out in all plots of the figure.

No computational or experimental data is available to validate the flow behaviour using this particular isothermal simulation setup. The Bainbridge case [16] can be used as reference for steady reacting cases presented in the next section.

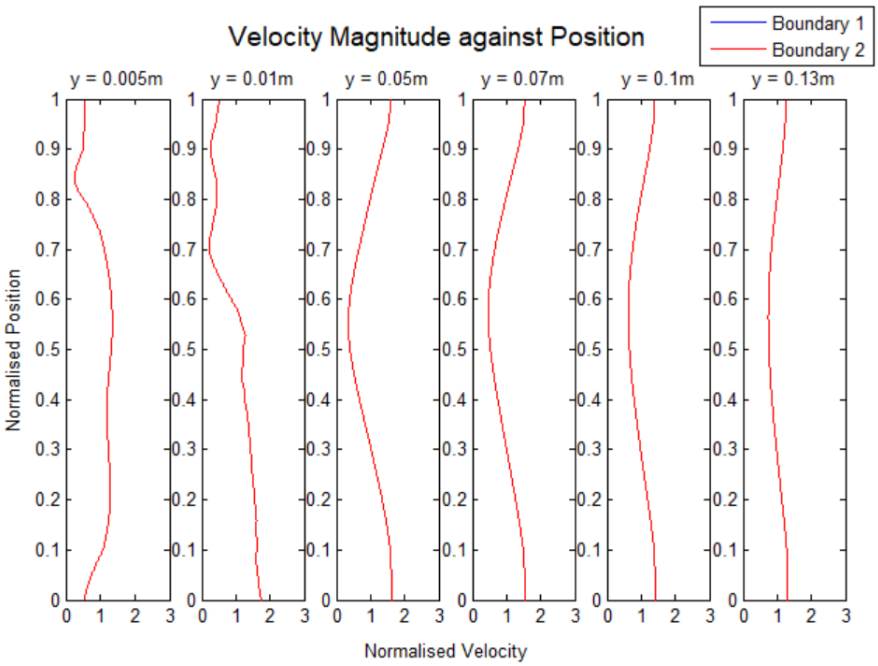

Fig. 5.23 Normalised velocity profiles along the cyclic boundary faces.

5.3.3 Unforced Reacting Flow

The isothermal cyclic case was ignited using a simulation setup that was similar to that of section 5.2.3, with the exception that cyclic boundaries were defined instead of wall conditions for the side faces of the geometry. A single burner tangential-normal cut was performed on the Bainbridge [16] data for comparison with the eddy-diffusivity case.

Figure 5.24 shows tangential-normal cuts coloured by temperature for the Bainbridge case (left) [16], wall ED case (centre) and cyclic ED case (right). In both the plot in the centre and on the right, the flow can be seen to extend towards the edges of the domain. When reaching this point, the notional interaction between neighbouring burners alters the flame shape in the cyclic case and directs the flame front inwards.

The notional distortion of the flame in the cyclic single burner produces similar flame shapes to that of the full burner Bainbridge case [16] on the left. As the Bainbridge flame reaches the location where interactions occur with other burners, the flow is directed towards the centre of the domain. The regions of interaction between flames are characterised in both cases by extended flame fronts compared to the wall case, with larger and irregular zones of low temperature reaching further downstream in the chamber.

Discrepancies between the cyclic ED case and the Bainbridge case [16] can be found in the aspect of the flame fronts. The flame front and inner recirculation zone seem to extend

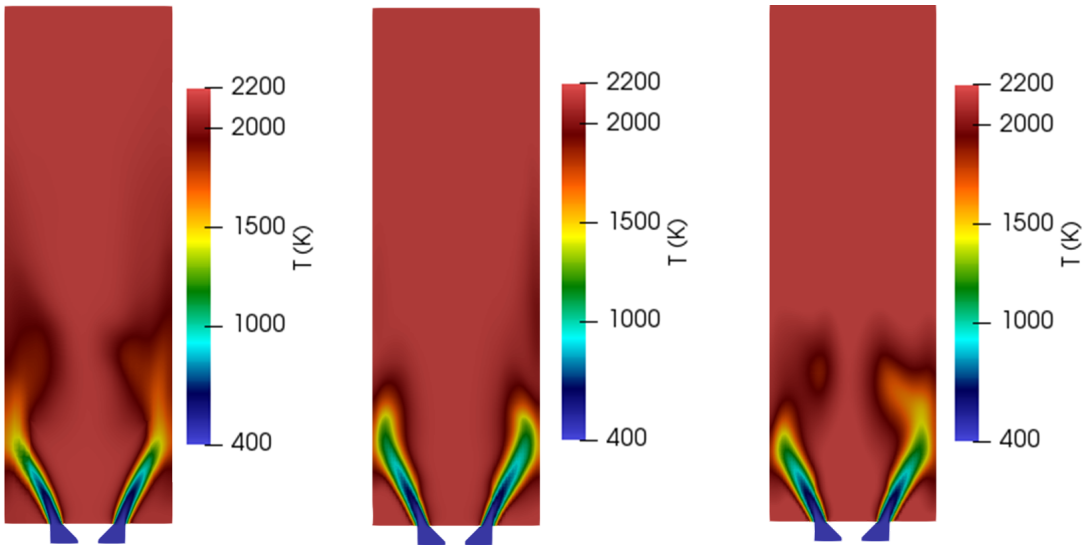

Fig. 5.24 Steady reacting flow temperature field for Bainbridge case (left) [16], wall boundary condition (centre) and cyclic boundary condition (right).

further in the chamber in the Bainbridge case, leading to smaller inward distortion than in the ED cyclic case.

The differences in flame behaviour between the three cases are also visible in the velocity magnitude fields shown in figure 5.25.

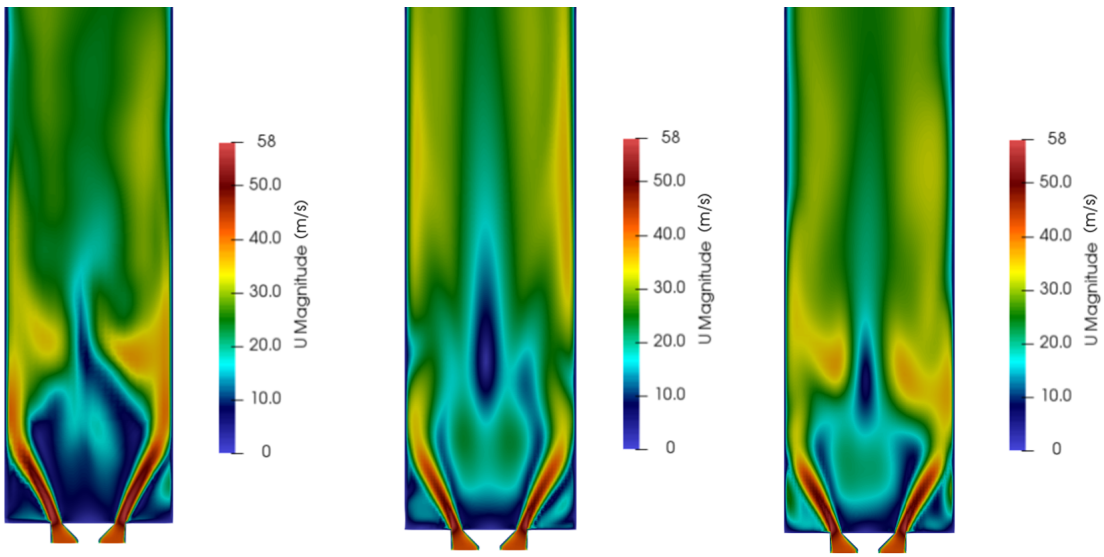

Fig. 5.25 Steady reacting flow velocity magnitude field for Bainbridge case (left) [16], wall boundary condition (centre) and cyclic boundary condition (right).

The wall ED simulation (centre) produced a relatively symmetrical velocity profile throughout the domain, with symmetry in the inner recirculation regions. The interaction between flames is made evident in the Bainbridge (left) [16] and cyclic (right) cases at the front of the jets, with larger high velocity regions propagating inwards and causing asymmetry in the flow field towards the outlet of the chamber. Flow asymmetry is more prominant in the Bainbridge case [16] than in the cyclic ED case.

Figure 5.26 shows velocity magnitude profiles at several axial locations along the chamber for all cases. Discrepancies in the inner recirculation regions that are found in figure 5.25 are reflected here in the plots at axial positions y = 0.03m and y = 0.04m, with high variations in velocity profile towards the centre between the three cases. From y = 0.07m to the outlet, the studies are in better agreement, as is also illustrated by the velocity fields in figure 5.25. The core difference between the data sets lies around an axial position of y = 0.05m. In figure 5.25, this corresponds to the location downstream of the high velocity zones where the jets are interacting with neighbouring burners in the Bainbridge and cyclic ED cases. Figure 5.26 demonstrates that at this point, the cyclic case is in better agreement with the Bainbridge data than the wall case, as expected from the previous qualitative assessment of figure 5.25.

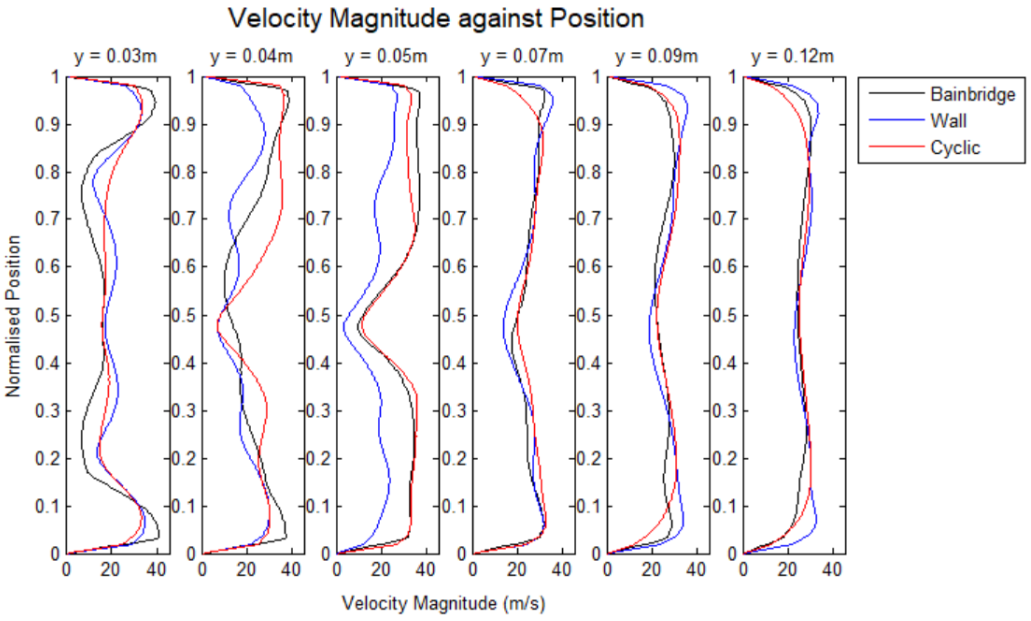

Fig. 5.26 Normalised velocity against position for the Bainbridge case (black), ED wall case (blue) and ED cyclic case (red) along the combustion chamber.

The variations in simulation setup between the Bainbridge [16] and single burner cyclic ED cases can explain the discrepancies obtained. The main difference between the two lies in the fact that all burners in the latter are assumed to behave in an identical fashion, whilst

this may not occur in the full geometry. More in-depth investigations of the effects of ED on the solution are required to assess the accuracy of the method in representing the full burner geometry. This is discussed in the multi-burner studies in chapter 6.

Despite the qualitative differences described, the ED cyclic case produced flame profiles that were noticeably closer to those in the Bainbridge case than the ED wall case. A significant improvement can be observed in the agreement between temperature profiles and velocity profiles when adding notional burners. Figure 5.27 shows axial-normal temperature profiles for the Bainbridge case (left) [16], ED wall case (centre) and ED cyclic case (right). The data was taken at the outlet of the combustion chamber and plotted along velocity streamlines for comparison.

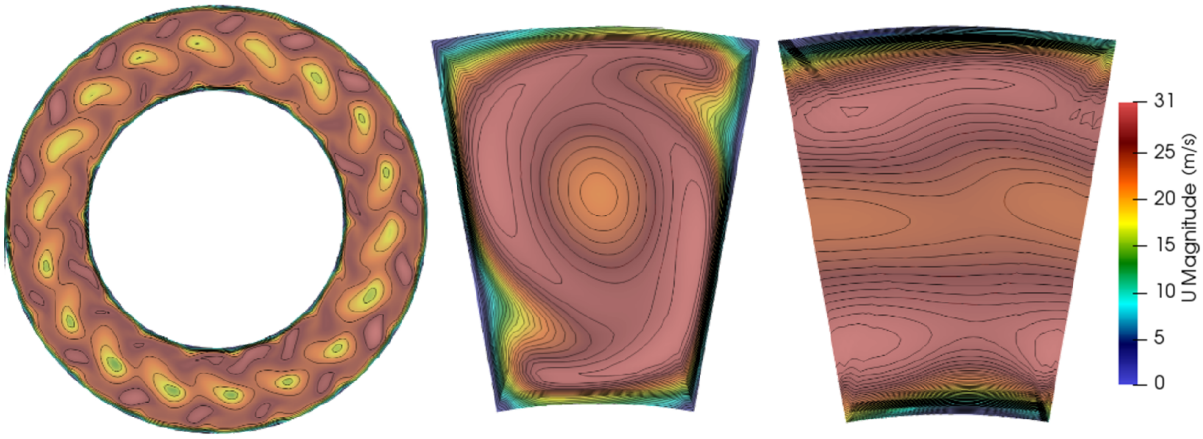

Fig. 5.27 Outlet velocity magnitude contours for base case (left), wall boundary condition (centre) and periodic boundary condition (right).

The most striking difference between the three plots is the absence of the distinct helix shape due to swirl in the Bainbridge and ED cyclic case. This can be explained by the flame-flame interaction effects induced by removing the wall between burners in the geometry. The two distinctive jets obtained in the enclosed single burner geometry form the swirling 'branches' of the S-shape spiral in the central plot. These branches have merged with other consecutive jets in the other two plots to form three separate velocity 'rings': two high-velocity rings towards the inner and outer walls, and one lower-velocity ring at the core due to the interactions between central recirculation regions of the helices.

The streamlines show that whilst flame-merging occurs, the individual burners still affect the flow pattern at the outlet. Separate regions centred around the inlet locations of the domain can be found in each velocity 'ring' of the Bainbridge and ED cyclic cases. The variations in shape of these regions in consecutive burners of the Bainbridge case indicate

that the flow behaviour may not be uniform across all burners around the annulus. Further investigation is required to appreciate the effects of this flow feature on the acoustic response of the flame, and is presented in chapter 6.

The trends in flow behaviour associated with the interaction between neighbouring burners was generally represented by the ED cyclic case in the steady reacting flow simulations. This provided significant improvement in the agreement with reference data compared to the ED wall case. This flame was subject to acoustic forcing and relevant results are presented in the following section.

5.3.4 Forced Reacting Flow

The Armitage case [41] demonstrated that greater levels of distortion in the flame shape can lead to higher levels of non-linearity in the heat release response to acoustic waves, with high amplitude harmonic peaks in the frequency domain representation.

It could be anticipated that the deformation of the flame induced by notional burner interactions would lead to differences in forced oscillating flame profiles between the cyclic and wall cases. This part of the project was used to assess the capabilities of the ED single burner simulation setup to show the effects of neighbouring burners on the flame response to acoustic excitation.

The steady cyclic reacting case was forced in an identical manner to the wall case presented in section 5.2. The results were taken at the timesteps indicated in figure 5.16. Figure 5.28 shows tangential-normal planar cuts coloured by temperature during one period of oscillation for the wall (top) and cyclic (bottom) ED cases. As in figure 5.17 and 5.18, the frames are numbered 1 to 6 from left to right.

The vortex mechanisms behind the distortion of the flame shape have been discussed extensively in section 5.2. The key differences between the two sets of results appear, as expected, at the times when flame-merging is likely to occur. This is represented by frames 2 to 4 in figure 5.28 where the jets extend to the side boundaries of the domain. The mushroom shapes in frame 2 are more pronounced in the cyclic case where larger low-temperature regions are found at the flame front. The flame detachment regions in frame 3 are less uniform in the cyclic case and can be seen to interact at the centre of the domain. The flame front in frame 4 extends further in the chamber for the cyclic case. Frames 1, 5 and 6 are similar between the two data sets. Frames 1 and 6 are identical to each other, thus demonstrating the repeatability of the oscillation pattern in the cyclic case.

Globally, the cyclic boundary conditions introduced more distortion to the flame shape during the oscillating period. This result was analysed quantitatively in figure 5.29 where frequency domain representations of the heat release response were plotted for the wall

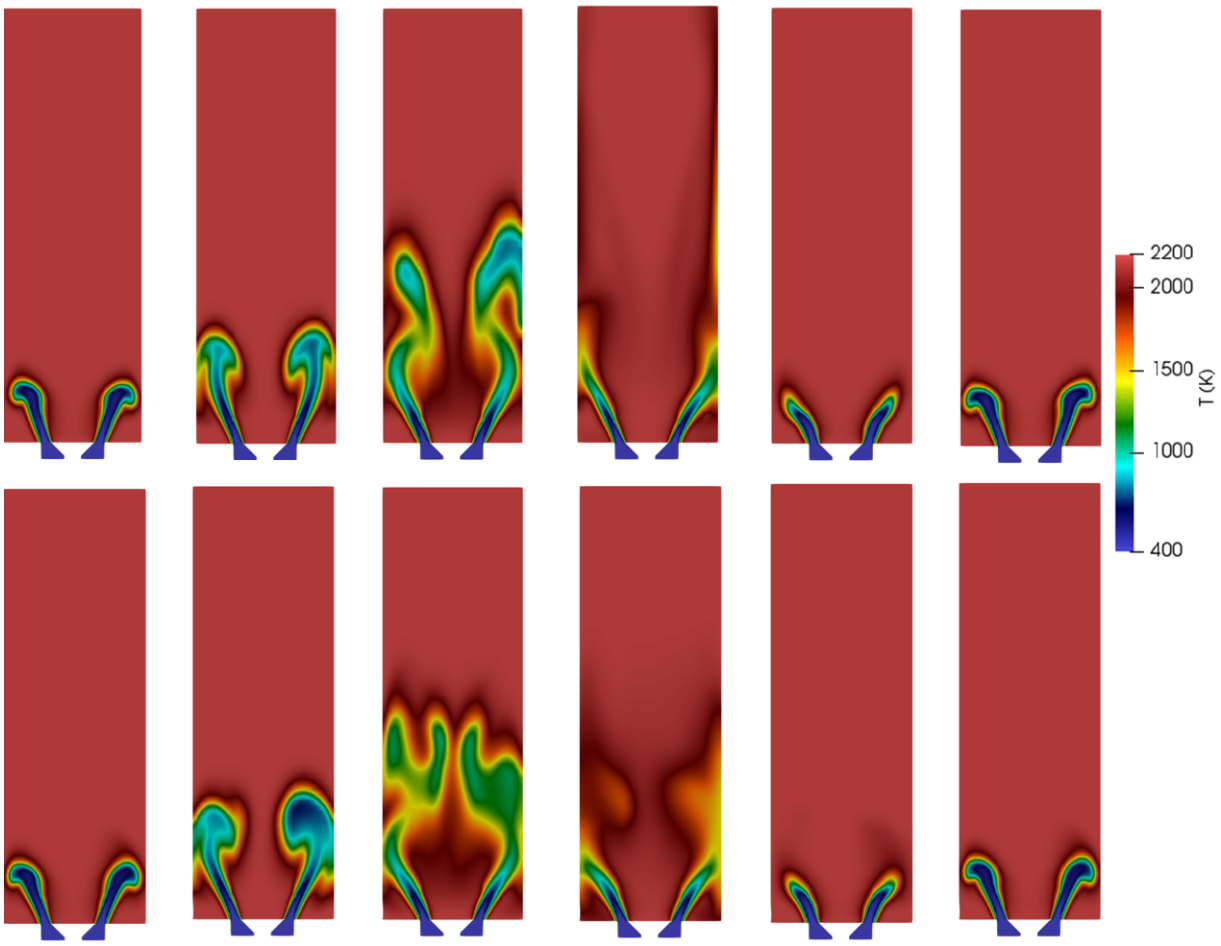

Fig. 5.28 Tangential-normal plots of temperature field during one oscillating cycle for wall (top) and cyclic (bottom) ED cases.

(blue) and cyclic (red) cases. In both data sets, a high amplitude peak is found at the forcing frequency of 160Hz. Harmonic peaks are also visible at multiples of the forcing frequency, indicating non-linear behaviour in both cases. The amplitude of the peaks is noticeably higher in the cyclic case, which is indicative of higher levels of non-linearity [41].

A global FDF was calculated for each case and the distribution of its gain in the computational domain is shown in figure 5.30. The FDF was calculated following the equation described previously in chapter 2. The data was extracted for each computational cell of the domain and interpolated back onto the surfaces shown in the figure. The visibility of the data is thus limited by the resolution of the grid.

The plots highlight some of the major differences between the wall and cyclic cases described by the quantitative data in figure 5.29. The wall case on the left shows a more symmetric distribution of the gain in the chamber compared to the cyclic case on the right.

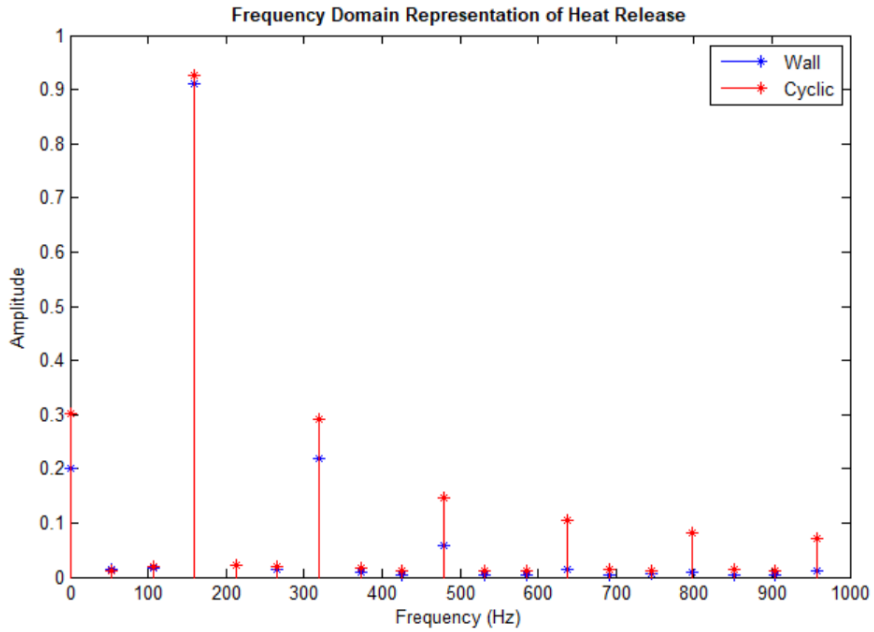

Fig. 5.29 Frequency domain representations of normalised heat release response for wall (top) and cyclic (bottom) ED cases, f = 160Hz and A = 0.65.

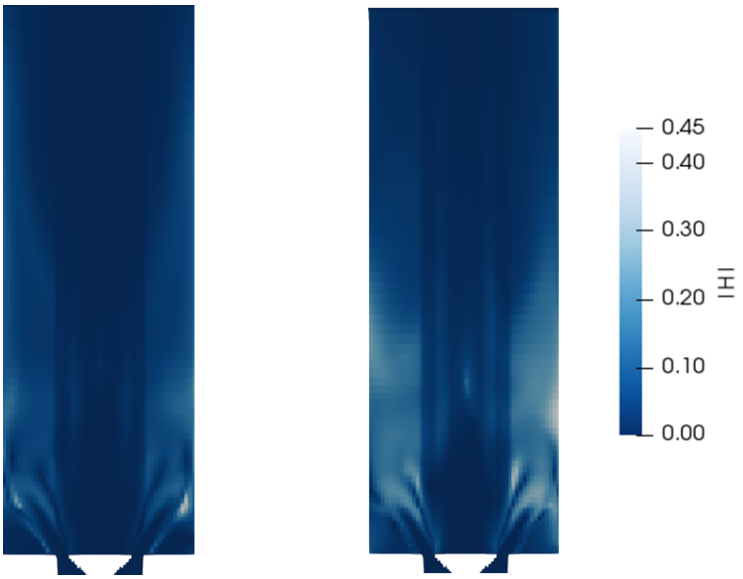

Fig. 5.30 FDF gain distribution for the wall (left) and cyclic (right) ED cases, f = 160Hz and A = 0.65.

The value of the gain is also globally higher in the cyclic case downstream of the jets, which mirrors the higher non-linearity represented by the results in figure 5.29.

The ED cyclic case was thus capable of highlighting the variation in oscillating flame behaviour induced by the notional representation of burner-burner interactions.

5.4 Summary

This chapter presented the step-by-step construction of the modelling methodology employed for the UCAM annular rig simulations. The analysis was divided into two sections in which comparative studies with reference data from Bainbridge [16] and Armitage et al. [41] were performed.

The first section included results from an isolated single burner geometry from the annular rig. Isothermal simulations were run to test the new swirl inlet velocity boundary condition that was created for the project, finalise the choice of turbulence model, and test mesh refinement settings. The combination of the eddy-diffusivity $k-\omega$ SST turbulence model and coarser mesh was chosen for its significant decrease in computational cost and agreement compared to reference data. Steady reacting simulations were then run to test the ignition method implemented and the choice of combustion model. The ignition method used led to faster convergence than the Bainbridge approach [16] and the results obtained with the PaSR combustion model represented the characteristic features described by experimental swirling jets from Billant et al. [34]. Finally, an oscillating inlet boundary condition was created to prescribe acoustic excitation to the flame. The results obtained showed that non-linearity induced by high amplitude forcing between the inlet signal and heat release response was illustrated by the eddy-diffusivity model and coarse mesh.

The second section followed a similar approach and presented results from a cyclic single burner geometry, which was used to model the interactions between neighbouring flames as repeated features around the annulus. The concept of cyclic boundary conditions was explained, and isothermal simulations were run to test its implementation in the single burner UCAM rig geometry. Steady cyclic reacting flow simulations were compared to data from the Bainbridge case [16] and showed improved agreement compared to the wall case. The final section detailed the comparison between the forced oscillating ED reacting cases and showed that the combination of oscillating swirl inlet boundary condition, ED model, coarse mesh, PaSR combustion and cyclic boundary conditions was capable of showing notional flame-merging effects on the heat release response of the flame effectively. As a consequence, the use of more expensive, higher-order computational models or meshes was not required.

It is of interest to test the adaptability of the modelling methodology to different simulation environments to assess its potential strengths and shortfalls in a more conclusive manner.

Chapter 6 uses reference data from Bainbridge [16], Armitage et al. [41], Lee et al. [59] and Zetterval et al. [46] to compare the results obtained from ED cases when varying initial conditions and burner configurations.

Chapter 6

Model Adaptability

This chapter focuses on the capabilities of the ED computational methodology detailed in chapter 5 to represent the main flow characteristics of the UCAM rig under various operating conditions. The analysis is divided into two sections. The first is concerned with parametric analyses of inlet conditions, performed on an enclosed single burner model to maintain low computational demands. The second is concerned with multi-burner simulations with a view to assess the use of cyclic boundary conditions.

6.1 Overview

6.1.1 Simulation Setup

All ED simulations presented in this chapter follow the setup described in chapter 5. The swirl inlet boundary condition was used along with the $k-\omega$ SST turbulence model and PaSR combustion model. The ignition method described in chapter 5 was employed for steady reacting cases. The oscillating inlet boundary condition was used in the forced reacting cases.

The coarse single burner mesh was used for all single burner studies and replicated to obtain the twin and full burner meshes as described in chapter 4. Wall boundary conditions were first used on the enclosed single burner geometry. Cyclic boundaries were implemented in the multi-burner analysis.

The inlet velocity was re-calibrated to match the experimental velocity of 18m/s at the entrance of the combustion chamber [7]. The inlet temperature was set to the experimental value of 300K [7]. This allowed for a direct comparison with LES data from Lee et al. [59] at multiple stages of the investigation. All other boundary conditions matched those described

in chapter 5. The colour scheme used for qualitative comparisons was modified to match results obtained by Lee et al.

Unless stated otherwise in parametric studies, the fuel used was ethylene and was pre-mixed with air at an equivalence ratio of 0.8 before entering the chamber.

6.1.2 Cases Summary

Relevant data from all reference cases described in chapter 3 are used in this part of the work. Table 6.1 below summarises the studies performed for this part of the project. All the cases in table 6.1 are detailed in the following sections of this chapter.

Table 6.1 Summary of cases presented in chapter 6.

Study	Type	Aim
Swirl BC	Isothermal	Re-calibrate inlet BC to experimental velocity
Unforced reacting flow	Reacting	Compare steady reacting flow to reference data
Inlet velocity / temperature	Reacting	Observe effects on the steady flame
Equivalence ratio	Reacting	Observe effects on the steady flame
Fuel	Reacting	Observe effects on the steady flame
Multi-burner	Reacting	Compare single, twin and full burner configurations for steady flame
Forcing amplitude	Forced Reacting	Observe effects of forcing amplitude on single burner flame
Multi-Burner	Forced Reacting	Compare single, twin and full burner configurations for oscillating flame

ED studies detailed in chapter 5 and this chapter were performed on the local machine presented in chapter 3. The efficiency of the final modelling methodology employed allowed for steady isothermal single burner results to be obtained in the order of 0.07s in terms of CPU time on this machine. The data recording interval affected the overall physical time of the simulations. On average, the physical time to obtain fully reacting single burner cases was in the region of three weeks, after performing meshing and initialising the simulation. This equates to a significantly lower cost than LES studies, where the use of the cluster described in chapter 3 was required at each stage as a local machine would not be able to answer the high computational demands. Whilst data for the exact computational cost of LES simulations performed by Lee et al. [59] is not available, the physical time required to obtain steady-state, fully reacting simulations was in the order of months using the high-performance cluster.

6.1.3 Presentation of Results

Results from the single burner analyses are presented in a similar way to those in chapter 5. Results from the multi-burner analyses are presented as shown in figure 6.1 for axial-normal planar cuts and in figure 6.2 for radial-normal cylindrical cuts.

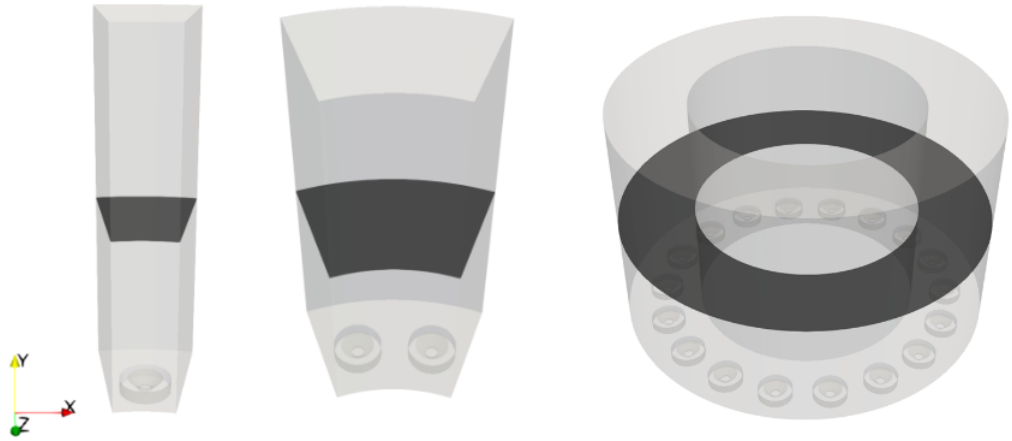

Fig. 6.1 Single burner (left), twin burner (centre) and full burner (right) axial-normal planar cuts.

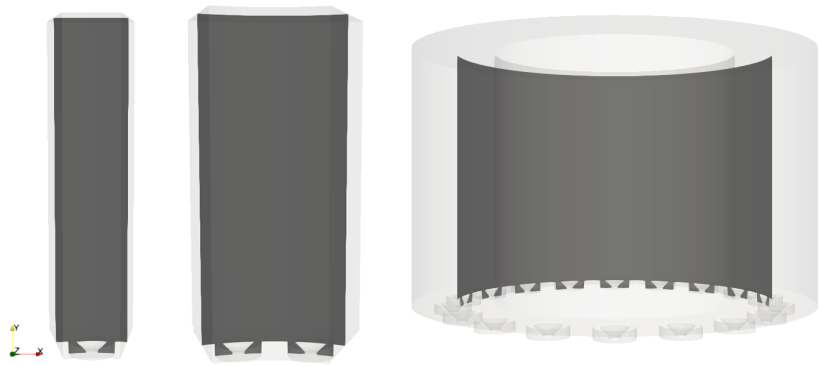

Fig. 6.2 Single burner (left), twin burner (centre) and full burner (right) radial-normal spherical cuts.

As in figure 5.1, the x-axis in figures 6.1 and 6.2 represents the tangential direction, y-axis the axial direction and z-axis the radial direction. The figures on the left show cuts for the single burner configuration, the figures in the centre, cuts for the twin burner configuration and the figures on the right, cuts for the full burner. Results from the twin burner geometry were also taken as shown in figure 6.3 to match planar cuts obtained by Lee et al. [59].

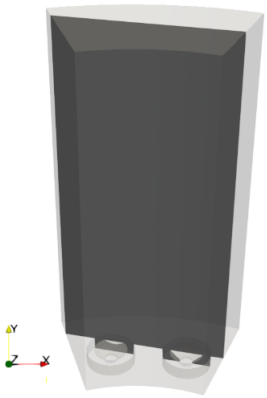

Fig. 6.3 Twin burner planar cut.

6.2 Closed Single Burner Configuration

This section details the parametric analyses performed on an isolated single burner configuration. An isothermal flow simulation was run to calibrate the swirl inlet velocity boundary condition to the experimental value obtained by Worth and Dawson [7]. The parametric studies were carried out on steady reacting flow simulations in which the effects of inlet velocity, equivalence ratio and fuel on the flame were observed.

6.2.1 Isothermal Flow

The swirl inlet velocity boundary condition implemented in chapter 5 matched the Bainbridge case [16] velocity profiles. The new inlet velocity components were evaluated based on area ratios in the geometry to obtain 18m/s at the top of the bluff body. The inlet velocity magnitude was evaluated at 13.35m/s, corresponding to 6.68m/s in the axial direction and 11.56m/s in the tangential direction for a swirl angle of 60°.

The qualitative results obtained for the isothermal flow were identical to the corresponding case in chapter 5 and are thus not presented here. Quantitative profiles were extracted at the entrance of the combustion chamber to validate the newly calibrated 18m/s velocity magnitude at this axial location. This is shown in figure 6.4, where the plot indicates that the peaks in velocity magnitude match the required value.

No experimental or computational data is available currently to validate this profile for the enclosed single burner UCAM configuration. However, an unforced reacting case by Bainbridge [16] can be used to compare the steady flame behaviour obtained after igniting this isothermal result.

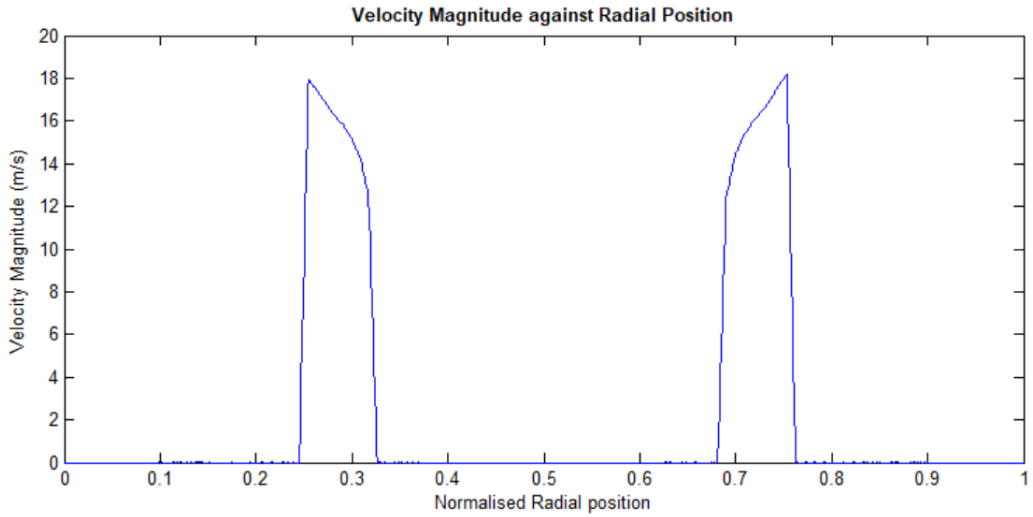

Fig. 6.4 ED wall case velocity magnitude profile at the entrance of the combustion chamber.

6.2.2 Unforced Reacting Flow

Steady Flow Validation

The isothermal ED case presented in section 6.2.1 was ignited using the method described in chapter 5 and run to steady-state. In the reference case by Bainbridge [16], an initial test of modelling methods was performed on an isolated single burner geometry. The temperature, inlet velocity, fuel and equivalence ratio were kept at the experimental values specified by Worth and Dawson [7]. A direct comparison with the ED case is therefore possible. Quantitative data was however not made available for this Bainbridge case.

Figure 6.5 shows tangential-normal cuts of the isolated single burner geometries from the Bainbridge case (left) [16] and the ED case (right). Both plots are coloured by temperature, and the Bainbridge plot illustrated the streamline pattern in the burner. The temperature scale for the ED case was adjusted to match that of the Bainbridge plot.

Small discrepancies in the thickness of the jets can be noted. The jets in the ED case seem slightly thicker and show a more gradual shift between low and high temperature zones. This can be attibuted to the differences in local mesh refinement, and to the turbulence modelling approach.

These variations in flame thickness are, however, not sufficiently pronounced to invalidate the data obtained in the ED case. The propagation of the jets is indeed comparable. The flow asymmetry due to the burner configuration is shown in that the jets on the left extends further in the chamber than the jets on the right. The recirculation patterns cause an inward roll

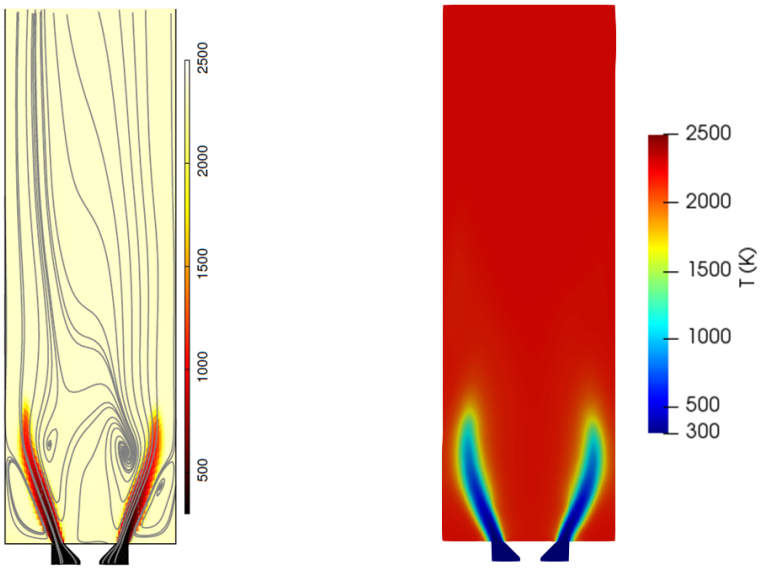

Fig. 6.5 Tangential-normal planar cuts coloured by temperature for the Bainbridge single burner case (left) [16] and ED wall case (right).

of the flame front, as can be seen by the curvature of the jets towards the centre of the domain.

Figure 6.5 shows that the steady reacting results in the ED case are comparable to the results obtained in the RSM case by Bainbridge [16]. This provides a basis for the parametric studies carried out in the following sections.

Parametric Analysis

The aim of this study was to assess the capabilities of eddy-diffusivity simulations to represent characteristic steady flame behaviour resulting from a variety of operating conditions. The effects of these parameters on the response of the flame to acoustic excitation were detailed in chapter 2.

Inlet Velocity and Inlet Temperature

Steady reacting ED wall cases were run for the Bainbridge setup [16] in chapter 5, and for the experimental setup [7] in this chapter. Both ED cases were run with ethylene fuel, an equivalence ratio of 0.8, and used the same modelling methodology. A direct comparison between the steady flames resulting from the two operating conditions can therefore be performed. The first case was run for an inlet temperature of 400K and velocity of 43m/s. The second case was run for an inlet temperature of 300K and velocity of 13.35m/s.

Figure 6.6 shows tangential-normal planar views of the temperature field (left) and velocity magnitude field (right) for the Bainbridge setup (left of each pair) and experimental setup (right of each pair) obtained in ED cases. The temperature scale was adjusted and velocity was normalised by the bulk flow velocity to obtain a direct comparison between the two cases.

The temperature and velocity fields obtained in figure 6.6 highlight the effects of the different operating conditions on the flow. The most significant differences appear in the propagation of the jets in the chamber. The velocity fields show that the Bainbridge setup on the left leads to a wider inner recirculation zone which in turn extends the jets further towards the walls. This is induced by the higher tangential velocity component defined in the swirl inlet velocity boundary condition. The resulting interactions between the jets and the walls in the Bainbridge setup create lower-velocity regions that extend to the outlet of the chamber. In contrast, higher flow velocities are carried through to the exit of the computational domain in the experimental setup on the right.

This behaviour is mirrored by the temperature plots on the left. The cold reactant jets extend further in the chamber and are sharper in experimental operating conditions. The interactions between the jets and the walls in the Bainbridge setup lead to a more gradual shift between cold reactant and hot product regions, indicating larger reaction zones.

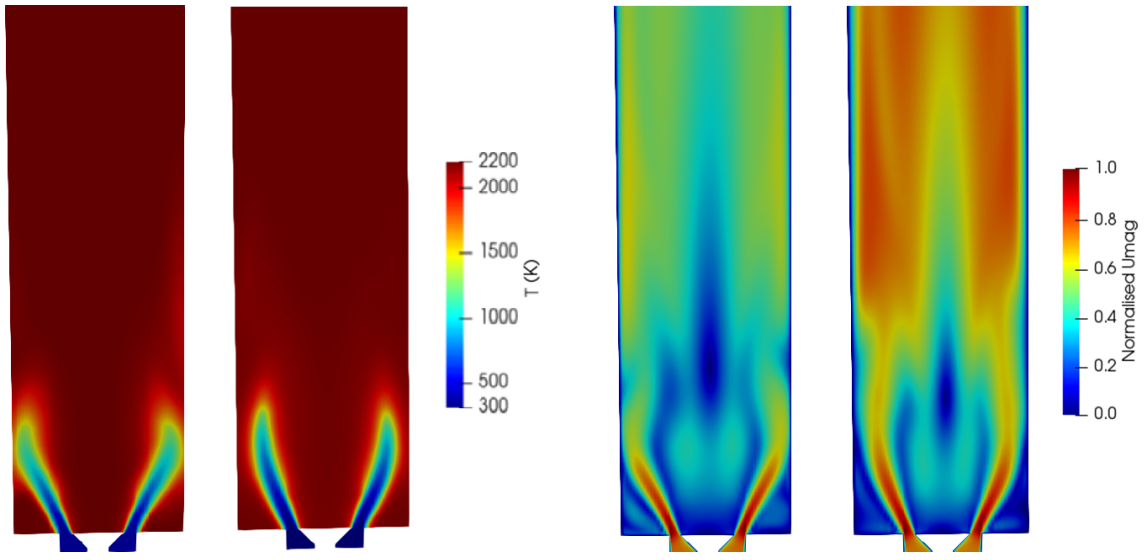

Fig. 6.6 Tangential-normal planar cuts coloured by temperature (left) and normalised velocity magnitude (right) for the Bainbridge simulation setup (left of each pair) and experimental setup (right of each pair).

The ED method is thus adaptable to varying inlet conditions. Additional validation against experimental data is required to assess the accuracy of the results, however major the

flames shapes obtained are noticeably different, as could be expected.

Equivalence Ratio

LES data was obtained from Lee et al. [59] for varying inlet equivalence ratios. The simulation setup used by Lee et al. was detailed in chapter 3, and the meshes were shown in chapter 4. This particular LES study was performed on a single burner configuration using the experimental operating conditions [7]. The inlet equivalence ratio was the only parameter altered and cases were run for values of 0.65 and 0.8. An additional eddy-diffusivity case was run using the methodology described in the previous sections, this time with an equivalence ratio of 0.65 to match the second LES simulation setup.

Figure 6.7 shows tangential-normal planes coloured by temperature (top) and velocity (bottom), with time-averaged results from Lee et al. [59] on the left, and results from ED cases on the right. In each pair of results, the plot on the left was obtained for a ϕ value of 0.65, and the plot on the right, for a ϕ value of 0.8. The LES was performed using cyclic boundary conditions [59], thus a detailed comparison of the flame shape is not possible with the ED wall cases. However, flow features such as recirculation zones, jet propagation and temperature scales are parameters that can be used to determine the agreement between the ED cases and reference data from Lee et al. [59].

The geometry considered in the Lee [59] case accounted for the physical swirler part. It was assumed in this section that the trends observed in the flow features listed would not be affected by the possible effects of the wakes created by the vanes on the flow. The effect of the swirler part was investigated further in the multi-burner analyses presented in section 6.3.

The velocity plots in figure 6.7 show that the lower equivalence ratio led to larger inner recirculation zones in both the LES and ED cases. In a similar fashion to the plots in the previous subsection, this affects the jet propagation towards the wall. The interactions between the jets and the walls in the lower ϕ cases produce low velocity regions that extend to the outlet of the domain. In contrast, the velocity magnitude is higher globally in the ϕ = 0.8 cases.

This behaviour is reflected in the temperature plots at the top. The cold reactant jets reach further downstream in the chamber for the high equivalence ratio cases. The lower equivalence ratio cases, however, show a significant increase in the size of reaction zones with larger low temperature regions at the flame front.

Figure 6.8 shows quantitative temperature data from the ED cases, taken across the chamber in a tangential-normal plane at the entrace of the combustion chamber. The blue

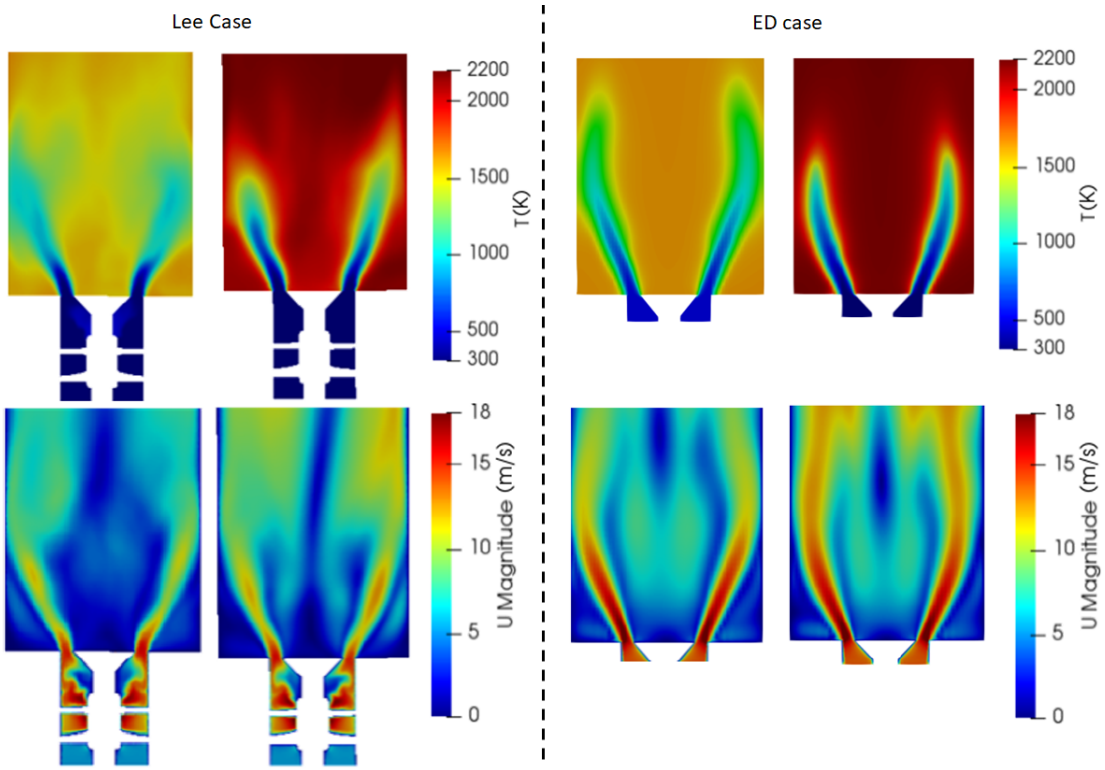

Fig. 6.7 Tangential-normal planar cuts coloured by temperature (top) and velocity magnitude (bottom) for the Lee cases (left) [59] and ED cases (right). Plots for $\phi = 0.65$ on the left of each pair, plots for $\phi = 0.8$ on the right of each pair.

line represents the higher equivalence ratio of 0.08, and the red, the lower equivalence ratio of 0.065. The adiabatic flame temperature for ethylene-air reactions at an equivalence ratio of 0.65 was expected to be in the region of 1900K [23, 113]. This value is well respected by the LES and ED simulations as shown by the temperature scales in the $\phi = 0.65$ cases.

Figures 6.7 thus shows that the ED and LES cases produced similar flow behaviour when subject to variations in equivalence ratio. The trends observed are in good agreement with the LES data obtained by Lee et al. [59]. Figure 6.8 also shows quantitatively that the ED temperature results agree with expected values from theoretical calculations.

Fuel

This study was aimed at assessing the adaptability of the ED modelling methodology to account for different fuels. An ED reacting case was run using a methane-air mixture at an equivalence ratio of 0.8. This allowed for a direct comparison with data obtained from the ethylene case at $\phi = 0.8$.

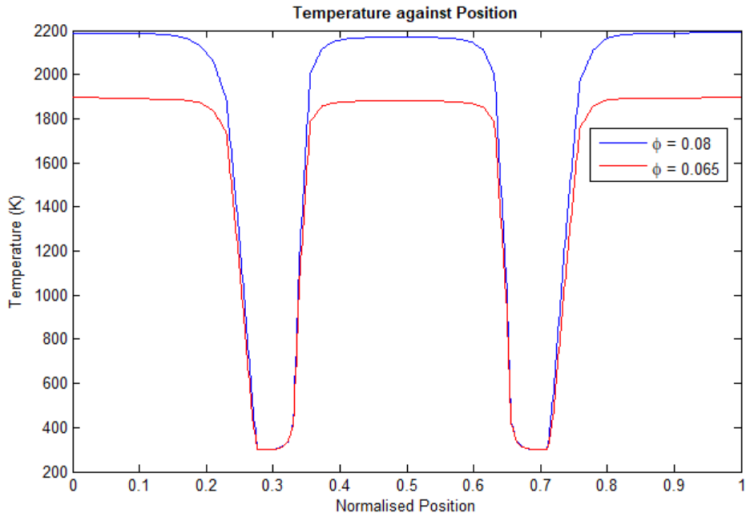

Fig. 6.8 Temperature against position for an equivalence ratio of 0.08 (blue) and 0.65 (red).

Zettervall et al. [46] conducted LES investigations of the full annular burner geometry subject to self-excited acoustic modes, and prescribed an inlet equivalence ratio of 0.85. A direct comparison between the Zettervall [46] and isolated single burner ED cases could not be performed as the ED cases were run to steady state at a lower equivalence ratio. However, the Zettervall case [46] could provide information for some of the key features expected from a variation in fuel. These included adiabatic flame temperature and fuel-dependence of the flame structure.

Figure 6.9 shows tangential-normal plots of temperature (left) and velocity magnitude (right) for ethylene (left of each pair) and methane (right of each pair). The temperature and velocity fields both show that the change in fuel severely impacts the physical appearance of the flame. The velocity plots highlight differences in thickness of the jets, with larger high-velocity regions towards the inlet for the methane case. Consequently, the size of the inner and outer recirculation zones is reduced for the methane case. The temperature plots show that the cold reactant jets propagate further downstream in the chamber in the ethylene case.

The temperature plots in figure 6.10 show that the adiabatic temperature was lower for the methane case compare to the ethylene case, with values of around 2000K and 2200K respectively. These values matched theoretical adiabatic flame temperatures and closely matched the results from the Zettervall case [46] where a value of 2212K was obtained for ethylene and 2067K was obtained for methane.

Whilst the ED temperature fields match the expected behaviour quantitatively, differences are observed when compared to experimental data from Worth and Dawson [7] and LES data

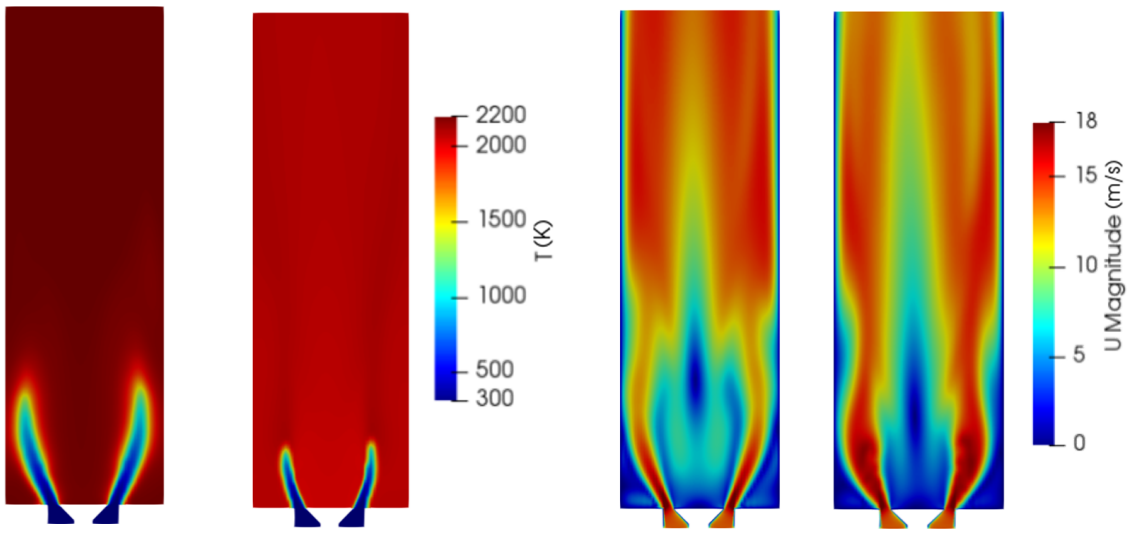

Fig. 6.9 Temperature against position for ethylene fuel (blue) and methane fuel (red).

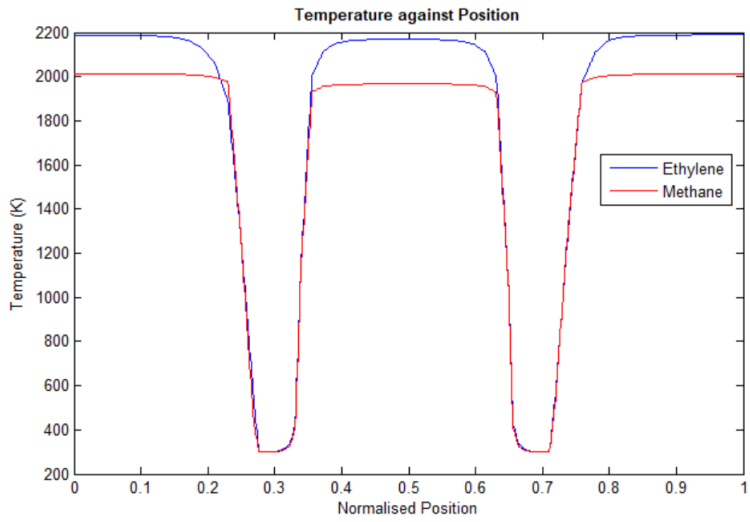

Fig. 6.10 Tangential-normal planar cuts coloured by temperature (left) and velocity magnitude (right) for the ethylene ED case (left of each pair) and methane ED case (right of each pair).

from Zettervall et al. [46]. The qualitative reference data shows that methane flames obtained were longer than ethylene flames, which is not represented here. Several compatibility issues between the solver, combustion model and thermochemistry model employed in the ED method for methane fuel can cause this discrepancy. Additional work on the implementation of methane thermochemistry would be required to obtain data in better agreement with

the references. Nonetheless, the plots show that the flow fields obtained in ED cases vary significantly with fuel type and that the ED method was sensitive to the fuel input.

6.2.3 Summary

The closed single burner configuration was simulated in steady isothermal and reacting conditions. The isothermal study demonstrated that the swirl inlet boundary condition was re-calibrated to match the experimental velocity of 18m/s at the entrance of the combustion chamber [7]. The steady reacting case run with the new inlet velocity was compared to data from Bainbridge [16]. The subsequent parametric studies on effects of inlet velocity and temperature, inlet equivalence ratio and fuel all demonstrated that the ED modelling approach responded to the changes in operating condition implemented. Finer tuning of the thermochemistry model is required to implement other fuel types successfully.

The following sections focus on the effects of burner geometry on the solution in steady isothermal and reacting conditions, as well as on the flame response to acoustic excitation.

6.3 Multi-Burner Analyses

Chapter 4 emphasised the importance of representing flame-flame interactions accurately in order to obtain a sensible flame response to acoustic waves. Forced reacting studies on cyclic boundary conditions in chapter 5 showed that the ED approach was able to highlight the effects of notional flame-flame interactions on the heat release response using a single burner geometry from the UCAM annular rig. In this case, cyclic boundary conditions imposed uniformity across the burners. It was therefore assumed that the flow behaviour would be identical in all burners around the annulus. The validity of this assumption is assessed in this part of the thesis by performing a comparative study between simulations results from single burner and multi-burner configurations.

This part of the analysis considered cyclic single burner, cyclic twin burner and full burner configurations. The twin burner was used as an intermediate step to representing interactions between neighbouring burners before performing more expensive full burner studies. At each stage, the ED cases were compared to reference data.

6.3.1 Isothermal Flow

Cyclic Single Burner Profile

Cyclic boundary conditions were implemented on the single burner geometry following the procedure detailed in chapter 5 and an ED isothermal flow simulation was run using the newly calibrated inlet velocity components. The results were compared qualitatively and quantitatively against LES data from the Lee case [59] in figures 6.11 and 6.12 respectively.

Figure 6.11 shows tangential-normal planar views of the velocity magnitude field for the Lee case (left) [59] and the ED case (right). The results from Lee et al. [59] were taken as instantaneous, thus the flow is less uniform qualitatively than in the ED case. In both cases, the higher velocity levels are located at area contractions of the geometry as indicated by the red regions around the bluff body. Both cases also present asymmetry between the two jets entering the chamber, which is attributed to the shape of the single burner cut as explained in chapter 5. The jets can be seen to reach further downstream in the chamber in the ED case. This is an effect of the presence of the physical swirler part in the Lee case [59].

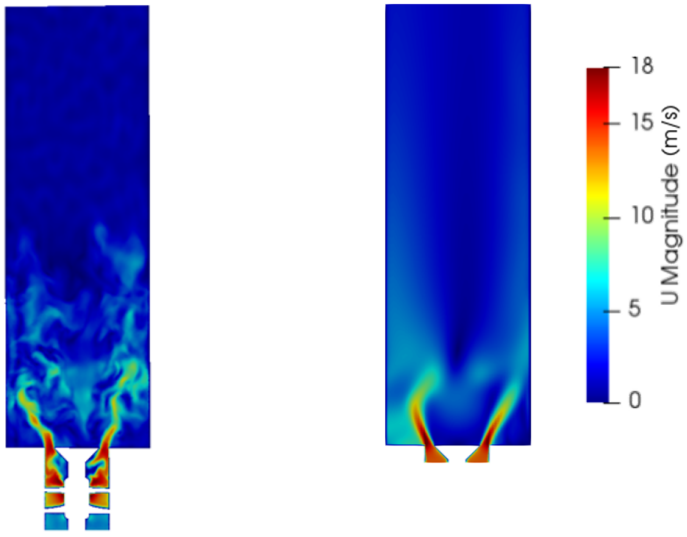

Fig. 6.11 Tangential cuts of isothermal velocity magnitude for LES (left) [59] and URANS (right).

Further comparisons are required between the Lee case [59] and the ED results. Indeed, the instantaneous nature of the LES results affect the downstream velocity profiles significantly and would thus not be able to validate ED profiles in the chamber fully. Averaged LES data would be required instead.

Time-averaged quantitative LES data from Lee et al. [59] was available at axial locations corresponding to the inlet of the ED case and the entrance of the combustion chamber. Figure

6.12 shows plots of normalised velocity magnitude for the Lee case [59] in red and the ED case in blue. The profiles at the ED inlet location are shown at the top, and the profiles at the entrance of the combustion chamber are shown at the bottom. Results in figure 6.12 were normalised by bulk velocity to highlight the differences in shape of the velocity profiles obtained in both studies.

The velocity increases and decreases sharply in the ED case at the inlet, whilst a more gradual change in velocity can be observed in the LES profile. These discrepancies in profiles at y = 0m were explained previously in chapter 5 and attributed to the difference in flow behaviour across an inlet plane and across a mesh location contained within walls.

The LES profiles are noticeably less uniform than the ED profiles. Both axial locations show similar characteristics in the LES case, with a step-like pattern in the velocity profiles towards the centre of the domain. In contrast, velocity gradients changed smoothly in the ED case. The step shape in the LES is less pronounced at the downstream axial position represented. Both LES plots show that the step was asymmetric in shape and size between the two jets, which is reflected qualitatively in the flow asymmetry past the swirler in figure 6.11. This asymmetry can be attributed to the fact that the data was obtained instantaneously.

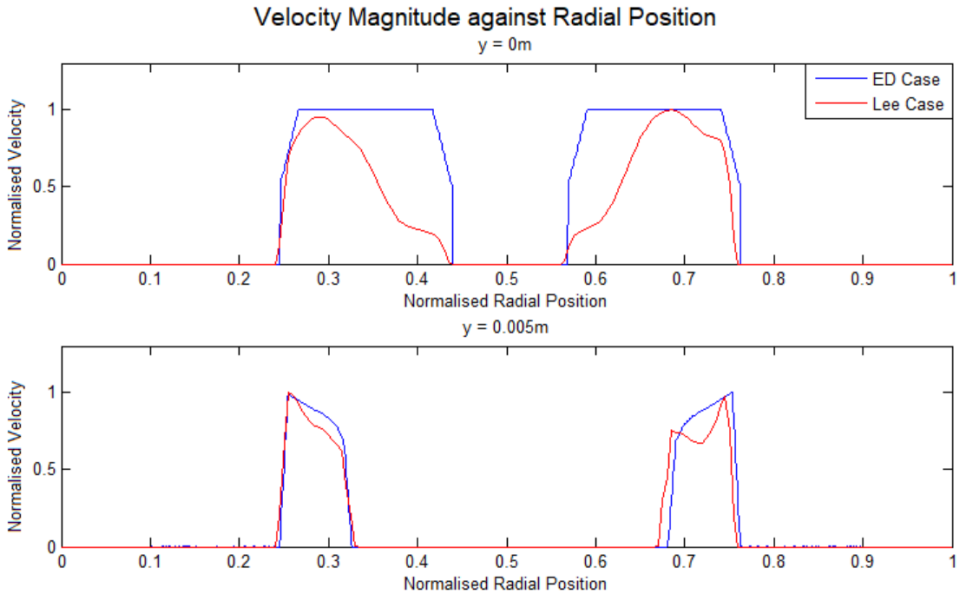

Fig. 6.12 Normalised velocity magnitude profiles for Lee case (red) [59] and ED case (blue) at ED case inlet (top) and entrance of the combustion chamber (bottom).

The location of the step shapes in the LES at the centre of the domain is indicative of an effect produced by the swirler part. This can be seen in the plot on the left hand side of figure 6.11, where zero-velocity regions are found around the bluff body and past the swirler.

These regions are not symmetric in shape and size, thus explaining the differences in LES jet profiles in figure 6.12.

At the entrance of the combustion chamber, the LES plot in figure 6.11 shows that the velocity is somewhat more uniform, with no visible pattern representative of this behaviour in the distribution of velocity magnitude around the bluff body. This is reflected in figure 6.12 with the smaller local variations in velocity at $y = 0.005$m in the Lee case [59].

Despite the discrepancies mentioned, the Lee et al. [59] and ED profiles are in agreement overall. The location of velocity peaks is very similar between the two cases as the flow evolves downstream, indicating that the swirl boundary condition was calibrated correctly. The smoother LES profiles at the entrance of the combustion chamber indicate that the effects of the swirler part on the flow have started to dissipate at this point. This allowed for a better comparison between the ED and Lee et al. [59] profiles at this location.

Further analysis is required to determine the effect of the swirler on the flame structure and its response to acoustic waves. However, the comparison with available data detailed in this section showed that the ED modelling approach represented the trends in isothermal flow for the cyclic single burner case when operating in experimental conditions.

Annular Uniformity

Experimental velocity magnitude profiles were taken across four burners around the annulus to check for uniformity in the design. Figure 6.13 shows the results obtained from isothermal experiments performed by Worth and Dawson. The data was not available publicly as the study formed part of preliminary investigations carried out on the UCAM rig design. The plots in figure 6.13 were adapted from data obtained by Worth and Dawson and provided for use in this thesis [114].

The α angles represent the azimuthal location of the burners from which hot wire measurements were taken radially. Each velocity measurement was taken twice per burner, to represent the two incoming jets. Each pair is coloured in the same way, with the first set of data represented by a solid line and the second by a dashed line. The velocity was normalised against bulk flow velocity.

An average profile was evaluated and plotted for reference in figure 6.13. It could be expected that the experimental velocity profiles would be very similar to each other. This is due to the location of the experimental inlet upstream of the plenum chamber, which was designed to distribute the air uniformly into the equally-spaced burners around the annulus. However, figure 6.13 shows that both the radial location and shapes of the velocity profiles are not consistent across all burners.

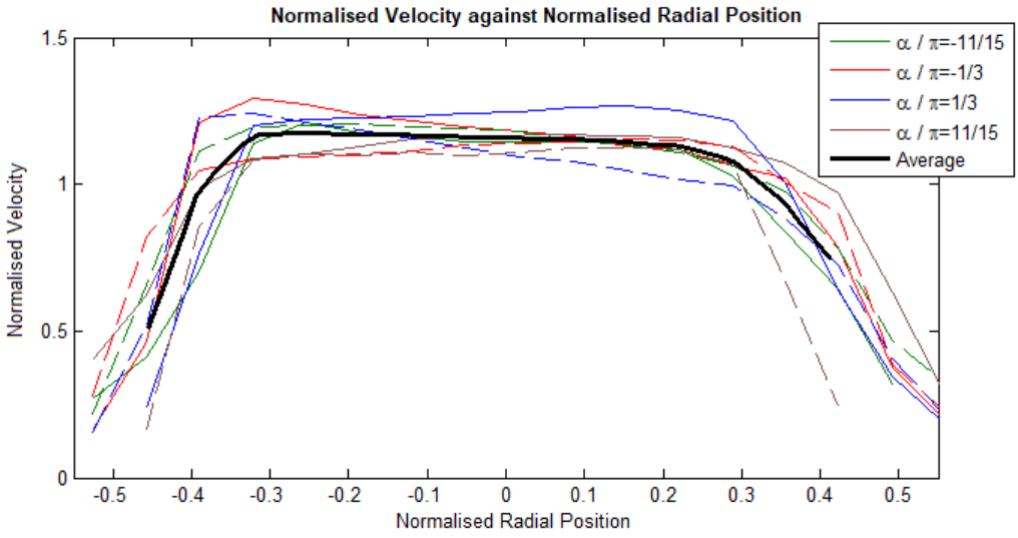

Fig. 6.13 Experimental normalised velocity magnitude profiles adapted from plots obtained by Worth and Dawson [114].

Several factors could impact the uniformity of the flow distribution. The first could stem from error in the hot-wire measurement methods employed. Another could be due to error in the experimental rig, such as inconsistent placement of swirlers around the annulus.

The non-uniform behaviour was reflected in reacting flow studies. It was noted in the experimental snapshots shown in figures 4.3 and 4.6 [7] in chapter 4 that the OH* chemiluminescence distribution was not the same between consecutive burners.

These results indicate that discrepancies in uniformity between the steady experimental and CFD flow fields can be expected in multi-burner studies. The inlet conditions prescribed in the simulations were indeed identical for all burners around the annulus without external factors impacting the equal distribution of the flow in the chamber.

Multi-Burner Configuration Simulation Setup

Simulations were run on single, twin and full burner configurations for which the meshes were shown in chapter 4. The initial conditions for the twin and full burner cases were identical to the cyclic single burner simulations. In these geometries, each inlet was treated as a separate part, therefore inlet values were prescribed independently for all burners. This allowed for flexibility in defining inlet parameters such as swirl direction in future investigations. For this thesis, the swirl was defined as CCW for all burners as was done by Bainbridge [16] and Lee et al. [59]. The centre of rotation parameter was defined as the centre of each corresponding burner inlet in the swirl inlet boundary condition.

Cyclic boundary conditions were specified on the sides of the twin burner geometry in a similar fashion to the single burner. The angle of rotation was changed from 20° to 40° to account for the second physical burner represented. All burners were represented physically in the full annular geometry thus no cyclic boundary conditions were required in this case.

Isothermal simulations were run then ignited using the procedure described in the ED cases in chapter 5. An ethylene-air mixture was defined with an equivalence ratio of 0.8 to match the experimental [7] and LES setup [59]. The resulting steady reacting flow solutions were then forced by prescribing the forced oscillating velocity boundary condition detailed in chapter 5 at each inlet of the geometry. No experimental or numerical data is available to compare ED isothermal flow fields for twin and full burner configurations. LES data from Lee et al. [59] and experimental data from Worth and Dawson [7] was used to compare reacting flow results instead.

6.3.2 Unforced Reacting Flow

Single Burner Configuration

Steady reacting flow profiles for the ED cyclic single burner configuration are compared to the corresponding Lee case [59] simulation in figure 6.14. The temperature range was adjusted in the ED case to match the scale defined in the instantaneous snapshot produced by Lee et al. [59]. Quantitative LES data was not available for steady flame simulations thus the comparisons remain qualitative at this stage.

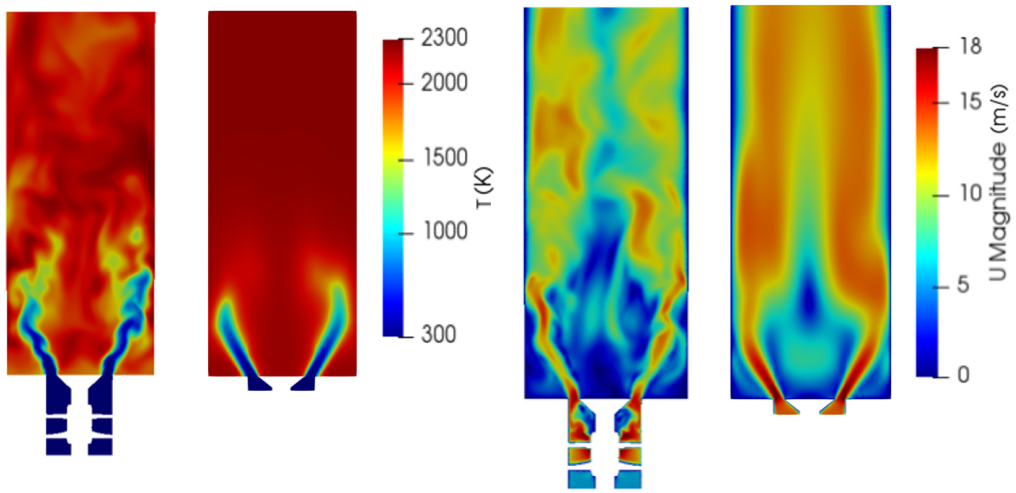

Fig. 6.14 Tangential-normal cuts of temperature (left) and velocity magnitude (right) for instantaneous LES (left of each pair) [59] and ED (right of each pair).

The instantaneous nature of the LES snapshots leads to a more chaotic aspect of the flow in the chamber. The asymmetry due to the shape of the chamber is shown by both data sets in the temperature profiles, with the jet on the right hand side extending further in the chamber than the jet on the left hand side. The roll up of the flame at the walls caused by the recirculation patterns is made evident in the temperature plots by the inward curvature of the cold jet fronts towards the centre of the domain.

The velocity values are similar qualitatively between the Lee [59] and ED cases throughout. The sizes and shapes of the inner recirculation regions indicated by zero-velocity zones in the Lee [59] and ED cases are also similar. A wider recirculation section is found above of the bluff body, which reduces in size when the flow is redirected inwards. The axial location at which the velocity jets start to merge again downstream of the inner recirculation zones is similar between the LES and ED cases.

The cyclic single burner flow fields obtained in the ED case were very similar to those obtained in the LES by Lee et al. [59]. As in the previous section, a better comparison would have been performed with time-averaged LES data instead.

Twin Burner Configuration

The twin burner geometry represented two consecutive burners around the annulus and was run to assess the potential improvements on the solution from a cyclic single burner when compared to the full burner. All ED twin and full burner configuration simulations were performed on High-Performance Clusters (HPCs) to reduce the time taken per case study, as mentioned in chapter 3.

The results are compared to data from Lee et al. [59] and to experimental profiles from Worth and Dawson [7]. Figure 6.15 shows radial-normal planar cuts as illustrated in figure 6.3 coloured by temperature. The plot on the left shows instantaneous data from the Lee case [59], the centre plot, time-averaged data from the LES [59], and the plot on the right, results from the ED case. Both plots from the Lee et al. [59] and the ED cases show similar temperature ranges throughout the domain, as expected from similarities identified in the single burner study.

The interaction between the two burners is made evident in both plots by the merging of the central jets, forming a larger reaction zone at this point. Similarly, the cyclic boundary conditions result in interactions between the outer jets and notional neighbouring burners, with extended zones of cold temperature at the edges of the domain. The jets in the ED case seem to reach further downstream in the chamber than in the Lee case [59]. Potential effects of this on acoustic forcing results are investigated in section 6.3.3.

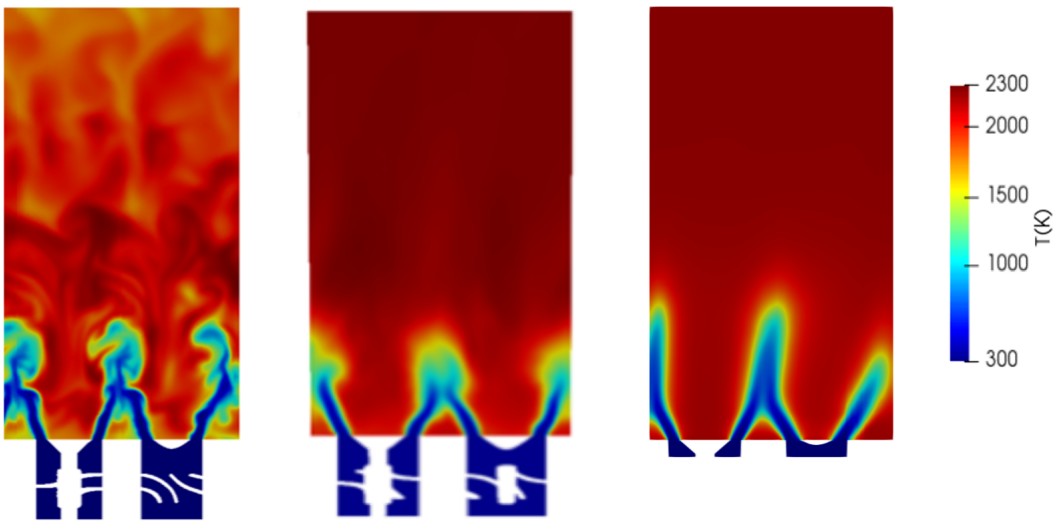

Fig. 6.15 Radial-normal planar cuts coloured by temperature for instantaneous LES (left) [59], averaged LES (centre) [59] and ED (right) cases.

Figure 6.16 shows an integrated line of sight experimental plot [7] for two consecutive burners from the full burner results presented in chapter 4, and presented originally by Lee et al. [59] for comparison with LES data. The plot shows that the OH* distribution between neighbouring burners is not entirely uniform, as was discussed in section 6.3.1. Nevertheless, the overall pattern is repeated around the annulus, with consecutive flow recirculation regions (blue) in between flame-merging regions (red) for each burner.

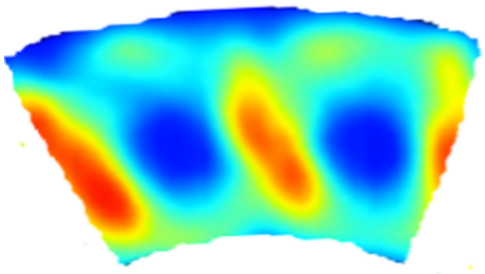

Fig. 6.16 Axial-normal plot of experimental OH* chemiluminescence results for two consecutive burners [7].

Figure 6.17 shows axial-normal plots obtained in the time-averaged LES case [59] (left) and the ED case (right). The streamline results were coloured by temperature. The LES plot

was taken at the top of the jets to highlight the effects of flame-merging, as it was thought that these would be more prominent at this axial location [59]. Consequently, all ED case axial-normal plots coloured by temperature presented from here onwards were taken at this plane. This corresponded to the axial location y = 0.04m in the ED cases. Whilst integrated heat release measurements would be a more representative method for a direct comparison with eperimental results, this was not made possible due to the limited availability of LES data. However the major flow characteristics such as repeated patterns and general shapes of the flame regions could be compared.

Results from the ED case are noticeably closer to the experimental data [7] qualitatively due to the instantaneous nature of the LES [59] snapshots. Indeed, the shape and size of flame merging regions indicated by red colouring in the experimental plot are in better agreement with those represented by blue colouring in the ED case than in the LES case.

Nevertheless, the three plots show similar characteristics with consecutive patterns of flow recirculation in between flame-merging regions for each burner. The recirculation zones are indicated in the experimental plot by the blue circular regions, and in the CFD plots by the red 'looped' patterns on either side of flame-interacting zones. The centre location of the recirculation regions correspond to the centre of each burner, indicating that these are due to the presence of swirl.

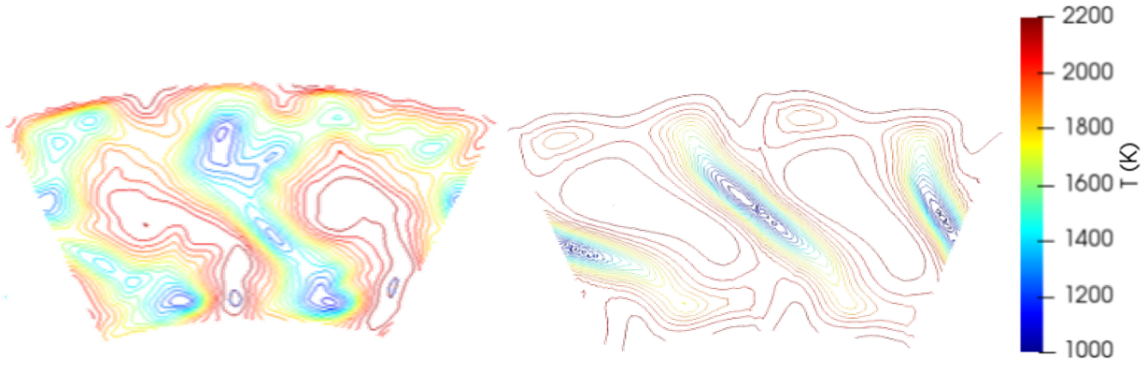

Fig. 6.17 Axial-normal streamline plots coloured by temperature for instantaneous LES [59] (left) and ED (right) cases.

Figures 6.16 and 6.17 showed that the ED modelling approach produced comparable flame characteristics to the Lee [59] case and experimental data [7] in the steady twin burner case.

Full Burner Configuration

Full burner steady reacting cases were run to provide a basis for comparison in acoustic forcing cases in section 6.3.3. The results are compared to LES data from Lee et al. [59] in figure 6.18 and to experimental data from Worth and Dawson [7] in figures 6.18 and 6.19.

Figure 6.18 shows views of the full burner computational domain cut in half tangentially for the LES [59] (left) and ED (right) cases. The plots at the top are coloured by temperature and the plots at the bottom are coloured by velocity magnitude. The substantial computational expense of running the full burner LES simulations was a limiting factor in obtaining time-averaged data from Lee et al. [59]. The corresponding mesh presented chapter 4 counted 120 million cells, which led to significant demands in cost and time both in running the case and post-processing the data. As a consequence, it was also decided by Lee et al. [59] to run LES acoustic forcing cases solely for the single and twin burner configurations.

The discussion on tangential-normal temperature and velocity profiles between instantaneous LES data [59] and results from the ED cases is similar to the cyclic single burner cases in the first part of section 6.3.2. Additional features were, however, highlighted by both modelling approaches in the full annular geometry. In particular, a notable characteristic is the axisymmetry in the jets induced by symmetry in the burner geometry. The temperature and velocity plots show that the jets extending towards the inner and outer chamber cylinders are identical respectively in the ED case. Whilst the instantaneous LES plots [59] show similar behaviour, time-averaged plots would be required to validate this result in the Lee case.

An integrated line of sight measurement was obtained from experimental results produced by Worth and Dawson [7], and is shown in figure 6.19. In this figure, the experimental plot on the left shows OH* chemiluminescence as were shown in figure 4.3 on the left and 4.6 on the right. Similar comments can be made as in the twin burner case. The repeated pattern of flame-merging and recirculation regions is shown here around the full annular geometry. Non-uniformity in consecutive burners is also found in this configuration, with varying shapes and sizes of the flame-merging areas in red.

As previously, a direct comparison with the CFD data was not plausible, but major flow features are expected to be represented by the ED results. A temperature plot was extracted from the ED case at the tip of the jets in a similar manner to the twin-burner configuration and is shown in figure 6.20.

The flow represented shares similarities with experimental data in the flame-merging patterns around the annulus, with equally-spaced regions of recirculation and flame-flame interaction as was found in the twin burner cases. The aspect of the flame-merging regions is close to an S-shape in both cases, with the two ‘branches’ of the S stemming from the

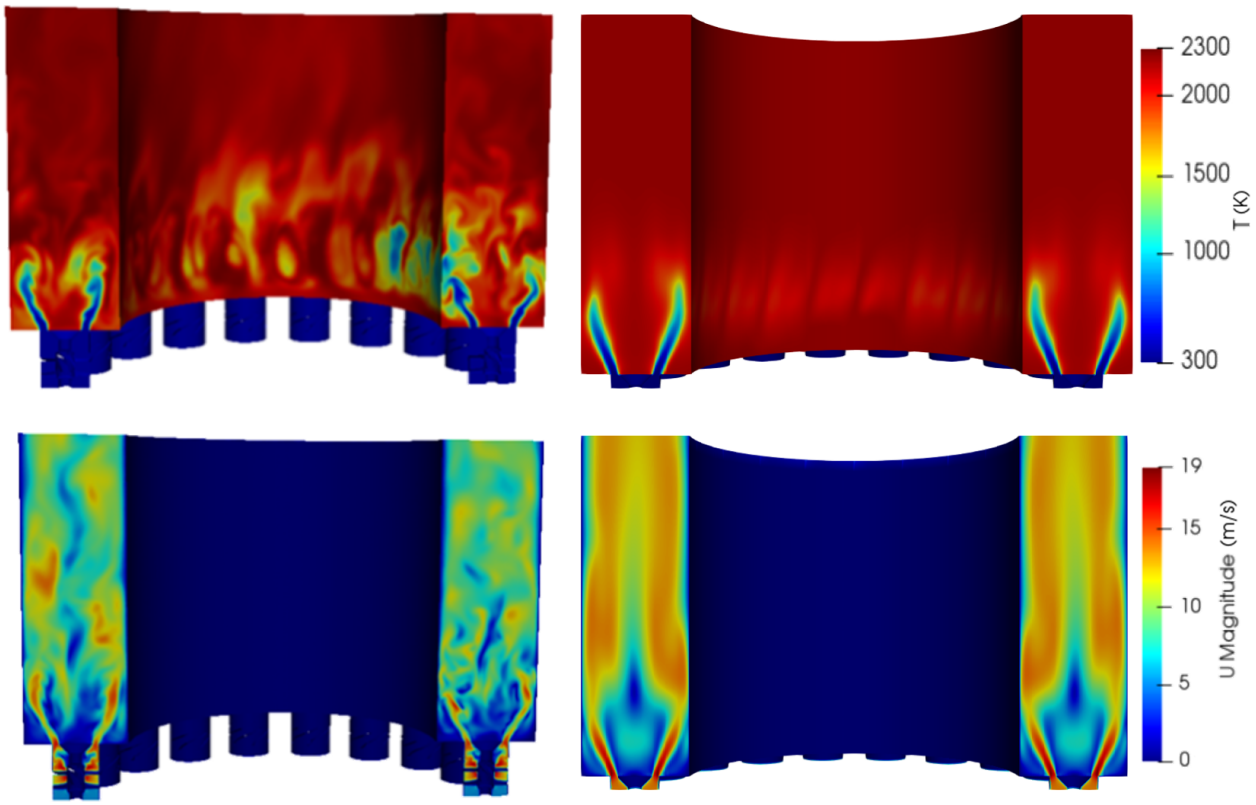

Fig. 6.18 Tangential-normal view of temperature (top) and velocity magnitude (bottom) distribution for LES [59] (left) and ED (right) simulations.

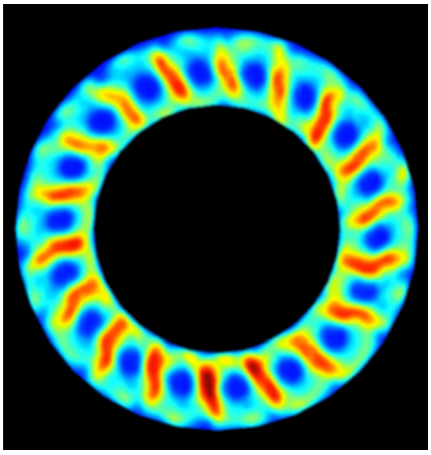

Fig. 6.19 Axial-normal view of full burner OH* chemiluminescence experimental results [7].

core of the chamber and extending to the external walls radially. This characteristic can be attributed to the presence of swirl in each burner. A notable difference between the ED and

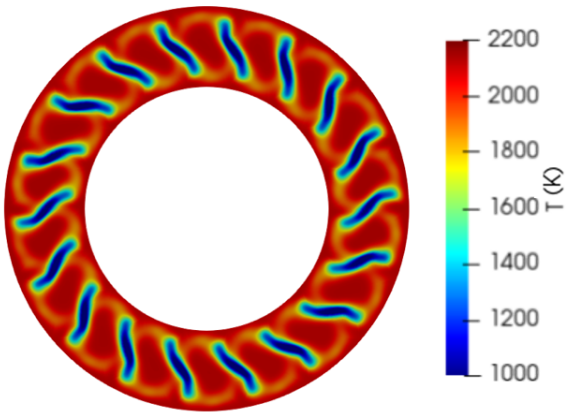

Fig. 6.20 Axial-normal view of full burner ED case temperature distribution.

experimental data is that of the repeatability of the flow patterns, as the ED case considers an ideal environment where the flow distribution would be uniform around the annulus.

The ED full burner case showed very regular and repeated flow behaviour around the annulus, which is expected from the geometry. Axisymmetry was well represented by the results obtained. Aside from the expected discrepancies in uniformity, the flow behaviour was similar qualitatively to the Lee [59] case and experimental data [7].

Comparative Study

A comparative study between the single, twin and full burner ED cases was conducted to highlight the possible differences in steady reacting flow behaviour between a cyclic boundary condition and physically-represented burners. If significant differences appeared, this study could also give insight into the differences that could be expected between the configurations when subject to acoustic forcing. The three configurations were first compared using radial-normal cylindrical cuts coloured by temperature as shown in figure 6.21. The radial-normal cut of the full burner was sliced in half to provide an inner view of the combustor. It was shown in the previous subsection that the results were axisymmetric, thus performing this cut would not affect the conclusions to be drawn from the plot.

In figure 6.21, the plot on the left shows results for a cyclic single burner configuration, the plot in the middle, for a cyclic twin burner configuration and the plot on the right, for the full burner configuration. The symmetrical nature of the data around the annulus is clearly represented in the twin and full burner results, where the physical aspect of the cold reactant jets penetrating the chamber is identical between the burners. The flow behaviour in the

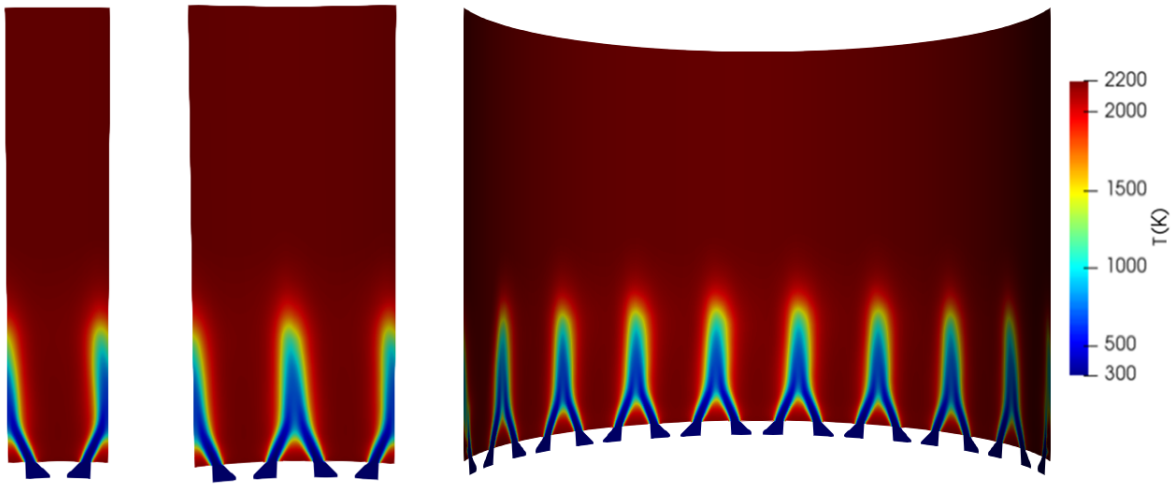

Fig. 6.21 Radial-normal cylindrical cuts coloured by temperature for the cyclic single burner (left), cyclic twin burner (centre) and full burner (right) configurations using the ED modelling approach.

single burner geometry is also identical to single-burner sections of the twin and full annular configurations.

Figure 6.22 shows the velocity magnitude profiles taken across burners in a tangential-normal plane, at several locations along the combustion chamber.

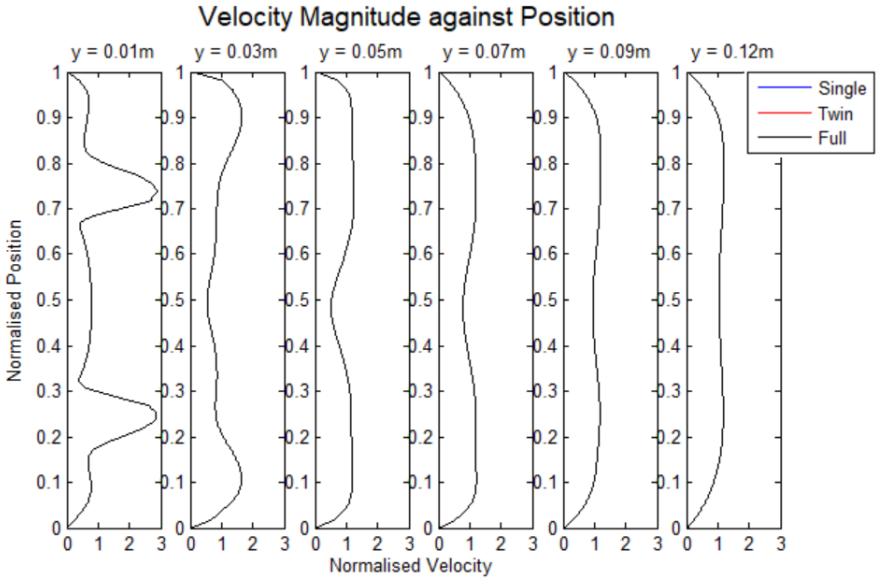

Fig. 6.22 Velocity against position along the combustion chamber for the single (blue), twin (red) and full (black) burner ED steady-flame simulations.

The twin and full burner results were taken across each burner and averaged for this plot. The velocity was normalised by the bulk flow velocity in each case. The figure shows that the cyclic single burner geometry resulted in identical velocity profiles to the twin and full burner geometries. The flame shape is shown to be identical in each burner, as could be anticipated from the boundary conditions implemented. The three ED cases thus agree with each other.

The presence of neighbouring burners in the twin and full geometries could, however, affect the results obtained when applying acoustic forcing boundary conditions at the inlet plane. The investigations in the next sections focused on the flame response to acoustic excitation in the cyclic single, cyclic twin and full burner configurations.

6.3.3 Forced Reacting Flow

Forcing Amplitude

The study by Armitage et al. [41] suggested that high frequency forcing would lead to noticeable differences in the flame response to acoustic excitation with varying oscillation amplitudes. The abilities of the ED modelling method to show these differences is investigated in the first set of forced reacting flow simulations. The results were compared to those obtained in the corresponding Lee case [59].

ED Case

The ED cyclic reacting single burner case was forced using a sinusoidal velocity inlet boundary condition. The frequency was set to 160Hz, and amplitude to 0.65 and 0.25. The resulting tangential-normal cuts coloured by temperature during one period of oscillation are presented in figure 6.23. The frames were taken at the same instants as for the ED forcing cases presented in chapter 5, and are numbered 1 to 6 from left to right for convenience. The temperature range was changed to match the LES plots from Lee et al. [59].

The data sets at both amplitudes show similar flame behaviour, with the flame front extending in the chamber from frames 1 to 4 then retreating from frames 4 to 6. This corresponded to an increase followed by a decrease in inlet velocity. The vortex mechanisms driving the behaviour of the flame during an oscillation period were discussed extensively in chapter 5 and will thus not be repeated here.

Some of the characteristic behaviour of high amplitude forcing detailed in chapter 5 is represented in the top row, which correspond to the forcing amplitude of 0.65. The mushroom shapes arising from the rollup of the flame can be seen to form from frames 2 to 4 where the low temperature areas at the top of the jets become progressively larger.

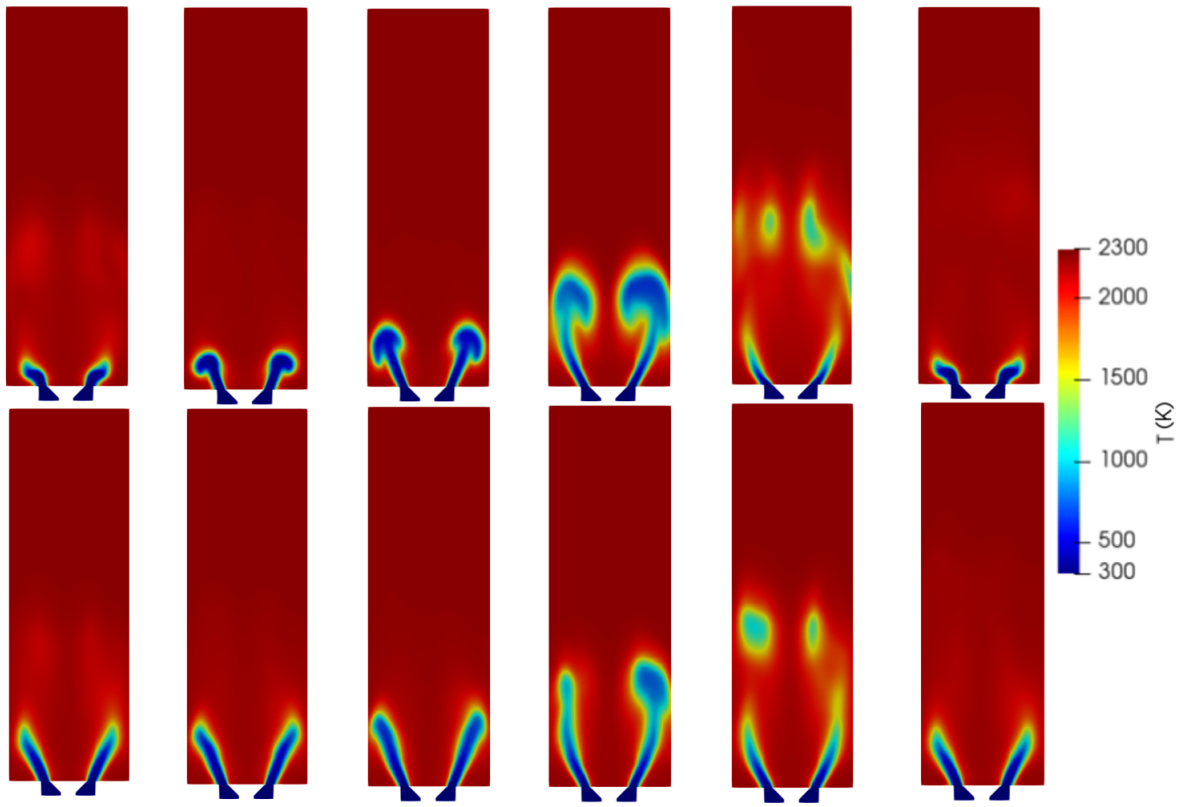

Fig. 6.23 Tangential-normal planar cuts coloured by temperature for the forced ED cyclic single burner case during one period of oscillation. Results for $A = 0.65$ are shown at the top, and results for $A = 0.25$ are shown at the bottom.

Flame detachment regions can be noticed in frame 5 as the flame front reached its peak axial location in the chamber. These are seen to propagate towards the outlet, as indicated by the yellow-coloured regions downstream in frame 6.

The transition from frame 6 to frame 1 shows that the cycle is repeated, with the downstream propagation of the flame detachment zones and the secondary roll up at the flame fronts that will then extend into new mushroom shapes. The repeatability of the cycle is also shown in the the lower forcing amplitude data set in the bottom row. The flame front can also be seen to extend from frame 1 to 4, then retract from frames 4 to 6.

Major qualitative differences between the two forcing amplitude cases emerge in the shape and size of the flame front and flame detachment regions. The difference in height of the jets is less pronounced from frame 1 to frame 4 in the lower amplitude data set, which can be anticipated due to the smaller difference in inlet velocity between the two frames in this case. As a result, the mushroom shapes shown in the high amplitude case are also less noticeable in the lower amplitude data.

The flame detachment regions also differ in shape and size. In frame 5, the detachment zones are clearly visible in both cases in the low temperature regions separated from the anchored flame propagating towards the outlet. In the $A = 0.65$ case, the zones stemming from both jets can be seen to interact downstream as can be observed in the merging of the lighter red regions past the flame front. In the $A = 0.25$ case, however, the lighter red regions downstream of both jets are thinner and disconnected, leading to less distortion of the downstream flow field.

This behaviour mirrors qualitative findings by Armitage et al. [41], who found that the flame shape was far less distorted at lower forcing amplitudes than at high amplitudes, as could be expected. At very low forcing amplitudes, Armitage et al. [41] found that flame detachment was not visible during the oscillating period.

High amplitude forcing thus generated more significant flame distortion throughout the oscillating period, which was a qualitative result found in the Armitage case [41]. This was analysed further quantitatively in figures 6.24 and 6.25. Figure 6.24 shows time series plots of inlet signal (blue) and heat release response (red) for $A = 0.25$ (top) and $A = 0.65$ (bottom). The data was gathered over 3 cycles, as was done previously for the oscillating cases in chapter 5.

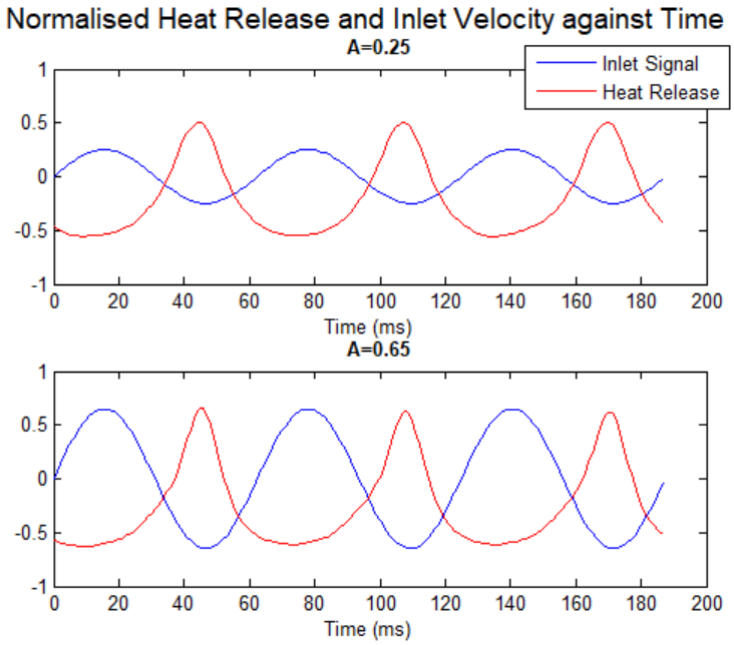

Fig. 6.24 ED case time-series of heat release response (red) and inlet velocity signal (blue) for $A = 0.25$ (top) and $A = 0.65$ (bottom).

The repeatability of the cycle is made evident by the regular patterns of heat release obtained in both amplitude forcing cases, in response to the sinusoidal inlet velocity function. A loss of sinusoidal shape can be observed in both heat release series, which was described in chapter 5 as indicative of non-linearity. The gradients at the peaks of heat release are noticeably steeper for the high amplitude case, mirroring the higher distortion of the flame in the qualitative plots in figure 6.23.

Phase differences are clearly visible in the time series plot, represented by the time delays between the velocity and heat release oscillations in both cases. The time delay is higher in the $A = 0.65$ case from blue to red peaks. However, the difference in amplitude between the blue and red peaks is lower for the same case. This implies that an FDF calculation for the high amplitude forcing case would result in higher phase and lower gain than for the low amplitude forcing case. An FDF plot is shown in figure 6.29 as part of the multi-burner acoustic forcing comparative studies.

Figure 6.25 shows frequency domain representations of inlet velocity (top) and heat release response (bottom) for the high amplitude (red) and low amplitude (blue) forcing cases. In both data sets, the inlet velocity signal shows a single peak at the forcing frequency of 160Hz. The amplitude values at 160Hz for each of the series correspond to the respective forcing amplitude applied. The data was gathered over the 3 cycles represented in figure 6.24.

Harmonic peaks are present at multiples of the forcing frequency in the heat release response for both forcing amplitudes. This indicates non-linearity in the system, as was found by Armitage et al. [41] and described in detail in chapter 5. The harmonic peaks are also visibly higher for the higher forcing amplitude case, thus indicating further non-linearity than in the lower forcing amplitude case. This was explained in chapter 5 as being a result of the higher distortion of the flame. The difference in amplitude variation between the heat release and velocity signals illustrated in figure 6.24 is also shown here. The heat release amplitude is indeed closer to that of the inlet signal in the $A = 0.65$ case at the forcing frequency. This confirms the trend observed in decreasing gain with increasing forcing amplitude.

This characteristic quantitative flame behaviour in the ED case was also found in high frequency forcing cases by Armitage et al. [41], where a plot of the flame transfer function parameters shows an increase in phase and decrease in gain with increasing forcing amplitude.

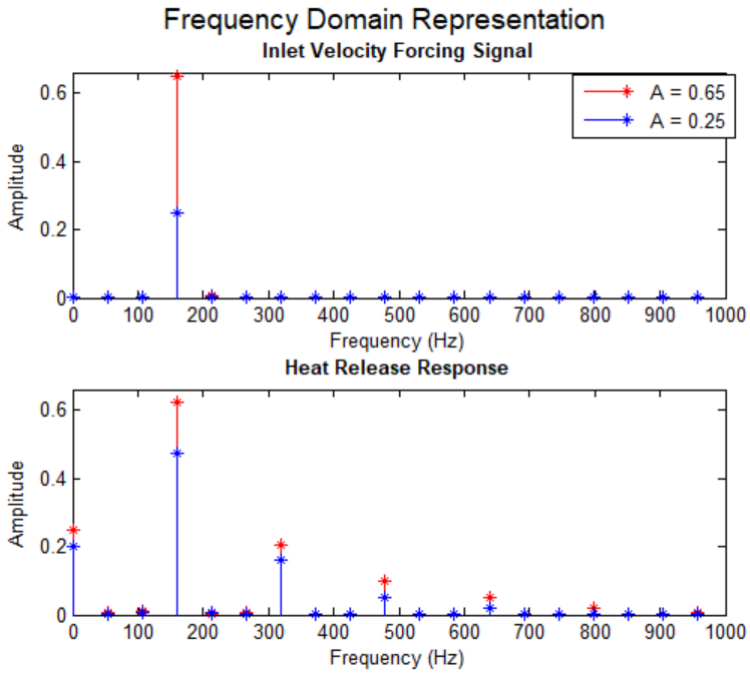

Fig. 6.25 ED case frequency domain representation of inlet velocity signal (top) and heat release response (bottom) for $A = 0.65$ (red) and $A = 0.25$ (blue).

The next subsection presents LES results obtained by Lee et al. [59] for comparison with the ED case.

Lee Case

LES forcing cases were run by Lee et al. [59] on a cyclic single burner configuration. The forcing parameters were identical to those applied to the ED cases. Plots were obtained by Lee et al. [59] instantaneously to show the variations in flame shape when forced. Six frames coloured by temperature were plotted in figure 6.26 for each forcing amplitude during a cycle of oscillation. The top row shows results for the Lee case [59] forced at an amplitude of 0.65, and the bottom row shows results for a forcing amplitude of 0.25. The frames are numbered 1 to 6 from left to right again for convenience.

The Lee case [59] data shows very similar qualitative characteristics to the ED case with varying forcing amplitude. Both series of plots show that the flame extends in the axial direction towards the outlet of the chamber with increasing velocity and retracts when the velocity decreases. The vortex mechanisms behind the extension (frames 1 to 4) and retraction (frames 4 to 6) of the flame during the oscillation period were detailed in chapter 5.

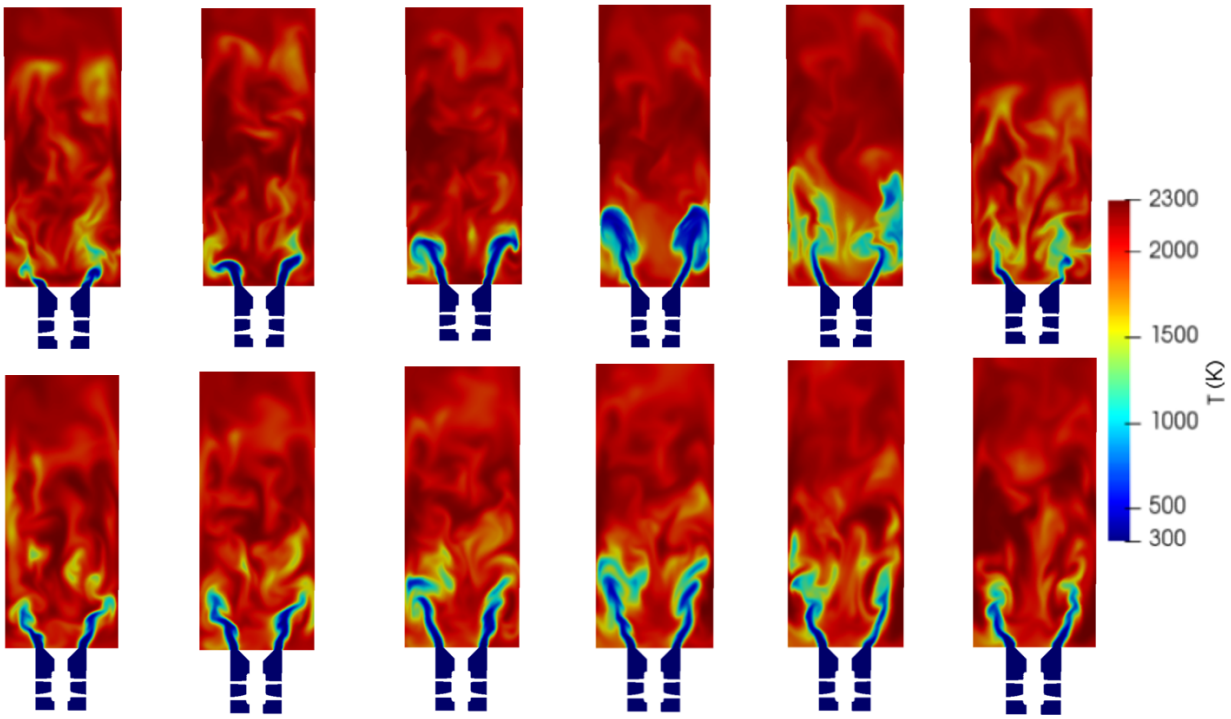

Fig. 6.26 Tangential-normal planar cuts coloured by temperature for the forced LES cyclic single burner [59] case during one period of oscillation. Results for $A = 0.65$ are shown at the top, and results for $A = 0.25$ are shown at the bottom.

Flame detachment regions are visible in frames 5 and 6 in the yellow-coloured regions. The detached flame zones propagate further downstream in the chamber in frames 1 and 2 until disappearing from frames 3 to 5.

Both series of results demonstrate the repeatability of the cycle in a similar fashion to the ED case. The secondary roll up at the flame fronts can be seen to form from frame 6 to frame 1. These will then extend into new mushroom shapes in the next cycle.

The qualitative differences produced by varying the forcing amplitude described in the ED case are also found here. The distortion of the flame front in the extension phase is more significant in the high amplitude case on the top row. Whilst the formation of mushroom shapes at the front of the cold reactant jets is not evident in the $A = 0.25$ plots, the shapes are clearly defined in frames 2 to 4 in the $A = 0.65$ case.

Frames 4 to 6 show that the flame detachment regions are more prominent in the high amplitude forcing case. This can be seen in the downstream propagating yellow-coloured regions, which are reduced in size considerably for the low amplitude forcing case. This result was again found in the ED data shown in figure 6.23.

In all, the characteristic differences observed in the ED case are validated by the behaviour observed in data from Lee et al. [59]. It can be noted that the instantaneous nature of the LES data hinders the visibility of these important features due to the highly chaotic appearance of the flow. In addition, whilst the results in the ED cases are directly comparable at each timestep, averaged data would be required over a number of cycles to obtain a good comparison between the varying forcing amplitude LES cases. This would involve significant additional computational costs compared to the ED modelling approach.

Quantitative investigations were performed by Lee et al. [59] in a similar manner to the ED case. Figure 6.27 shows a time series plot for normalised inlet velocity and heat release during 15 oscillating cycles on the left. The plot on the right shows the corresponding frequency domain representations. In both plots, the dotted line represents the data for the 0.25 amplitude case and the solid line, the data for the 0.65 case. The heat release response is shown in the red lines and inlet velocity signal in the blue lines.

Similar observations to those made in figures 6.24 and 6.25 can be made here. Phase differences can be noticed in the time-series plot between inlet velocity signal and heat release response, which indicates non-linearity. The phase difference is higher between blue and red peaks in the high amplitude case, and the amplitude difference is lower for the same case. Similar comments to the ED case can thus be made regarding the gain and phase of the FDF resulting from these Lee et al. [59] simulations, in that it can be expected that a higher phase and lower gain would be obtained with increasing forcing amplitude.

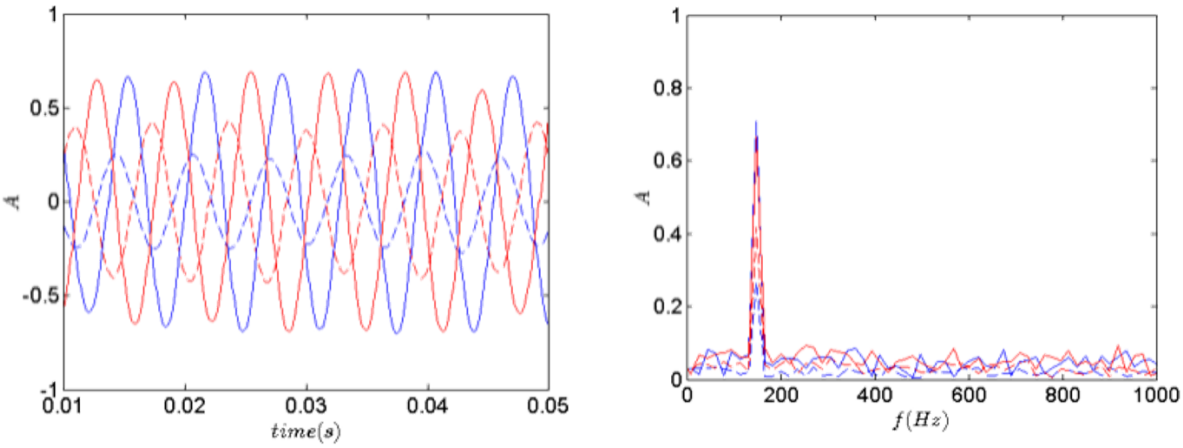

Fig. 6.27 LES time-series (left) and frequency domain representations (right) of heat release response (red) and inlet velocity signal (blue) for $A = 0.65$ (solid lines) and $A = 0.25$ (dotted lines) [59].

The frequency domain plot on the right shows a peak of amplitude at the forcing frequency of 160Hz for all data. The harmonic peaks are difficult to distinguish due to the nature of

the plot. However, Lee et al. [59] described higher harmonic peaks for the higher forcing amplitude, which was found in the ED cases as well.

Whilst a single amplitude amplitude peak found in the velocity signals in the ED cases, variations are also noticeable in both inlet velocity signals in data from Lee et al. [59]. Discrepancies can be further noticed in the non-uniformity of the amplitude between consecutive peaks in the LES time-series plots. This behaviour highlights the need for averaged data in the Lee case [59] to obtain a better appreciation of the flame response during a cycle of oscillation.

In conclusion, the ED modelling approach was capable of illustrating the main trends and characteristics pertaining to high frequency forcing with varying amplitude. The results were compared to reference cases by Lee et al. [59] qualitatively and quantitatively. The reference case by Armitage et al. [41] provided additional comparisons for both the LES [59] and ED cases. It can also be noted at this point that the absence of the physical swirler part in the ED cases did not affect the accuracy of the trends observed in the forced reacting data, which further validates the use of the swirl boundary condition in the single burner geometry.

The tests in this part of the analysis were performed on a cyclic single burner configuration. The next subsection assesses the accuracy of the cyclic boundary condition with regard to the representation of trends in the forced UCAM annular rig.

Multi-Burner Acoustic Forcing

The acoustic forcing boundary condition was applied to the cyclic twin and full burner configurations using the ED modelling approach. The forcing frequency was kept at the value of 160Hz to match the cyclic single burner case described in the previous section and the LES data from Lee et al. [59]. The higher amplitude of 0.65 was chosen as it was anticipated that higher levels of flame distortion would highlight the possible differences between the three burner geometries further. The results were first compared qualitatively in figure 6.28. Quantitative trends were then compared to acoustic multi-burner studies from the Lee case [59] and to trends observed in the Armitage case [41] in figure 6.29.

It was anticipated that the major discrepancies between the data sets would stem from the differences in the flame-flame interactive behaviour. Figure 6.28 shows axial-normal planar cuts coloured by temperature, taken at the tip of the jets in each configuration. This was done similarly to the steady reacting cases in section 6.2 to highlight the effects of flame-merging, which are of interest in this part of the analysis.

The plots on the left represent the results from the cyclic single burner, plots in the middle, from the cyclic twin burner, and plots on the right, from the full burner. The snapshots were

taken at four instants of time during a cycle of oscillation and are numbered frames 1 to 4 from top to bottom for convenience.

The times considered were at the start of a period of oscillation, as velocity rises, decreases, then at the end of the period. The flame behaviour during the cycle as shown in the previous sections would be characterised by an extension and retraction of the flame front. As such, the temperature scales at the single axial location chosen for the planar cuts had to be adjusted at each instant to account for the longitudinal movements of the cold reactant jets.

The three data sets show similar characteristics as the flame front propagates axially. The extension of the cold reactant jets from frame 1 to frame 2 is shown by the increased area of low temperature zones coloured in blue. Conversely, the retraction of the jets from frames 2 to 3 is shown by the larger high temperature regions coloured in red. Frame 4 is identical to frame 1 in the three cases, demonstrating the repeatability of the cycle.

Results from the three configurations show flame-merging regions around the annulus. As in the steady full burner ED reacting case shown in figure 6.20, these are illustrated by the blue regions in all frames. The shape and size of these flame-flame interaction zones at this axial location both depend on the time instant, as expected from the longitudinal movement of the flame front.

Frame 1 shows small discrepancies between the three cases in the flame behaviour at the inner and outer cylinder, as well as between individual burners. The interaction between the jets and the walls produce more prominent flame distortion in the full burner case as demonstrated by the yellow-coloured regions at the inner cylinder. This is represented at the outer cylinder by yellow-coloured ‘strands’ extending from one blue jet-merging region to the next. These two flow features can be attributed to the merging of the swirl-induced central recirculation zones in the full burner, which is not as obviously shown by the cyclic boundary condition simulations in figure 6.28. The twin burner configuration did, however, show this effect in more detail than the single burner geometry as shown by the low velocity region at the inner cylinder near the central blue region.

This trend is also found in frames 2 and 3. The low temperature zones in frame 2 at the inner and outer cylinders are qualitatively different between the three configurations. The cyclic boundary condition somewhat overpredicts flame merging at this instant. Discrepancies can be noticed in the size and shape of the jets between flame-merging regions. Large, cold temperature areas are present in the single and twin burner geometries as indicated by the blue colouring at the inner and outer walls of the domain. In contrast, thinner ‘strands’ link the major flame-merging regions in the full burner geometry, as was found in frame 1.

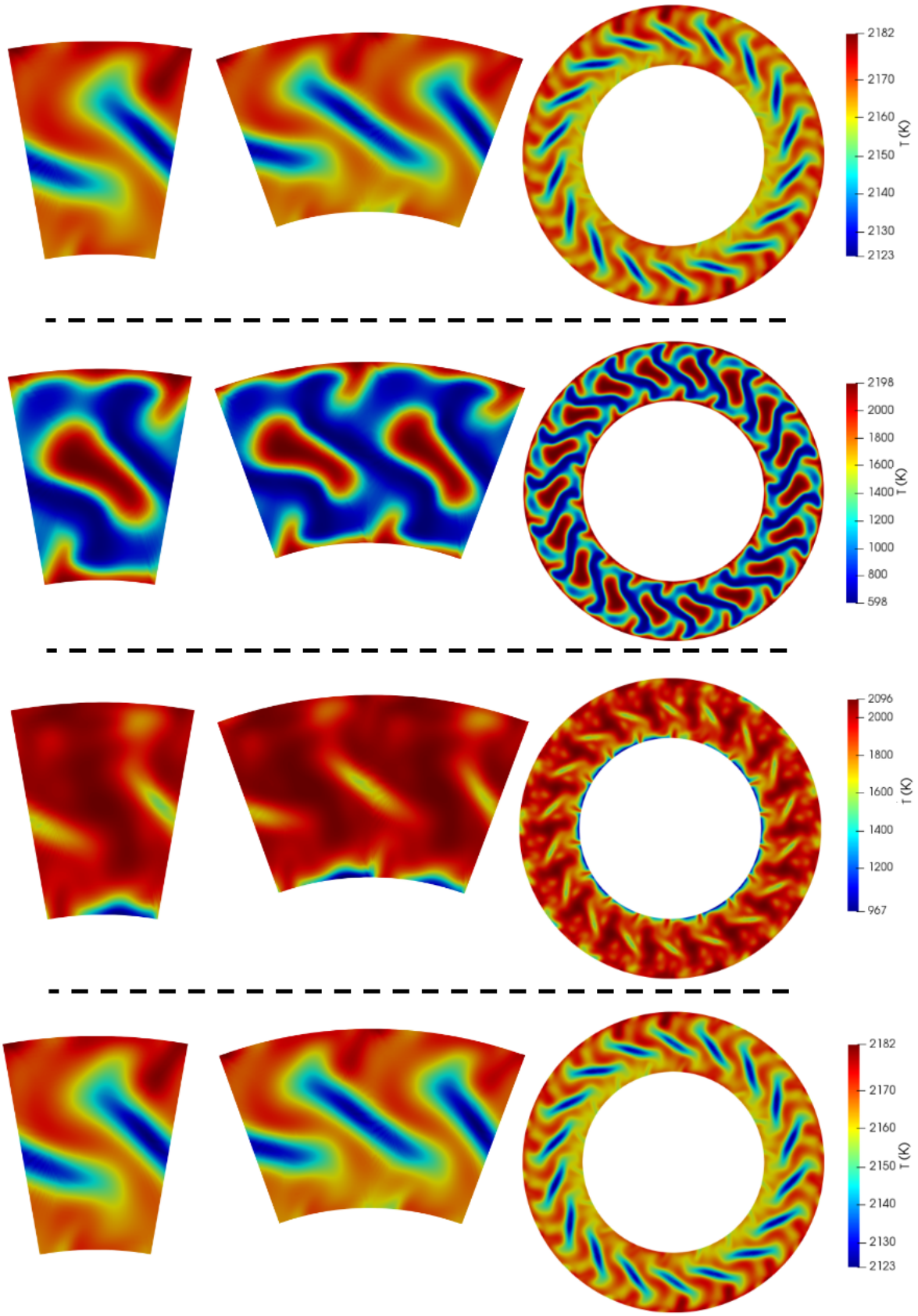

Fig. 6.28 ED case axial-normal plots coloured by temperature during one cycle of oscillation for the cyclic single burner (left), cyclic twin burner (middle) and full burner (right) cases. Frames 1 to 4 numbered from top to bottom.

The flame in frame 3 shows small lower-temperature structures illustrated by lighter-coloured areas scattered around the annulus in the full burner geometry. In contrast, the cyclic single and twin burner geometries produced a smoother transition between burners, with consistent high-temperature zones between flame-merging regions.

Despite the discrepancies mentioned above, the overall aspect of the flame is very similar qualitatively between the three configurations during the cycle of oscillation. The twin burner configuration generated a slight increase in flame distortion compared to the single burner. The full burner geometry globally produced more flame distortion than the cyclic boundary condition cases. This was analysed quantitatively using flame describing functions as shown in figure 6.29.

Flame describing functions were evaluated using the procedure described in chapter 2. Figure 6.29 shows results from the Lee cases [59] on the left, and the ED cases on the right. The gain (top plots) and phase (bottom plots) characterising the quantitative relation between inlet velocity signal and heat release response were obtained for each unsteady simulation.

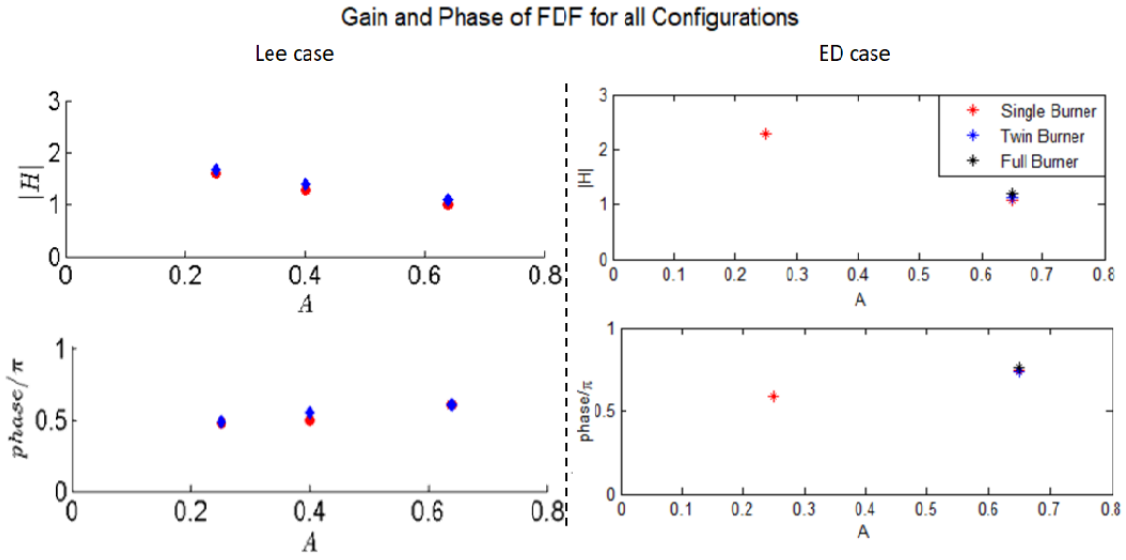

Fig. 6.29 Gain (top) and phase (bottom) of flame describing functions for all configurations forced in the Lee case [59] (left) and ED case (right).

The LES was run by Lee et al. [59] for a frequency of 160Hz and varying amplitude. The single and twin burner geometries were forced at amplitudes of 0.25, 0.4 and 0.65. The full burner geometry was not run in unsteady conditions in the Lee case [59] due to the high computational cost. The plot on the left shows the gain (top) and phase (bottom) of the FDFs. The trends observed in the time-series plots shown in figure 6.24 are confirmed here, with a decrease in gain and increase in phase with increasing forcing amplitude. This trend was

also confirmed previously with reference data from the Armitage case [41]. The gain of the FDF was slightly under-predicted by the single burner configuration compared to the twin burner geometry in all cases. This was attributed to increases in flame distortion induced by the physical presence of a consecutive burner in the mesh, compared to a cyclic boundary condition. This behaviour indicates that the cyclic boundary conditions in OpenFOAM may not be completely accurate. Investigating sources of error in cyclic boundary condition formulation in the OpenFOAM environment was considered beyond the scope of the project.

The plot on the right in figure 6.29 shows the results obtained for the ED simulations. The trends in gain and phase are in agreement with reference data. The single burner configuration led to an increase in phase and a decrease in gain with rising forcing amplitude, as expected from the Lee et al. [59] and Armitage et al. [41] studies. The discrepancies in gain and phase between the ED and LES [59] cases can be attributed to the difference in data acquisition method between the two methodologies. For instance, the instantaneous nature of the LES data gathered by Lee et al. [59] produced irregularities in the inlet velocity signal as shown in figure 6.27, which were not present in results from the ED case shown in figure 6.24.

The three configurations tested with the ED modelling approach produced very similar phase results at $A = 0.65$. The cyclic boundary condition cases led to identical values, but seemed to underestimate the phase very slightly when compared to the full annular geometry. This confirms the observations made qualitatively in figure 6.28, in which it was found that the flame in the full burner configuration was more distorted during the oscillating cycle.

This observation is mirrored in the gain plot at the top. The discrepancies found in gain values in the Lee [59] case between single and twin burner configurations are visible in the ED case on the right and can be attributed to the small increase in flame distortion in the twin burner during the oscillating cycle. The full burner configuration produced a higher gain value than the cyclic boundary condition geometries, which can again be attributed to a further increase in flame distortion in this case.

The ED results in this section were compared against the Lee [59] and Armitage [41] reference cases. The differences between the LES [59] and ED FDF data can be attributed to the instantaneous nature of the LES results. A more in-depth comparison with time-averaged LES or experimental data is required to assess the accuracy of the gain and phase values obtained.

However, it can be said that the ED data during a period of oscillation was very similar between the geometries tested both qualitatively and quantitatively. Despite the small differences, the three ED cases produced FDF parameters that were very similar. The cyclic single burner simulation was also able to represent the trends expected with varying forcing

amplitude at high forcing frequency. It can be noted here again that the absence of the physical swirler in the ED cases did not affect the trends observed.

The combination of ED modelling methodology and cyclic single burner geometry was therefore sufficient to illustrate the trends in flow behaviour obtained in the higher-order reference cases described.

6.4 Summary

This chapter first explored the capabilities of the ED modelling method to represent the effects of operating conditions on steady flame behaviour. The inlet velocity was re-calibrated from the value imposed in chapter 5 to obtain direct comparisons with new reference data. This part of the analysis proved that the ED approach was able to represent the impact of inlet temperature and velocity, inlet equivalence ratio and fuel on steady flame behaviour in a single burner geometry.

The steady multi-burner study in the second part was used to compare results obtained in the ED cases for cyclic single, cyclic twin and full burner configurations. The uniformity of the flow distribution was also discussed. Whilst the ED cases produced consistent and repeating flow distribution between burners, the experimental [7] and Lee cases [59] showed variations in flame shape around the annulus. It was established that non-uniformity in the reference data can be attributed to experimental and numerical error. The error was expected to affect the results obtained in acoustic forcing investigations due to the resulting differences in flame shape between the ED and Lee et al. [59] studies.

The forced-inlet studies in the final part of the chapter showed that the combination of cyclic single burner geometry and ED modelling method was capable of providing insight into the trends in longitudinal oscillatory flame behaviour in the UCAM annular rig. The results were comparable to those obtained in the full annular geometry. Additional work is required to assess the ability of the configuration to capture the acoustic modes expected from the full burner. It was shown in this chapter that if required, the ED modelling approach offers the capability to model the full UCAM annular burner efficiently and in agreement with reference data.

Chapter 7

Conclusions

This chapter summarises the main observations and findings from the work in this thesis. Recommendations for further study on the CFD modelling of oscillatory behaviour in the UCAM rig are also detailed.

7.1 Thesis Summary

The project set out to produce a method capable of providing essential information concerning flame behaviour in the UCAM annular combustor rig under forced oscillating conditions. Due to the industrial nature of the work, the major requirements imposed on the method were to maximise computational efficiency in cost and time all the while maintaining good accuracy.

The first of the main objectives described in chapter 1 consisted in investigating low-cost CFD approaches that would bridge the gap between lower-order modelling and higher-order CFD and experiments. The second consisted in creating a modular geometry and an efficient meshing approach. The third focused on comparing the methodology against data available from previous CFD and experimental studies.

7.1.1 Numerical Models

Chapters 2 and 3 provided background on oscillatory behaviour, analysis methods and numerical modelling. Reference studies by Bainbridge [16], Zettervall et al. [46], Armitage et al. [41] and Lee et al. [59] used to compare data in chapters 5 and 6 were also presented. This literature review was used to identify the options available to address the first objective.

The sole previous CFD study concerned with forced oscillations in the UCAM annular rig was performed by Lee et al. [59] via LES. Lower-cost CFD methods such as eddy-

diffusivity modelling had not been investigated in this context as yet. The thesis assessed the implementation of these models with a view to represent forced-oscillating flame behaviour. Previous studies on swirling flows detailed in chapter 3 and a brief turbulence modelling analysis in chapter 5 both concluded that the $k-\omega$ SST turbulence model was a good option for the investigations in this project.

In addition to this, the PaSR combustion model and one-step chemistry were implemented. The PISO numerical scheme was employed along with a blended Crank-Nicholson scheme for time marching. A second-order central differencing scheme was used for spatial discretisation in smooth regions, and was flux-limited to a first-order scheme in high-gradient areas to ensure boundedness. The reactingFoam solver available within OpenFOAM was used for both isothermal and reacting simulations.

7.1.2 Geometry and Mesh

The second objective was the focus of chapter 4, where the effects of the individual parts of an annular combustor on the flame response were analysed. The study was divided between the main components of the UCAM annular rig, which included the annular enclosure cylinders, the plenum chamber, swirlers and consecutive burners around the annulus. The investigation was used to create parts of a modular CAD geometry.

The final CAD models extracted for analysis included single, twin and full burner configurations. The annular enclosure cylinder heights were adjusted to match, which produced geometries that were comparable with those used in the Bainbridge [16] and Lee et al. [59] cases directly. All configurations were also cut downstream of the plenum chamber to reduce the computational domain, as it was assumed that the effects of swirl and flame-flame interactions would dominate the flame response to acoustic waves.

The swirlers were complex and expensive features to mesh. CAD models cut downstream of the swirlers were therefore also extracted. A swirl inlet velocity boundary condition was created for the simulations run on these configurations and was calibrated against reference data in chapters 5 and 6. The swirl boundary condition allowed for any swirl number and direction to be applied, which thus provided more flexibility in inlet conditions compared to cases using the physical swirler part.

The meshing methods implemented included unstructured Delaunay tetra/hexacore for geometries with swirlers, and unstructured blocking for geometries in which a swirl boundary condition was applied. The blocking method reduced the number of cells required in the mesh significantly.

7.1.3 Modelling Method Validation

The simulations answering the final objective of the thesis were presented in chapters 5 and 6. Testing of the numerical tool was performed in chapter 5 against data from Bainbridge [16] and Armitage et al. [41]. The results in chapter 5 were obtained for a single burner configuration to reduce the computational demands at this stage in the project. The first part of this analysis focused on formulating and calibrating the swirl inlet velocity boundary condition, choosing a turbulence model, and performing a mesh refinement study. Ignition methods were then investigated, the combustion model was chosen, and a forced-oscillation inlet boundary condition was created in combination with the swirl inlet boundary condition. Finally, cyclic boundary conditions were applied to the single burner geometry.

The efficient modelling methodology developed in this project was finalised from the results obtained in chapter 5 and was referred to as the 'ED' modelling approach. It consisted in a combination of the following: $k-\omega$ SST turbulence model, PaSR combustion model, enthalpy spot ignition method, swirl inlet boundary condition for unforced cases and forced-oscillating swirl inlet boundary condition for forced reacting cases. The coarse single burner mesh of 230,000 cells was sufficient to represent the main features of flow behaviour. The cyclic boundary conditions improved the agreement between results from the single burner configuration and results from the full-burner Bainbridge case [16] noticeably.

The ED methodology highlighted the non-linearity between the heat release response of the flame and the inlet signal. The cyclic boundary conditions showed additional non-linear effects induced by the notional flame-flame interactions prescribed.

The adaptability of the ED methodology to various operating conditions was investigated in chapter 6. The results were compared against reference data from Lee et al. [59], Zettervall et al. [46], Armitage et al. [41] and Bainbridge [16]. The first part of the analysis was performed on an enclosed single burner configuration, and showed that the ED method was adaptable to varying inlet temperatures and velocities, varying inlet equivalence ratios, and changing fuels. Additional work on thermochemistry modelling is required to implement a wider variety of fuels.

Multi-burner analyses were then performed to determine the accuracy of the cyclic boundary condition. Small discrepancies were found between cyclic boundary condition cases and full burner studies, which were attributed to inaccuracies in the formulation of cyclic boundaries in the OpenFOAM source code. It was, however, concluded that the trends in forced oscillatory behaviour were comparable between all test cases. The trends obtained were also comparable to those obtained via LES by Lee et al. [59].

In conclusion, the ED modelling methodology was found to fit the efficiency requirements set for the numerical tool that was to be developed. The objectives defined at the start of the thesis were addressed successfully throughout the project. The results obtained demonstrated the ability of the method to illustrate trends in forced oscillatory behaviour in the UCAM rig observed in the reference data efficiently. The next section describes possible extensions to this work.

7.2 Future Work

Possible extensions to the project can be divided into several categories: work on the UCAM rig geometry, and investigations on operating conditions.

The modular CAD geometry allows for any part of the combustor to be re-implemented or modified further in the future. A first possible investigation could be concerned with validating the assumption made in this project regarding the plenum chamber. The capabilities of the ED modelling approach to capture the coupling between acoustic waves in the annular plenum chamber and in the annular combustion chamber could be assessed.

The combustion chamber cylinder heights were adjusted to be equal to each other for the work in this thesis, as was done by Bainbridge [16] and Lee et al. [59]. Bainbridge [16] modified inlet conditions from the original experimental setup to encourage self-excited oscillations in this configuration. Eddy-diffusivity models were not able to capture self-sustained oscillations in this geometry in the Bainbridge [16] study. However, the results in chapters 5 and 6 showed that forced oscillatory behaviour was well represented by the ED modelling approach. A second potential future investigations could then be concerned with the effects of cylinder heights and downstream boundary conditions on the ability of the ED methodology to represent self-excited oscillations.

Future studies on operating conditions could include additional validation of the fuel study presented in chapter 6, for which the available reference data was limited. The flame separation distance could also be modified by increasing the distance between burners to assess the capability of the ED method to mirror the corresponding experimental data obtained by Worth and Dawson [7] presented in chapter 4. In a similar fashion, the effects of swirl direction and swirl number could be investigated using the swirl inlet velocity boundary condition.

A more comprehensive FDF study could also be carried out using the ED method. The twin and full burner configurations were forced at a single high amplitude value as presented in chapter 6. Further validation of the modelling methodology could be achieved by forcing

these geometries at the lower amplitudes to observe the trends obtained compared to the single burner configuration. In addition, the effects of forcing frequency could be investigated to assess the accuracy of the ED method in capturing the corresponding trends in FDF observed by Armitage et al. [41]. This can be achieved by forcing the single, twin, and full burner geometries at a range of frequencies using the oscillating swirl inlet boundary condition.

Finally, the UCAM annular rig was forced longitudinally in the present work. The effects of transverse forcing can, however, also be of interest due to the presence of azimuthal modes in annular combustor geometries. Acoustic studies could be performed to analyse the modes captured by the ED modelling approach in comparison with reference data. The effects of cyclic boundary conditions could also be observed in this context, with a comparative study between acoustic modes captured in the full UCAM annular rig and those captured in smaller sectors extracted from the full geometry.

References

[1] A. H. Lefebvre and D. R. Ballal. *Gas turbine combustion: alternative fuels and emissions*. CRC press, 2010.

[2] Rolls-Royce Plc. Trent 1000 - Rolls-Royce. [online] https://www.rolls-royce.com/products-and-services/civil-aerospace/airlines/trent-1000.aspx#technology. Accessed: 30/10/2018.

[3] A. Conrado, P. Teixeira Lacava, A. C. Pereira Filho, and M. de Souza Sanches. Basic Design Principles for Gas Turbine Combustor. In *Proceeding of 10th Brazilian Congress of Thermal Sciences and Engineering*, Rio de Janeiro, 2004.

[4] M. Khosravy el Hossaini. Review of the new combustion technologies in modern gas turbines. In *Progress in Gas Turbine Performance*. InTech, 2013.

[5] T. Lancien, K. Prieur, D. Durox, S. Candel, and R. Vicquelin. Large eddy simulation of light-round in an annular combustor with liquid spray injection and comparison with experiments. *Journal of Engineering for Gas Turbines and Power*, 140(2):021504, 2018.

[6] M. P. Boyce. *Gas Turbine Engineering Handbook (Fourth Edition)*. Butterworth-Heinemann, 2012.

[7] N. A. Worth and J. R. Dawson. Modal dynamics of self-excited azimuthal instabilities in an annular combustion chamber. *Combustion and Flame*, 160(11):2476–2489, 2013.

[8] S. R. Stow and A. P. Dowling. Thermoacoustic oscillations in an annular combustor. In *ASME Turbo Expo 2001: Power for Land, Sea, and Air*, volume 2, 2001.

[9] J. W. S. Rayleigh. The explanation of certain acoustical phenomena. *Nature*, 18:319–320, 1878.

[10] J. W. S. Rayleigh. The theory of sound, vol. 2. *reprinted by New York: Dover*, 1945.

[11] J. O'Connor, S. Natarajan, M. Malanoski, Da. Noble, and T. Lieuwen. Response of an annular burner nozzle to transverse acoustic excitation. In *48th AIAA Aerospace Sciences Meeting Including the New Horizons Forum and Aerospace Exposition*, page 1151, 2010.

[12] C. Y. Lee. *Numerical investigation of combustion instabilities in afterburners*. PhD thesis, University of Cambridge, 2015.

[13] T. Poinsot and D. Veynante. *Theoretical and numerical combustion*. RT Edwards, Inc., 2005.

[14] G. Staffelbach. *Simulation aux grandes echelles et analyse acoustique de turbines a gaz industrielles multi-bruleurs*. PhD thesis, Toulouse, INPT, 2006.

[15] T. Makuni. Thermo-acoustic Instabilities in a Model Annular Gas Turbine Combustor. Master's Thesis, 2012.

[16] W. Bainbridge. *The Numerical Simulation of Oscillations in Gas Turbine Combustion Chambers*. PhD thesis, University of Cambridge, 2013.

[17] M. J. Lighthill. On sound generated aerodynamically I. General theory. *Proc. R. Soc. Lond. A*, 211(1107):564–587, 1952.

[18] W. C. Strahle. Combustion noise. *Progress in Energy and Combustion Science*, 4(3):157–176, 1978.

[19] F. E. Marble and S. M. Candel. Acoustic disturbance from gas non-uniformities convected through a nozzle. *Journal of Sound and Vibration*, 55(2):225–243, 1977.

[20] M. Ihme, J. O'Brien, and J. Kim. Compositional inhomogeneities as a source of indirect combustion noise: Physical mechanisms and fuel effects. In *24th International Congress on Sound and Vibration, ICSV 2017*, 2017.

[21] A. S. Morgans, C. S. Goh, and J. A. Dahan. The dissipation and shear dispersion of entropy waves in combustor thermoacoustics. *Journal of Fluid Mechanics*, 733, 2013.

[22] F. De Domenico, E. O. Rolland, and S. Hochgreb. Detection of direct and indirect noise generated by synthetic hot spots in a duct. *Journal of Sound and Vibration*, 394:220–236, 2017.

[23] F. A. Williams. *Combustion theory*. CRC Press, 1985.

[24] T. Loiseleux, J. M. Chomaz, and P. Huerre. The effect of swirl on jets and wakes: Linear instability of the rankine vortex with axial flow. *Physics of Fluids*, 10(5):1120–1134, 1998.

[25] P. Huerre and P. Monkewitz. Local and global instabilities in spatially developing flows. *Annual Review of Fluid Mechanics*, 22(1):473–537, 1990.

[26] P. G. Drazin. *Introduction to Hydrodynamic Stability*. Cambridge University Press, Cambridge, 2002.

[27] Helmholtz. On discontinuous movements of fluids. *The London, Edinburgh, and Dublin Philosophical Magazine and Journal of Science*, 36(244):337–346, 1868.

[28] W. T. Kelvin. Hydrokinetic solutions and observations. *The London, Edinburgh, and Dublin Philosophical Magazine and Journal of Science*, 42(281):362–377, 1871.

[29] P. Knoop, F. E. C. Culick, and E. E. Zukoski. Extension of the stability of motions in a combustion chamber by nonlinear active control based on hysteresis. *Combustion science and technology*, 123(1-6):363–376, 1997.

[30] T. Lieuwen and Y. Neumeier. Nonlinear pressure-heat release transfer function measurements in a premixed combustor. *Proceedings of the Combustion Institute*, 29(1):99–105, 2002.

[31] Y. Huang and V. Yang. Bifurcation of flame structure in a lean-premixed swirl-stabilized combustor: transition from stable to unstable flame. *Combustion and Flame*, 136(3):383–389, 2004.

[32] M. Juniper. Absolute and convective instability in gas turbine fuel injectors. *Proceedings of the ASME Turbo Expo*, 2, 2012.

[33] A. K. Gupta, D. G. Lilley, and N. Syred. *Swirl Flows*. Abacus Press, 1984.

[34] P. Billant, J. Chomaz, and P. Huerre. Experimental study of vortex breakdown in swirling jets. *Journal of Fluid Mechanics*, 376:183–219, 1998.

[35] K. Oberleithner, M. Sieber, C. Nayeri, C. Paschereit, C. Petz, H-C. Hege, B. Noack, and I. Wygnanski. Three-dimensional coherent structures in a swirling jet undergoing vortex breakdown: Stability analysis and empirical mode construction. *Journal of Fluid Mechanics*, 679:383–414, 2011.

[36] K. Manoharan, S. Hansford, J. O' Connor, and S. Hemchandra. Instability mechanism in a swirl flow combustor: Precession of vortex core and influence of density gradient. *Proceedings of the ASME Turbo Expo*, 2015.

[37] R. Balachandran. *Experimental investigation of the non linear response of turbulent premixed flames to imposed inlet velocity oscillations*. PhD thesis, University of Cambridge, 2005.

[38] P. L. Rijke. Notice of a new method of causing a vibration of the air contained in a tube open at both ends. *The London, Edinburgh, and Dublin Philosophical Magazine and Journal of Science*, 17(116):419–422, 1859.

[39] N. P. Jamieson, G. Rigas, and M. P. Juniper. Experimental sensitivity analysis via a secondary heat source in an oscillating thermoacoustic system. *International Journal of Spray and Combustion Dynamics*, 9(4):230–240, 2017.

[40] F. Nicoud and T. Poinsot. Thermoacoustic instabilities: Should the Rayleigh criterion be extended to include entropy changes? *Combustion and Flame*, 142(1-2):153–159, 2005.

[41] C. A. Armitage, R. Balachandran, E. Mastorakos, and R. S. Cant. Investigation of the nonlinear response of turbulent premixed flames to imposed inlet velocity oscillations. *Combustion and Flame*, 146(3):419–436, 2006.

[42] L. Crocco and S. Cheng. Theory of combustion instability in liquid propellant rocket motors. Technical report, Princeton University, 1956.

[43] J. O. Keller, T. T. Bramlette, C. K. Westbrook, and J. E. Dec. Pulse combustion: The quantification of characteristic times. *Combustion and flame*, 79(2):151–161, 1990.

[44] H. Zhao, G. Li, D. Zhao, Z. Zhang, D. Sun, W. Yang, S. Li, Z. Lu, and Y. Zheng. Experimental study of equivalence ratio and fuel flow rate effects on nonlinear thermoacoustic instability in a swirl combustor. *Applied Energy*, 208:123–131, 2017.

[45] N. A. Worth and J. R. Dawson. Effect of equivalence ratio on the modal dynamics of azimuthal combustion instabilities. *Proceedings of the Combustion Institute*, 36(3):3743–3751, 2017.

[46] N. Zettervall, N. A. Worth, M. Mazur, J. R. Dawson, and C. Fureby. Large eddy simulation of ch4-air and c2h4-air combustion in a model annular gas turbine combustor. *Proceedings of the Combustion Institute*, 2018.

[47] A. P. Dowling and S. R. Stow. Acoustic analysis of gas turbine combustors. *Journal of propulsion and power*, 19(5):751–764, 2003.

[48] D. Fanaca. *Influence of burner-burner interactions on the flame dynamics in an annular combustor*. PhD thesis, Technische Universität München, 2010.

[49] D. Laera, G. Campa, S. M. Camporeale, E. Bertolotto, S. Rizzo, F. Bonzani, A. Ferrante, and A. Saponaro. Modelling of thermoacoustic combustion instabilities phenomena: Application to an experimental test rig. *Energy Procedia*, 45:1392–1401, 2014.

[50] G. Staffelbach, L. Y. M. Gicquel, G. Boudier, and T. Poinsot. Large eddy simulation of self excited azimuthal modes in annular combustors. *Proceedings of the Combustion Institute*, 32(2):2909–2916, 2009.

[51] P. Wolf, G. Staffelbach, L. Y. M. Gicquel, J. Müller, and T. Poinsot. Acoustic and large eddy simulation studies of azimuthal modes in annular combustion chambers. *Combustion and Flame*, 159(11):3398–3413, 2012.

[52] G. Ghirardo and M. P. Juniper. Azimuthal instabilities in annular combustors: standing and spinning modes. *Proceedings of the Royal Society A*, 469(2157), 2013.

[53] G. Ghirardo. *Nonlinear analysis of thermoacoustic modes in axisymmetric annular combustors*. PhD thesis, University of Cambridge, 2016.

[54] G. J. Bloxsidge, A. P. Dowling, and P. J. Langhorne. Reheat buzz: an acoustically coupled combustion instability. part 2. theory. *Journal of fluid mechanics*, 193:445–473, 1988.

[55] C. A. Armitage, R. S. Cant, A. P. Dowling, and T. P. Hynes. Linearised theory for LPP combustion dynamics. In *ASME Turbo Expo 2003, collocated with the 2003 International Joint Power Generation Conference*, pages 499–508. American Society of Mechanical Engineers, 2003.

[56] C. A. Armitage, A. J. Riley, R. S. Cant, A. P. Dowling, and S. R. Stow. Flame transfer function for swirled LPP combustion from experiments and CFD. In *ASME Turbo Expo 2004: Power for Land, Sea, and Air*, pages 527–537. American Society of Mechanical Engineers, 2004.

[57] D. Laera. Nonlinear combustion instabilities analysis of azimuthal mode in annular chamber. *Energy Procedia*, 82:921–928, 2015.

[58] Y. Xia, D. Laera, and A. S. Morgans. Effect of Flame-to-flame interaction on the flame describing function of a turbulent swirling flame in an annular combustor. In *25th International Congress on Sound and Vibration*, Hiroshima, Japan, 2018.

[59] C. Y. Lee and R. S. Cant. AMEL Project Deliverable 3.3: Validated CFD Methods for Prediction of Full Annular Combustor Instabilities. Technical report, 2016.

[60] C. Hirsch. *Numerical computation of internal and external flows: The fundamentals of computational fluid dynamics*. Butterworth-Heinemann, 2007.

[61] S. E. Norris. *A Parallel Navier Stokes Solver for Natural convection and Free Surface Flow*. PhD thesis, 2000.

[62] R. S. Cant. Direct numerical simulation of premixed turbulent flames. *Philosophical Transactions of the Royal Society of London A: Mathematical, Physical and Engineering Sciences*, 357(1764):3583–3604, 1999.

[63] M. Schäfer. *Computational engineering: Introduction to numerical methods*. Springer, 2006.

[64] P. K. Sweby. High resolution schemes using flux limiters for hyperbolic conservation laws. *SIAM journal on numerical analysis*, 21(5):995–1011, 1984.

[65] J. Crank and P. Nicolson. A practical method for numerical evaluation of solutions of partial differential equations of the heat-conduction type. In *Mathematical Proceedings of the Cambridge Philosophical Society*, volume 43, pages 50–67. Cambridge University Press, 1947.

[66] OpenCFD Ltd. OpenFOAM: Open source CFD. [online] https://www.openfoam.com/documentation/cpp-guide/html/index.html. Accessed: 30/10/2018.

[67] S. Seng, C. Monroy, and S. Malenica. On the use of euler and Crank-Nicolson time-stepping schemes for seakeeping simulations in Openfoam. *7th International Conference on Computational Methods in Marine Engineering, MARINE 2017*, 2017:905–920, 2017.

[68] R. I. Issa. Solution of the implicitly discretised fluid flow equations by operator-splitting. *Journal of computational physics*, 62(1):40–65, 1986.

[69] M. Chapuis, C. Fureby, E. Fedina, N. Alin, and J. Tegnér. Les modeling of combustion applications using openfoam. In *Proceeding of the 5th European Conference on Computational Fluid Dynamics*, pages 14–17, 2010.

[70] C. Fureby. LES of a multi-burner annular gas turbine combustor. *Flow, turbulence and combustion*, 84(3):543–564, 2010.

[71] W. P. Jones and B. E. Launder. The prediction of laminarization with a two-equation model of turbulence. *International journal of heat and mass transfer*, 15(2):301–314, 1972.

[72] S. B. Pope. An explanation of the turbulent round-jet/plane-jet anomaly. *AIAA journal*, 16(3):279–281, 1978.

[73] R. Weber, B. M. Visser, and F. Boysan. Assessment of turbulence modeling for engineering prediction of swirling vortices in the near burner zone. *International Journal of Heat and Fluid Flow*, 11(3):225–235, 1990.

[74] P. A. Durbin. On the k-epsilon stagnation point anomaly. *International Journal of Heat and Fluid Flow*, 17(1):89–90, 1996.

[75] B.E. Launder and D.B. Spalding. The numerical computation of turbulent flows. *Computer Methods in Applied Mechanics and Engineering*, 3(2):269–289, 1974.

[76] T. Shih, W. Liou, S. A., Z. Yang, and J. Zhu. A new k- eddy viscosity model for high reynolds number turbulent flows. *Computers & Fluids*, 24(3):227–238, 1995.

[77] V. Yakhot, S. A. Orszag, S. Thangam, T. B. Gatski, and C. G. Speziale. Development of turbulence models for shear flows by a double expansion technique. *Physics of Fluids A: Fluid Dynamics*, 4(7):1510–1520, 1992.

[78] D. Díaz and D. F. Hinz. Performance of eddy-viscosity turbulence models for predicting swirling pipe-flow: Simulations and laser-doppler velocimetry. *arXiv preprint arXiv:1507.04648*, 2015.

[79] D. C. Wilcox. Reassessment of the scale-determining equation for advanced turbulence models. *AIAA journal*, 26(11):1299–1310, 1988.

[80] F. R. Menter. Influence of freestream values on k-omega turbulence model predictions. *AIAA journal*, 30(6):1657–1659, 1992.

[81] F. R. Menter. Two-equation eddy-viscosity turbulence models for engineering applications. *AIAA journal*, 32(8):1598–1605, 1994.

[82] M. N. A. Nazri. *Effect of Different Turbulence Models on Combustion Chamber Pressure Using Computational Fluid Dynamic (CFD)*. PhD thesis, UMP, 2009.

[83] H. M. Abdel-Gayed, W. A. Abdelghaffar, and K. El Shorbagy. Flame vortex interactions in a lean premixed swirl stabilized gas turbine combustor–numerical computations. *American Journal of Scientific and Industrial Research*, pages 449–467, 2013.

[84] T. J. Craft, B. E. Launder, and K. Suga. Development and application of a cubic eddy-viscosity model of turbulence. *International Journal of Heat and Fluid Flow*, 17(2):108–115, 1996.

[85] B. E. Launder, G. Reece, and W. Rodi. Progress in the development of a reynolds-stress turbulence closure. *Journal of fluid mechanics*, 68(3):537–566, 1975.

[86] C. G. Speziale, S. Sarkar, and T. B. Gatski. Modelling the pressure–strain correlation of turbulence: an invariant dynamical systems approach. *Journal of fluid mechanics*, 227:245–272, 1991.

[87] S. B. Pope. Turbulent flows, 2000.

[88] A. Leonard. Energy cascade in large-eddy simulations of turbulent fluid flows. In *Advances in geophysics*, volume 18, pages 237–248. Elsevier, 1975.

[89] B. J. Daly and F. H. Harlow. Transport equations in turbulence. *The Physics of Fluids*, 13(11):2634–2649, 1970.

[90] J. Smagorinsky. General circulation experiments with the primitive equations: I. the basic experiment. *Monthly weather review*, 91(3):99–164, 1963.

[91] K. Lilly. The representation of small-scale turbulence in numerical simulation experiments. *Proceedings of the IBM Scientific Computing Symposium on Environmental Sciences*, pages 195–210, 1966.

[92] R. S. Cant and E. Mastorakos. *An introduction to turbulent reacting flows*. Imperial College Press, 2008.

[93] D. B. Spalding. Mixing and chemical reaction in steady confined turbulent flames. In *Symposium (International) on Combustion*, volume 13, pages 649–657. Elsevier, 1971.

[94] B. F. Magnussen and B. H. Hjertager. On mathematical modeling of turbulent combustion with special emphasis on soot formation and combustion. In *Symposium (international) on Combustion*, volume 16, pages 719–729. Elsevier, 1977.

[95] P. A. Nordin. *Complex chemistry modeling of diesel spray combustion*. Chalmers University of Technology, 2001.

[96] R. Bulirsch and J. Stoer. Numerical treatment of ordinary differential equations by extrapolation methods. *Numerische Mathematik*, 8(1):1–13, 1966.

[97] H. Pitsch. Large-eddy simulation of turbulent combustion. *Annual Review of Fluid Mechanics*, 38:453–482, 2006.

[98] K. T. Kim, J. G. Lee, H. J. Lee, B. D. Quay, and D. A. Santavicca. Characterization of forced flame response of swirl-stabilized turbulent lean-premixed flames in a gas turbine combustor. *Journal of engineering for gas turbines and power*, 132(4):041502, 2010.

[99] S. Jaensch and W. Polifke. Uncertainty encountered when modelling self-excited thermoacoustic oscillations with artificial neural networks. *International Journal of Spray and Combustion Dynamics*, 9(4):367–379, 2017.

[100] R. Balachandran. *Experimental investigation of the response of turbulent premixed flames to acoustic oscillations*. PhD thesis, University of Cambridge, 2005.

[101] C. Fureby and E. Fedina. A computational study of multi-burner annular aero gas turbine. *27th Congress of the International Council of the Aeronautical Sciences 2010, ICAS 2010*, 4:1–10, 2010.

[102] University of Cambridge. Research Computing Services. [online] https://www.hpc.cam.ac.uk/. Accessed: 30/10/2018.

[103] M. Bauerheim and T. Poinsot. Analytical methods for azimuthal thermo-acoustic modes in annular combustion chambers. *Center for Turbulence Research Annual Research Briefs*, 2015.

[104] L. Benoit. Calculations of thermo-acoustic eigenmodes of an annular combustion chamber. *CERFACS/Lehrstuhl für Thermodynamik, Toulouse, France, Technical Report No. TR/CFD/04/44*, 2004.

[105] C. Basson. *An investigation of the effect of inlet-swirl on the flow through a micro-gas turbine combustion chamber*. PhD thesis, Stellenbosch University, 2016.

[106] E. Machover and E. Mastorakos. Experimental investigation on spark ignition of annular premixed combustors. *Combustion and Flame*, 178:148–157, 2017.

[107] A. Bakker. Lecture notes on meshing, 2006.

[108] A. Revell. Lecture notes on advanced aerodynamics, 2014.

[109] P. Tucker. Lecture notes on computational fluid dynamics, 2014.

[110] OpenFOAM. Openfoam-2.3.x github. [online] https://github.com/OpenFOAM/OpenFOAM-2.3.x/tree/master/applications/utilities/mesh. Accessed: 13/07/2018.

[111] S. J. Owen. An introduction to automatic mesh generation algorithms-part ii. Technical report, Sandia National Lab.(SNL-NM), Albuquerque, NM (United States), 2016.

[112] S. Tiribuzi. CFD modelling of combustion instabilities in gas turbine combustors by means of VRG approach. *Italian Section of Combustion Institute, Pisa*, 2006.

[113] K. K. Kuo. *Principles of combustion*. Wiley-Interscience, 2005.

[114] N. A. Worth and J. R. Dawson. Isothermal Experimental Measurements - Private Communication, 2018.